To the Graduate Council:

I am submitting herewith a dissertation written by Bryan Russell Becker entitled "Cooling Tower Recirculation as Influenced by the Local Atmospheric Flow Field, A Numerical Study." I recommend that it be accepted in partial fulfillment of the requirements for the degree of Doctor of Philosophy, with a major in Engineering Science.

Walter Frost

Walter Frost, Major Professor

We have read this dissertation
and recommend its acceptance:

James E Park

John E. Caruthers

James R. Mann

J. Fagan

R L Young

Accepted for the Council:

L Evans Roth

Vice Chancellor
Graduate Studies and Research

Thesis
79b
.B333
cop.2

COOLING TOWER RECIRCULATION AS INFLUENCED BY THE LOCAL ATMOSPHERIC FLOW FIELD, A NUMERICAL STUDY

A Dissertation

Presented for the

Doctor of Philosophy

Degree

The University of Tennessee, Knoxville

Bryan Russell Becker

December 1979

1406079

DEDICATION

To Nancy and Gerhardt

ACKNOWLEDGMENTS

The author would like to take this opportunity to thank some of the many people who have helped him during the course of this study. He would like to express his gratitude to W. Frost, his dissertation advisor, who stole time from his own hectic schedule to review the author's progress periodically and who made many pertinent suggestions. The author wishes to express his appreciation to J. E. Caruthers and J. E. Park, both of whom also periodically reviewed the author's work and gave him technical advice and encouragement. Thanks also to the other members of the author's doctoral committee, T. Feagin, J. R. Maus, and R. L. Young, for their painstaking review of this dissertation.

The author would like to acknowledge J. M. Vance and S. H. Park of the Enrichment Technology Division, Union Carbide Corporation, Nuclear Division for their encouragement and support which made this work possible.

The author is indebted to R. W. Henderson and N. H. Van Wie of the Computer Sciences Division, Union Carbide Corporation, Nuclear Division, for their supportive management.

Special thanks go to S. E. Boles for the many hours she spent patiently typing and retyping the manuscript. The author is indebted to J. S. Cashion and M. H. Cuthbert for their assistance in the preparation of the figures presented in Chapter 5.

The author's thanks go to the entire Computer Services staff of the Oak Ridge Gaseous Diffusion Plant, Union Carbide Corporation, Nuclear

Division. Of this staff, there are several people who deserve special thanks for their support and cooperation: L. H. Edds, P. L. Hicks, S. B. Hopwood, N. L. Lane, and J. D. McCarthy.

The original development work on the atmospheric flow algorithm was supported by NASA (Contract No. NAS8-29584). This work was supported by the Enrichment Technology Division of the Oak Ridge Gaseous Diffusion Plant, operated by Union Carbide Corporation, Nuclear Division, for the United States Department of Energy under U. S. Government Contract W-7405 eng-26.

ABSTRACT

Cooling tower performance is adversely affected by the recirculation of the stack effluent into the tower intake louvers. This recirculation results from a portion of the warm saturated effluent leaving a mechanical draft cooling tower and being reintroduced into the tower by the large captive eddy and corresponding pressure gradients downwind of the tower. This problem is further aggravated by the turbulent mixing which entrains fluid from the plume into the separated wake region from which it is ingested into the cooling tower. The ingested stack effluent enters at an elevated temperature and humidity relative to the ambient and thus reduces the efficiency or effective size of the cooling tower.

A survey of the literature shows that existing methods of numerically modeling cooling tower plume recirculation ignore the aerodynamic effects of the atmospheric flow over the cooling tower. This investigation describes a method of numerically modeling cooling tower plume recirculation which is unique in two respects. First, the structure of the wake region behind the tower is resolved using the two-dimensional turbulent Navier-Stokes equations. Second, the flow field within the cooling tower is modeled as flow through porous media. This interior flow field is then coupled to the atmospheric flow over the tower by matching both pressures and mass flow rates at the cooling tower louvers.

The atmospheric flow over a cooling tower is approximated by a two-dimensional flow field in terms of stream function and vorticity transport equations with the Boussinesq approximation used to account for buoyancy effects. The turbulence effects are modeled using a turbulent viscosity based upon the turbulence kinetic energy and turbulence length

scale, both of which are calculated from transport equations. A transport equation is also used to determine the temperature distribution in the wake region from which the plume profile and recirculation can be determined. The flow field within the cooling tower is calculated as a Darcy flow through porous media. This calculation yields the pressure distribution within the tower. Calculations made with the model are presented. These calculations agree reasonably well with laboratory and field measurements reported in the literature.

TABLE OF CONTENTS

CHAPTER		PAGE
1.	INTRODUCTION	1
2.	NUMERICAL MODEL OF ATMOSPHERIC FLOW OVER A TWO-DIMENSIONAL COOLING TOWER	11
	General Discussion	11
	Governing Equations	13
	Inflow Boundary	20
	Outflow Boundary	24
	Upper Boundary	26
	Ground Level Boundary	27
	Cooling Tower Boundary	31
	Wind Field Pressure Calculation	42
3.	COOLING TOWER INTERNAL PRESSURE MODEL	46
	General Discussion	46
	Discussion of Porous Medium Model	52
	Discussion of the Finite Element Solution Method and Boundary Conditions	54
	Discussion of the Calculation of the Mass Flux Through the Cooling Tower Inlet Louvers	57
	Coupling of the Wind Field Model and the Cooling Tower Internal Pressure Model	64
4.	COMPUTATIONAL TECHNIQUE	67
	Initial Conditions	67
	Convergence Criterion	68

CHAPTER PAGE

4. (Continued)

Resolution of Two Computational Anomalies 70

Computer Usage Statistics 74

5. RESULTS 77

General Discussion 77

Flow Direction and Velocity Profiles 80

Streamlines, Recirculation Bubble and Reattachment Point 120

Wind Field Pressure Distribution 122

Wind Field Temperature Distribution and Turbulent Diffusion 123

Plume Rise and Buoyancy Effects 125

General Discussion of Cooling Tower Recirculation 129

Comparison of Computed Results and Wind Tunnel Experimental Data 130

Comparison of Computed Results and Water Flume Experimental Data 134

Comparison of Computed Results and Field Measurement Data 141

Cooling Tower Performance Degradation Due to Recirculation 145

6. CONCLUSIONS 147

LIST OF REFERENCES 151

CHAPTER PAGE

APPENDICES 158

A. DEVELOPMENT OF THE WIND FIELD EQUATIONS 159

Time Averaged Momentum and Continuity Equations 159

Boussinesq Approximation 161

Introduction of the Stream Function and Vorticity 163

Temperature Transport Equation 165

Turbulence Modeling 167

Turbulence Kinetic Energy Equation 168

Turbulence Length Scale Equation 171

Coefficient Functions 172

Wind Field Pressure Equation 175

B. BOUNDARY CONDITIONS APPLIED TO THE WIND FIELD PRESSURE CALCULATION 182

C. APPLICATION OF THE METHOD OF WEIGHTED RESIDUALS WITH THE GALERKIN PROCESS TO THE COOLING TOWER INTERNAL PRESSURE MODEL 186

D. METHOD OF DATA INPUT 193

VITA 208

LIST OF TABLES

TABLE PAGE

4.1. Values of V_{Floor} Used in the Current Model 71

4.2. Computational Time and Number of Iterations Required for Convergence 75

5.1. Values of the Friction Velocity, u_*, Used in this Study 79

5.2. Reattachment Point Location Measured Downwind from Back of Cooling Tower 121

5.3. Comparison of Current Model to the Plume Rise Equation Given by Briggs [29] 126

5.4. Comparison of Current Model to Wind Tunnel Test Data Reported by Reisman [20] 135

5.5. Comparison of Current Model to Water Flume Data Reported by Kennedy and Fordyce [21] 140

5.6. Comparison of Current Model to Field Test Data Reported by Moore et al. [22] 143

5.7. Cooling Tower Effective Size and Required Design Oversize Due to Recirculation 146

A.1. Derivative of Equation (A.61) 177

A.2. Derivative of Equation (A.62) 179

C.1. Values of the Shape Functions at the Nodes of Region Q Shown in Figure C.1. 189

C.2. Evaluation of the Products of the Gradients of the Shape Functions on the Subelements of Figure C.1. 192

LIST OF FIGURES

FIGURE		PAGE
1.1.	Schematic Depicting Recirculation in a Mechanical Draft Cooling Tower	3
2.1.	Wind Field Computational Region	12
2.2.	Map of the Area Surrounding the Cooling Towers at the Oak Ridge Gaseous Diffusion Plant	14
2.3.	Top View of the Cooling Towers at the Oak Ridge Gaseous Diffusion Plant	15
2.4.	Schematic of the Solution Technique	16
2.5.	Details of the Cooling Tower Boundary of the Wind Field Computational Region	32
2.6.	Velocity Profile from a Typical Fan on the K-31 Cooling Tower	34
2.7.	Example of the Evaluation of the Vorticity for a Node, (i,j), at the Edge of the Plane Jet	37
2.8.	Example of the Evaluation of the Vorticity for a Node, (i,j), at the Edge of the Plane Jet Using the Stokes Theorem to Relate the Vorticity Strength to the Circulation	38
2.9.	Example of the Evaluation of the Vorticity for a Node, (i,j), Within the Plane Jet	40
3.1.	Elevation View of the K-31 Cooling Tower	47
3.2.	Typical Transverse Elevation of One Bay and One Story of a K-31 Fill Rack	48

FIGURE PAGE

3.3. Typical Longitudinal Elevation of One Bay and One Story of a K-31 Fill Rack 49

3.4. Sketch of a Drift Eliminator Rack of the K-31 Cooling Tower 50

3.5. Cooling Tower Finite Element Discretization 55

3.6. Schematic of the Procedure to Set the Stream Function Values at the Cooling Tower Inlet Louvers 59

3.7. Detail of a Section of a Louver Area of the Finite Element Cooling Tower Internal Pressure Model 61

3.8. A Typical Subelement, e_1, Used in the Wilson-Nickell [62] Finite Element Algorithm 62

5.1. Flow Direction for Wind Speed of 12 m/s 81

5.2. Profiles of the Horizontal Velocity for Wind Speed of 12 m/s 82

5.3. Stream Function Contours for Wind Speed of 12 m/s 83

5.4. Pressure Contours for Wind Speed of 12 m/s 84

5.5. Temperature Contours for Wind Speed of 12 m/s 85

5.6. Profiles of Temperature Ratio, $(\overline{T} - \overline{T}_G)/(\overline{T}_{fan} - \overline{T}_G)$, for Wind Speed of 12 m/s 86

5.7. Effective Thermal Diffusivity Contours for Wind Speed of 12 m/s 87

5.8. Turbulence Kinetic Energy Contours for Wind Speed of 12 m/s (low range contours) 88

5.9. Turbulence Kinetic Energy Contours for Wind Speed of 12 m/s (high range contours) 89

FIGURE PAGE

5.10. Turbulence Length Scale Contours for Wind Speed of 12 m/s 90

5.11. Flow Direction for Wind Speed of 6 m/s 91

5.12. Profiles of the Horizontal Velocity for Wind Speed of 6 m/s 92

5.13. Stream Function Contours for Wind Speed of 6 m/s 93

5.14. Pressure Contours for Wind Speed of 6 m/s 94

5.15. Temperature Contours for Wind Speed of 6 m/s 95

5.16. Profiles of Temperature Ratio, $(\overline{T} - \overline{T}_G)/(\overline{T}_{fan} - \overline{T}_G)$, for Wind Speed of 6 m/s 96

5.17. Effective Thermal Diffusivity Contours for Wind Speed of 6 m/s 97

5.18. Turbulence Kinetic Energy Contours for Wind Speed of 6 m/s 98

5.19. Turbulence Length Scale Contours for Wind Speed of 6 m/s 99

5.20. Flow Direction for Wind Speed of 4 m/s 100

5.21. Profiles of the Horizontal Velocity for Wind Speed of 4 m/s 101

5.22. Stream Function Contours for Wind Speed of 4 m/s 102

5.23. Pressure Contours for Wind Speed of 4 m/s 103

5.24. Temperature Contours for Wind Speed of 4 m/s 104

5.25. Profiles of Temperature Ratio, $(\overline{T} - \overline{T}_G)/(\overline{T}_{fan} - \overline{T}_G)$, for Wind Speed of 4 m/s 105

FIGURE PAGE

5.26. Effective Thermal Diffusivity Contours for Wind Speed of 4 m/s 106

5.27. Turbulence Kinetic Energy Contours for Wind Speed of 4 m/s 107

5.28. Turbulence Length Scale Contours for Wind Speed of 4 m/s 108

5.29. Flow Direction for Wind Speed of 2 m/s 109

5.30. Profiles of the Horizontal Velocity for Wind Speed of 2 m/s 110

5.31. Stream Function Contours for Wind Speed of 2 m/s 111

5.32. Pressure Contours for Wind Speed of 2 m/s 112

5.33. Temperature Contours for Wind Speed of 2 m/s 113

5.34. Profiles of Temperature Ratio, $(\overline{T} - \overline{T}_G)/(\overline{T}_{fan} - \overline{T}_G)$, for Wind Speed of 2 m/s 114

5.35. Effective Thermal Diffusivity Contours for Wind Speed of 2 m/s 115

5.36. Turbulence Kinetic Energy Contours for Wind Speed of 2 m/s 116

5.37. Turbulence Length Scale Contours for Wind Speed of 2 m/s 117

5.38. Schematic of Cooling Tower Model and Associated Equipment Used in Wind Tunnel Investigations by Reisman [20] 131

5.39. Atmospheric Velocity Profile Used in Wind Tunnel Investigations by Reisman [20] 133

FIGURE PAGE

5.40. Top View of Water Flume Used in Cooling Tower Recirculation Investigation by Kennedy and Fordyce [21] 136

5.41. Elevation View of Cooling Tower Model and Water Flume Used by Kennedy and Fordyce [21] 137

5.42. Increase in the Inlet Wet Bulb Temperature as a Function of the Normal Wind Velocity 144

C.1. Schematic of the Subdivision of Quadrilateral Region Q 187

D.1. Example of the BLOCK DATA Program Segment Used to Initialize the Values of the Wind Field Parameters 194

D.2. Example of the Wind Field Alphabetic Data Which is Read from Logical Unit 5 200

D.3. Example of the Data Which Controls the Cooling Tower Internal Pressure Model and is Read from Logical Unit 25 202

NOMENCLATURE

A	Turbulent shear stress profile coefficient, Eq. (2.18)
B	Body force term of momentum equation, Eq. (A.1)
B_E, B_W, B_N, B_S	Coefficients in the Poisson pressure equation, Eq. (2.66)
C_B	Turbulence length scale reduction coefficient function, Eq. (A.57)
C_{B_∞}	Turbulence length scale reduction asymptotic coefficient, Eq. (A.59)
C_D	Turbulence kinetic energy dissipation coefficient function, Eq. (A.55)
C_{D_∞}	Turbulence kinetic energy dissipation asymptotic coefficient, Eq. (A.56)
C_ℓ, C_m, C_n	Center nodes of the finite element internal pressure model, Figure 3.7
C_p	Constant pressure specific heat, Eq. (A.27)
C_S	Turbulence length scale growth coefficient function, Eq. (A.58)
C_{S_∞}	Turbulence length scale growth asymptotic coefficient, Eq. (A.60)
C_μ	Turbulent viscosity coefficient function, Eq. (A.53)
C_{μ_∞}	Turbulent viscosity asymptotic coefficient, Eq. (A.51)
f	Coriolis parameter, Eq. (2.18)
F	Forcing function of Poisson pressure equation, Eq. (2.65)
F_x	Forcing function of the horizontal momentum equation, Eq. (B.3)

F_z	Forcing function of the vertical momentum equation, Eq. (B.4)
g	Gravitational constant
i	Horizontal grid line number, Figure 2.1
IN	Maximum horizontal grid line number, Figure 2.1
j	Vertical grid line number, Figure 2.1
JN	Maximum vertical grid line number, Figure 2.1
k	Molecular thermal conductivity, Eq. (A.27)
K	Turbulence kinetic energy, Eq. (A.40)
$\underline{K}$	Hydraulic conductivity, Eq. (3.1)
K'	Hydraulic mass conductivity, Eq. (3.3)
ℓ	Turbulence length scale, Eq. (A.48)
N_i	Linear shape function associated with node i of the cooling tower internal pressure model, Eq. (C.1) and Eq. (3.14)
p	Turbulent pressure fluctuation about the mean, Eq. (A.40)
P	Pressure, Eq. (A.1)
$\overline{P}$	Mean wind field pressure, Eq. (A.15)
Pr	Prandtl number, Eq. (A.31)
Pr_{eff}	Effective Prandtl number, Eq. (A.35) and Eq. (A.50)
Pr_t	Turbulent Prandtl number, Eq. (A.33)
$\vec{q}$	Specific flux vector, Eq. (3.1)
R_t	Turbulence Reynolds number, Eq. (A.54)
$Sc_{K,eff}$	Effective Schmidt number for turbulence kinetic energy, Eq. (A.41)
$Sc_{\ell,eff}$	Effective Schmidt number for turbulence length scale, Eq. (A.48)

S_ω	Source term for vorticity transport equation, Eq. (A.24) and Eq. (A.25)
t	Turbulent temperature fluctuation about the mean, Eq. (A.28)
T	Temperature, Eq. (A.26)
$\overline{T}$	Mean wind field temperature, Eq. (A.15)
$\overline{T}_0$	Mean temperature of an adiabatic atmosphere, Eq. (2.17)
$\overline{T}_{fan}$	Mean temperature at the fan exit atop the cooling tower, Eq. (2.56)
$\overline{T}_G$	Specified mean ambient temperature at the ground, Eq. (2.17)
u,v,w	Turbulent fluctuation of the horizontal, lateral, and vertical velocities, respectively, about their mean values, Eq. (A.38)
$\overline{U}$	Mean horizontal velocity, Eq. (A.16)
u_i,u_j	Turbulent fluctuation of the general velocity components about the mean, used in tensor notation, Eq. (A.4)
$\overline{U}_i,\overline{U}_j$	Mean value of the general velocity components, used in tensor notation, Eq. (A.1)
u_*	Friction velocity, Eq. (2.9)
$\overline{W}$	Mean vertical velocity, Eq. (A.17)
$\overline{W}_{exit}$	Mean vertical velocity at the fan exit atop the cooling tower, Eq. (2.54)
x	Horizontal coordinate, Figure 2.1
x_i,x_j	General coordinates, used in tensor notation, Eq. (A.1)
z	Vertical coordinate, Figure 2.1
z_0	Surface roughness, Eq. (2.8)

Greek Symbols

α	Molecular thermal diffusivity, Eq. (A.27)
κ	Von Karman's constant, Eq. (2.8)
μ	Molecular viscosity, Eq. (A.1)
μ_{eff}	Effective viscosity, Eq. (A.39)
μ_t	Turbulent viscosity, Eq. (A.37)
ρ	Density
$\rho\vec{q}$	Mass flux vector, Eq. (3.4)
τ	Turbulent shear stress, Eq. (2.19)
τ_w	Surface shear stress, Eq. (2.9)
ϕ	Piezometric head, Eq. (3.2)
ψ	Stream function, Eq. (A.19) and Eq. (A.20)
ω	Vorticity, Eq. (A.21)

Superscripts

$\sim$	Denotes instantaneous value of the variable, Eq. (A.3)
$-$	Denotes mean value of the variable, Eq. (A.3)

Subscripts

i,j	Indices used in tensor notation, Eq. (A.1)
E,W,N,S	Denotes the value of the variable at the adjacent node to the east, west, north, or south, respectively, Eq. (2.66)
Floor	Denotes the magnitude of the value of a variable typical of the smallest meaningful nonzero value of the variable, Eq. (4.1)

CHAPTER 1

INTRODUCTION

The local atmospheric flow over a cooling tower affects the characteristics of the cooling tower operation. Drift deposition, fog, icing, and weather effects are environmental problems influenced by the local wind field. Another result of the local flow field, plume recirculation, is a thermal efficiency or cooling tower performance problem which can have very detrimental effects on the overall plant production capability and thus should be considered in cooling tower design.

Cooling tower drift consists of water droplets formed by the splashing of circulating water, as opposed to cloud or fog droplets formed by condensation of the plume [1]. These drift droplets are then carried aloft by the air stream exiting from the tower. Since the cooling tower circulating water may contain chromium compounds or other corrosion inhibitors, the drift droplets may also contain these chemicals. The deposition of these droplets downwind of the tower can affect vegetation, animals and structures.

Fog and cloud droplets are formed by the condensation of the plume in the atmosphere and are relatively free of impurities. However, fog and icing due to condensation of cloud droplets can be potential hazards if there are structures or roadways in the vicinity of the cooling tower.

It has also been suggested that, on a broader scale, large complexes of cooling towers could produce weather effects such as cloudiness, precipitation, and even initiation or triggering of thunderstorms [2]. These events become more plausible as the magnitude of moisture and heat

released by a cooling tower complex approaches the magnitude of moisture and heat involved in weather phenomena.

A considerable number of reports have been written which deal with cooling tower plumes and their environmental effects. Higgins [3], Stewart [4], Lowry [5], Hewson [6], Aynsley [7], and Decker [8] were early reviewers of the possible effects of cooling towers. Later reviewers of the environmental effects of cooling tower plumes were Ackermann [9], Hanna and Swisher [10], Carson [11, 12], Boyack and Kearney [13], Moore [14], Aynsley and Carson [15], and Roffman et al. [16]. More discussion of these sources can be found in the ASME review [2]. Also, Glade has compiled, to date, three bibliographies of publications concerning cooling towers [17, 18, 19]. The author has not attempted to supply a complete discussion of all published work in this area. For more information on this topic, the reader is directed to the sources mentioned above.

In addition to the environmental effects discussed above, a second area of cooling tower operation which is influenced by the local flow field is that of plume recirculation, depicted in Figure 1.1. Cooling tower performance is adversely affected by the recirculation of the stack effluent into the tower intake louvers. This recirculation results from a portion of the warm saturated effluent leaving a mechanical draft cooling tower and being reintroduced into the tower by the large captive eddy and corresponding pressure gradients downwind of the tower. This problem is further aggravated by the turbulent mixing which entrains fluid from the plume into the separated wake region from which it is ingested into the cooling tower. The ingested stack effluent enters at an elevated

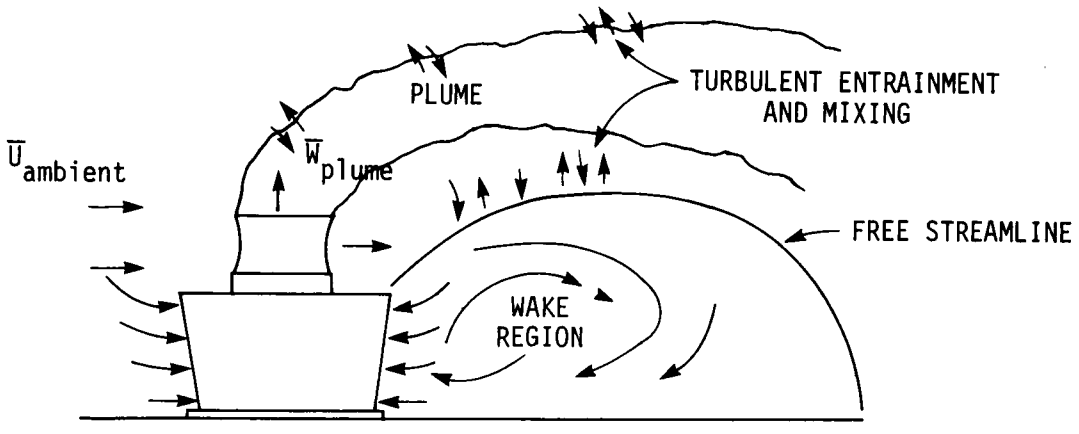


Figure 1.1. Schematic depicting recirculation in a mechanical draft cooling tower.

temperature and humidity relative to the ambient and thus reduces the efficiency or effective size of the cooling tower.

If a power plant or other type of process plant is operating near the design limits of its cooling towers, plume recirculation may produce inefficient operation of the plant or reduce the production capability of the plant. Thus, the impact of recirculation upon the cooling tower efficiency should be considered in the design and sizing of the towers for a particular application.

In summary, the interaction of a cooling tower and the local atmospheric flow field can produce environmental as well as performance efficiency problems. Although the model described in this investigation could be extended to account for environmental effects such as drift deposition, fog, and icing, the current study is specifically concerned with plume recirculation and the resulting effects on tower performance. Several studies of plume recirculation have been reported in the literature.

Reisman [20] conducted wind tunnel model investigations to determine the relative magnitude of the aerodynamically induced pressure gradients with different wind orientations for various structural configurations. He found that the leeward pressure drop and, hence, the recirculation was largest as the wind orientation became perpendicular to the cooling tower axis. In this orientation, he found the recirculation to be greater for longer towers, hence, a two-dimensional model represented a worst case for recirculation. He also found that in the perpendicular orientation the recirculation increased with increasing wind speed to a maximum recirculation which occurred at the wind speed of 8 mph (3.6 m/s)

measured at a model height equivalent to 10 meters. At higher wind speeds, the recirculation tended to diminish due to the increased dilution effect of the strong wind blowing normal to the tower. The exhaust plume was dispersed and diluted with ambient air, thus reducing the recirculation.

Kennedy and Fordyce [21] conducted model investigations in a laboratory water flume to determine downwind temperature distributions and recirculation characteristics of buoyant jets issuing from mechanical draft cooling towers. They found that the flow pattern around the cooling tower was strongly affected by both structural and atmospheric surroundings. The combination of momentum and buoyancy forces acting on the plume from a mechanical draft cooling tower caused it to behave differently than a simple jet (momentum only) or a simple plume (buoyancy only). The crosswind affected the recirculation much more than the density difference between the jet and the ambient fluid. They reported that the maximum recirculation occurred with the crosswind perpendicular to the major axis of the tower. For a given plume exit velocity, as the crosswind was increased from zero velocity, the recirculation increased. However, as the crosswind velocity became greater than the plume exit velocity, the plume was diluted in the downstream region which reduced the recirculation. Also, recirculation increased with increasing length-to-height ratio of the tower so that the two-dimensional case gave an upper asymptotic value of recirculation as this ratio became large. They also reported that for a multiple cell tower, the forced plumes from each cell merged to form a single plume which was similar to a plane jet. This plane jet plume acted as a porous curtain which blocked the

atmospheric flow to produce a large separation region behind the jet. This separation bubble strongly affected the recirculation by forming a reservoir of effluent uniformly mixed with ambient from which the tower ingested air through the downwind louvers. They also reported that near the tower fans the upwind side of the plume was more diluted than the downwind side due to the entrainment of the impinging crosswind.

Moore et al. [22] conducted field tests on large rectangular cross flow mechanical draft cooling towers. Measurements were made of the inlet wet bulb temperature along both the upwind and downwind louver faces of the tower as well as at positions upwind of the tower consistent with the method specified in the ASME Test Code for Atmospheric Water Cooling Equipment, PTC-23, 1958. They found that even under light winds (< 4.5 m/s) recirculation can result in a degradation of tower capability on the order of 5 - 10%. They also determined that even though recirculation was site-dependent, significant wind-induced recirculation can occur at all sites. They recommended that performance reductions which result from recirculation be considered in a tower design. Their data showed that the component of wind perpendicular to the tower's major axis was most directly responsible for recirculation and degradation of performance.

Numerous models of cooling tower plumes have been developed [30 - 45]. Several articles have appeared which review and compare these models [23, 24, 25]. In 1975, the ASME issued a review of the state-of-the-art in cooling tower plume modeling and drift measurement [2]. This ASME review divided the plume models into four general categories: 1) gaussian plume models; 2) buoyant plume models; 3) mathematical models solved in a step-wise fashion; and 4) models based on the fundamental equations of hydrodynamics.

The gaussian plume models, which are basically empirical, assume that the distribution of the diffusing material in the plume is gaussian in the crosswind and vertical directions. It is also assumed that the standard deviations of these distributions are functions of distance from the source and are usually given either as power law functions of distance or are taken from the empirical curves given by Gifford [26] and Pasquill [27]. Typically, these models calculate the plume height separately by some empirical plume rise equation such as the one originally described by Morton, Taylor, and Turner [28], and later advanced by Briggs [29]. Some examples of the gaussian plume model include the work of Wessels and Wisse [30], McVehil [31], Altomare [32], and Hanna [1]. This type of model ignores all aerodynamic effects of the atmospheric flow over the cooling tower.

The buoyant plume models, which are also basically empirical, assume that the distribution of the diffusing material is constant over any plume cross section. The size of plume cross section is dictated by an equation involving an empirical entrainment constant. This type of model also determines the plume height by using an expression similar to that given by Briggs [29]. Examples of buoyant plume models are given by Csanady [33], Wigley and Slawson [34], Hanna [35, 36, 37], Slawson et al. [38], and Meyer et al. [39]. Buoyant plume models, like the gaussian models, ignore the aerodynamics of the wind field near the cooling tower.

The third type of model, the stepwise mathematical models, are usually extensions of the simpler models so as to account for more general types of conditions. These models include equations which are solved numerically in a stepwise fashion upward from the cooling tower fan. In

this way, the mathematical models can account for vertical gradients in the ambient conditions as well as phase changes within the rising plume. However, aerodynamic effects are again unresolved by these models. Examples of this type of model are given by EG & G, Inc. [40], Stephen and Moroz [41], Bogh [42], and Winiarski and Frick [43].

The fourth type of plume model is based on the fundamental equations of hydrodynamics. A model of this type numerically solves a system of partial differential equations which governs the velocity, pressure, and efflux distributions in the vicinity of the cooling tower. Such a model would be capable of resolving the atmospheric flow field over a cooling tower and the resulting wake region downwind of the tower. Hence, this type of model could be used to determine plume recirculation. England et al. [44], Taft [45], and Junod et al. [46] have reported plume models of this type; however, their models do not simulate the interaction between the cooling tower and the local wind field. Hence, the existing plume models do not resolve the details of the local flow conditions necessary to predict plume recirculation and corresponding tower performance degradation.

This study describes a method of numerically modeling cooling tower plume recirculation which is unique in two respects. First, the structure of the wake region behind the tower is resolved using the two-dimensional turbulent Navier-Stokes equations. Second, the flow field within the cooling tower is modeled as flow through porous media. This interior flow field is then coupled to the atmospheric flow over the tower by matching both pressures and mass flow rates at the cooling tower louvers.

The current model uses a computer algorithm originally proposed by Gosman et al. [47]. This computer code was subsequently modified and developed to handle atmospheric flow over a two-dimensional bluff body by Bitte and Frost [48], Shieh, Frost, and Bitte [49], and finally by Pechinthorn [50]. These earlier investigators treated the bluff body as a solid surface obstruction with no interior flow field. Thus, the major contribution of this current dissertation is the modeling of the flow field within the bluff body and the coupling of this interior flow field to the existing wind field model. This coupled interior flow field model, which is the major thrust of this dissertation, is essential to the numerical modeling of cooling tower recirculation as influenced by the local atmospheric flow field.

Chapter 2 discusses the numerical model of the atmospheric flow over a two-dimensional cooling tower. The governing equations of this wind field model are discussed as well as the boundary conditions which are applied at each boundary of the wind field. The alternating direct implicit technique which is used to calculate the wind field pressure distribution is also discussed.

Chapter 3 presents the cooling tower internal pressure model. The air flow path through the cooling tower is discussed which leads naturally to the porous medium model for the internal pressure. The governing equations for this model are developed and the finite element solution technique used in this model is presented. Finally, the coupling of the atmospheric flow field model and the cooling tower internal pressure model is discussed in detail. This coupling completes the numerical model of cooling tower recirculation as influenced by the local atmospheric flow field.

Chapter 4 discusses some computational aspects of the current model such as the initial conditions and the convergence criterion. The use of a previously converged solution as the initial conditions for a new case is described. There is some discussion of the resolution of two computational anomalies which were encountered in the development of the current model. Also, this chapter presents statistics concerning the number of iterations and the computational time required for convergence of the cases run in this study. Some recommendations are made concerning the computing economy of the current model.

Chapter 5 is concerned with the results of the numerical model of cooling tower recirculation as influenced by the local atmospheric flow field. The numerical results are compared to field data and laboratory experimental data which have been reported in the literature.

Chapter 6 presents conclusions concerning the accuracy of the numerical model. Possible applications of this model by the cooling tower industry are discussed. Finally, recommendations are made for future developmental work on the current model.

CHAPTER 2

NUMERICAL MODEL OF ATMOSPHERIC FLOW OVER A TWO-DIMENSIONAL COOLING TOWER

1. GENERAL DISCUSSION

In the current investigation, cooling tower recirculation is studied by numerically modeling the wind flowing over a cooling tower. For purposes of this simulation, the atmospheric flow over a cooling tower is simplified as a two-dimensional steady-state flow in a plane perpendicular to the longitudinal axis of the cooling tower. This solution plane is treated as passing through the center of one of the exhaust fans atop the tower. The cooling tower is modeled as a two-dimensional sharp edged rectangular block with fluid flowing out of the top at a specified velocity and temperature, and into the sides at a velocity and temperature dependent upon the flow field conditions internal and external to the tower. The fluid flowing out of the top of the tower is modeled as a two-dimensional plane jet exiting into the atmosphere. Figure 2.1 shows the computational region in which the atmospheric flow over a cooling tower is simulated.

The justification for the two-dimensional model comes partly from the work done by Reisman [20], Kennedy and Fordyce [21], and Moore et al. [22] as discussed in Chapter 1. These investigators all found experimentally that cooling tower recirculation was greatest for wind flow perpendicular to the major axis of the tower. Kennedy and Fordyce also reported that the plumes from the cells of a multiple cell cooling tower merged to form a plane jet exiting into the atmosphere. Additional

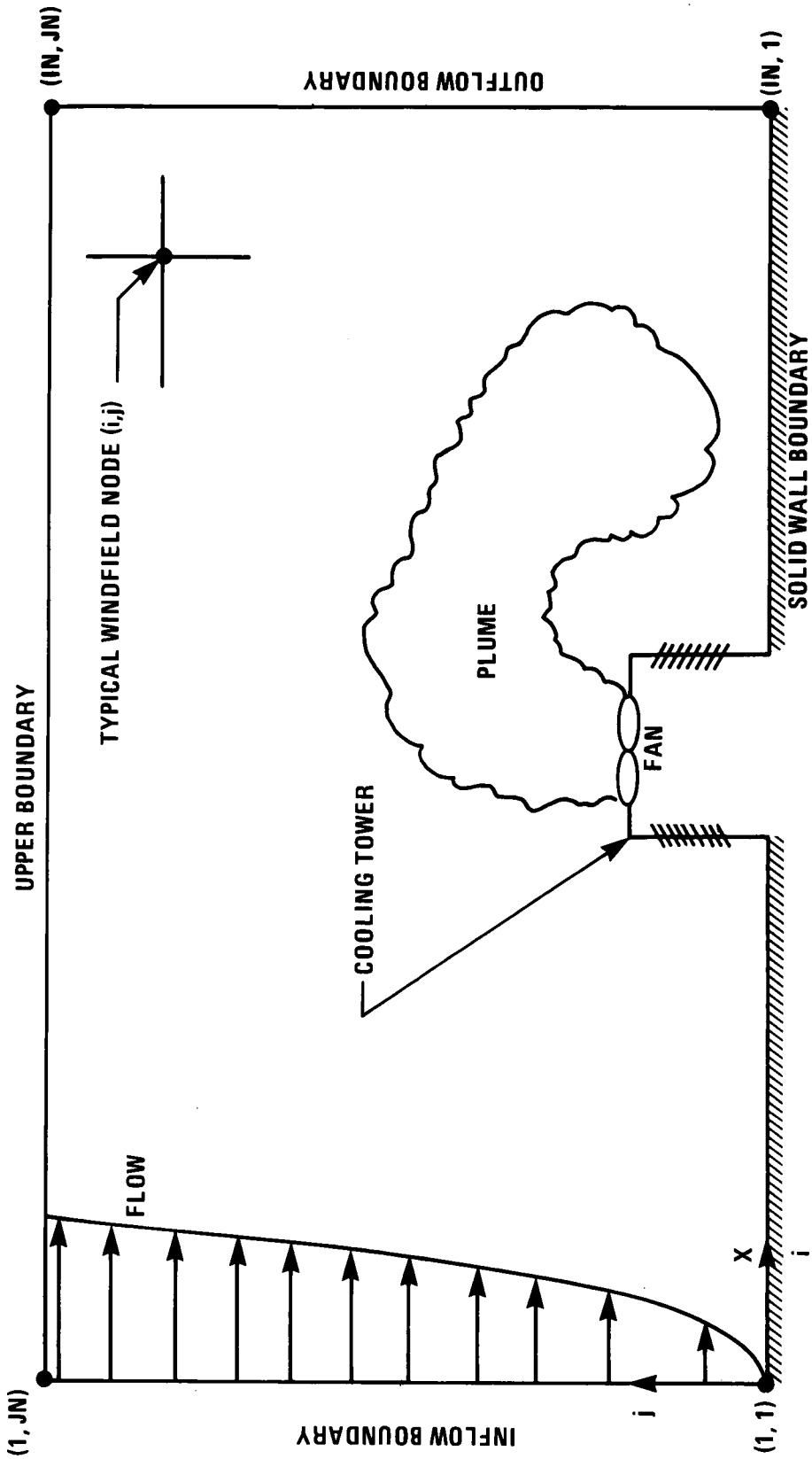


Figure 2.1. Wind field computational region (not drawn to scale).

justification comes from the fact that large mechanical draft cooling towers are usually long structures with several fans positioned along the longitudinal axis. For example, the map in Figure 2.2 shows the location of the Oak Ridge Gaseous Diffusion Plant and the associated cooling towers. The K-33 cooling tower is of the counter flow design and is 21 m high, 283 m long, and 20 m wide. This tower is divided into two sections, each of which consists of two parallel rows of 11 fans. Each fan is 6.2 m in diameter. The K-31 tower is of the cross flow design and is 11.3 m high, 117 m long and 19 m wide. This consists of a single row of 16 fans. Each fan is 6.8 m in diameter. A top view of these towers is given in Figure 2.3. For cooling towers such as these, the wind flow around the ends of the tower affects only a small part of the total length of the tower. Thus, for most of the length of the tower, the wind field is essentially due to two-dimensional flow over the tower and the long row of large fans at the top of the tower is approximately equivalent to a two-dimensional plane jet issuing vertically into the atmosphere.

The interaction between the atmospheric flow exterior to the cooling tower and the flow field within the cooling tower is simulated by the coupling of the wind field model to a cooling tower internal pressure model as shown in the schematic of the solution technique, Figure 2.4. These two models are coupled by matching both pressures and mass flow rates at the cooling tower louvers.

2. GOVERNING EQUATIONS

The wind field exterior to the cooling tower is modeled by a system of five nonlinear, coupled partial differential equations. This system of equations is solved using a successive substitution method based

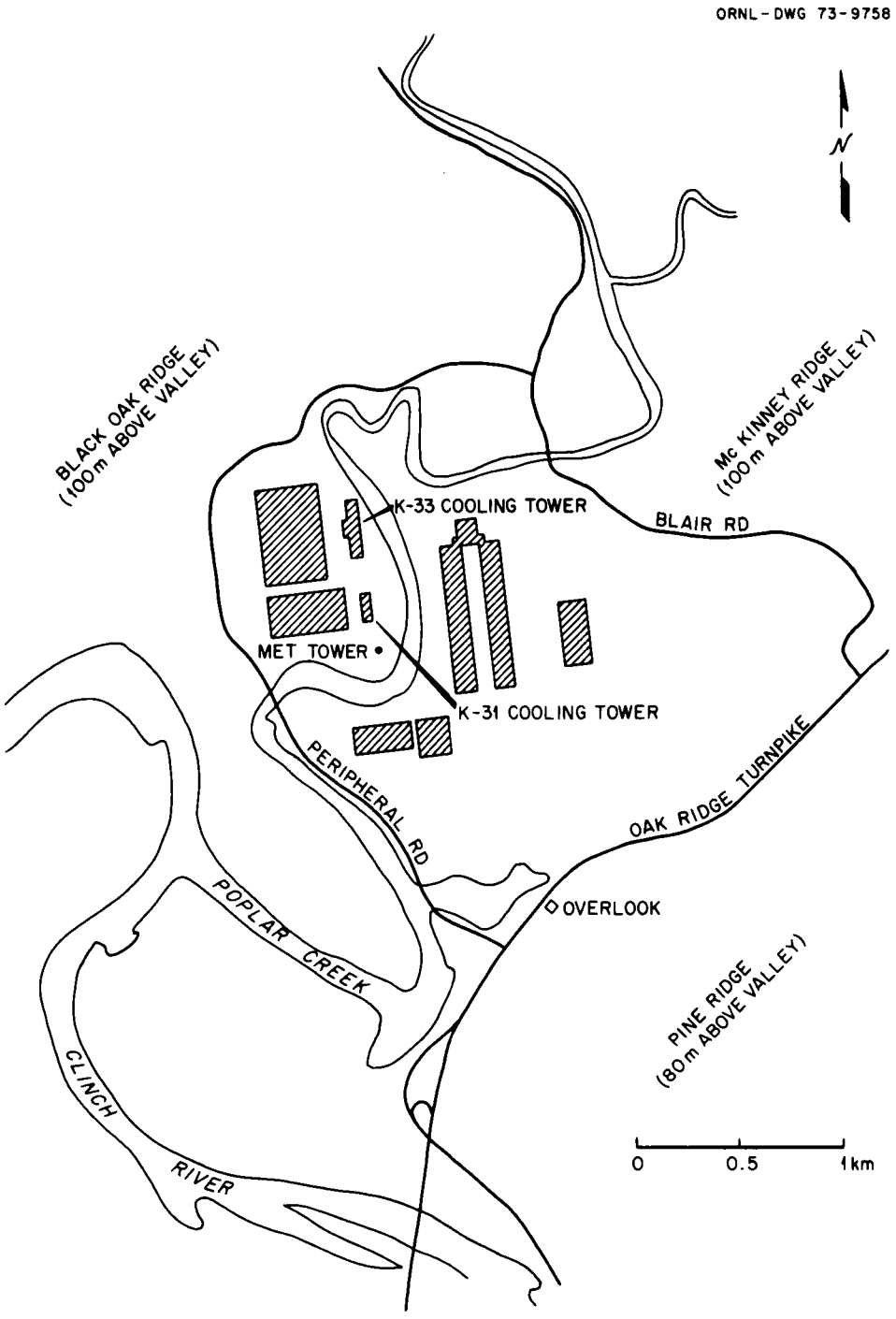


Figure 2.2. Map of the area surrounding the cooling towers at the Oak Ridge Gaseous Diffusion Plant.

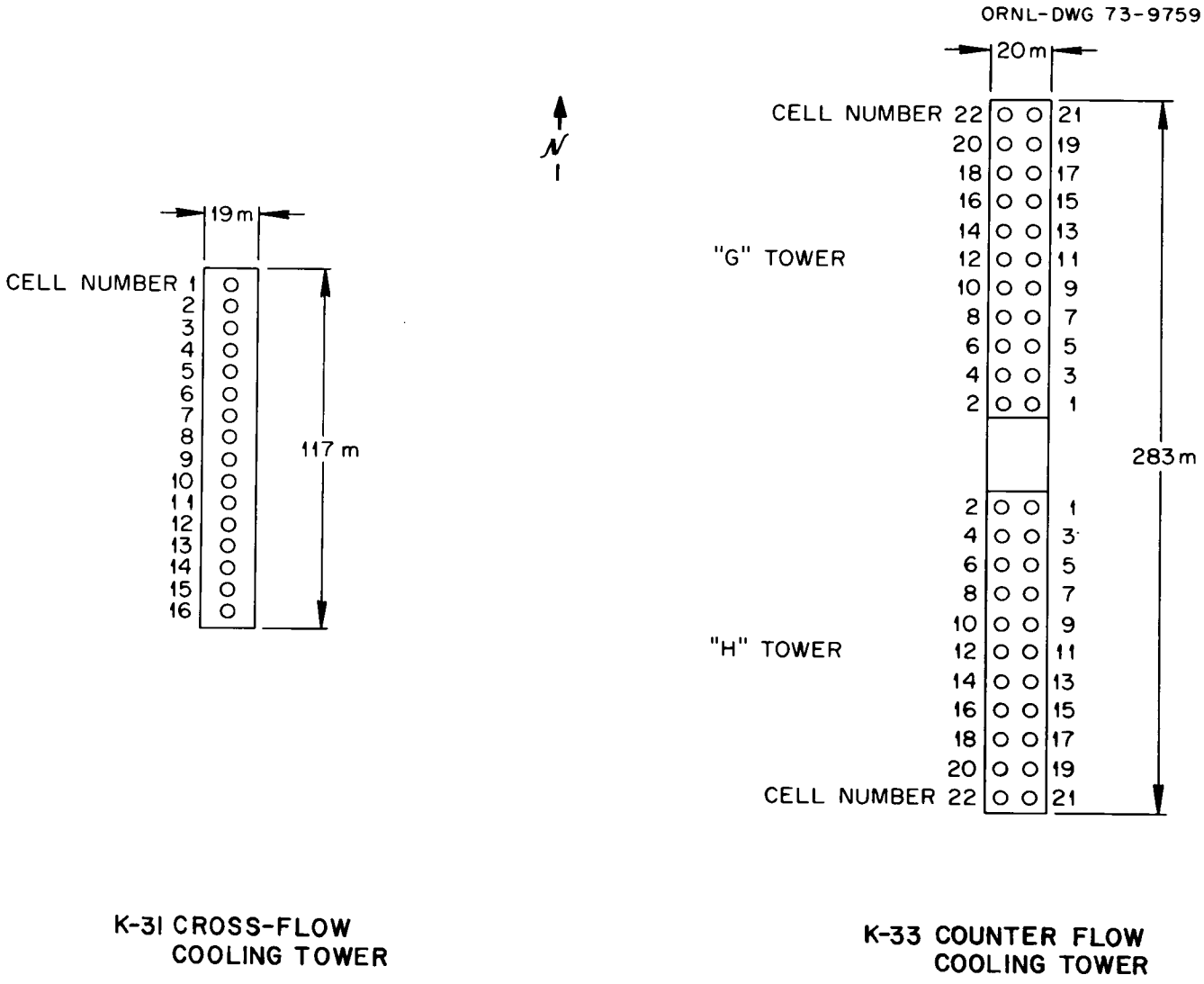


Figure 2.3. Top view of the cooling towers at the Oak Ridge Gaseous Diffusion Plant.

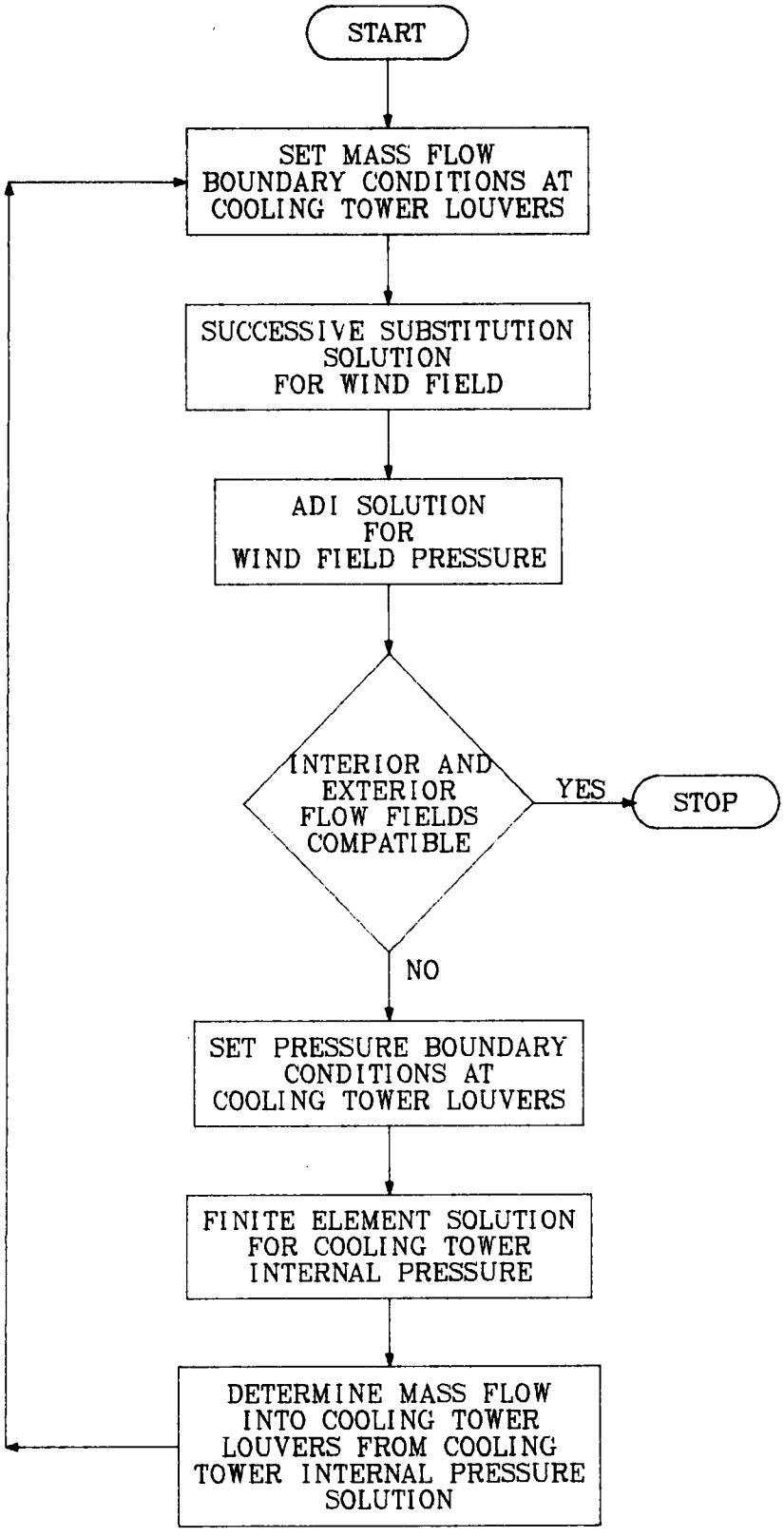


Figure 2.4. Schematic of the solution technique.

upon an algorithm originally proposed by Gosman, et al. [47]. This code was subsequently modified and developed to handle atmospheric flow over two-dimensional bluff surface obstructions by Bitte and Frost [48]. They added a transport equation for the turbulence length scale and incorporated a turbulence model. The code was then further developed by Shieh, Frost, and Bitte [49] to model neutrally stable atmospheric flow over a two-dimensional rectangular block. Finally, buoyancy effects due to flow field temperature variation were added to the code by Pechinthorn [50].

In this governing system, the fundamental momentum and continuity equations are replaced by transport equations for stream function and vorticity. The Boussinesq approximation is used to account for the buoyancy effects due to spatial perturbations of the mean flow field temperature about the adiabatic temperature profile. These buoyancy effects are considered only in the body force term of the vorticity equation.

The turbulence effects are modeled using the Prandtl-Kolmogorov formulation of the turbulent viscosity, whereby the turbulent viscosity is assumed to be dependent upon the turbulence kinetic energy and the turbulence length scale. Both the turbulence kinetic energy and turbulence length scale are calculated from transport equations. Thus, the value of the turbulent viscosity varies throughout the flow field as a function of the turbulence level in the flow. The effective viscosity, defined as the sum of the turbulent viscosity and the molecular viscosity, is used in the vorticity transport equation to account for the total of both the turbulent and molecular diffusivities.

A transport equation for the flow field temperature is derived from the equation for the transport of a scalar quantity by a turbulent

flow. The effects of flow field turbulence are included in this equation by using an effective thermal diffusivity which is defined in terms of the effective viscosity.

After the wind field solution has converged for a given set of boundary conditions, a post solution calculation is made for the wind field pressure distribution. This distribution is governed by a Poisson equation derived from the fundamental continuity and momentum equations. The pressure formulation includes the buoyancy and turbulence effects which are modeled in the same manner as described above. An alternating direction implicit technique, which employs a tridiagonal system solver by Park [51], is used to solve the resulting Poisson equation for the wind field pressure distribution. In particular, this calculation gives the pressure distribution along the cooling tower inlet louvers which serves as a boundary condition to the cooling tower internal pressure model.

The governing system of equations comprising the wind field model, including the pressure distribution, is given as follows:

Stream function

$$\frac{\partial^2 \psi}{\partial x^2} + \frac{\partial^2 \psi}{\partial z^2} = - \rho\omega \qquad (2.1)$$

Vorticity

$$\frac{\partial}{\partial x}\left[\omega \frac{\partial \psi}{\partial z}\right] - \frac{\partial}{\partial z}\left[\omega \frac{\partial \psi}{\partial x}\right] - \frac{\partial^2}{\partial x^2}\left[\mu_{eff}\omega\right]$$

$$- \frac{\partial^2}{\partial z^2}\left[\mu_{eff}\omega\right] - S_\omega = 0 \quad ,$$

where

$$S_\omega = 2\{-\frac{\partial^2}{\partial x \partial z}\left[\mu_{eff}\left[\frac{\partial \overline{U}}{\partial x} - \frac{\partial \overline{W}}{\partial z}\right]\right] + \frac{\partial^2}{\partial x^2}\left[\mu_{eff}\frac{\partial \overline{U}}{\partial z}\right]$$

$$- \frac{\partial^2}{\partial z^2}\left[\mu_{eff}\frac{\partial \overline{W}}{\partial x}\right]\} + \frac{\rho g}{\overline{T}_0}\frac{\partial \overline{T}}{\partial x} \quad . \tag{2.2}$$

Effective viscosity

$$\mu_{eff} = \mu + \mu_t$$

$$= \mu + C_{\mu_\infty}\rho K^{1/2}\ell \quad . \tag{2.3}$$

Turbulence kinetic energy

$$\rho\overline{U}_j\frac{\partial K}{\partial x_j} = \frac{\partial}{\partial x_j}\left[\frac{\mu_{eff}}{Sc_{K,eff}}\frac{\partial K}{\partial x_j}\right] + \mu_t\left[\frac{\partial \overline{U}_i}{\partial x_j} + \frac{\partial \overline{U}_j}{\partial x_i}\right]\frac{\partial \overline{U}_i}{\partial x_j}$$

$$- C_D\frac{\rho K^{3/2}}{\ell} - \frac{g_j}{\overline{T}_0}\frac{\mu_t}{Pr_t}\frac{\partial \overline{T}}{\partial x_j} \quad . \tag{2.4}$$

Turbulence length scale

$$\rho\overline{U}_j\frac{\partial \ell}{\partial x_j} = \frac{\partial}{\partial x_j}\left[\frac{\mu_{eff}}{Sc_{\ell,eff}}\frac{\partial \ell}{\partial x_j}\right] - C_B\mu_t\left[\frac{\partial \overline{U}_j}{\partial x_i} + \frac{\partial \overline{U}_i}{\partial x_j}\right]\frac{\partial \overline{U}_i}{\partial x_j}\frac{\ell}{K}$$

$$+ C_S\rho K^{1/2} - \frac{\ell}{K}\frac{\mu_t}{Pr_t}\frac{g_i}{\overline{T}_0}\frac{\partial \overline{T}}{\partial x_i} \quad . \tag{2.5}$$

Temperature

$$\rho\overline{U}_j\frac{\partial \overline{T}}{\partial x_j} = \frac{\partial}{\partial x_j}\left[\frac{\mu_{eff}}{Pr_{eff}}\frac{\partial \overline{T}}{\partial x_j}\right] \quad . \tag{2.6}$$

Pressure

$$\frac{\partial^2 \overline{P}}{\partial x^2} + \frac{\partial^2 \overline{P}}{\partial z^2} = 2\rho\left[\frac{\partial \overline{U}}{\partial x} \cdot \frac{\partial \overline{W}}{\partial z} - \frac{\partial \overline{U}}{\partial z} \cdot \frac{\partial \overline{W}}{\partial x}\right] - 2 \frac{\partial \mu_{eff}}{\partial x} \frac{\partial \omega}{\partial z} + 2 \frac{\partial \mu_{eff}}{\partial z} \frac{\partial \omega}{\partial x}$$

$$+ 2 \frac{\partial^2 \mu_{eff}}{\partial z \partial x} \left[\frac{\partial \overline{U}}{\partial z} + \frac{\partial \overline{W}}{\partial x}\right] + 2 \frac{\partial^2 \mu_{eff}}{\partial x^2} \frac{\partial \overline{U}}{\partial x}$$

$$+ 2 \frac{\partial^2 \mu_{eff}}{\partial z^2} \frac{\partial \overline{W}}{\partial z} + \frac{\rho g}{\overline{T}_0} \frac{\partial \overline{T}}{\partial z} \quad . \tag{2.7}$$

A more complete discussion and derivation of these equations is given in Appendix A. This set of governing equations with the appropriate boundary conditions constitutes the numerical model of the atmospheric flow field over a cooling tower. The boundaries of the wind field computational region are shown in Figure 2.1. The conditions specified at each of these boundaries are discussed below.

3. INFLOW BOUNDARY

The boundary conditions at the inflow boundary result from the assumptions concerning the approaching wind. The atmosphere is assumed to be neutrally stable; that is, the temperature profile of the approaching wind is assumed to exhibit a dry adiabatic lapse rate [52]. The Coriolis effects induced by the rotation of the earth are treated in the manner advocated by Tennekes [53]. He reports that, although a logarithmic wind velocity profile was valid to a height of at least 100 m, the shear stress decreased by as much as 30% over that vertical distance. Thus, a logarithmic velocity profile is assumed valid for the undisturbed approaching wind. However, the shear stress in the undisturbed

approaching wind is assumed to vary according to the profile reported by Tennekes.

The logarithmic velocity profile for the mean horizontal velocity at the inflow boundary is given by

$$\overline{U} = \frac{u_*}{\kappa} \ln\left(\frac{z + z_0}{z_0}\right) \quad , \tag{2.8}$$

wherein κ is Von Karman's constant; z_0 is the surface roughness; and u_* is the friction velocity defined in terms of the surface shear stress, τ_w, and the fluid density, ρ,

$$u_*^2 = \tau_w/\rho \quad . \tag{2.9}$$

The parameters z_0 and u_* are used to determine the shape and magnitude of the mean horizontal velocity profile.

The boundary condition on the stream function at the inflow is determined by integrating Eq. (2.8) which results in a prescribed value along that boundary,

$$\psi(z) = \rho \frac{u_*}{\kappa} [(z + z_0) \ln\left(\frac{z + z_0}{z_0}\right) - z] \quad . \tag{2.10}$$

The inflow boundary condition on vorticity is determined from the definition of the vorticity,

$$\omega(z) = \frac{\partial \overline{W}}{\partial x} - \frac{\partial \overline{U}}{\partial z} \quad . \tag{2.11}$$

The first term of Eq. (2.11) is allowed to develop as part of the solution by setting the second derivative to zero at the inflow,

$$\left.\frac{\partial^2 \overline{W}}{\partial x^2}\right|_{(1,j)} = 0 \quad . \tag{2.12}$$

This implies the following equality concerning the first derivative,

$$\left.\frac{\partial \overline{W}}{\partial x}\right|_{(1,j)} = \left.\frac{\partial \overline{W}}{\partial x}\right|_{(2,j)} = -\frac{1}{\rho}\left.\frac{\partial^2 \psi}{\partial x^2}\right|_{(2,j)} \quad . \tag{2.13}$$

The second term of Eq. (2.11) is evaluated by differentiating the logarithmic velocity profile, Eq. (2.8),

$$\frac{\partial \overline{U}}{\partial z} = \frac{u_*}{\kappa}\,\frac{1}{z + z_0} \tag{2.14}$$

The substitution of Eq. (2.13) and Eq. (2.14) into Eq. (2.11) yields the vorticity boundary condition,

$$\omega(z(j)) = -\frac{1}{\rho}\left.\frac{\partial^2 \psi}{\partial x^2}\right|_{(2,j)} - \frac{u_*}{\kappa}\,\frac{1}{z(j) + z_0} \quad . \tag{2.15}$$

The dry adiabatic lapse rate of the neutrally stable approaching wind dictates the temperature boundary condition at the inflow. The ratio of the acceleration of gravity, g, divided by the constant pressure specific heat of air, C_p, gives the dry adiabatic lapse rate [52],

$$\frac{g}{C_p} = 0.9842 \times 10^{-2}\,\frac{K}{m} \quad . \tag{2.16}$$

The temperature boundary condition at the inflow is then given as

$$\overline{T}(z) = \overline{T}_0(z) = \overline{T}_G - \frac{g}{C_p}\,z \quad , \tag{2.17}$$

where $\overline{T}_G$ is the specified constant temperature at the ground level boundary and $\overline{T}_0$ is the mean temperature of an adiabatic atmosphere.

The inflow boundary condition on the turbulence kinetic energy is determined by equating the turbulent shear stress profile proposed by

Tennekes [53] to the Prandtl-Kolmogorov formulation of the turbulent shear stress. Tennekes [53] gives the turbulent shear stress profile as

$$\tau(z) = -\rho\overline{uw} = \rho u_*^2[1.0 - \frac{A}{\kappa}\ \frac{fz}{u_*}] \quad , \tag{2.18}$$

where A is an empirical constant equal to 5.0. Tennekes and Lumley [54] report that the Coriolis parameter, f, has the value 10^{-4} s^{-1} at 40° latitude. Bitte and Frost [48] give the Prandtl-Kolmogorov formulation of the turbulent shear stress as

$$\tau(z) = C_{\mu_\infty} \rho K^{1/2} \ell \frac{\partial \overline{U}}{\partial z} \quad , \tag{2.19}$$

where C_{μ_∞} is an empirical coefficient discussed in Appendix A, K is the turbulence kinetic energy, and ℓ is the turbulence length scale given as

$$\ell(z) = \kappa(z + z_0) \quad . \tag{2.20}$$

In Eq. (2.19), the derivative of horizontal velocity can be evaluated from the logarithmic velocity profile, Eq. (2.8), with the use of Eq. (2.20),

$$\frac{\partial \overline{U}}{\partial z} = \frac{u_*}{\kappa}\ \frac{z_0}{z + z_0}\ \frac{1}{z_0} = \frac{u_*}{\ell} \quad . \tag{2.21}$$

The inflow boundary condition on the turbulence kinetic energy results from equating Eq. (2.18) to Eq. (2.19) with the derivative of horizontal velocity expressed as in Eq. (2.21),

$$K(z) = \left(\frac{u_*}{C_{\mu_\infty}}\right)^2 [1.0 - \frac{A}{\kappa}\ \frac{fz}{u_*}]^2 \quad . \tag{2.22}$$

The turbulence length scale boundary condition is determined from a mixing length hypothesis which has been demonstrated as valid for boundary layer flows such as the inflow condition assumed [49]. Thus, the mixing length is assumed to be linearly related to the normal distance from the surface and approaches a size on the order of the surface roughness as the normal distance goes to zero. This condition is given by

$$\ell(z) = \kappa(z + z_0) \quad . \tag{2.23}$$

4. OUTFLOW BOUNDARY

The boundary conditions at the outflow arise from the assumption that information is not transmitted upwind in the flow field. That is, the conditions which exist at the outflow boundary are a result of the conditions within the computational region rather than a result of any occurrence downstream of the region. The validity of this assumption depends upon the fact that the outflow boundary is located well beyond the reattachment point of the recirculation bubble which develops behind the cooling tower. Thus, there is no flow into the computational region through the outflow boundary which implies that no information is transmitted upstream through that boundary. The boundary conditions at the outflow boundary are, in general, less restrictive than those at the inflow boundary.

The boundary condition on the stream function at the outflow derives from the assumption that the vertical component of velocity is zero at that boundary,

$$\overline{W} = 0 \quad . \tag{2.24}$$

By applying the definition of the stream function, this condition implies that the horizontal derivative of the stream function vanishes at the outflow boundary,

$$\overline{W} = -\frac{1}{\rho}\frac{\partial \psi}{\partial x} = 0 \quad . \tag{2.25}$$

In finite difference form, Eq. (2.25) can be written as

$$\psi(IN,j) = \psi(IN-1,j) \quad . \tag{2.26}$$

This condition forces the flow to behave as parallel horizontal flow at the outflow boundary of the computational region.

The outflow boundary conditions on vorticity, temperature, turbulence kinetic energy and turbulence length scale are all determined as vanishing derivatives in the horizontal direction. This condition derives from the assumption that these quantities are swept out of the computational region by the atmospheric flow and that the values of these variables at the outflow boundary nodes are equal to the values at the adjacent interior nodes. These boundary conditions are given as follows:

$$\frac{\partial \omega}{\partial x} = 0 \implies \omega(IN,j) = \omega(IN-1,j) \quad , \tag{2.27}$$

$$\frac{\partial \overline{T}}{\partial x} = 0 \implies \overline{T}(IN,j) = \overline{T}(IN-1,j) \quad , \tag{2.28}$$

$$\frac{\partial K}{\partial x} = 0 \implies K(IN,j) = K(IN-1,j) \quad , \tag{2.29}$$

and

$$\frac{\partial \ell}{\partial x} = 0 \implies \ell(IN,j) = \ell(IN-1,j) \quad . \tag{2.30}$$

These outflow boundary conditions on the vorticity, temperature, turbulence

kinetic energy, and turbulence length scale are consistent with the assumption of parallel horizontal flow used to set the stream function at this boundary since this parallel flow carries these quantities out of the computational mesh along a horizontal path.

5. UPPER BOUNDARY

The upper boundary of the computational region is located 273 m above the ground level and 262 m above the top of the cooling tower. In terms of cooling tower heights, the upper boundary is located 25 tower heights above the ground level boundary. It is assumed that this upper boundary is located high enough so that the flow field there is unaffected by any disturbance at the lower boundary or at the cooling tower.

Consistent with this assumption, the boundary condition on the stream function is determined by considering the flow to be horizontal at the upper boundary, so that the upper boundary forms a streamline. The value of the stream function at this boundary is determined from the logarithmic velocity profile used at the inflow, Eq. (2.10),

$$\psi(i,JN) = \psi(1,JN) = \rho \frac{u_*}{\kappa} [(z(JN) + z_0) \cdot \ln(\frac{z(JN) + z_0}{z_0}) - z(JN)] \quad . \tag{2.31}$$

The vorticity boundary condition at the upper boundary is given by a zero derivative in vertical direction. This condition is based on the assumption that the flow field conditions do not change with the vertical coordinate at the altitude of the upper boundary,

$$\frac{\partial \omega}{\partial z} = 0 \implies \omega(i,JN) = \omega(i,JN-1) \quad . \tag{2.32}$$

The boundary condition on the temperature at the upper boundary is determined from the adiabatic lapse rate applied at the inflow, Eq. (2.17),

$$\overline{T}(i,JN) = \overline{T}(i,JN-1) - \frac{g}{C_p} [z(JN) - z(JN-1)] \quad . \tag{2.33}$$

The boundary conditions on the turbulence kinetic energy and the turbulence length scale are given as zero derivatives in the vertical direction. This condition is based on the same assumption as applied to the vorticity at the upper boundary,

$$\frac{\partial K}{\partial z} = 0 \implies K(i,JN) = K(i,JN-1) \quad , \tag{2.34}$$

and

$$\frac{\partial \ell}{\partial z} = 0 \implies \ell(i,JN) = \ell(i,JN-1) \quad . \tag{2.35}$$

6. GROUND LEVEL BOUNDARY

The ground level boundary is a no-flow, no-slip boundary. This assumption implies that both components of velocity are zero at the ground level.

The condition of no mass flux through the ground level boundary dictates that the stream function be constant along that boundary. Conventionally, the stream function is set to zero at the ground,

$$\psi(i,1) = 0 \quad . \tag{2.36}$$

This value is consistent with the logarithmic velocity profile as applied to the inflow boundary, Eq. (2.10).

The vorticity boundary condition at the ground results from both components of velocity being zero there. The stream function at an adjacent interior node, (i,2), can be written as a Taylor series expansion about the corresponding ground level boundary node, (i,1), as follows [55],

$$\psi(i,2) = \psi(i,1) + \left.\frac{\partial\psi}{\partial z}\right|_{(i,1)} \cdot \Delta z + \frac{1}{2} \left.\frac{\partial^2\psi}{\partial z^2}\right|_{(i,1)} \cdot (\Delta z)^2$$

$$+ \frac{1}{6} \left.\frac{\partial^3\psi}{\partial z^3}\right|_{(i,1)} \cdot (\Delta z)^3 + \text{H.O.T.} \quad . \tag{2.37}$$

The no-slip condition on the horizontal velocity component at the ground gives

$$\overline{U}(i,1) = \frac{1}{\rho} \left.\frac{\partial\psi}{\partial z}\right|_{(i,1)} = 0 \quad . \tag{2.38}$$

Since the vertical component of velocity is zero at all ground level boundary points, the horizontal derivative of the vertical velocity also vanishes along this boundary,

$$\left.\frac{\partial\overline{W}}{\partial x}\right|_{(i,1)} = 0 \quad . \tag{2.39}$$

Substituting Eq. (2.38) and Eq. (2.39) into the definition of the vorticity, Eq. (2.11), gives

$$\omega(i,1) = \left.\frac{\partial\overline{W}}{\partial x}\right|_{(i,1)} - \left.\frac{\partial\overline{U}}{\partial z}\right|_{(i,1)} = -\frac{1}{\rho} \left.\frac{\partial^2\psi}{\partial z^2}\right|_{(i,1)} \quad . \tag{2.40}$$

Equation (2.38) and Eq. (2.40) can be substituted into Eq. (2.37) to give the following,

$$\psi(i,2) = \psi(i,1) - \frac{1}{2}\rho\omega(i,1) \cdot (\Delta z)^2 - \frac{1}{6}\left.\frac{\partial}{\partial z}(\rho\omega)\right|_{(i,1)} \cdot (\Delta z)^3 + H.O.T. \tag{2.41}$$

The derivative of vorticity in Eq. (2.41) can be approximated as

$$\left.\frac{\partial}{\partial z}(\rho\omega)\right|_{(i,1)} = \rho\,\frac{\omega(i,2) - \omega(i,1)}{\Delta z} \tag{2.42}$$

Then, neglecting the higher order terms, Eq. (2.41) with the inclusion of Eq. (2.42) can be solved for the vorticity at the ground level boundary,

$$\omega(i,1) = \frac{3(\psi(i,1) - \psi(i,2))}{\rho(\Delta z)^2} - \frac{1}{2}\omega(i,2) \quad . \tag{2.43}$$

This is the vorticity boundary condition imposed at the ground level boundary.

The temperature at the ground level boundary is a specified constant value,

$$T(i,1) = T_G \quad . \tag{2.44}$$

This boundary condition is consistent with that imposed by the adiabatic lapse rate at the inflow, Eq. (2.17).

The turbulence kinetic energy boundary condition along the ground level boundary is set by applying the same condition as at the inflow, Eq. (2.22), evaluated at the bottom of the mesh,

$$K(z=0) = \left(\frac{u_*}{C_{\mu_\infty}}\right)^2 \left[1 - \frac{A}{\kappa}\,\frac{fz_0}{u_*}\right]^2 \quad . \tag{2.45}$$

Neglecting the Coriolis correction term in Eq. (2.45) results in an error on the order of 0.1% at the ground level. By neglecting this term, Eq. (2.45) is simplified as follows,

$$K(z=0) = \left(\frac{u_*}{C_{\mu_\infty}}\right)^2 \quad . \tag{2.46}$$

Differentiating the logarithmic velocity profile, Eq. (2.8), and solving for the friction velocity gives the following result at the ground level,

$$u_* = \kappa z_0 \left.\frac{\partial \bar{U}}{\partial z}\right|_{(i,1)} \quad . \tag{2.47}$$

Equation (2.39) and Eq. (2.40) imply that the derivative in Eq. (2.47) is related to the vorticity at the ground,

$$\omega(i,1) = - \left.\frac{\partial \bar{U}}{\partial z}\right|_{(i,1)} \quad . \tag{2.48}$$

Substituting Eq. (2.47) with Eq. (2.48) into Eq. (2.46) gives the turbulence kinetic energy boundary condition at the ground level,

$$K(i,1) = \left[\frac{\kappa \cdot z_0 \cdot \omega(i,1)}{C_{\mu_\infty}}\right]^2 \quad . \tag{2.49}$$

The ground level boundary condition on the turbulence length scale is given by the same expression as applied at the inflow, Eq. (2.23), evaluated at the ground level,

$$\ell = \kappa z_0 \quad . \tag{2.50}$$

7. COOLING TOWER BOUNDARY

In the simulation of the atmospheric flow field, the cooling tower is modeled as a two-dimensional sharp edged rectangular block with fluid flowing out of the top at a specified velocity and temperature and flowing into the sides at a velocity and temperature dependent upon the flow field conditions. In relationship to the atmospheric flow field, the cooling tower is represented by three boundaries, two vertical and one horizontal, as shown in Figure 2.1, page 12. The cooling tower boundary of the wind field computational region is shown in detail in Figure 2.5. The vertical boundaries represent the upwind and downwind sides of the cooling tower. These vertical boundaries contain inlet louvers through which the cooling tower draws air from the atmosphere. The horizontal boundary represents the top of the cooling tower. This boundary contains a large fan which discharges warm moist air from the cooling tower into the atmosphere.

The conditions on the stream function at the cooling tower boundaries are determined by the physical conditions of mass flow rate at these boundaries. First, the conditions along the top boundary will be discussed, followed by those along the vertical boundaries.

The mass flux out of the cooling tower top boundary is a function of the fan operating characteristics. The angular velocity of the fan is governed so as to achieve approximately constant power usage by its motor. Thus, for modeling purposes, Park [56] reports that the fan may be approximated as a constant volumetric flow rate device which maintains a constant mass flow rate of warm moist air from the top of the tower.

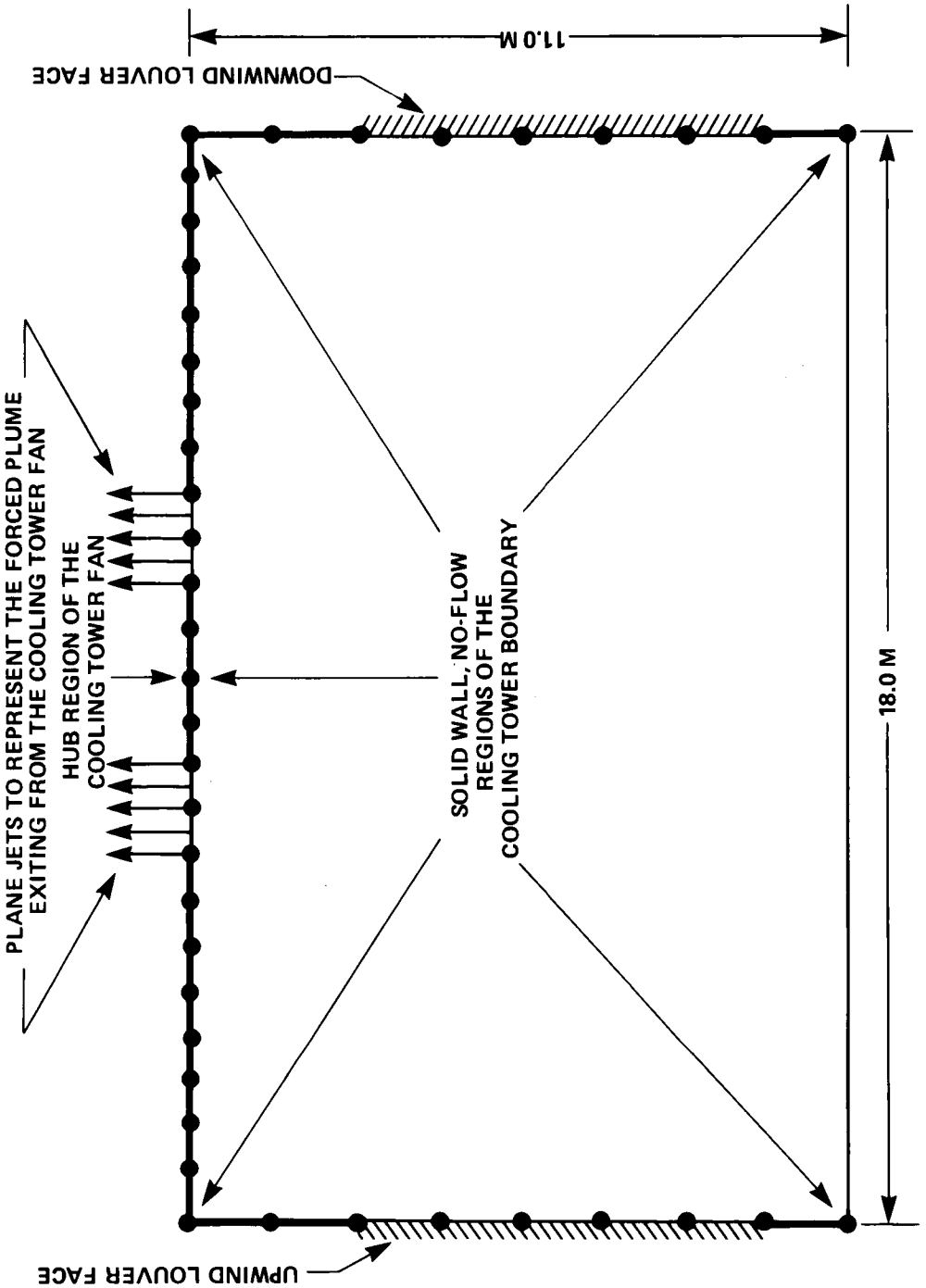


Figure 2.5. Details of the cooling tower boundary of the wind field computational region.

Hanna [36] gives a velocity profile from a typical fan in the K-31 cross flow cooling tower at ORGDP. This velocity profile is shown in Figure 2.6. Hanna reports a volume flow rate of 330 m^3/s (699,230 ft^3/min) for each fan. Uglow [57] reports a volume flow rate of 273 m^3/s (578,600 ft^3/min) for the same fans. For modeling purposes, the velocity profile reported by Hanna is simplified as the "top hat" velocity profile, also given in Figure 2.6. Integrating under this profile gives a volume flow rate of 300 m^3/s (637,000 ft^3/min).

This velocity profile is actually annular in the full three-dimensional situation. In the two-dimensional model, this annulus is represented by a pair of plane jets issuing vertically from the horizontal boundary of the tower. There is a region of practically no flow in the center of the annulus. This is the region occupied by the fan hub and is represented as a solid no-flow boundary between the pair of plane jets in the two-dimensional model as shown in Figure 2.5.

The boundary condition on the stream function at the horizontal boundary is determined from the "top hat" velocity profile given in Figure 2.6. This is done by integrating the following equation along the top of the cooling tower,

$$\frac{\partial \psi(x)}{\partial x} = - \rho \overline{W}(x) \quad , \tag{2.51}$$

where $\overline{W}(x)$ is given by the top hat velocity profile.

The mass flux into the cooling tower through the vertical boundaries is a function of both the pressure differential across the inlet louvers and the hydraulic conductivity of these louvers. This mass flux is used to determine the conditions on the stream function at these boundaries.

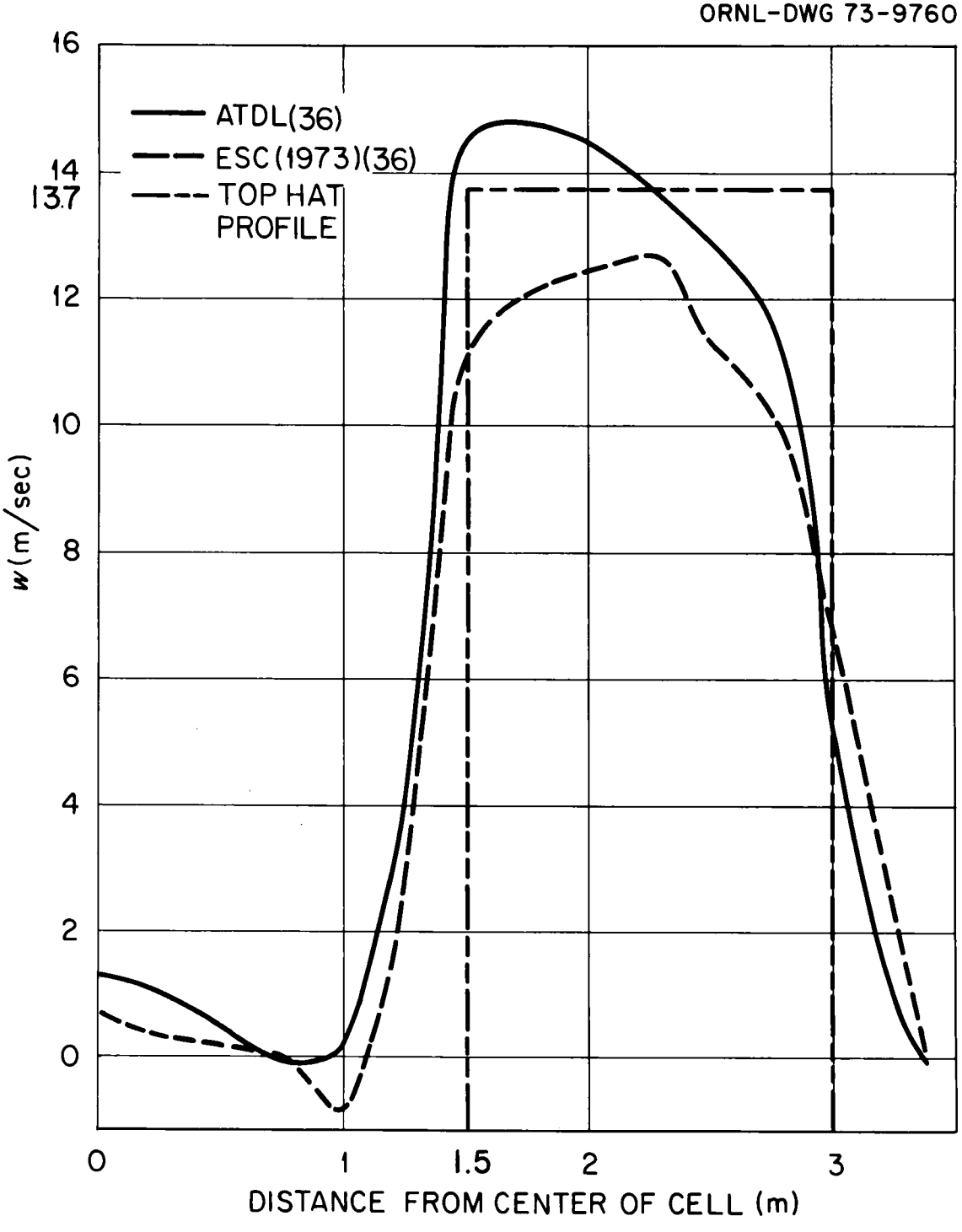


Figure 2.6. Velocity profile from a typical fan on the K-31 cooling tower.

The method used to set these boundary conditions is summarized in Figure 2.4, page 16. A more detailed description of the procedure is given forthwith.

First, as mentioned earlier in this chapter, after the wind field has converged for a given set of boundary conditions, a post solution calculation is made for the wind field pressure distribution using Eq. (2.7).

Second, the pressure field within the cooling tower is determined by the cooling tower internal pressure model. The pressures at the inlet louvers as determined by the wind field pressure calculation (step one above) serve as boundary conditions to the internal pressure model. This model is discussed in detail in Chapter 3.

Third, the mass flow into the cooling tower inlet louvers is calculated from the internal pressure distribution determined in step two above. More detail on this calculation is given in Chapter 3.

Fourth, as a means of removing numerical round off error and thereby improving convergence, the mass flow into the louvers is adjusted to insure mass continuity. That is, the total mass flow into the cooling tower through the inlet louvers on the vertical boundaries must equal the total mass flow out of the cooling tower through the fan on the horizontal boundary. This is achieved by multiplying the new mass flow rates determined in step three by the quotient of total outflow divided by total inflow.

Finally, the corrected mass flow rates through the inlet louvers located in the vertical boundaries of the tower are used to determine the conditions on the stream function at these boundaries. These boundary conditions are set by integrating the following equation at the inlet louvers,

$$\frac{\partial \psi}{\partial z} = \overline{U} \quad . \tag{2.52}$$

The vorticity boundary condition at the solid portions of the cooling tower is the same as applied at the ground level boundary, Eq. (2.43). As shown in Figure 2.5, on the horizontal boundary of the cooling tower there are two plane jets which represent the forced plume exiting from the top of the tower. The space between these two plane jets represents the hub region of the fan through which there is very little flow as shown in the exit velocity profile, Figure 2.6.

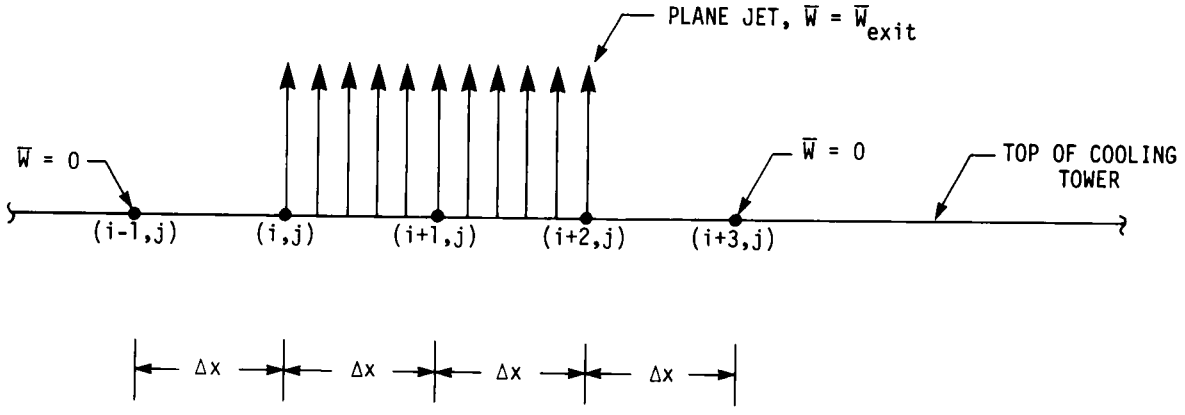
At each edge of the plane jets, there occurs a sharp velocity discontinuity. Such a velocity discontinuity generates a region of strong vorticity. The boundary condition applied at these points can be derived from the definition of the vorticity, Eq. (2.11). Since the flow is predominantly in the vertical direction at the edge of the plane jet, the second term of Eq. (2.11) is neglected. The vorticity is then determined as the horizontal derivative of the vertical velocity expressed as a central difference approximation of the second derivative of the stream function evaluated at node (i,j) on the edge of the plane jet,

$$\omega(i,j) = -\frac{1}{\Delta x}\left[\frac{\psi(i+1,j) - \psi(i,j)}{\rho \cdot \Delta x} - \frac{\psi(i,j) - \psi(i-1,j)}{\rho \cdot \Delta x}\right] \quad . \qquad (2.53)$$

As shown in Figure 2.7, expressed in terms of the exit velocity, $\overline{W}_{exit}$, Eq. (2.53) gives the vorticity at the node, (i,j), on the edge of the plane jet as

$$\omega(i,j) = \frac{\overline{W}_{exit}}{\Delta x} \quad . \qquad (2.54)$$

By an application of the Stokes theorem, the vortex strength necessary to maintain a velocity discontinuity can be calculated as the circulation around a contour enclosing the point of velocity discontinuity. As shown in Figure 2.8, performing such an integration around the node

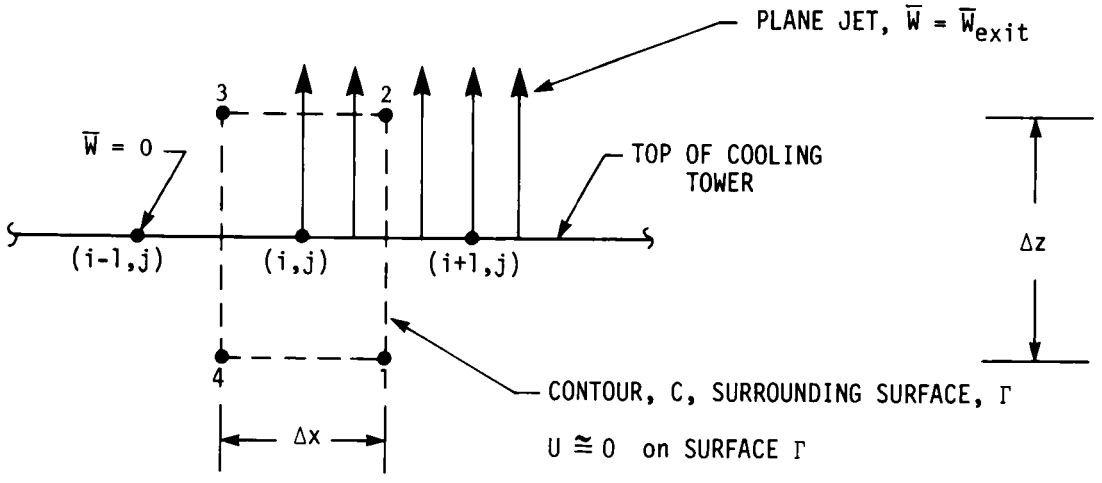


$$\omega(i,j) = -\frac{1}{\Delta x}\left[\frac{\psi(i+1,j) - \psi(i,j)}{\rho \cdot \Delta x} - \frac{\psi(i,j) - \psi(i-1,j)}{\rho \cdot \Delta x}\right]$$

$$= -\frac{1}{\Delta x}\left[-\overline{W}_{exit} + 0\right]$$

$$= \frac{\overline{W}_{exit}}{\Delta x}$$

Figure 2.7. Example of the evaluation of the vorticity for a node, (i,j), at the edge of the plane jet.



$$\text{VORTICITY STRENGTH ON } \Gamma = \iint_{\Gamma} (\vec{\nabla} \times \vec{V}) \cdot d\vec{A} = (\omega(i,j))\ \Delta x \Delta z$$

$$\text{CIRCULATION AROUND C} = \oint_{C} \vec{V} \cdot d\vec{s} = \int_{1}^{2} \overline{W} dz - \int_{2}^{3} \overline{U} dx - \int_{3}^{4} \overline{W} dz + \int_{4}^{1} \overline{U} dx$$

$$= (\overline{W}_{exit})\ \Delta z - 0 - 0 + 0$$

BY STOKES THEOREM,

$$\iint_{\Gamma} (\vec{\nabla} \times \vec{V}) \cdot d\vec{A} = \oint_{C} \vec{V} \cdot d\vec{s}$$

$$(\omega(i,j))\ \Delta x \Delta z = (\overline{W}_{exit})\ \Delta z$$

THEN,

$$\omega(i,j) = \frac{\overline{W}_{exit}}{\Delta x}$$

Figure 2.8. Example of the evaluation of the vorticity for a node, (i,j), at the edge of the plane jet using the Stokes theorem to relate the vorticity strength to the circulation.

(i,j) at the edge of the plane jet gives the same result, Eq. (2.54), as given by the central difference formulation, Eq. (2.53). Thus, potential flow theory helps to substantiate the boundary conditions applied at edges of the plane jets on the horizontal boundary of the cooling tower.

Within the jets themselves, the flow is considered to be uniform parallel flow. Consistent with this type of flow, the vorticity is considered to be zero at the points (i,j) within either of the plane jets,

$$\omega(i,j) = 0 \quad . \tag{2.55}$$

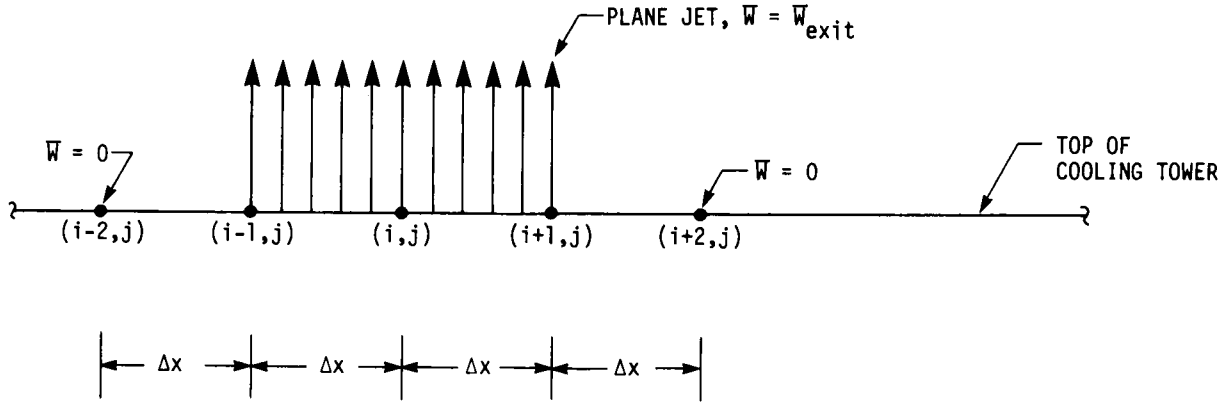
As shown in Figure 2.9, this condition is consistent with the central difference formulation given in Eq. (2.53).

The temperature boundary condition at the solid portions of the cooling tower is the same as applied at the ground level boundary, Eq. (2.44). At those nodes, (i,j), which represent the fan on the horizontal boundary of the cooling tower, the temperature is set to a constant value, $\overline{T}_{fan}$, which is determined by the operating conditions of the tower [57],

$$\overline{T}(i,j) = \overline{T}_{fan} \quad . \tag{2.56}$$

The turbulence kinetic energy boundary condition at the solid portions of the cooling tower is the same as applied at the ground level, Eq. (2.49), with a different surface roughness to distinguish between the cooling tower and the ground level. The plane jets which represent the fan on the horizontal boundary of the cooling tower are modeled as uniform flow. With this justification, the turbulence kinetic energy at these nodes is set to zero,

$$K(i,j) = 0 \quad . \tag{2.57}$$



$$\omega(i,j) = -\frac{1}{\Delta x}\left[\frac{\psi(i+1,j) - \psi(i,j)}{\rho \cdot \Delta x} - \frac{\psi(i,j) - \psi(i-1,j)}{\rho \cdot \Delta x}\right]$$

$$= -\frac{1}{\Delta x}\left[-\bar{W}_{exit} + \bar{W}_{exit}\right]$$

$$= 0$$

Figure 2.9. Example of the evaluation of the vorticity for a node, (i,j), within the plane jet.

This same condition, Eq. (2.57), was used by Gosman, et al. [47] to model a plane turbulent jet.

As with the turbulence kinetic energy, the boundary condition applied to the turbulence length scale at the solid portions of the cooling tower is the same as used at the ground level, Eq. (2.50). Again, a different surface roughness is used in Eq. (2.50) to account for the cooling tower. Launder and Spalding [58] give a length scale boundary condition for a plane jet which is applied at the nodes (i,j) which represent the fan on the horizontal boundary of the cooling tower,

$$\ell(i,j) = (.09) \cdot (\text{half width of the jet}) \quad . \tag{2.58}$$

The inlet louver boundary conditions on the vorticity, temperature, turbulence kinetic energy and turbulence length scale are all derived from the flow conditions at the louvers. Since the fluid flows into the cooling tower through the louvers on the vertical boundaries at a fairly high rate, 2.5 m/s to 3.8 m/s (500 ft/min to 750 ft/min, depending upon cooling tower design), disturbances within the cooling tower will not be conducted out into the flow field [59]. Hence, effects from within the tower will not be felt at the inlet louvers. Thus, the vorticity, temperature, turbulence kinetic energy, and turbulence length scale of the fluid passing through the louvers of the tower will be essentially the same as that of the nearby flow field. Hence, the boundary conditions of these variables at the inlet louver nodes, (i,j), on the vertical boundaries will be given as zero horizontal derivatives,

$$\left.\frac{\partial \omega}{\partial x}\right|_{(i,j)} = 0 \quad \Rightarrow \quad \omega(i,j) = \omega(n,j) \quad , \tag{2.59}$$

$$\left.\frac{\partial \bar{T}}{\partial x}\right|_{(i,j)} = 0 \Rightarrow \bar{T}(i,j) = \bar{T}(n,j) \quad , \tag{2.60}$$

$$\left.\frac{\partial K}{\partial x}\right|_{(i,j)} = 0 \Rightarrow K(i,j) = K(n,j) \quad , \tag{2.61}$$

and

$$\left.\frac{\partial \ell}{\partial x}\right|_{(i,j)} = 0 \Rightarrow \ell(i,j) = \ell(n,j) \quad , \tag{2.62}$$

where, at the front louver face,

$$n = i - 1 \quad , \tag{2.63}$$

and, at the back louver face,

$$n = i + 1 \quad . \tag{2.64}$$

8. WIND FIELD PRESSURE CALCULATION

As discussed earlier, after the wind field has converged for a given set of boundary conditions, the wind field pressure distribution is calculated. The results of this calculation yield boundary conditions for the internal pressure model which, in turn, yields mass flow rates into the cooling tower louvers. These mass flow rates are then used to reset the wind field boundary conditions for the next iteration of the wind field algorithm.

The wind field pressure distribution is determined by solving Eq. (2.7) with an alternating direct implicit technique. A derivation of Eq. (2.7), the Poisson equation for pressure, is given in Appendix A. Letting F denote the right-hand side or forcing function, Eq. (2.7)

becomes

$$\frac{\partial^2 \overline{P}}{\partial x^2} + \frac{\partial^2 \overline{P}}{\partial z^2} = F \quad . \tag{2.65}$$

The left-hand side of Eq. (2.65) is differenced using the same central difference technique as used by Gosman, et al. [47].

In differenced form, when evaluated for node i, Eq. (2.65) becomes

$$B_E \overline{P}_E + B_W \overline{P}_W + B_S \overline{P}_S + B_N \overline{P}_N - (B_E + B_W + B_S + B_N) \overline{P}_i = \frac{F}{2} \quad . \tag{2.66}$$

In Eq. (2.66), the subscripts E, W, S, and N denote, respectively, east, west, south, and north. Then $\overline{P}_E$ is the pressure at the node adjacent to and east of node i. The coefficients B_E, B_W, B_S, and B_N arise from the differencing procedure and are related only to the geometry of the x and z grid lines of the wind field computational region.

In the alternating direction implicit technique, the wind field computational region is swept first by rows and then by columns. For the row iteration, Eq. (2.66) is rewritten as

$$B_E \overline{P}_E - (B_E + B_W + B_S + B_N) \overline{P}_i + B_W \overline{P}_W = \frac{F}{2} - B_S \overline{P}_S - B_N \overline{P}_N \quad . \tag{2.67}$$

For the column iteration, Eq. (2.66) is rewritten as

$$B_S \overline{P}_S - (B_E + B_W + B_S + B_N) \overline{P}_i + B_N \overline{P}_N = \frac{F}{2} - B_E \overline{P}_E - B_W \overline{P}_W \quad . \tag{2.68}$$

For the row iteration, it is necessary to supply boundary conditions at the inflow, outflow, cooling tower front face, and cooling tower back face. These boundary conditions are derived by applying the Reynolds averaged momentum equations, Eq. (A.16) and Eq. (A.17).

The z-direction momentum equation, Eq. (A.17), can be rearranged using the definitions of vorticity, Eq. (2.11), and stream function, Eq. (A.19) and Eq. (A.20), as follows,

$$\frac{\partial \bar{P}}{\partial z} = - \rho\bar{U} \frac{\partial \bar{W}}{\partial x} - \rho\bar{W} \frac{\partial \bar{W}}{\partial z} + 2 \frac{\partial \mu_{eff}}{\partial z} \frac{\partial \bar{W}}{\partial z} + \frac{\partial \mu_{eff}}{\partial x} \left(\frac{\partial \bar{U}}{\partial z} + \frac{\partial \bar{W}}{\partial x}\right)$$

$$+ \mu_{eff} \frac{\partial \omega}{\partial x} + \frac{\rho g \bar{T}}{\bar{T}_0} - 2\rho g \quad . \tag{2.69}$$

At the inflow boundary, Eq. (2.69) is integrated from the ground level to the upper boundary to give the inflow boundary condition on the pressure. This integration is started from the ground level pressure at the inflow. This pressure, which is specified to be the local ambient barometric pressure, sets the level of the solution.

The x-direction momentum equation, Eq. (A.16), can be rearranged using the definitions of vorticity, Eq. (2.11), and stream function, Eq. (A.19) and Eq. (A.20), as follows,

$$\frac{\partial \bar{P}}{\partial x} = - \rho\bar{U} \frac{\partial \bar{U}}{\partial x} - \rho\bar{W} \frac{\partial \bar{U}}{\partial z} + 2 \frac{\partial \mu_{eff}}{\partial x} \frac{\partial \bar{U}}{\partial x}$$

$$+ \frac{\partial \mu_{eff}}{\partial z} \left(\frac{\partial \bar{U}}{\partial z} + \frac{\partial \bar{W}}{\partial x}\right) - \mu_{eff} \frac{\partial \omega}{\partial z} \quad . \tag{2.70}$$

At the front face of the cooling tower and at the outflow boundary, the condition on the pressure is given by Eq. (2.70) using a backward difference formulation. At the back face of the tower, the pressure boundary condition is given by Eq. (2.70) with a forward difference formulation. These conditions are given in detail in Appendix B.

For the column iteration, boundary conditions are needed at the upper boundary, ground level boundary, and along the top of the cooling

tower. At the upper boundary, the condition on the pressure is given by Eq. (2.69) using a backward difference formulation. At the ground level boundary and along the top of the cooling tower, the pressure boundary condition is given by Eq. (2.69) with a forward difference formulation. These conditions are also given in detail in Appendix B.

Equation (2.7) with the boundary conditions discussed above determines the wind field pressure distribution. In particular, this calculation dictates the pressures along the inlet louvers of the cooling tower front and back faces. These pressures serve as a Dirichlet boundary condition on the cooling tower internal pressure model. This model is used to determine the pressure distribution within the cooling tower which dictates the mass flow rates into the tower inlet louvers. These mass flow rates are then used to determine the stream function boundary conditions along the cooling tower inlet louvers. The cooling tower internal pressure model is discussed in detail in the following chapter.

CHAPTER 3

COOLING TOWER INTERNAL PRESSURE MODEL

1. GENERAL DISCUSSION

A wet cooling tower is a heat exchanger which transfers thermal energy from the circulating water of a power plant or other type of process plant to the atmosphere. Such a tower provides for the intimate mixing of the circulating water with the ambient air, thereby cooling the circulating water. This cooling is accomplished mostly by the exchange of the latent heat of vaporization resulting from the evaporation of a portion of the circulating water. There is also some transfer of sensible heat to the air which changes both its wet bulb and dry bulb temperature.

As shown in Figure 3.1, the interior of the K-31 cooling tower, a typical cross flow, mechanical draft tower, contains fill racks, drift eliminators, and open or void areas. Figure 3.2 shows a transverse elevation of one bay and one story of a K-31 fill rack. Figure 3.3 shows a longitudinal elevation of the same. Figure 3.4 is a sketch of a portion of the K-31 drift eliminator.

The air flow path through the cooling tower originates at the inlet louvers. After the air passes through the inlet louvers, it transverses a small void area and then encounters the fill material. It is here, within the fill, that most of the mixing with and cooling of the circulating water takes place. As shown in Figures 3.2 and 3.3, the flow path through the fill material is complex and tortuous. Once

DWG. NO. K/G-79-1319
(U)

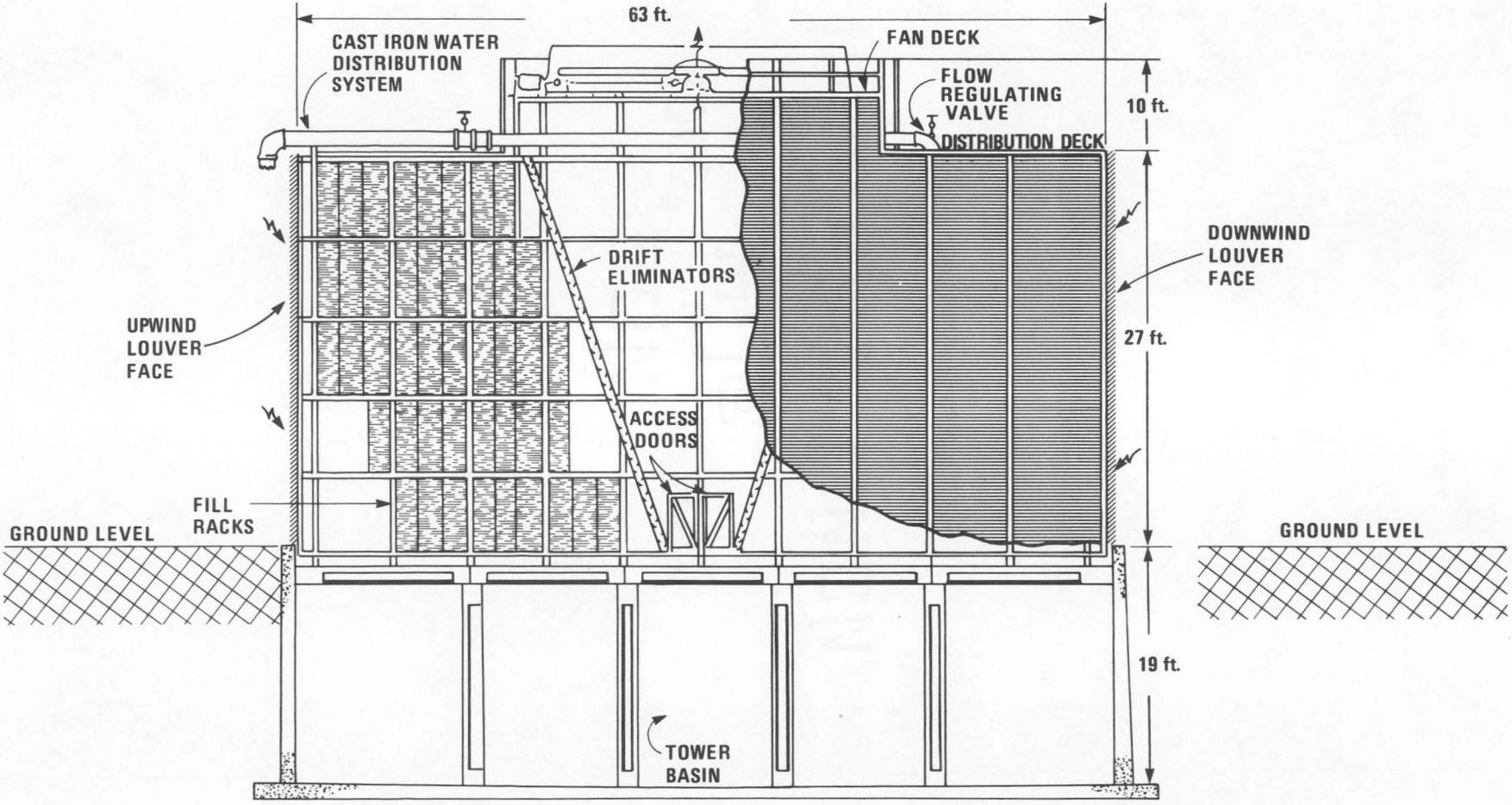


Figure 3.1. Elevation view of the K-31 cooling tower.

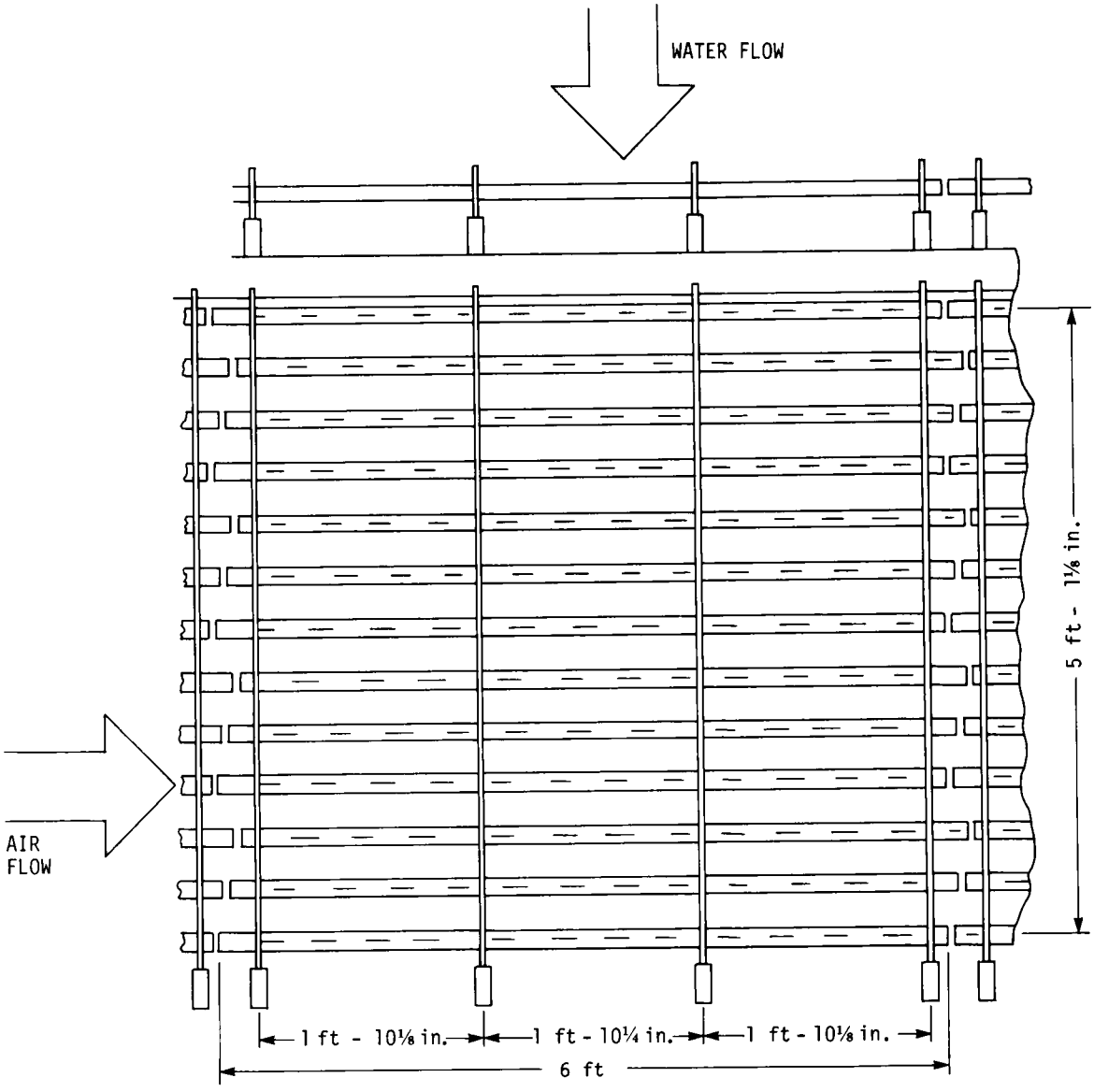


Figure 3.2. Typical transverse elevation of one bay and one story of a K-31 fill rack.

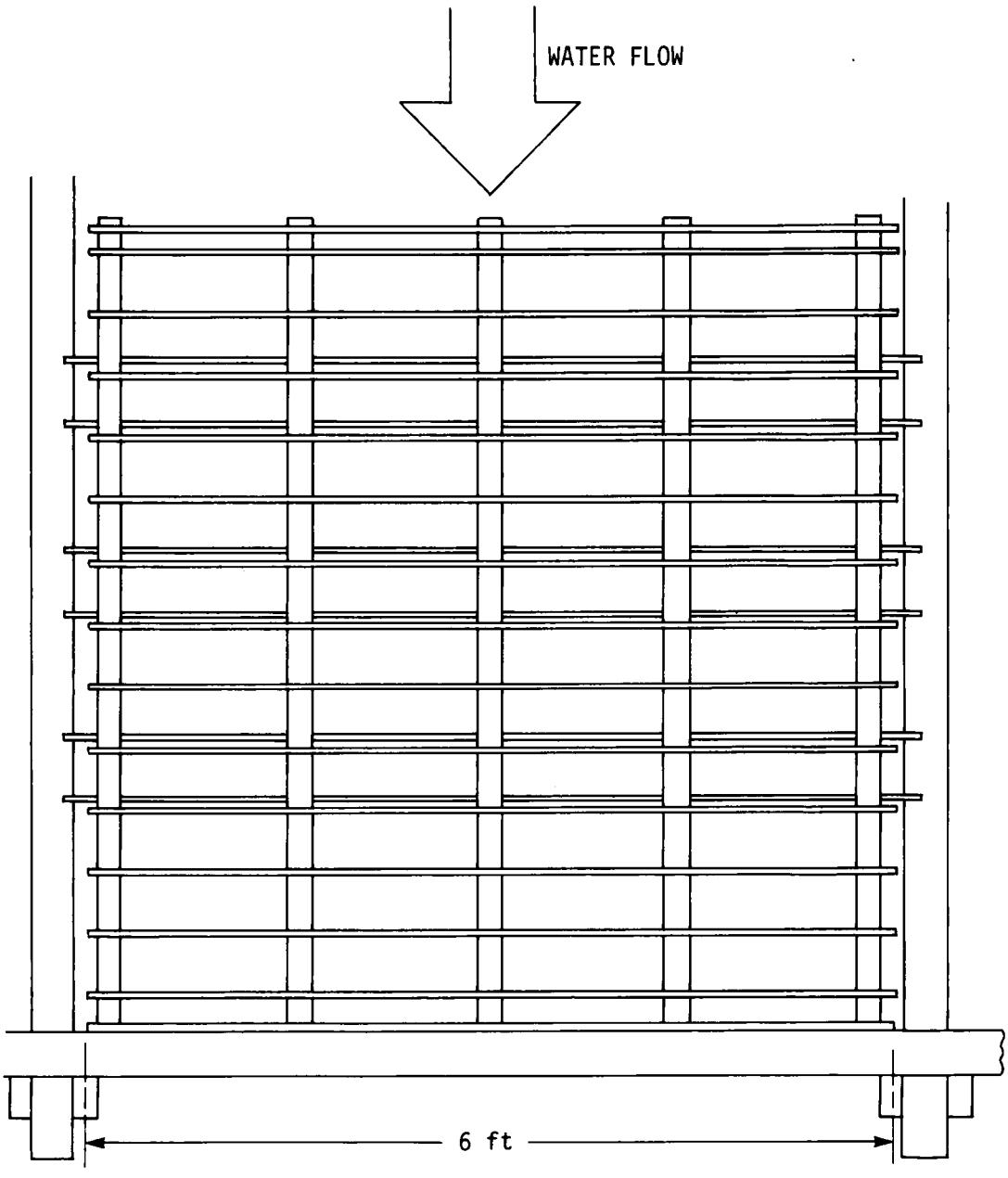


Figure 3.3. Typical longitudinal elevation of one bay and one story of a K-31 fill rack. Air flow is directed normal to and into the page.

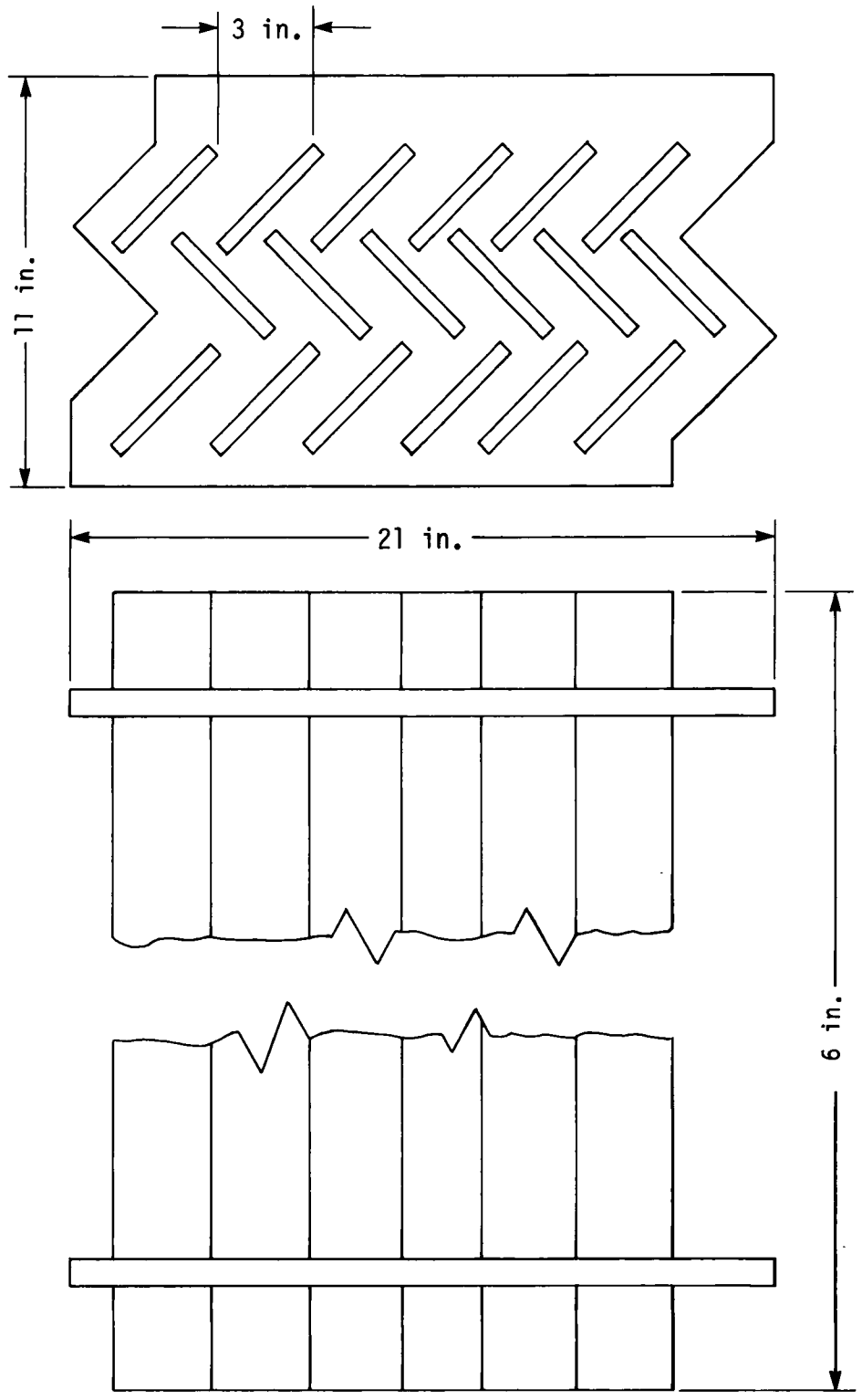


Figure 3.4. Sketch of a drift eliminator rack of the K-31 cooling tower.

through the fill material, the air transverses another small void area followed by the drift eliminators. As can be determined from Figure 3.4, the drift eliminators afford another complex, restricted flow path. After leaving the drift eliminators, the air flows through a large void or open plenum area and exits through the fan to the atmosphere.

A portion of the K-31 water distribution system is visible in Figure 3.1. The hot circulating water (128°F) is distributed across the top of the cooling tower, falling and splashing through the fill material. As the water makes its way through the fill material, it is cooled to 85°F. This water is collected at the base of the tower and recirculated to the gaseous diffusion plant.

Uglow [57] reports that the water loading on the K-31 cooling tower is 55,000 gallons per minute (3.5 m^3/s). The plan area of the K-31 tower is approximately 24,255 square feet 2253 m^2). Thus, the water flow rate through the K-31 fill material is approximately 2.27 gallons per square foot of horizontal plan area per minute (1.54 dm^3/m^2-s). This water flowing through the fill material further complicates and restricts the air flow within the cooling tower.

The restricted, complex and tortuous path described above suggests modeling the air flow through the cooling tower as flow through a porous medium. Bear [60] defines a porous medium as being made up of multiphase matter, at least one phase of which is not solid. The solid phase is in the form of a material matrix with high specific surface area and many narrow, interconnected void or pore spaces.

2. DISCUSSION OF POROUS MEDIUM MODEL

In principle, the air flow through the cooling tower could be determined by the use of the Navier-Stokes equations with proper boundary conditions applied at all fluid-solid interfaces. However, as can be seen from the description of the air flow path, it would be practically impossible to do so.

In the porous medium model, the cooling tower is replaced by a fictitious continuum. This continuum is a structureless substance, at any point of which material parameters or coefficients can be assigned to accommodate observed experimental phenomena. These parameters are then regarded as functions of space alone for a linear steady state analysis.

The basic equation governing fluid motion through porous media is known as Darcy's Law. Bear [60] gives Darcy's Law for an isotropic medium as

$$\vec{q} = - \underline{K} \vec{\nabla} \phi \quad . \tag{3.1}$$

The specific flux vector, $\vec{q}$, has units of volumetric flow rate per unit area. The hydraulic conductivity, $\underline{K}$, is a property of the medium which is usually determined from experimental data. The piezometric head, ϕ, is defined by

$$\phi = z + \frac{P}{\rho g} \tag{3.2}$$

where z is the elevation relative to a datum, P is the fluid pressure, ρ is the fluid density which is assumed to be constant, and g is the acceleration imparted by the gravitational field.

A hydraulic mass conductivity, K', can be defined as

$$K' = \rho \cdot \underline{K} \quad . \tag{3.3}$$

Multiplying Eq. (3.1) by ρ and introducing K' gives

$$\rho\vec{q} = - K'\vec{\nabla}\phi \tag{3.4}$$

where $\rho\vec{q}$ is the mass flux vector.

As described above, the interior of the K-31 cooling tower contains fill racks, drift eliminators, and void areas. Each of these distinct portions of the tower is modeled as a different porous medium. Each medium is assigned a hydraulic mass conductivity to reflect its resistance to air flow. These hydraulic mass conductivities are determined from empirical pressure drop data given by Kelly [61].

Kelly reports that the hydraulic mass conductivity of the fill is a function of the water loading on the cooling tower. Uglow [57] gives the water load on the K-31 cooling tower as 55,000 gal/min (3.5 m^3/s). Assuming the load to be evenly distributed over the plan area of the K-31 tower gives a water load of approximately 1133 lb_m of water/hr-ft^2 (1.54 kg/m^2-s). From the experimental data given by Kelly, which corresponds approximately to the fill material used in the K-31 tower, the hydraulic mass conductivity of the fill is calculated to be

$$K'_{fill} = 1.06 \frac{\frac{\text{kg - air}}{\text{sec - m}^2}}{\frac{\text{Pa}}{\text{m}}} \quad . \tag{3.5}$$

Using a similar analysis, the hydraulic mass conductivity of the drift eliminators and the inlet louvers is determined to be

$$K'_{\substack{\text{inlet}\\\text{louvers}}} = K'_{\substack{\text{drift}\\\text{eliminators}}} = 0.16 \frac{\frac{\text{kg - air}}{\text{sec - m}^2}}{\frac{\text{Pa}}{\text{m}}} \quad . \tag{3.6}$$

The hydraulic mass conductivity of the void or open plenum areas is set at two orders of magnitude larger than that of the fill material. Thus, the piezometric head varies much less in the void areas than in the fill, inlet louver, or drift eliminator areas.

3. DISCUSSION OF THE FINITE ELEMENT SOLUTION METHOD AND BOUNDARY CONDITIONS

Applying the incompressible form of the mass continuity equation by taking the divergence of Eq. (3.4) gives the following result:

$$\vec{\nabla} \cdot (\rho\vec{q}) = - \vec{\nabla} \cdot (K'\vec{\nabla}\phi) = 0 \quad . \tag{3.7}$$

This equation has the same form as the steady state heat conduction equation with the piezometric head, ϕ, taking the role of the temperature and the mass flux, $\rho\vec{q}$, taking the role of the heat flux.

Wilson and Nickell [62] give a finite element algorithm for the analysis of heat transfer in plane and axisymmetric structures which is based upon the work of Zienkiewicz and Cheung [63]. This algorithm is used to determine the pressure distribution within the cooling tower.

The finite element discretization of the K-31 cooling tower is given in Figure 3.5. The plane jet fan ports and the louver faces, as discussed in Section 7, Chapter 2, are also shown in this figure. Comparison of Figure 3.1, page 47, and Figure 3.5 shows that two

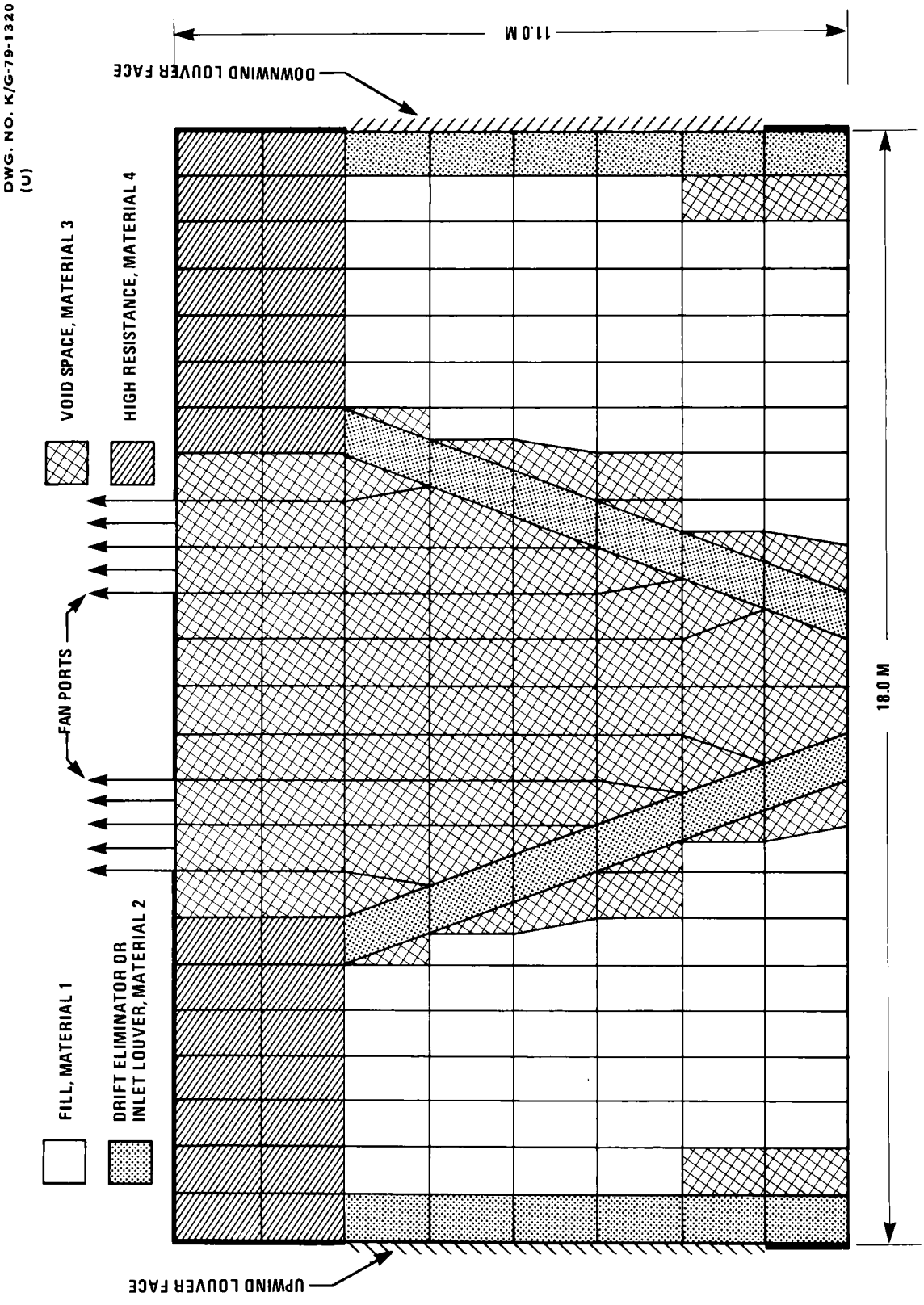


Figure 3.5. Cooling tower finite element discretization.

regions of "high resistance material" have been added to the finite element model which do not exist in the physical configuration. These regions were added to simplify the geometry specifications of the boundary at the top corners of the cooling tower in the wind field calculation. The hydraulic mass conductivity of this "high resistance material" is set to be six orders of magnitude less than that of the drift eliminators and the inlet louvers. Thus, essentially no flow passes through the "high resistance material."

As discussed in Section 7, Chapter 2, the exhaust fan atop the cooling tower is modeled as a pair of plane jets issuing vertically from the fan ports with the top hat velocity profile shown in Figure 2.6, page 34. Specification of the mass flux through these fan ports on the boundary of the cooling tower dictates a Neumann boundary condition at the fan nodes of the cooling tower interior pressure model. The mass flux, M(i,j), associated with fan node (i,j) is determined by integrating the top hat velocity profile:

$$M(i,j) = \int_A^B K' \frac{\partial \phi}{\partial n} \, ds = \int_A^B \rho \overline{W}_{exit} \, (x) \, dx \quad . \tag{3.8}$$

In Eq. (3.8), A is the midpoint between node (i-1,j) and node (i,j); B is the midpoint between node (i,j) and node (i+1,j).

Also as discussed in Section 7, Chapter 2, the wind field pressure calculation yields the pressure distribution along the upwind and downwind louver faces. This wind field pressure distribution dictates a Dirichlet boundary condition at the cooling tower inlet louvers of the internal pressure model. For node (i,j) on the louver face of the internal

pressure model, this condition is given as

$$\phi(i,j) = \frac{P_{\text{wind field}}(i,j)}{\rho g} \quad , \tag{3.9}$$

where $P_{\text{wind field}}(i,j)$ is the pressure at the corresponding node in the wind field calculation.

That portion of the boundary of the cooling tower internal pressure model which is neither fan port nor louver face is treated as an insulated no-flux boundary. For a node (i,j) on this solid wall boundary, a Neumann boundary condition is specified:

$$\left.\frac{\partial \phi}{\partial n}\right|_{(i,j)} = 0 \quad . \tag{3.10}$$

The distribution of the piezometric head within the cooling tower is then determined using the Wilson-Nickell [62] finite element algorithm to solve Eq. (3.7) with the boundary conditions as specified by Eq. (3.8), Eq. (3.9), and Eq. (3.10). The resulting distribution of piezometric head is then used to determine the mass flux through the cooling tower louver faces as discussed in the following section.

4. DISCUSSION OF THE CALCULATION OF THE MASS FLUX THROUGH THE COOLING TOWER INLET LOUVERS

The transfer of mass between the external finite difference wind field model and the internal finite element pressure model occurs at the cooling tower fan ports and at the cooling tower inlet louvers. The mass flux at the fan ports is discussed in Section 5, Chapter 3. The mass flux through the cooling tower inlet louvers is discussed forthwith.

The mass flow rate at any node on the louver faces is calculated as a function of the piezometric head using Eq. (3.4). This calculation involves approximating the normal derivative of the piezometric head at the louvers,

$$\rho\bar{U}(x_i,z) = - K' \left.\frac{\partial\phi}{\partial x}\right|_{(x_i,z)} \quad , \tag{3.11}$$

where x_i is the horizontal coordinate of the louver face shown in Figure 3.6. As discussed in Section 7, Chapter 2, this mass flow rate is then used to evaluate the stream function by integrating Eq. (2.52). Thus, to determine the stream function at node (i,j+1), shown in Figure 3.6, the following integration must be performed,

$$\psi(i,j+1) = \psi(i,j) + \int_{z_j}^{z_{j+1}} \rho\bar{U}(x_i,z)\, dz \quad . \tag{3.12}$$

Substituting Eq. (3.11) into Eq. (3.12) gives

$$\psi(i,j+1) = \psi(i,j) + \int_{z_j}^{z_{j+1}} - K' \left.\frac{\partial\phi}{\partial x}\right|_{(x_i,z)} dz \quad , \tag{3.13}$$

which is then used to set the stream function boundary conditions along the cooling tower louvers of the wind field model.

To evaluate Eq. (3.13), it is necessary to approximate the horizontal derivative of the piezometric head in a manner compatible with the finite element formulation of the internal pressure model. The Wilson-Nickell algorithm uses a linear triangular element to approximate the field variable [62]. Thus, each quadrilateral element shown in

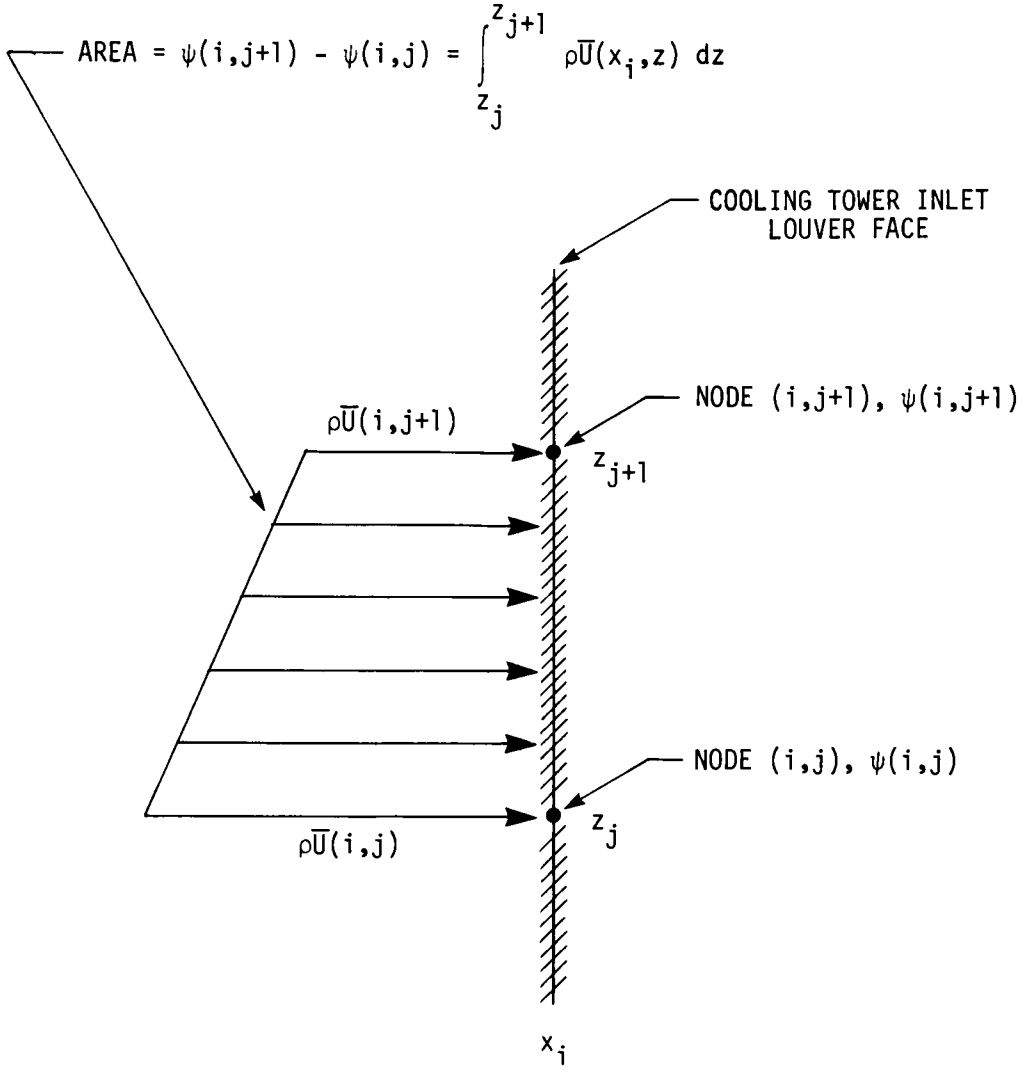


Figure 3.6. Schematic of the procedure to set the stream function values at the cooling tower inlet louvers.

Figure 3.5, page 55, is subdivided into four triangular subelements as shown in Figure 3.7. In this process, an additional node is created in the center of each quadrilateral, denoted as C_ℓ, C_m, and C_n in Figure 3.7.

Within each of these subelements, the continuous field variable is represented by a linear interpolation between the values of the field variable at the nodes [63]. Thus, within the subelement e_1 with nodes t, u, and v, shown in Figure 3.8, the field variable ϕ is given as

$$\phi(x,z) = \phi_t N_t(x,z) + \phi_u N_u(x,z) + \phi_v N_v(x,z) \quad , \tag{3.14}$$

where the functions N_i are linear functions of the coordinates and the ϕ_i are the values of the field variable at the corresponding nodes. Thus, on each subelement, ϕ is a linear function with constant slope. Also, at each node point and across the boundary of each subelement, ϕ is a continuous function; however, the derivatives of ϕ are in general discontinuous at the node points and across subelement boundaries.

In particular, the horizontal derivative of the piezometric head is constant on each subelement and can be evaluated at the louver face by a finite difference expression. For example, along the louver face between nodes 5 and 7, shown in Figure 3.7, page 61, the required derivative is given as

$$\left.\frac{\partial \phi}{\partial x}\right|_{\substack{x=x_i \\ z_3 < z < z_4}} = \frac{\phi_{C_n} - \frac{1}{2}(\phi_5 + \phi_7)}{\Delta x/2} \quad . \tag{3.15}$$

By applying the method of weighted residuals with the Galerkin process to the linear triangular subelements depicted in Figure 3.7,

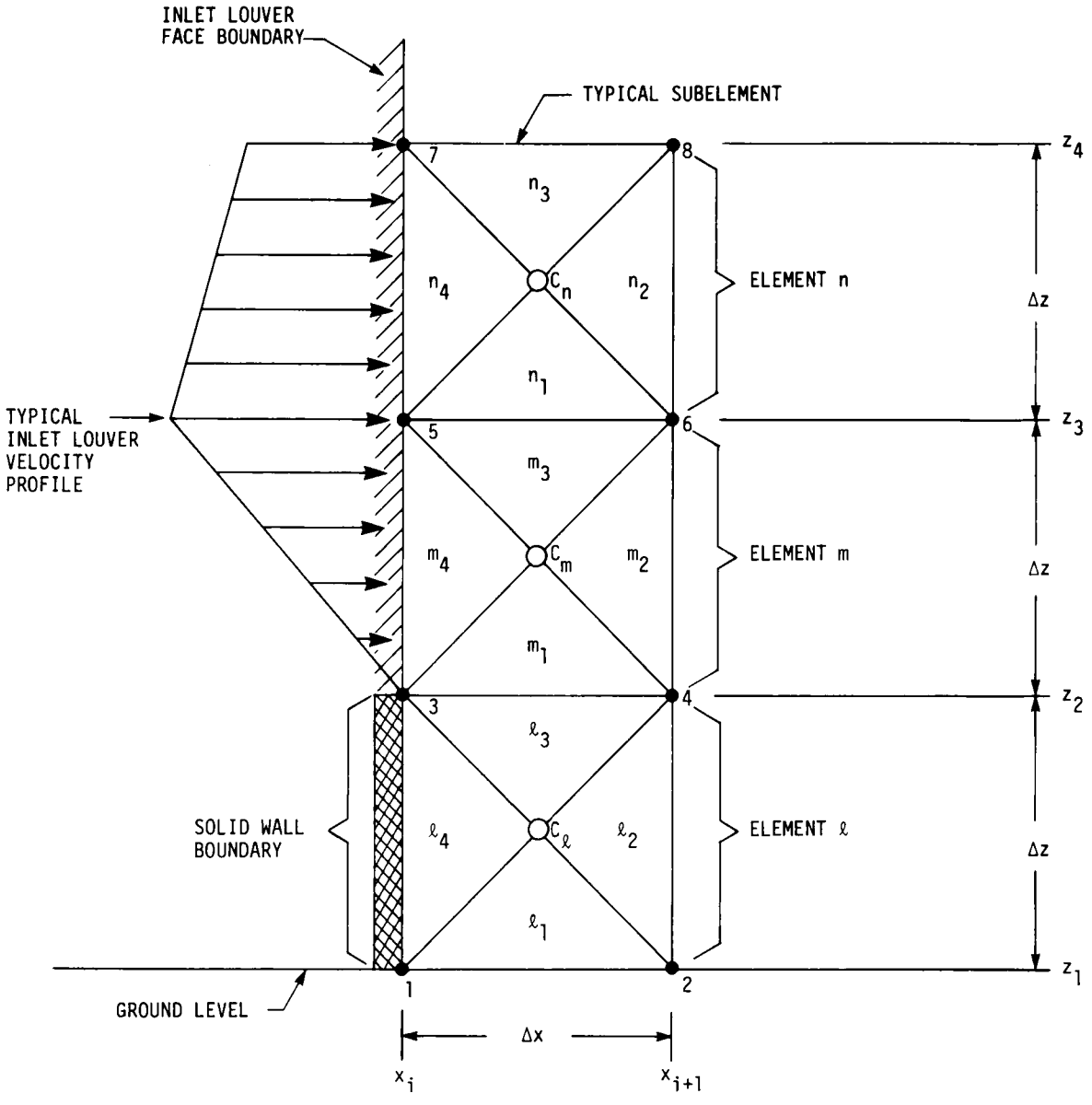


Figure 3.7. Detail of a section of a louver area of the finite element cooling tower internal pressure model.

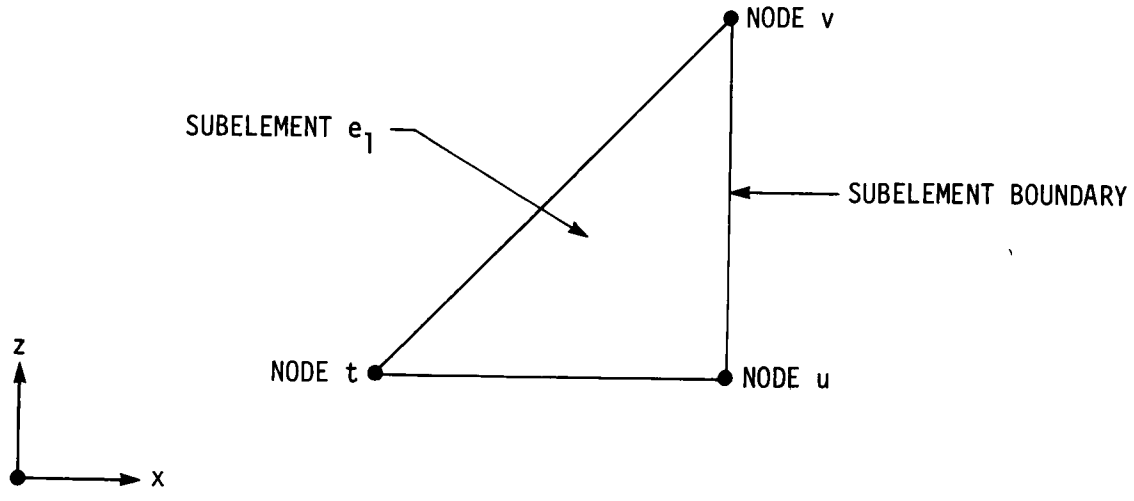


Figure 3.8. A typical subelement, e_1, used in the Wilson-Nickell [62] finite element algorithm.

it can be shown that

$$\phi_{C_n} = (\phi_5 + \phi_6 + \phi_7 + \phi_8)/4 \quad . \tag{3.16}$$

Details of the derivation of Eq. (3.16) are given in Appendix C.

Substituting Eq. (3.16) into Eq. (3.15) and rearranging the result gives the following

$$\left.\frac{\partial \phi}{\partial x}\right|_{\substack{x=x_i \\ z_3 < z < z_4}} = \frac{1}{2}\left[\frac{\phi_6 - \phi_5}{\Delta x} + \frac{\phi_8 - \phi_7}{\Delta x}\right] \quad . \tag{3.17}$$

Then, with an expression such as Eq. (3.17) used to evaluate the required derivative, Eq. (3.13) can be used to set the stream function boundary conditions along the inlet louvers.

Due to the discontinuity of the horizontal derivative of the piezometric head at a node point and along subelement boundaries as discussed above, there is some uncertainty as to the proper value of this derivative at points such as nodes 3, 5, and 7 in Figure 3.7. At nodes within the louver face, such as node 5 and node 7, this discontinuity may affect the numerical result, but only slightly. However, at a node which lies between the solid wall and the louver face, this discontinuity becomes more troublesome. For example, at node 3 of Figure 3.7, the mass flow rate as given by Eq. (3.17) evaluated using subelement m_4 would, in general, be nonzero. However, since node 3 is on the upper edge of the solid wall boundary, the mass flux at node 3 should be zero by definition. Hence, to approximate the transition from the solid wall boundary to the louver face boundary and to ensure no mass flux through the solid wall boundary, the mass flow rate is set to zero at the upper

and lower edges of the louver faces. For example, in element m of Figure 3.7, Eq. (3.17) is evaluated as

$$\left.\frac{\partial\phi}{\partial x}\right|_{\substack{x=x_i \\ z_2 < z < z_3}} = \frac{1}{2}\left[\frac{\phi_4 - \phi_3}{\Delta x} + \frac{\phi_6 - \phi_5}{\Delta x}\right]$$

$$= \frac{1}{2}\left[\frac{\phi_6 - \phi_5}{\Delta x}\right] \quad , \tag{3.18}$$

since the first term is set to zero to ensure no mass flow through the solid wall boundary,

$$\frac{\phi_4 - \phi_3}{\Delta x} = 0 \quad . \tag{3.19}$$

Although the above approximation cannot be strictly defended in a rigorous mathematical manner, the calculated results from the numerical model show that this approximation does in fact preserve mass conservation within the control volume formed by the boundaries of the cooling tower internal pressure model. This conservation of mass as well as the matching of pressures at the louvers serves to couple the cooling tower internal pressure model and the wind field model as discussed in the following section.

5. COUPLING OF THE WIND FIELD MODEL AND THE COOLING TOWER INTERNAL PRESSURE MODEL

The interface between the finite difference model of the atmospheric flow field over the cooling tower and the finite element model of the cooling tower internal pressure occurs at the boundary of the cooling tower which is shown in both Figure 2.5, page 32, and Figure 3.5,

page 55. In particular, the interaction between the two models occurs at the fan ports and at the louver faces. This interaction or coupling is accomplished by matching mass fluxes at the fan ports and pressures and mass fluxes at the louver faces.

The matching of the mass fluxes at the fan ports is accomplished by using the same plane jet, top hat velocity profile to set the boundary conditions for both the wind field (external) model and the internal pressure model. As described in Chapter 2, Eq. (2.51), Eq. (2.53), Eq. (2.54), and Eq. (2.55) use this velocity profile directly to set conditions on the stream function and the vorticity at the fan nodes. The assumption of a plane jet is used to set conditions on the temperature, the turbulence kinetic energy, and the turbulence length scale in Eq. (2.56), Eq. (2.57), and Eq. (2.58). Likewise, the top hat velocity profile is integrated in Eq. (3.8) to set the boundary condition at the fan ports of the internal pressure model. Thus, internal and external models are coupled at the fan ports by matching the mass fluxes there.

The external model communicates to the internal model at the cooling tower louver nodes through the Dirichlet boundary condition imposed upon the internal model at these nodes. This is accomplished in Eq. (3.9), where the pressure at a louver boundary node of the internal model is set equal to the value of the wind field pressure at the corresponding node in the external model. The internal model communicates to the external model at the louver nodes by dictating the mass flux there. As discussed in Section 4, Chapter 3, the mass flux at the louver nodes is calculated from the distribution of the piezometric head within

the cooling tower which is determined by the internal model. As discussed in Section 7, Chapter 2, and Section 4, Chapter 3, this mass flux at the cooling tower louvers is used in the integration of Eq. (2.52) to set the conditions on the stream function at the louver boundary nodes of the external model. Thus, internal and external models are coupled at the cooling tower louvers: external model dictates pressure to the internal; internal model dictates mass flux to the external.

The wind field model, as discussed in Chapter 2, coupled with the cooling tower internal pressure model, discussed in this chapter, form a complete model of cooling tower recirculation as influenced by the local atmospheric flow field. Some computational aspects of this complete model are discussed in the following chapter.

CHAPTER 4

COMPUTATIONAL TECHNIQUE

1. INITIAL CONDITIONS

As previously discussed in Sections 1 and 2 of Chapter 2, the wind field solution algorithm is a successive relaxation iterative numerical scheme. The convergence ability of this scheme can be destroyed by the use of improper initial conditions. The initial conditions throughout the computational region must be "approximately continuous" functions of space with no sharp discontinuities. One successful method of determining these initial conditions is to set the inflow boundary conditions and then sweep these values across the computational region in the major flow direction, that is, in the direction of increasing horizontal coordinate. Another successful technique is to start a new case from the converged solution of a previous case. As discussed in Section 4 of this chapter, this later method can reduce the computations required to achieve convergence in the new case.

A detailed discussion of the wind field pressure calculation is presented in Section 8 of Chapter 2. This algorithm is an alternating direction implicit technique and as such is also an iterative scheme which is sensitive to its initial conditions. The same two techniques for setting initial conditions as described above apply to the wind field pressure algorithm.

In the use of a previously converged solution as the initial conditions for a new case, experience has shown that changing the ambient,

inflow boundary conditions in a series of small increments is more expedient than applying one large change. For example, to calculate a 6 m/s case starting from a 4 m/s solution, it is recommended to change the inflow velocity profile in increments of 0.5 m/s. In doing so, a series of converged solutions will be attained for 4.5 m/s, 5.0 m/s, 5.5 m/s, and finally 6.0 m/s. This series of converged solutions will usually require fewer iterations than that required to directly calculate 6.0 m/s from the 4.0 m/s solution.

This same technique should be applied to changes in the flow rate through the cooling tower. For example, in the calculation of a given case without the benefit of a previously converged solution as initial conditions, it is recommended to first attain a solution for the case with no flow through the cooling tower. After this case has converged, then the flow rate through the cooling tower should be gradually increased to the desired value. For example, experience has shown that to achieve a vertical velocity of 13.7 m/s from the cooling tower fan, it may be necessary, depending upon the ambient velocity, to use increments as small as 0.5 m/s. If larger increments are used, depending upon the ambient flow, the solution may become unstable, which leads to an overflow type computational error.

2. CONVERGENCE CRITERION

The wind field solution technique uses a convergence criterion based on the maximum relative change of each of the variables between two successive iterations. Let $V^{\nu}(i,j)$ denote the value of variable V at node (i,j) after iteration number ν, then the convergence criterion

applied at node (i,j) after iteration number $\nu + 1$ would be

$$\left| \frac{V^{\nu+1}(i,j) - V^{\nu}(i,j)}{|V^{\nu+1}(i,j)| + V_{Floor}} \right| \quad . \tag{4.1}$$

In Eq. (4.1), V_{Floor} is a positive constant which is set equal to the magnitude of a value typical of the smallest meaningful nonzero value of the variable V which appears in the computational region.

Without the constant V_{Floor}, the convergence criterion expressed in Eq. (4.1) could cause excessive iteration of a solution which was actually well converged. If node (i,j) happened to be located near the boundary between a region where variable V was positive and a region where variable V was negative, then the value of variable V at node (i,j) could become very small, approaching zero. In this situation, the value of the expression given in Eq. (4.1) without the inclusion of V_{Floor} would become very large, even if the numerator of Eq. (4.1) was small.

To avoid this problem, a "floor" value of each variable was determined from a typical converged solution. These "floor" values, V_{Floor}, were then incorporated in the convergence criterion as given in Eq. (4.1). Thus, if $V^{\nu+1}(i,j)$ is very, very small, the change in V(i,j) from iteration ν to iteration $\nu + 1$, $V^{\nu+1}(i,j) - V^{\nu}(i,j)$, would be measured relative to V_{Floor} rather than relative to $V^{\nu+1}(i,j)$. In this way, unnecessary iterations are avoided.

Care should be taken that appropriate values of V_{Floor} are used for all variables being calculated. A successful method of choosing V_{Floor} is to visually scan a converged solution to determine an appropriate meaningful small value of variable V which is then used as V_{Floor} for future cases.

The values of V_{Floor} used in the present study were obtained by visually scanning the results of a calculation made for an ambient wind speed of 12 m/s. This 12 m/s case was iterated until the value of the following criterion,

$$\left| \frac{V^{\nu+1}(i,j) - V^{\nu}(i,j)}{V^{\nu+1}(i,j)} \right| \quad , \tag{4.2}$$

was less than 0.05 for all calculated variables at all nodes. This is a tighter criterion than given in Eq. (4.1); if Eq. (4.2) is less than 0.05 for all calculated variables at all nodes, then Eq. (4.1) will also be. Thus, the results for the 12 m/s case were well converged. Values of V_{Floor}, given in Table 4.1, were then determined from these results. The expression given in Eq. (4.1) with these values of V_{Floor} was then used as the convergence criterion for the remaining cases in this study.

3. RESOLUTION OF TWO COMPUTATIONAL ANOMALIES

In the development of the current model, there were two major difficulties which presented themselves. These difficulties as well as their solutions are discussed presently in a somewhat chronological order.

The first difficulty involved the vorticity at the two plane jets which are used to simulate the fan atop the cooling tower. At the edge of these jets there occurs a sharp velocity discontinuity as shown in Figure 2.7, page 37, which initially caused some uncertainty as to the correct vorticity boundary condition to be applied there. For example, just to the left of node (i,j) in Figure 2.7, there is a solid wall boundary where the vorticity would be given by Eq. (2.43). Just to the right of the same node (i,j) is the uniform parallel flow of the jet

TABLE 4.1

Values of V_{Floor} Used in the Current Model

Variable Calculated	Value of V_{Floor}
Vorticity	0.001
Stream Function	10.0
Turbulence Kinetic Energy	1000.0
Turbulence Length Scale	10.0

exiting from the top of the cooling tower in which the vorticity is zero as shown in Figure 2.9, page 40.

As a first approximation, a node (i,j) at the edge of the plane jet was considered to be within the jet itself and hence the vorticity was set to zero there,

$$\omega(i,j) = 0 \quad . \tag{4.3}$$

This completely disregarded the velocity discontinuity at such nodes and resulted in a very unrealistic wind field solution with very little plume rise.

Next, the vorticity at the jet edges was set by using the definition of the vorticity, Eq. (2.11), with the second term set to zero because the flow is predominantly in the vertical direction. Thus, the vorticity at a node such as node (i,j) of Figure 2.7, page 37, was set as

$$\omega(i,j) = \frac{\partial \overline{W}}{\partial x} \quad , \tag{4.4}$$

with the derivative expressed in terms of the velocity profile rather than the stream function, referring to Figure 2.7,

$$\omega(i,j) = \frac{\overline{W}(i+1,j) - \overline{W}(i-1,j)}{2\Delta x}$$

$$= \frac{\overline{W}_{exit} - 0}{2\Delta x}$$

$$= \frac{\overline{W}_{exit}}{2\Delta x} \quad . \tag{4.5}$$

This boundary condition greatly improved the wind field solution and the plume rise as compared to the first boundary condition. However, the plume

rise still did not agree well with observation or with values reported by Briggs [29]. Also, by applying Stokes Theorem as discussed in Section 7, Chapter 2, it became evident that this boundary condition did not provide sufficient vortex strength to support the velocity discontinuity at the edge of the jets.

The final form of this boundary condition, as given in Eq. (2.54), was used because it did generate the required vortex strength to support the velocity discontinuity as shown in Figure 2.8, page 38. Also, this form of the boundary condition followed naturally from the central difference formulation of the second derivative of the stream function, Eq. (2.53), as shown in Figure 2.7, page 37. The formulation given in Eq. (2.53) is a more accurate approximation to the horizontal derivative of the vertical velocity than the formulation given in Eq. (4.5) because Eq. (2.53) uses values of the vertical velocity nearer node (i,j) to evaluate the derivative at node (i,j). As is discussed in Chapter 5, this form of the boundary condition gave realistic values of plume rise which agree well with those reported by Briggs [29].

The second major difficulty concerned the calculation of the mass flux through the cooling tower louvers. As shown in Section 4, Chapter 3, this calculation involves approximating the normal derivative of the piezometric head at the louvers. Also, as pointed out in that section, the evaluation of this derivative at nodes such as node 3 of Figure 3.7, page 61, was troublesome because these are the nodes which lie between the solid wall and the louver face.

In the first approximation, the value of this derivative and, hence, the mass flow at a node such as node 3 was determined in the same

manner as that used at nodes within the louver face, such as node 5 and node 7 of Figure 3.7, page 61. This method proved unsuccessful, however, because it provided a larger effective louver flow area than exists in the actual cooling tower. This larger area allowed more mass flow through the inlet louvers than out through the fan atop the tower which caused outflow to occur at the louvers on both the upwind and downwind faces, an unrealistic situation. These outflow conditions at the louvers in turn caused the wind field solution to become unstable, which led to an overflow type computational error.

To remedy this problem, the mass flow was set to zero at those nodes which lie between the solid wall and the louver face. As discussed in Section 4 of Chapter 3, this remedy did in fact preserve mass conservation within the cooling tower and ensured no mass flux through the solid wall boundary.

4. COMPUTER USAGE STATISTICS

The current study was run on an IBM 360/195 computer. Execution of the current model required approximately 650K bytes of main storage. Each iteration of the model required approximately 2.3 seconds on the central processing unit of the IBM 360/195.

Table 4.2 gives a comparison of the number of iterations and the computational time required for convergence of the cases run in this study. The 12 m/s case and 6 m/s case were both started from initial conditions which were derived from the inflow boundary conditions as discussed in the first section of this chapter. The 4 m/s case was started using the results of the 6 m/s case as initial conditions; the 2 m/s case was started from the 4 m/s solution.

TABLE 4.2

Computational Time and Number of Iterations Required for Convergence

Nominal Ambient Wind Speed (m/s)	Initial Conditions	Number of Iterations Required for Convergence	CPU Time Required for Convergence (CPU min.)
12	Inflow Boundary Conditions	3502	134
6	Inflow Boundary Conditions	6101	234
4	6 m/s Solution	4927	189
2*	4 m/s Solution	3150	121

*As discussed in Chapter 5, this case was not as well converged as the other cases in this study.

Comparison of the requirements for the 12 m/s case and 6 m/s case shows that, when using the same type of initial conditions, computational requirements increase as the ambient wind speed decreases. However, the 4 m/s case shows that these requirements can be reduced by using a converged solution as the initial conditions for a new case. As is discussed in Chapter 5, the 2 m/s case was not as well converged as the other three cases in this study. Hence, the requirements for this case cannot be directly compared to those of the other cases.

Two recommendations can be made concerning economy in the use of the current model. First, the computational time required for convergence of a particular case is directly dependent upon the number of grid lines used. Thus, judicious choice of the size and degree of refinement of the grid is important when considering computational economy. Second, a proper ordering of the cases to be run in a particular study would also be helpful so that one converged solution could provide the initial conditions for the next case. As shown in Table 4.2, this method of setting the initial conditions will reduce the number of iterations and, hence, the computational time required for convergence of a particular case.

CHAPTER 5

RESULTS

1. GENERAL DISCUSSION

In the current investigation, cooling tower recirculation is studied by numerically modeling the wind flowing over a cooling tower. In this model, the atmosphere is assumed to be neutrally stable; that is, the temperature profile of the approaching wind, as given in Eq. (2.17), is assumed to exhibit the dry adiabatic lapse rate of Eq. (2.16). The ambient temperature at the ground is specified to be 293 K (20°C). The Coriolis effects induced by the rotation of the earth are treated in the manner advocated by Tennekes [53]. He reports that, although a logarithmic wind velocity profile was valid to a height of at least 100 m, the shear stress decreased by as much as 30% over that vertical distance. Thus, the logarithmic velocity profile, given in Eq. (2.8), is assumed valid for the undisturbed approaching wind. However, the shear stress in the undisturbed approaching wind is assumed to vary according to the profile reported by Tennekes and given in Eq. (2.18). The air is considered to be incompressible with a constant density of 1.25×10^{-3} gm/cm^3. Also, in the approaching ambient flow, the barometric pressure at the ground is specified to be the local ambient value, 98.6 KPa (14.3 psi) [56].

As discussed in Section 3 of Chapter 2, the logarithmic velocity profile, Eq. (2.8), contains two parameters which are used to control the shape and magnitude of the profile: z_0, the surface roughness and u_*,

the friction velocity. In the current study, z_0 is specified to be 0.4 m which corresponds to a roughness typical of the surrounding area [64]. The value of u_* is then set to give the desired wind velocity at an altitude of 10 m. Table 5.1 gives the values of u_* which correspond to the four ambient wind speeds used in this study: 2 m/s, 4 m/s, 6 m/s, and 12 m/s, measured at a height of 10 m. More discussion of the logarithmic velocity profile is presented in Section 2 of this chapter.

In the current study, the cooling tower is modeled as a two-dimensional sharp edged rectangular block with fluid flowing out of the top at a specified velocity and temperature, and into the sides at a velocity and temperature dependent upon the flow field conditions internal and external to the tower. The fluid flowing out of the top of the tower is modeled as a two-dimensional plane jet exiting into the atmosphere.

The cooling tower in this study measures 18.0 m wide and 11.0 m tall. The louver areas on both the upwind and downwind faces of the tower are 6.9 m tall. The fan atop the tower is 6.0 m in diameter with a center hub which is 3.0 m in diameter. The temperature of the effluent from the tower is 323 K (50°C) and the efflux velocity is 13.7 m/s.

The present model has been used to calculate the atmospheric flow over a cooling tower for four cases corresponding to the four different ambient wind speeds given in Table 5.1. The convergence criterion used for these cases is discussed in Section 2 of Chapter 4. Three of these cases, for wind speeds of 4 m/s, 6 m/s, and 12 m/s (measured at a height of 10 m), are well converged. These three cases were iterated until the expression given in Eq. (4.1) was less than 0.05 for all calculated variables. Due to a shortage of funds to

TABLE 5.1

Values of the Friction Velocity, u_*, Used In This Study

Wind Speed (m/s)	u_* (m/s)
2.0	0.25
4.0	0.50
6.0	0.74
12.0	1.47

support continued computer work, the calculation for the fourth case, 2 m/s, was not iterated to as tight a convergence tolerance as used in the other cases. At the termination of the 2 m/s case, the convergence criterion given in Eq. (4.1) was less than 0.5 for the stream function, turbulence kinetic energy, and turbulence length scale. It was less than 0.01 for the temperature; however, it was as large as 0.9 for the vorticity. The results of the 2 m/s case are included for completeness although they are not as accurate as those of the other three cases. Figures 5.1 - 5.10 show the results of the 12 m/s case; Figures 5.11 - 5.19, the 6 m/s case; Figures 5.20 - 5.28, the 4 m/s case; and, finally, Figures 5.29 - 5.37 give the results for the 2 m/s case.

2. FLOW DIRECTION AND VELOCITY PROFILES

Comparison of the flow direction plots, Figures 5.1, 5.11, 5.20, and 5.29, shows some details of the flow fields. These figures show that as the wind speed decreases, the center of the eddy behind the tower is shifted. First, as the speed decreased from 12 m/s to 6 m/s, the center moved approximately 5.0 m upward and 5.0 m downwind. Then, as the speed decreased from 6 m/s to 4 m/s, this center continued to move 1.5 m higher but reversed the earlier horizontal trend by moving 5.0 m upwind, nearer to the tower centerline. Finally, as the speed decreased from 4 m/s to 2 m/s, the center of the eddy maintained the same altitude but moved 11.9 m nearer to the tower centerline.

The flow direction plots also show that in the 12 m/s case, the jet exiting from the tower is bent over almost immediately, while at the lower wind speeds, the jet retains a more vertical direction. In the

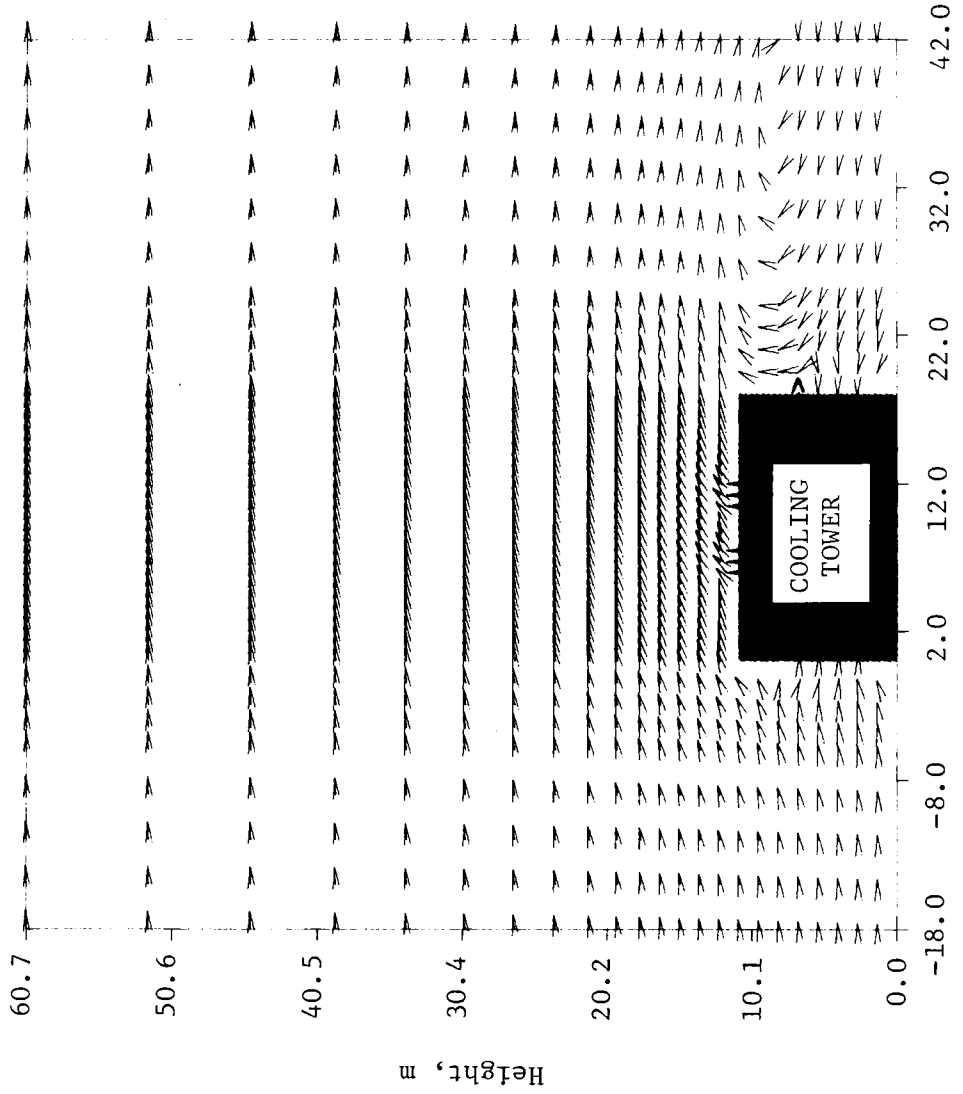


Figure 5.1. Flow direction for wind speed of 12 m/s.

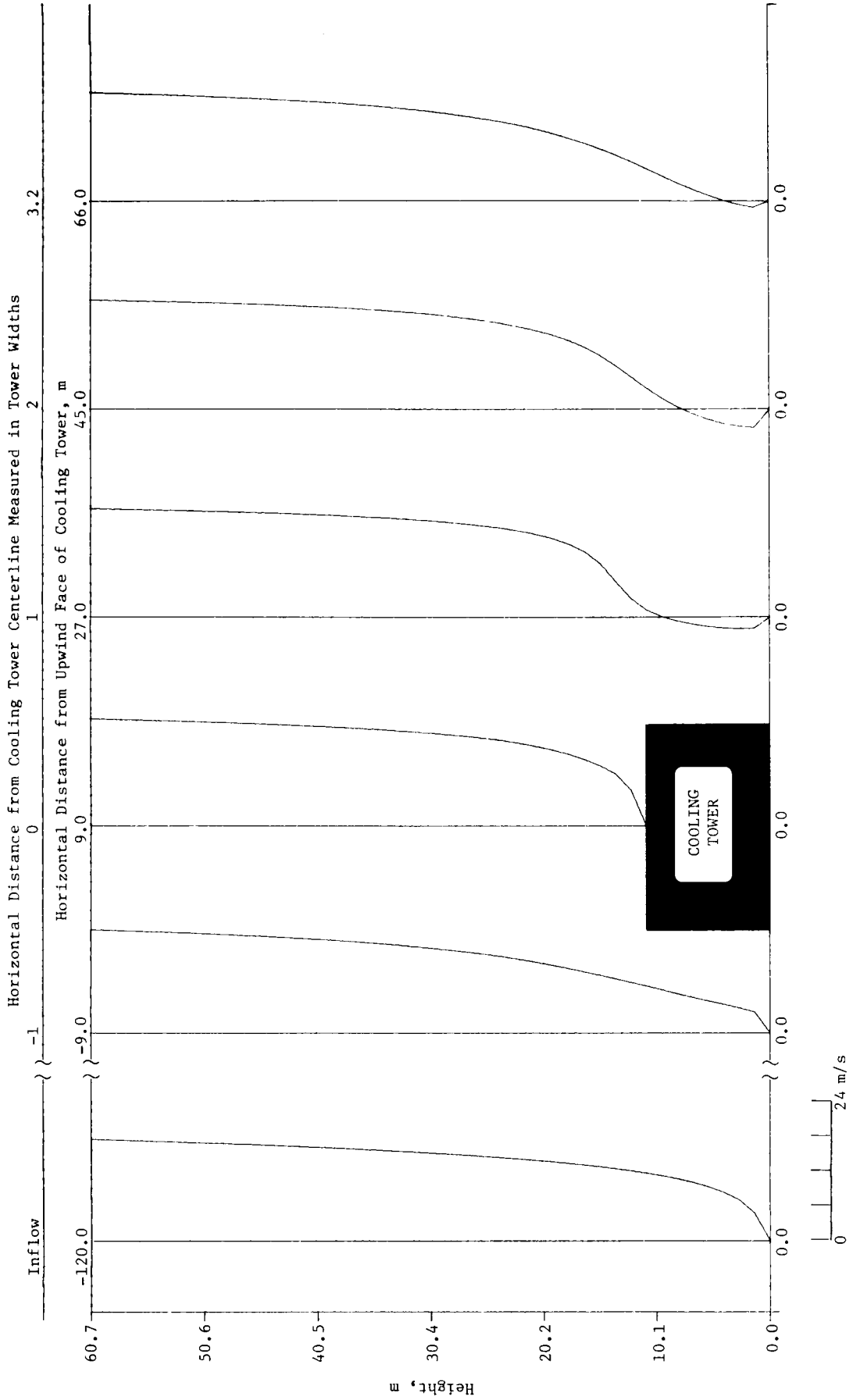


Figure 5.2. Profiles of the horizontal velocity for wind speed of 12 m/s.

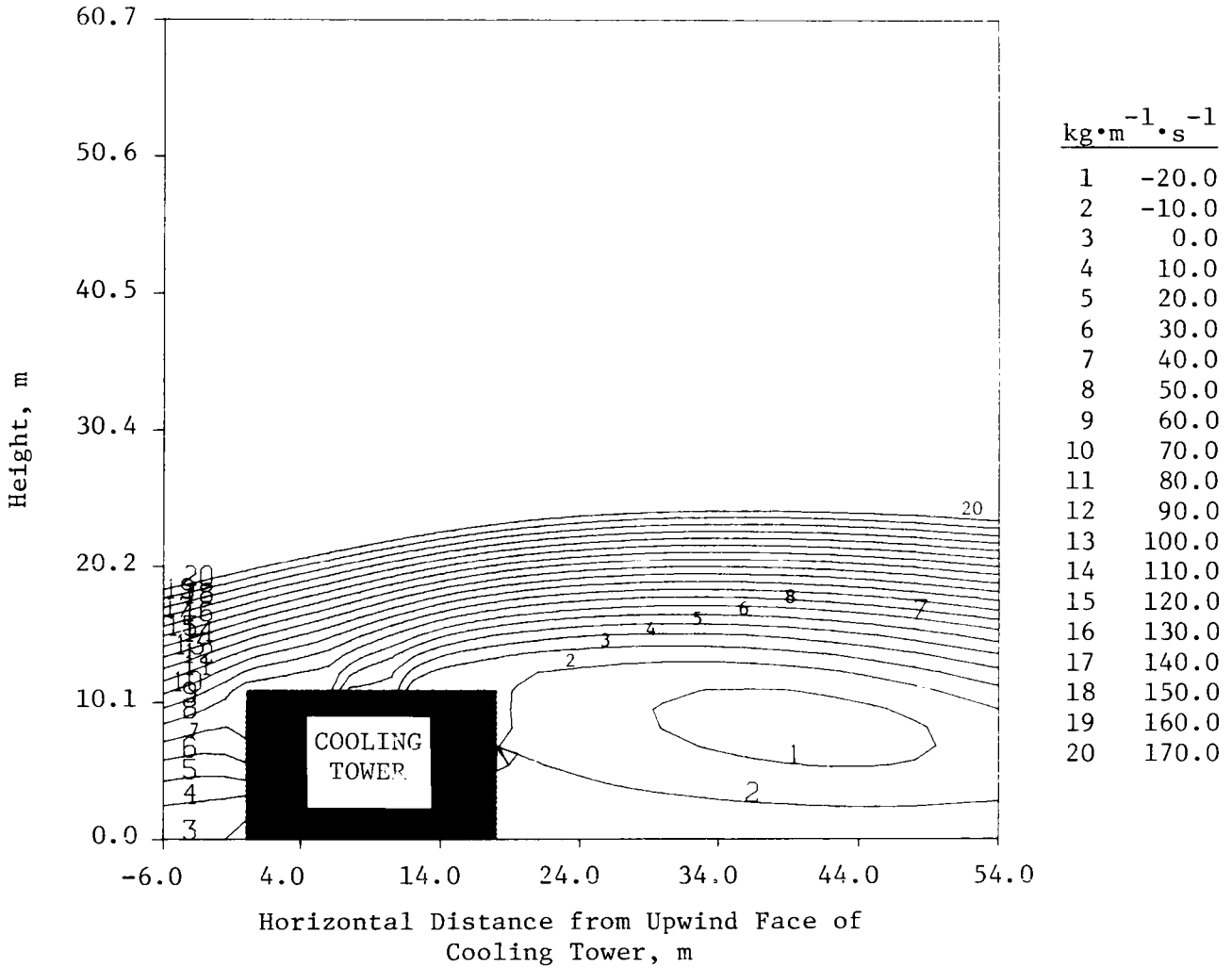


Figure 5.3. Stream function contours for wind speed of 12 m/s.

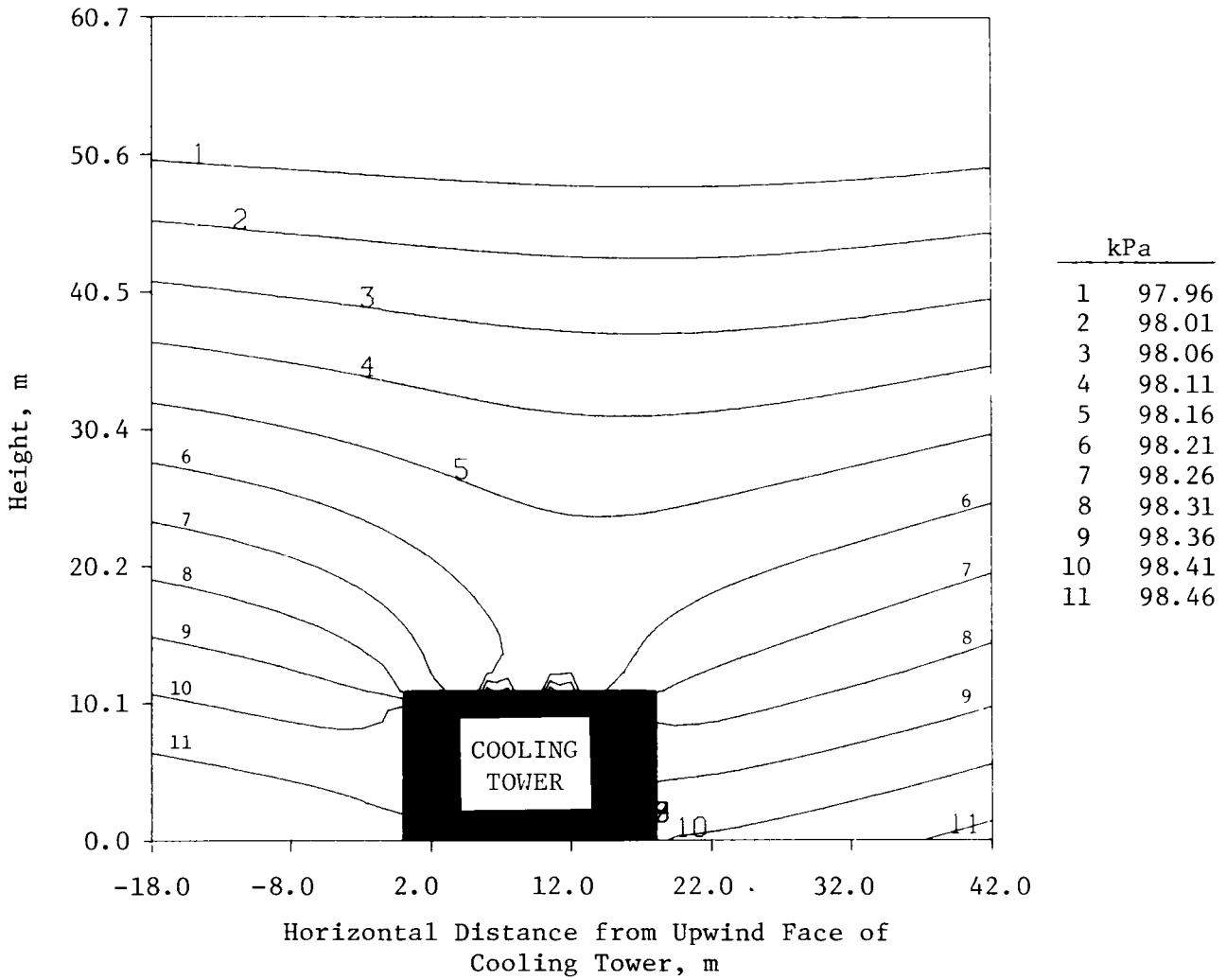


Figure 5.4. Pressure contours for wind speed of 12 m/s.

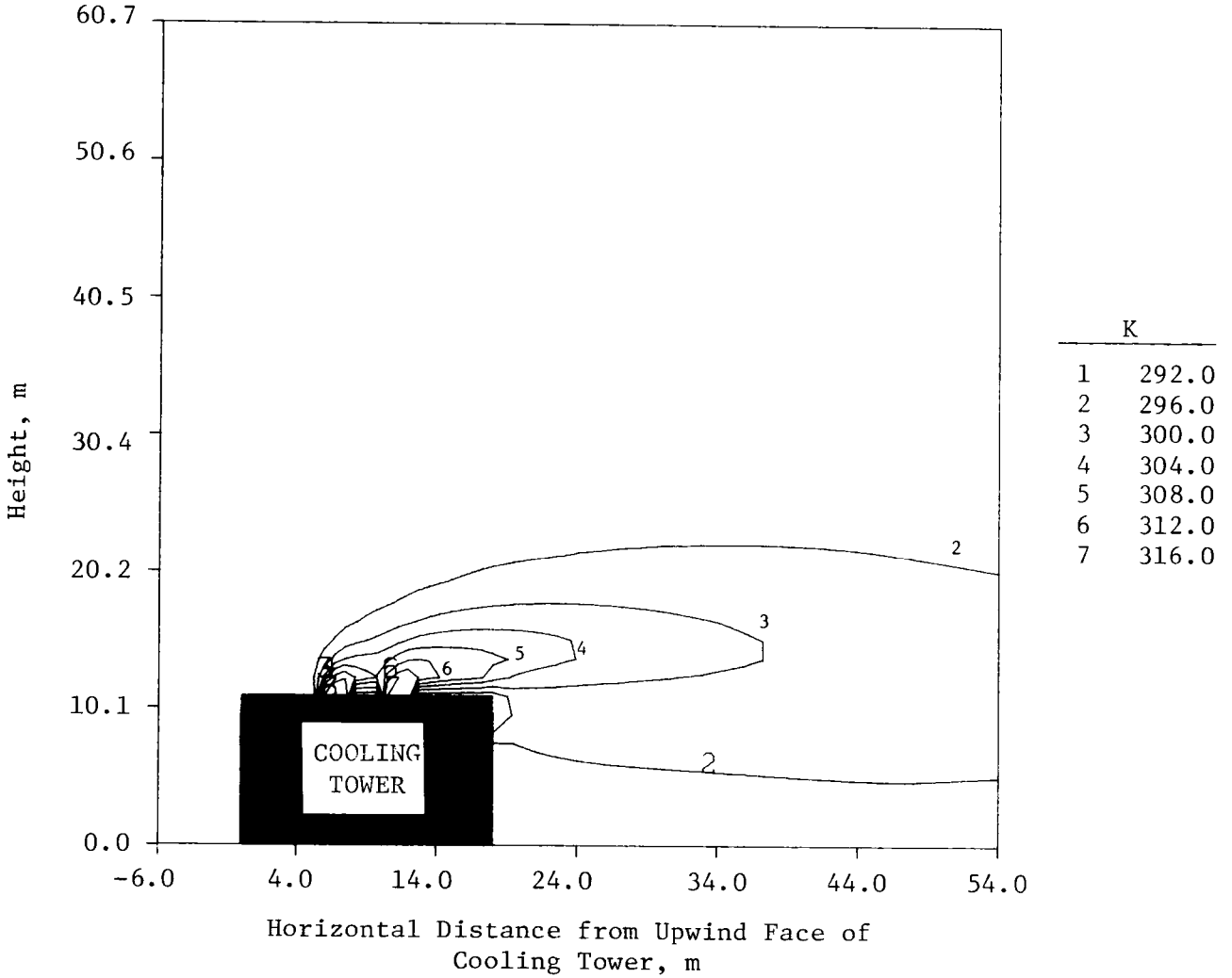


Figure 5.5. Temperature contours for wind speed of 12 m/s.

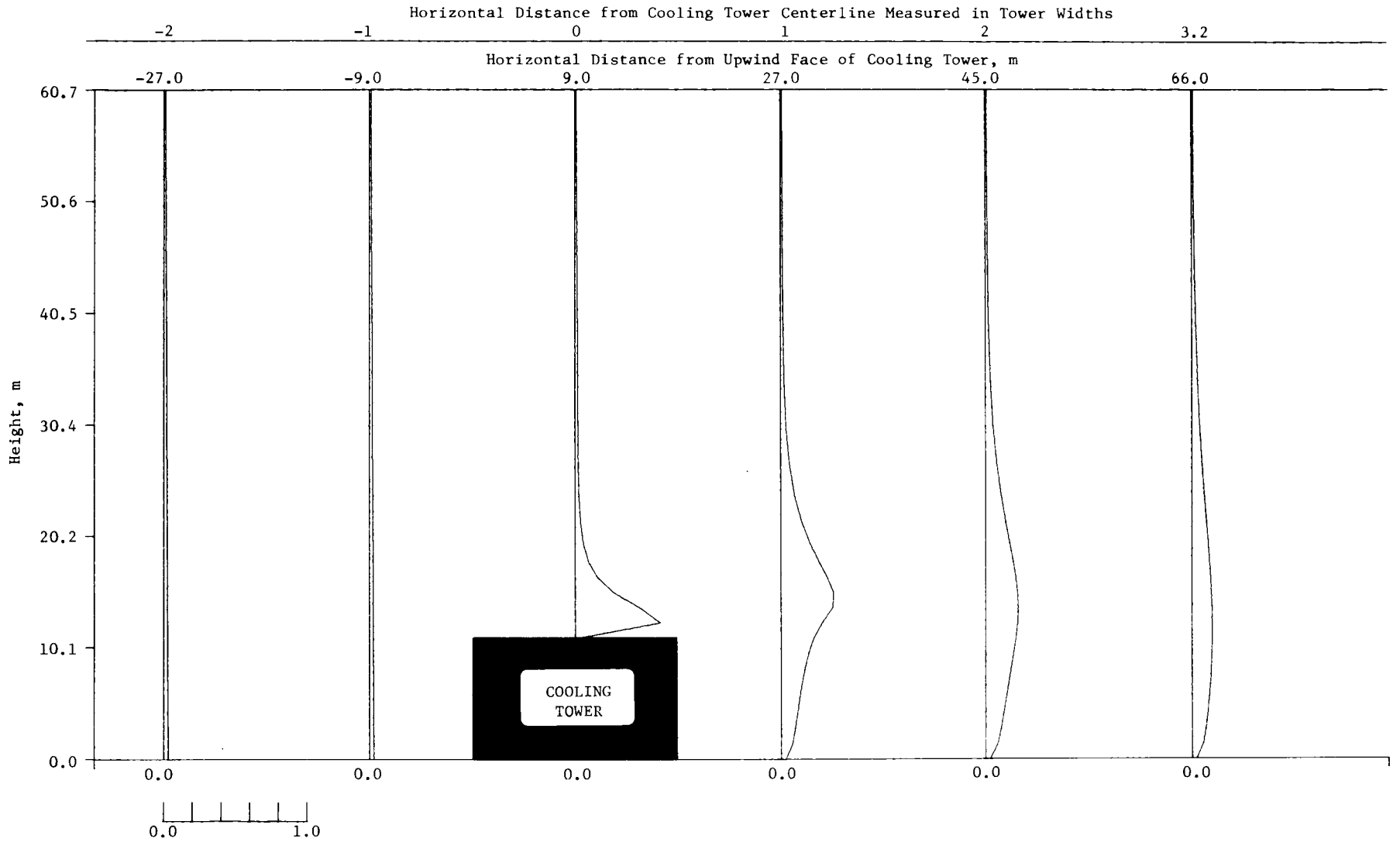


Figure 5.6. Profiles of temperature ratio, $(\overline{T} - \overline{T}_G)/(\overline{T}_{fan} - \overline{T}_G)$, for wind speed of 12 m/s.

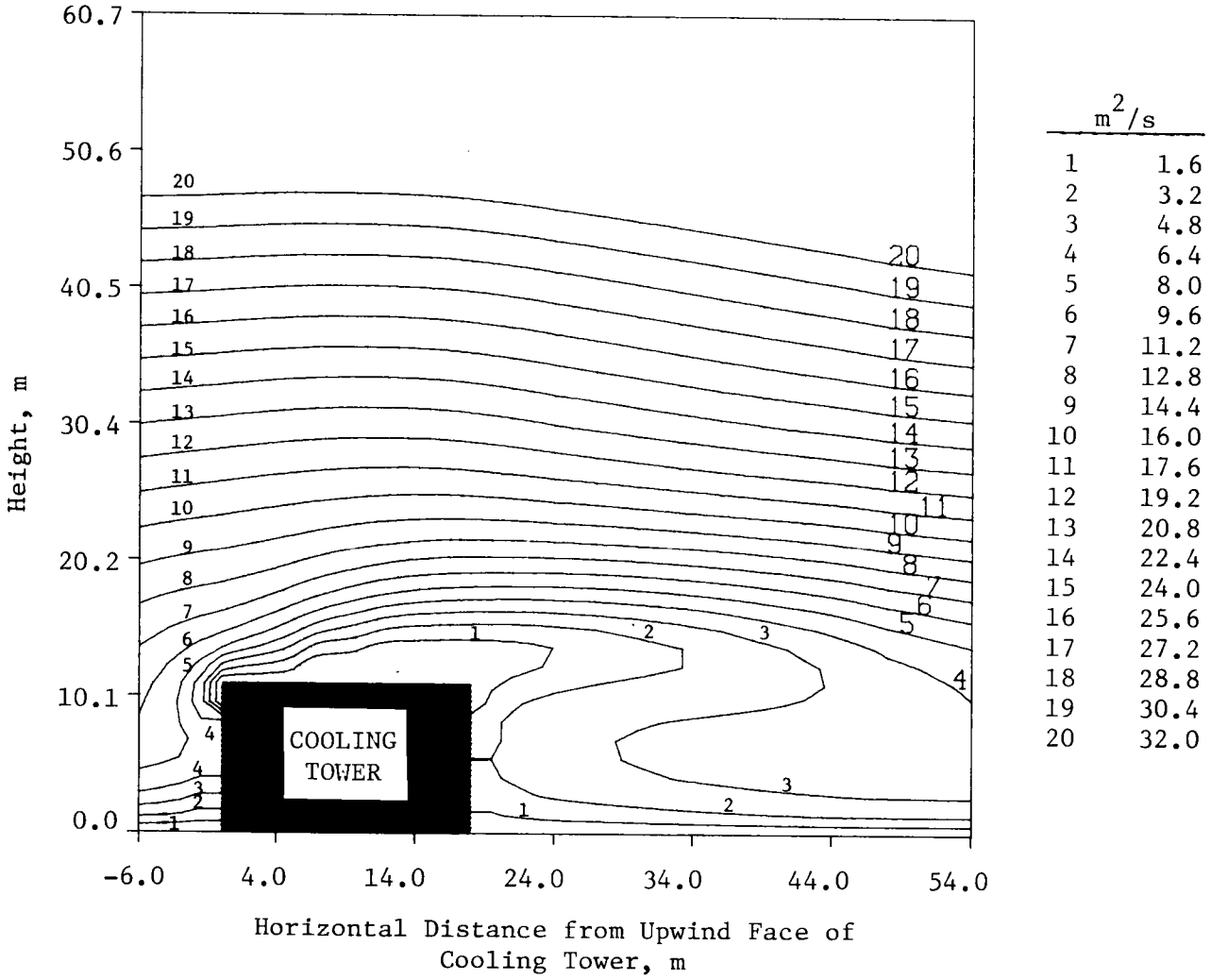


Figure 5.7. Effective thermal diffusivity contours for wind speed of 12 m/s.

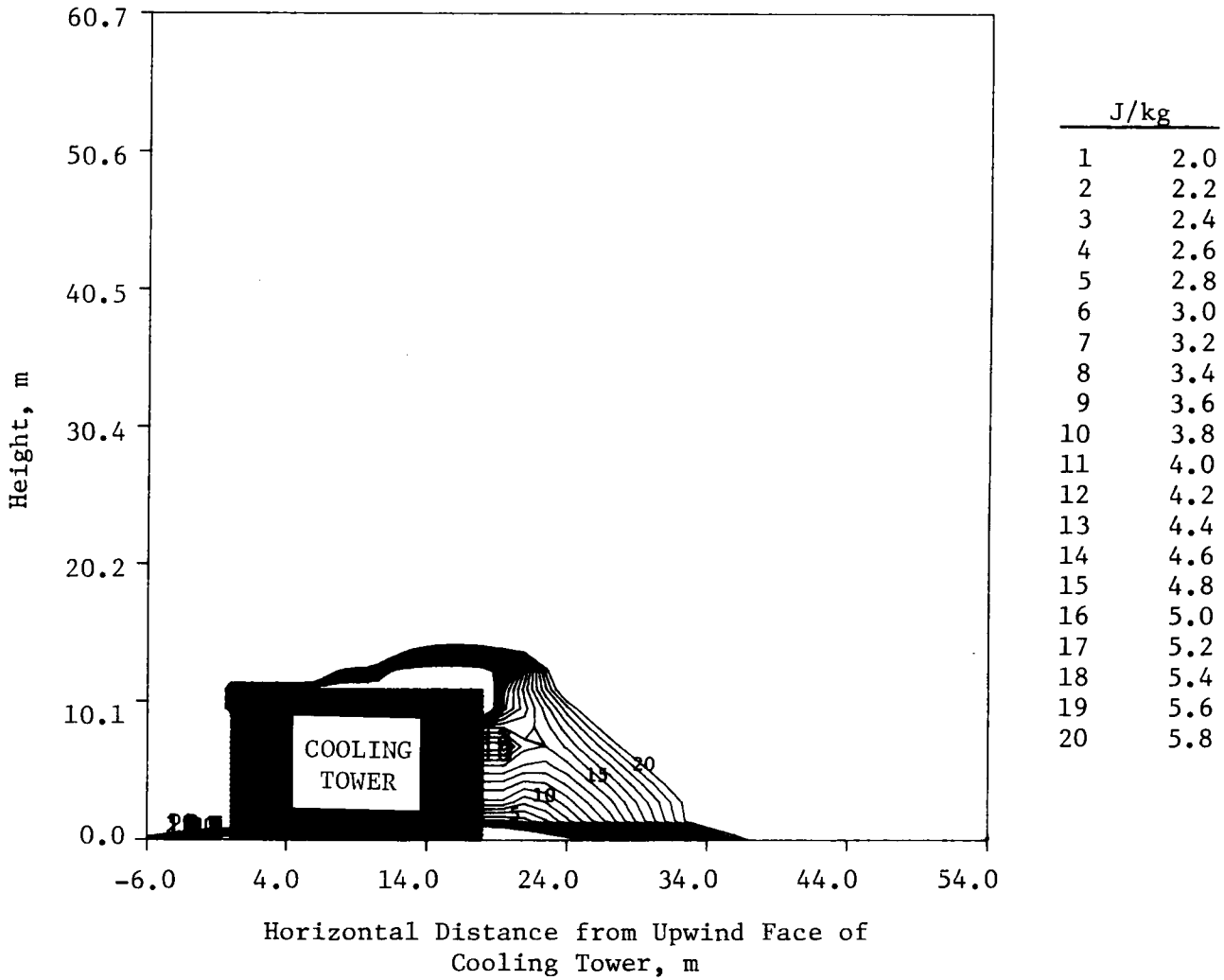


Figure 5.8. Turbulence kinetic energy contours for wind speed of 12 m/s (low range contours).

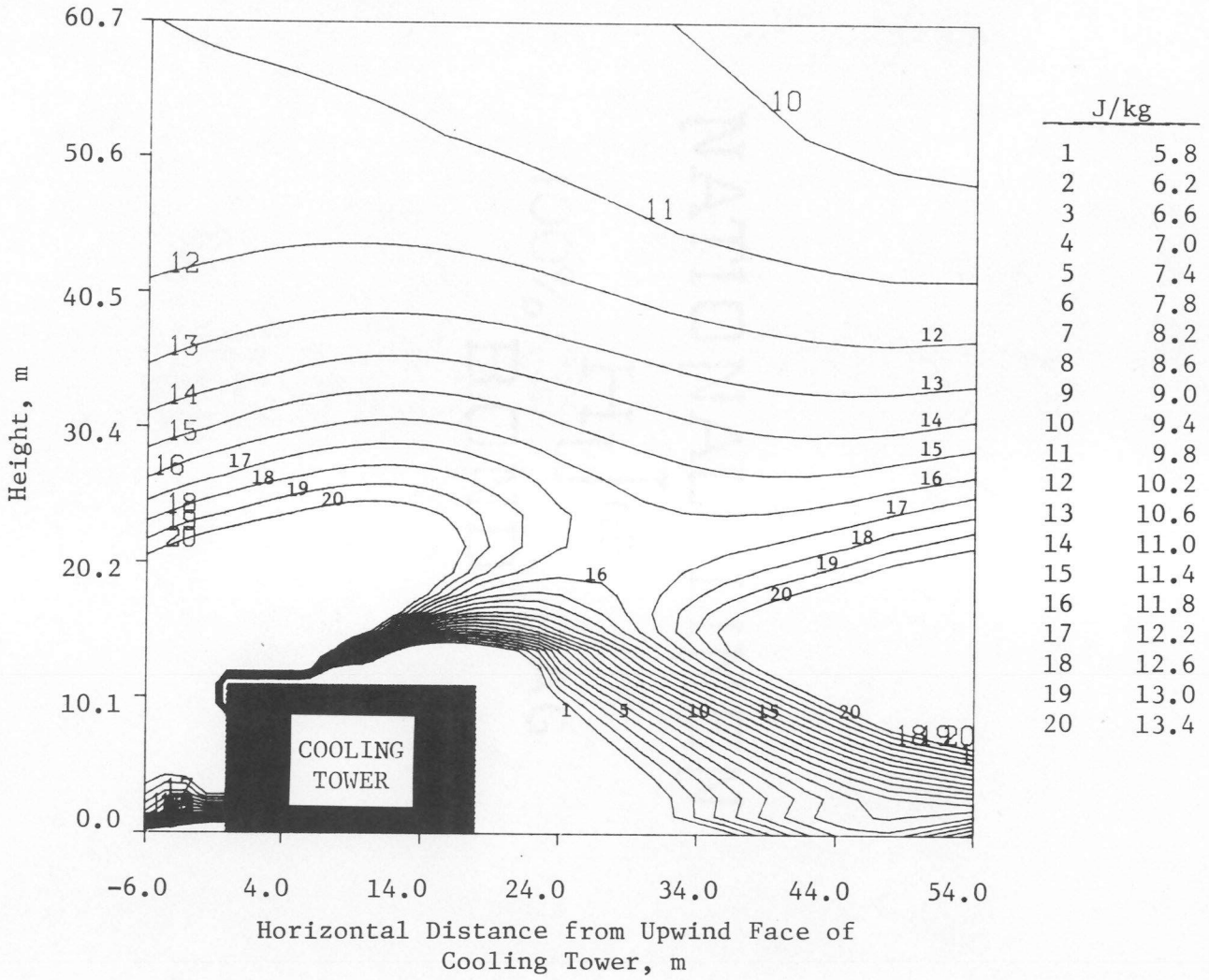


Figure 5.9. Turbulence kinetic energy contours for wind speed of 12 m/s (high range contours).

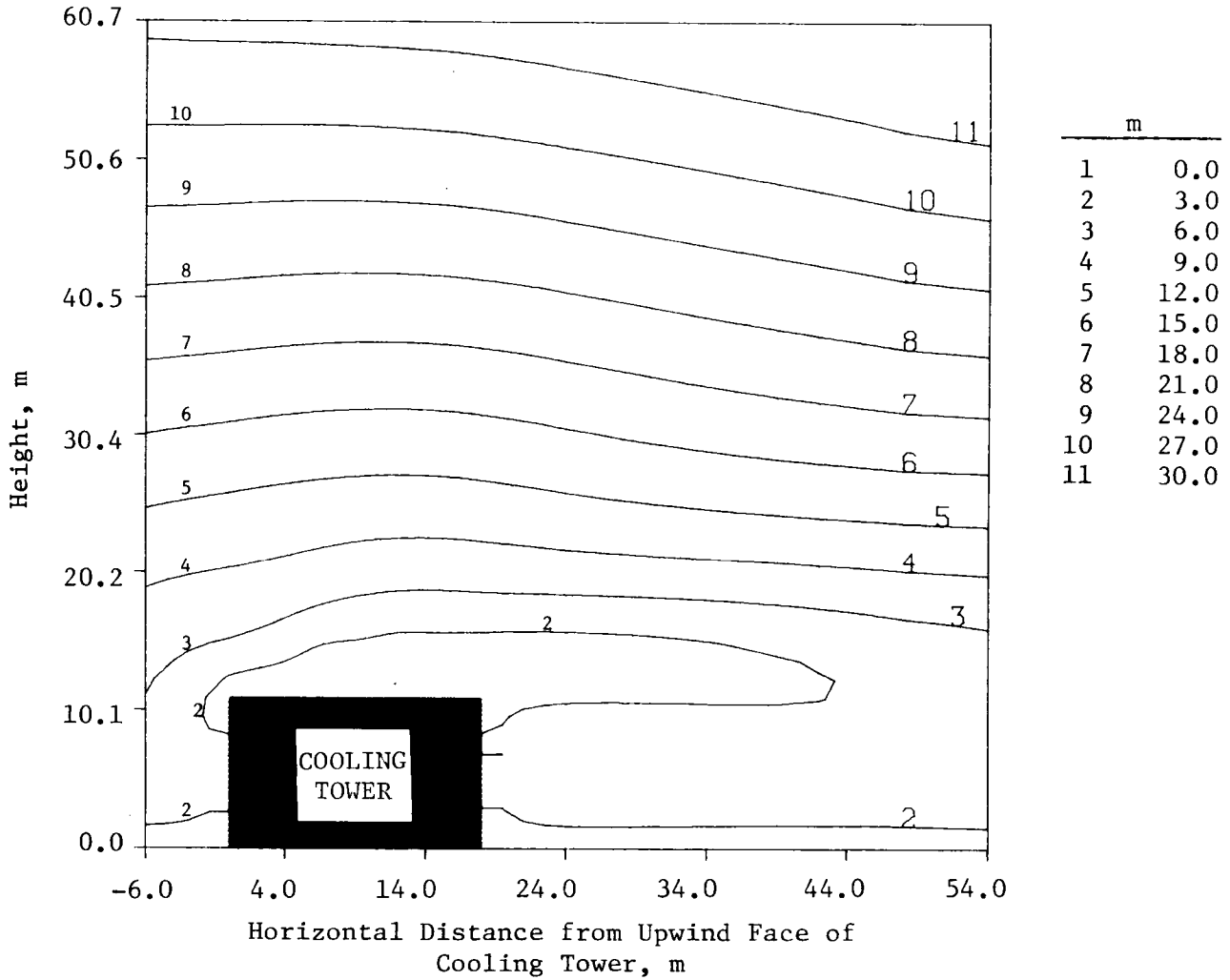


Figure 5.10. Turbulence length scale contours for wind speed of 12 m/s.

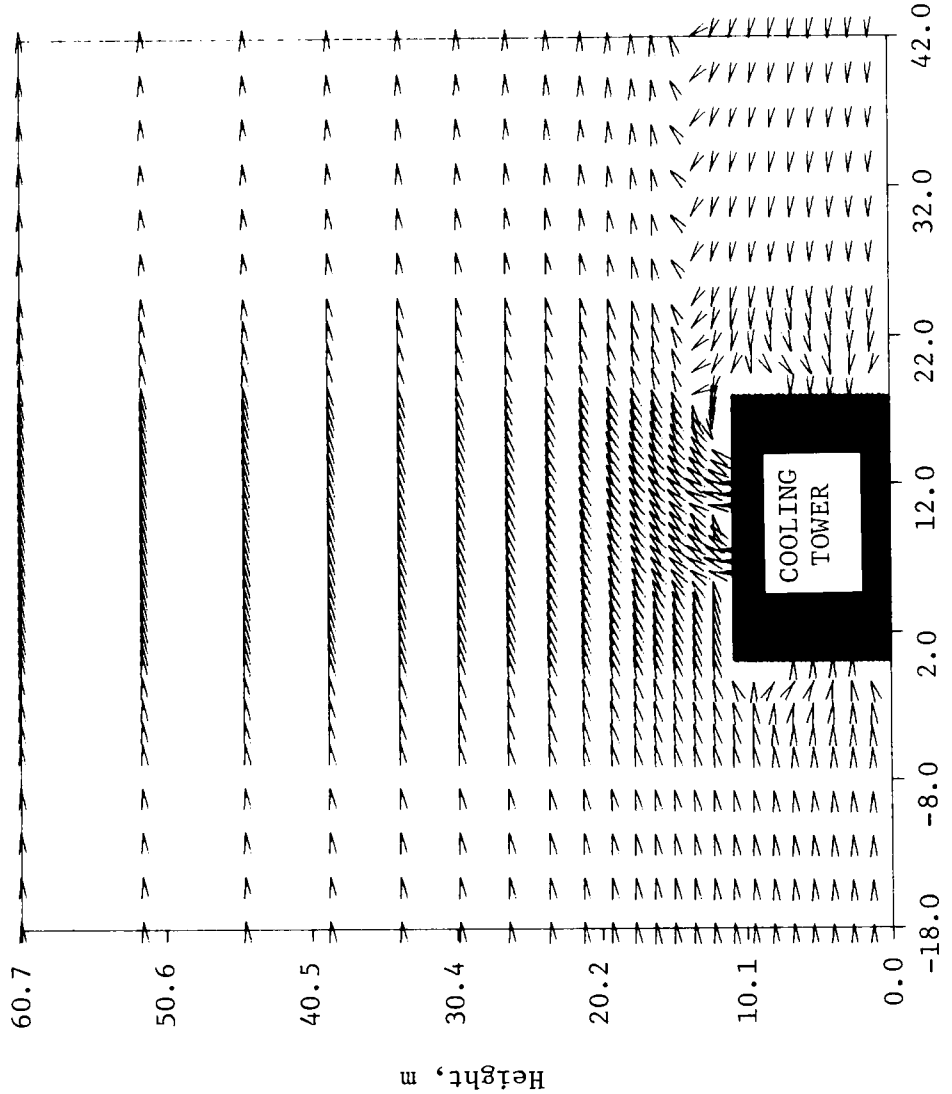


Figure 5.11. Flow direction for wind speed of 6 m/s.

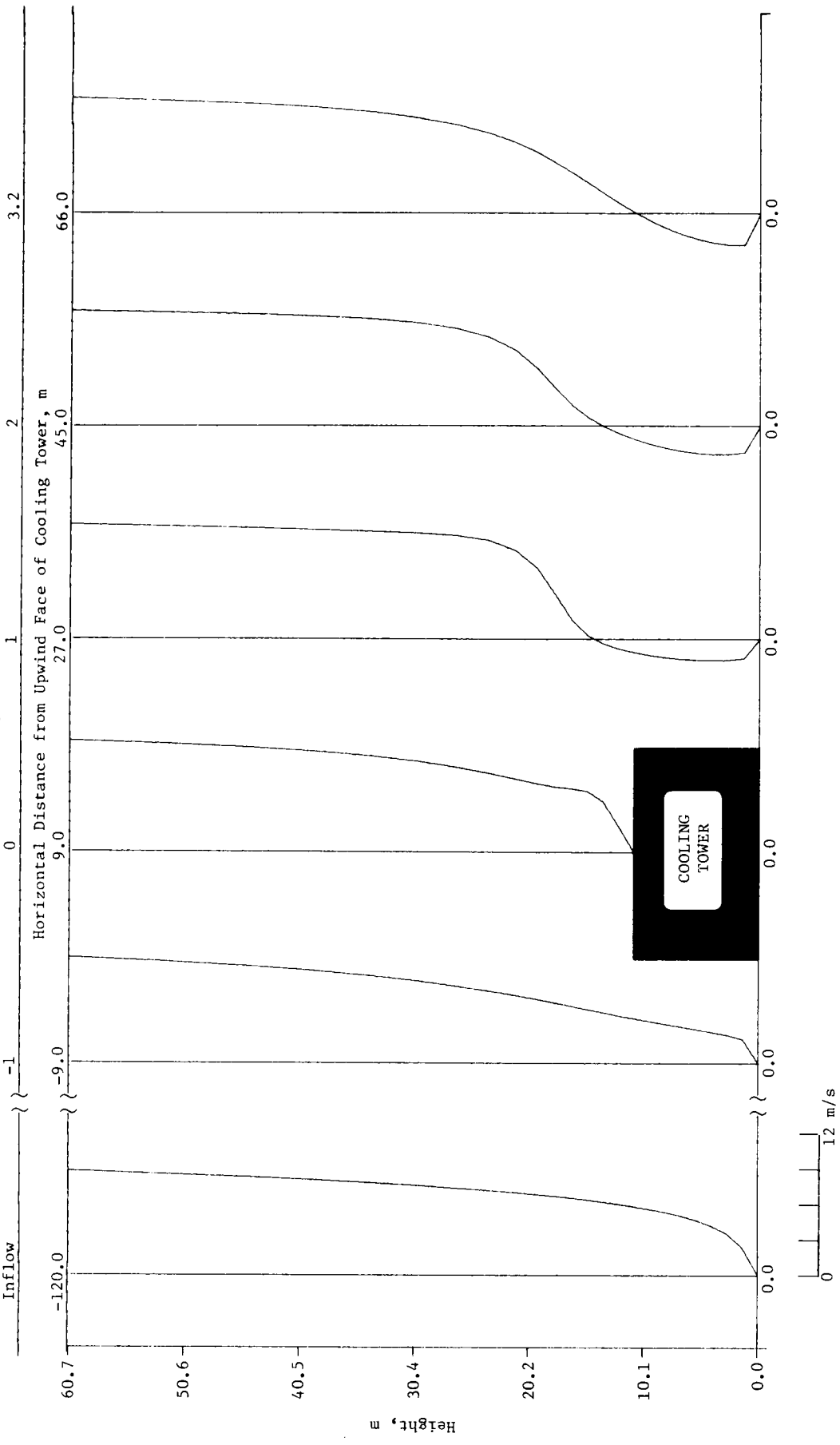


Figure 5.12. Profiles of the horizontal velocity for wind speed of 6 m/s.

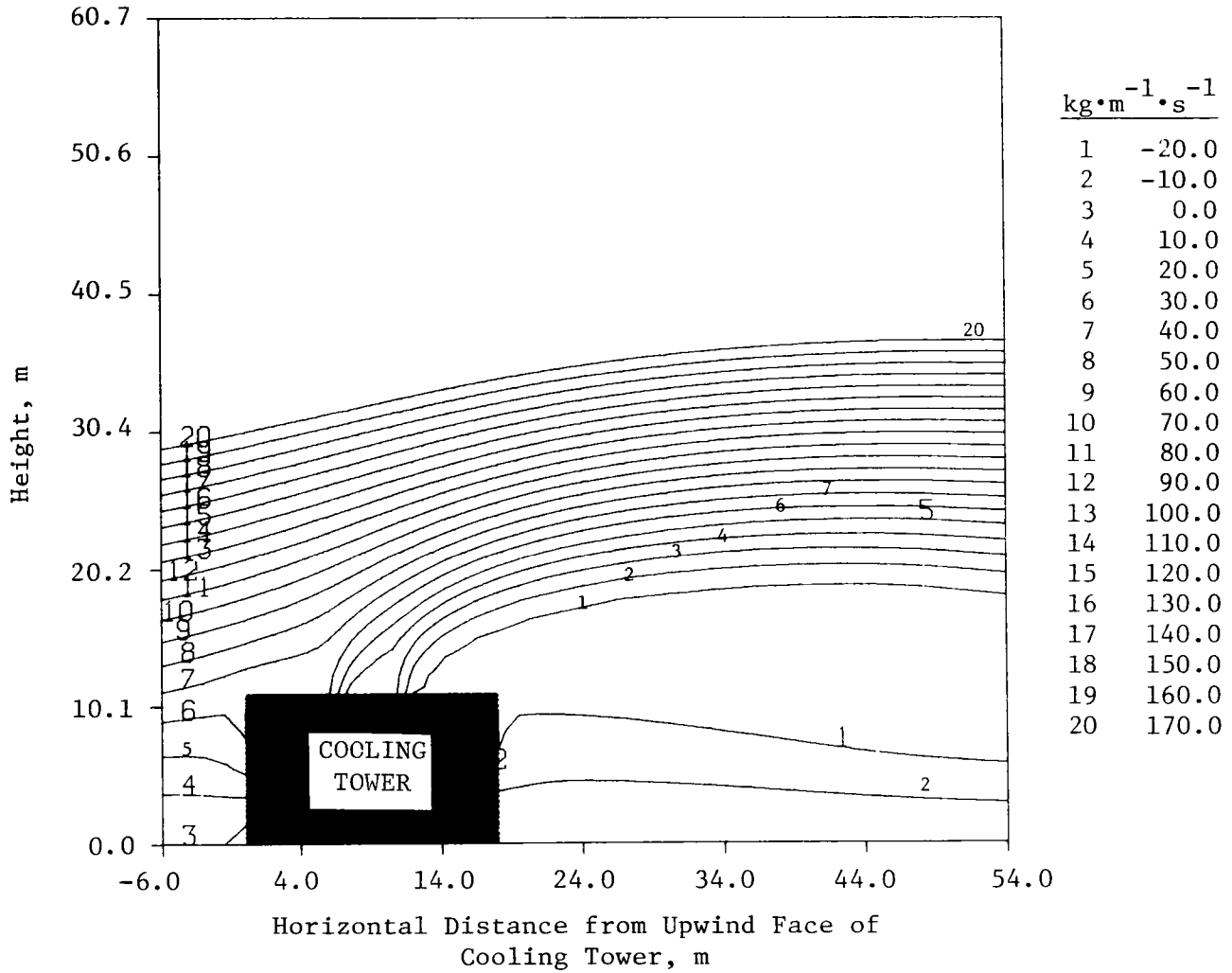


Figure 5.13. Stream function contours for wind speed of 6 m/s.

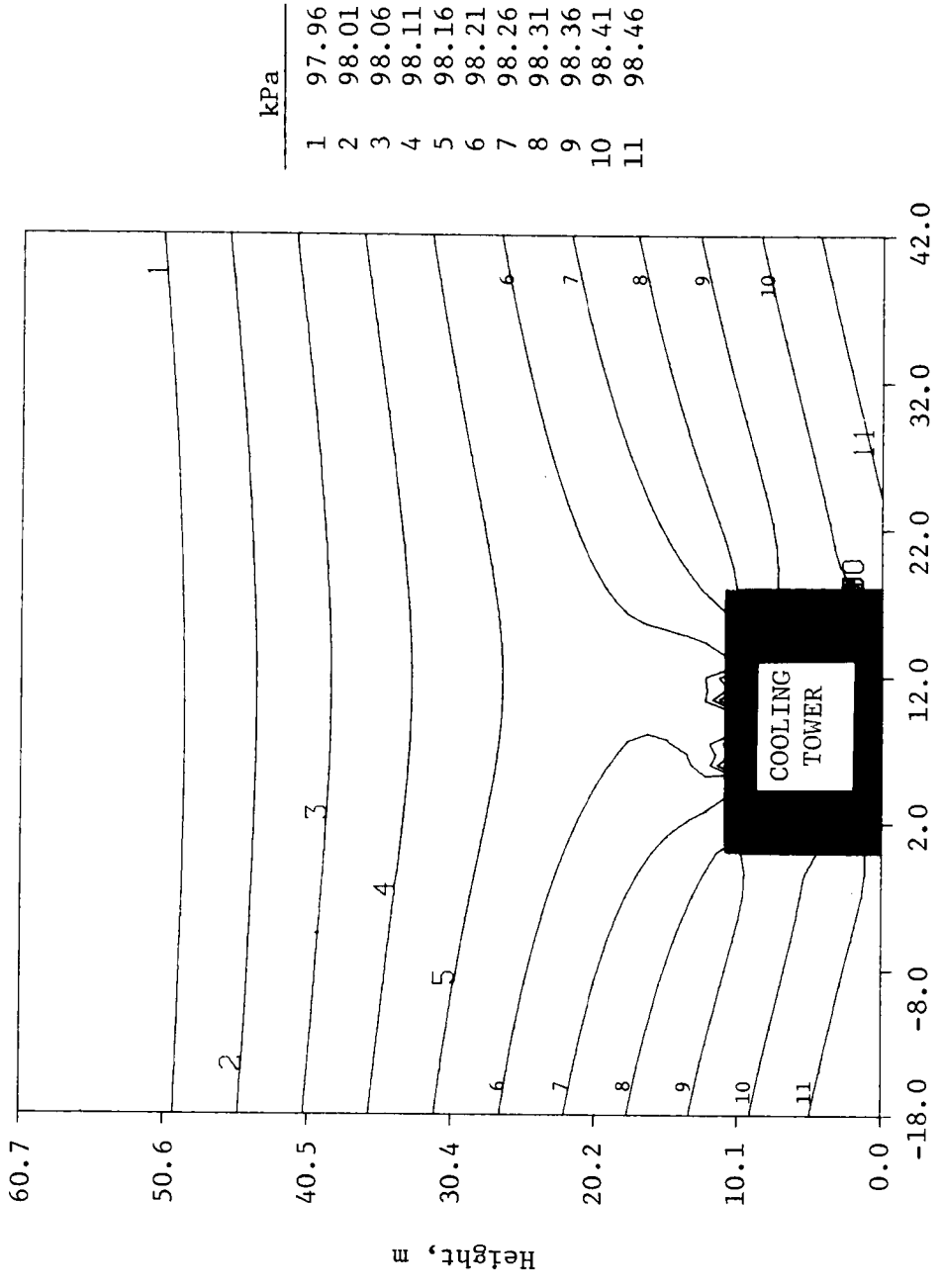


Figure 5.14. Pressure contours for wind speed of 6 m/s.

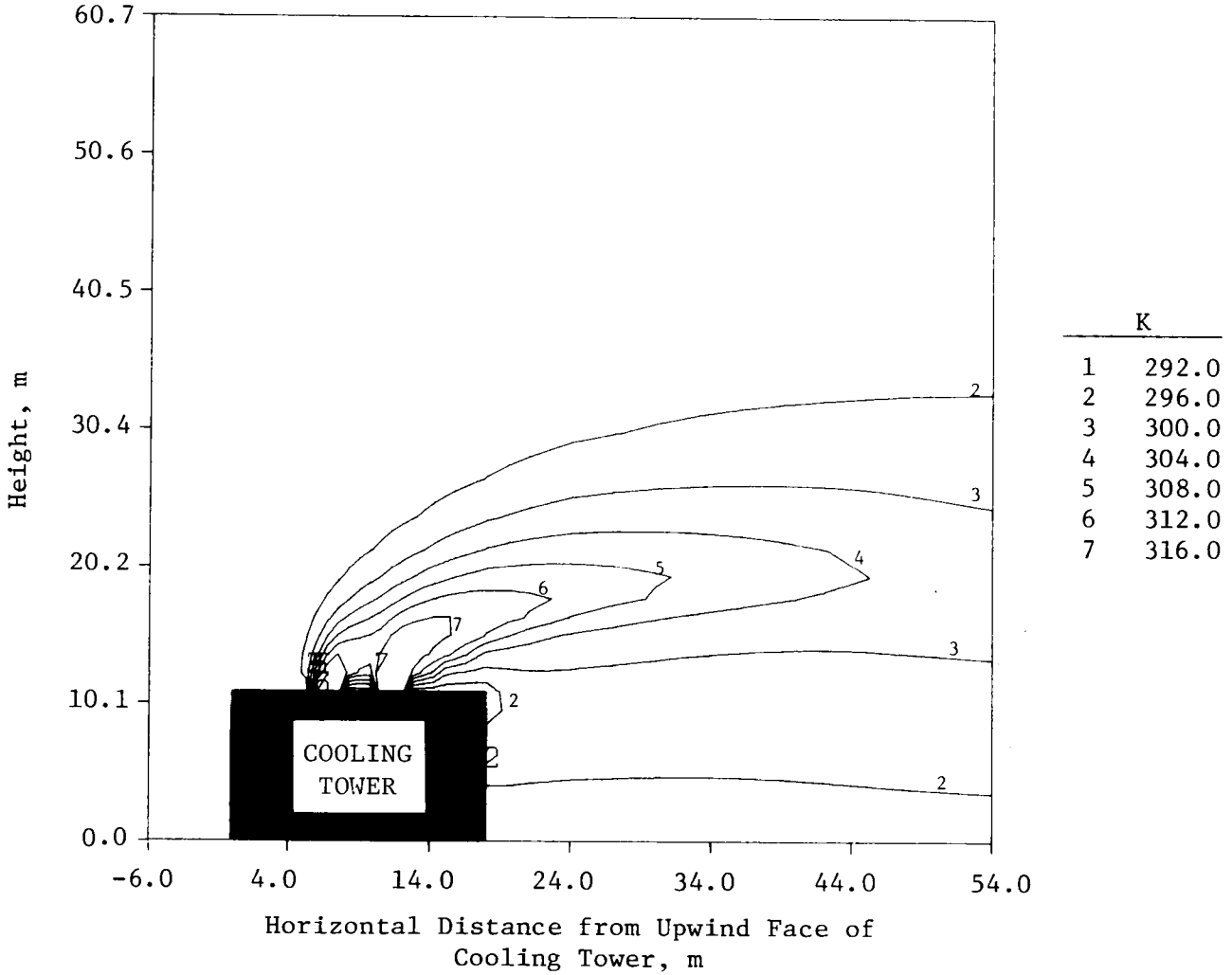


Figure 5.15. Temperature contours for wind speed of 6 m/s.

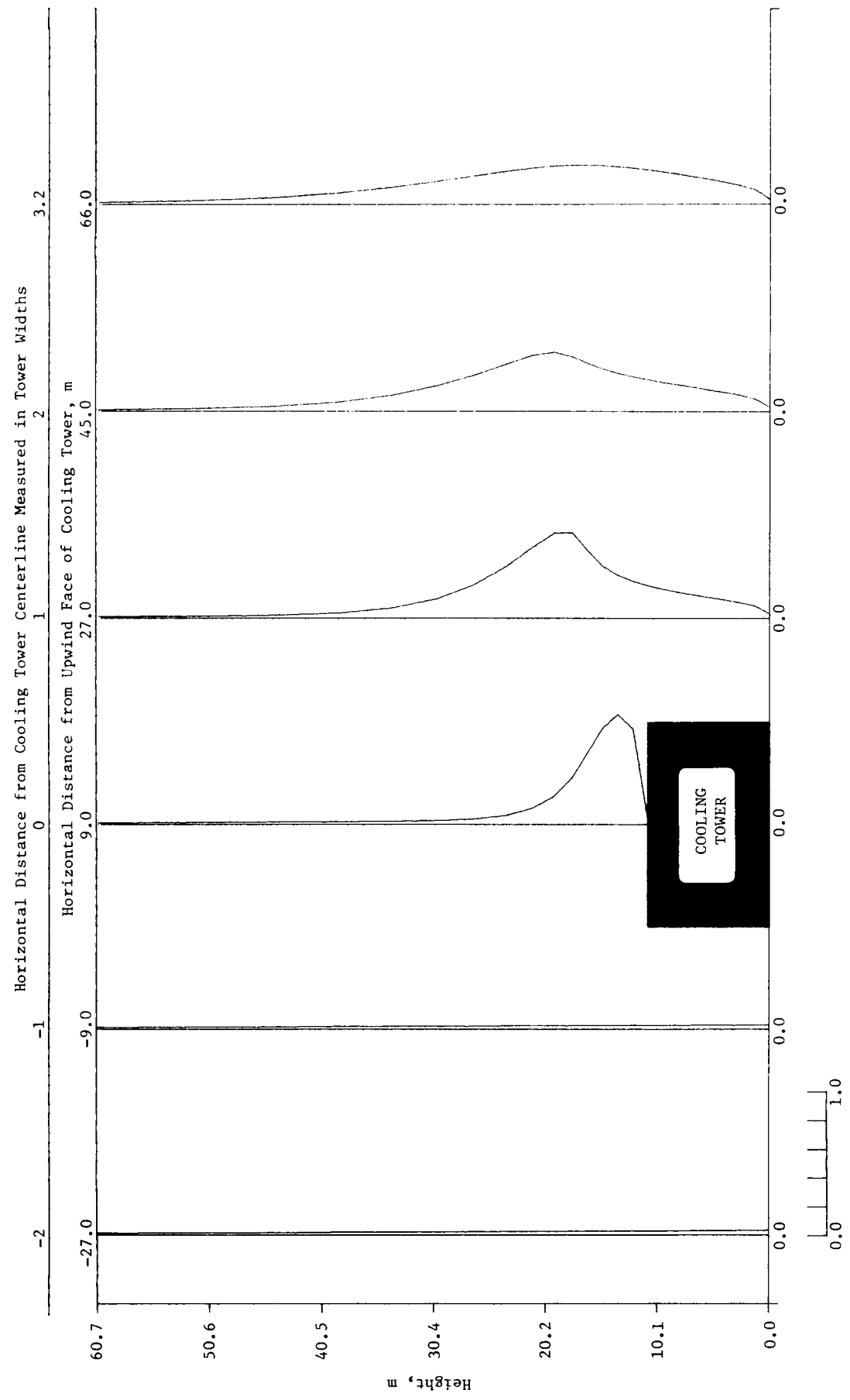


Figure 5.16. Profiles of temperature ratio, $(\overline{T} - \overline{T}_G)/(\overline{T}_{fan} - \overline{T}_G)$, for wind speed of 6 m/s.

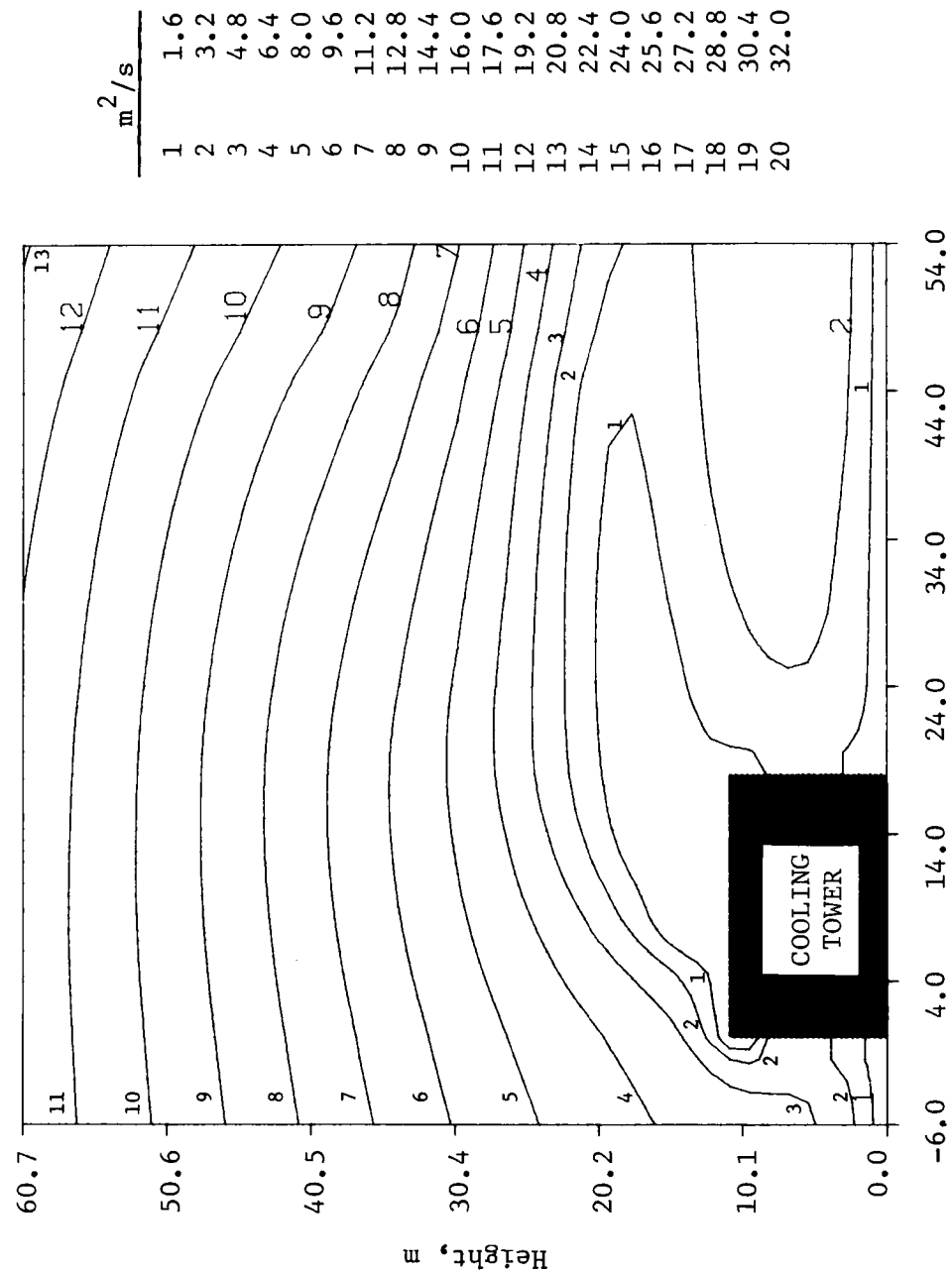


Figure 5.17. Effective thermal diffusivity contours for wind speed of 6 m/s.

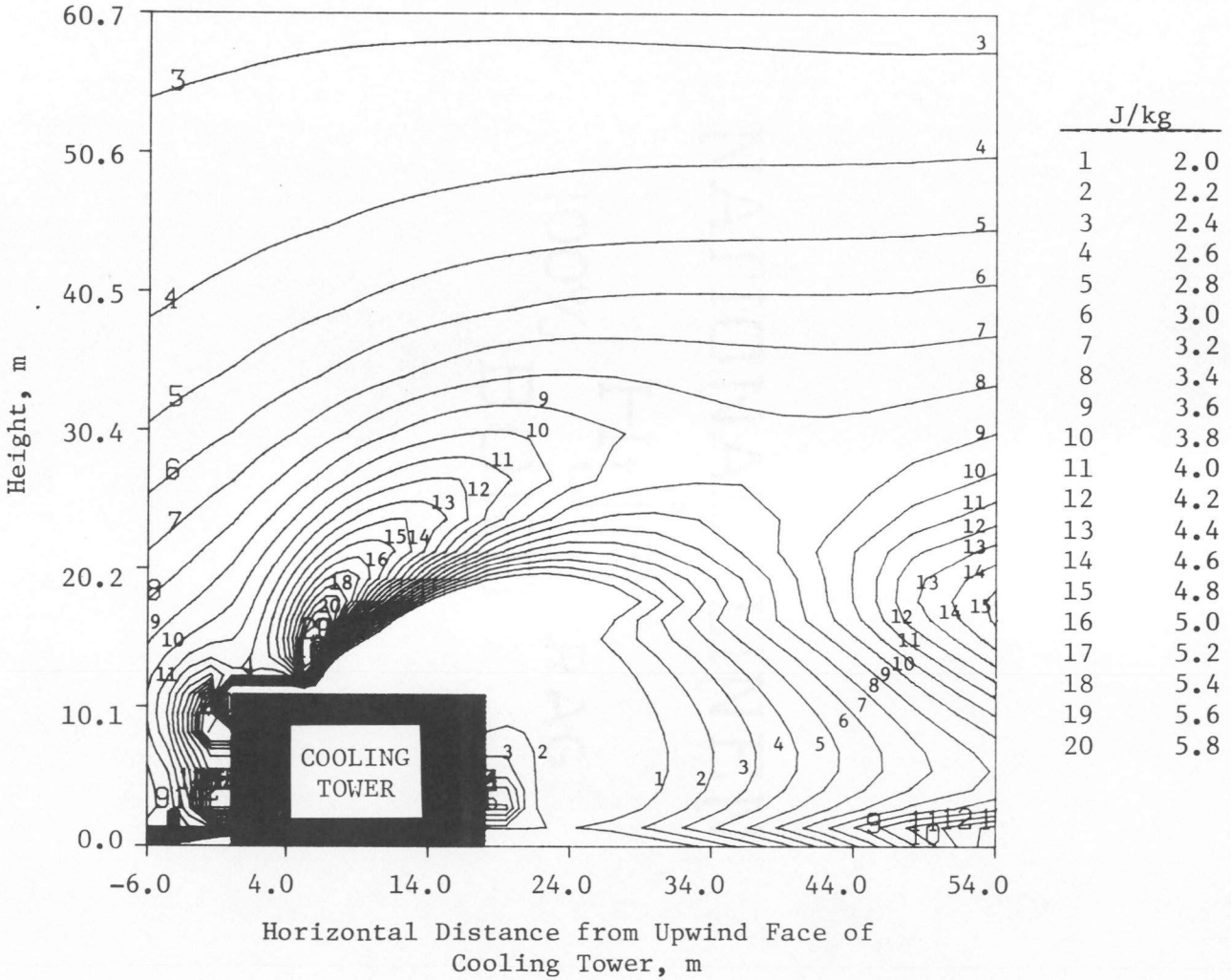


Figure 5.18. Turbulence kinetic energy contours for wind speed of 6 m/s.

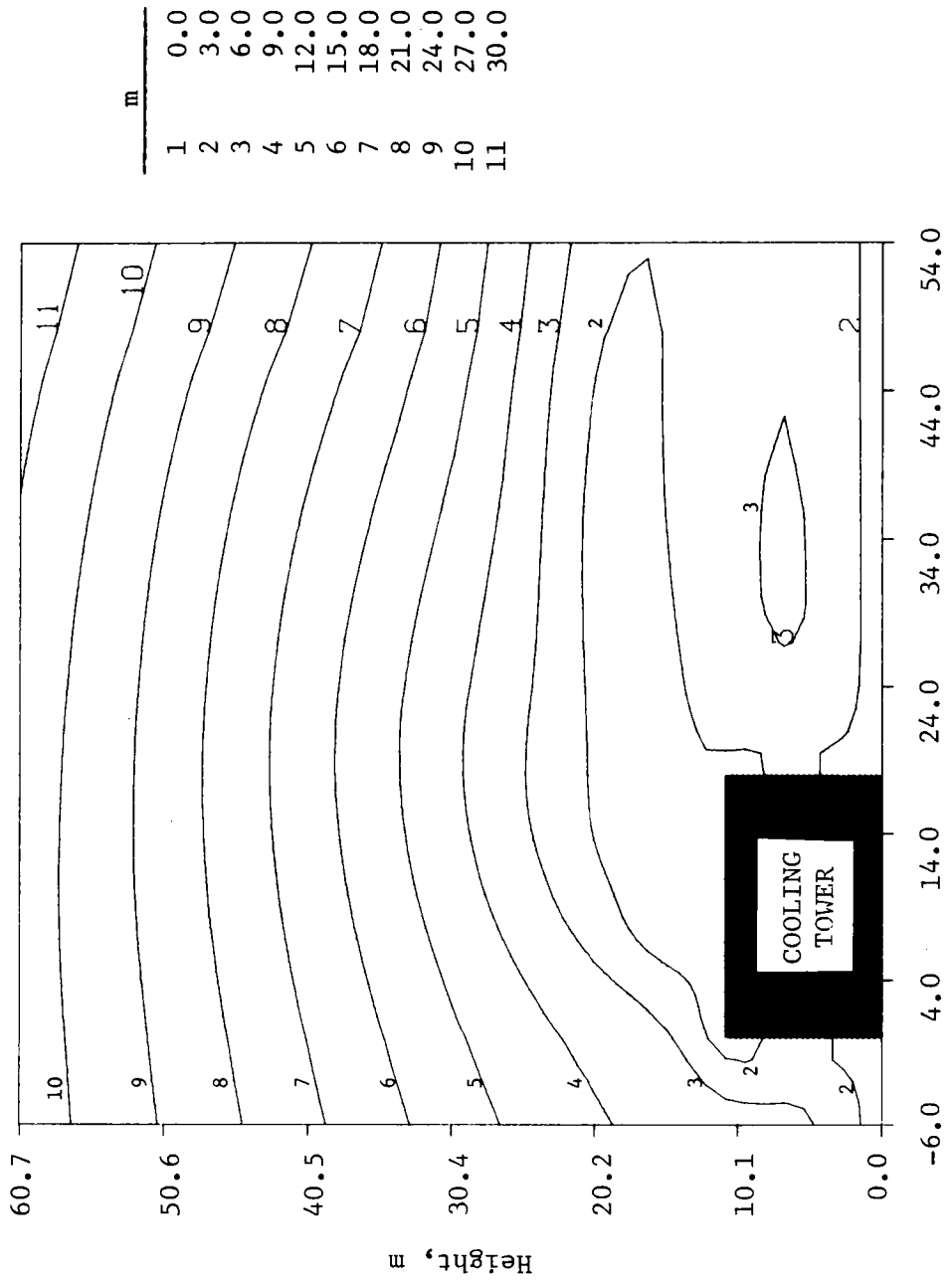


Figure 5.19. Turbulence length scale contours for wind speed of 6 m/s.

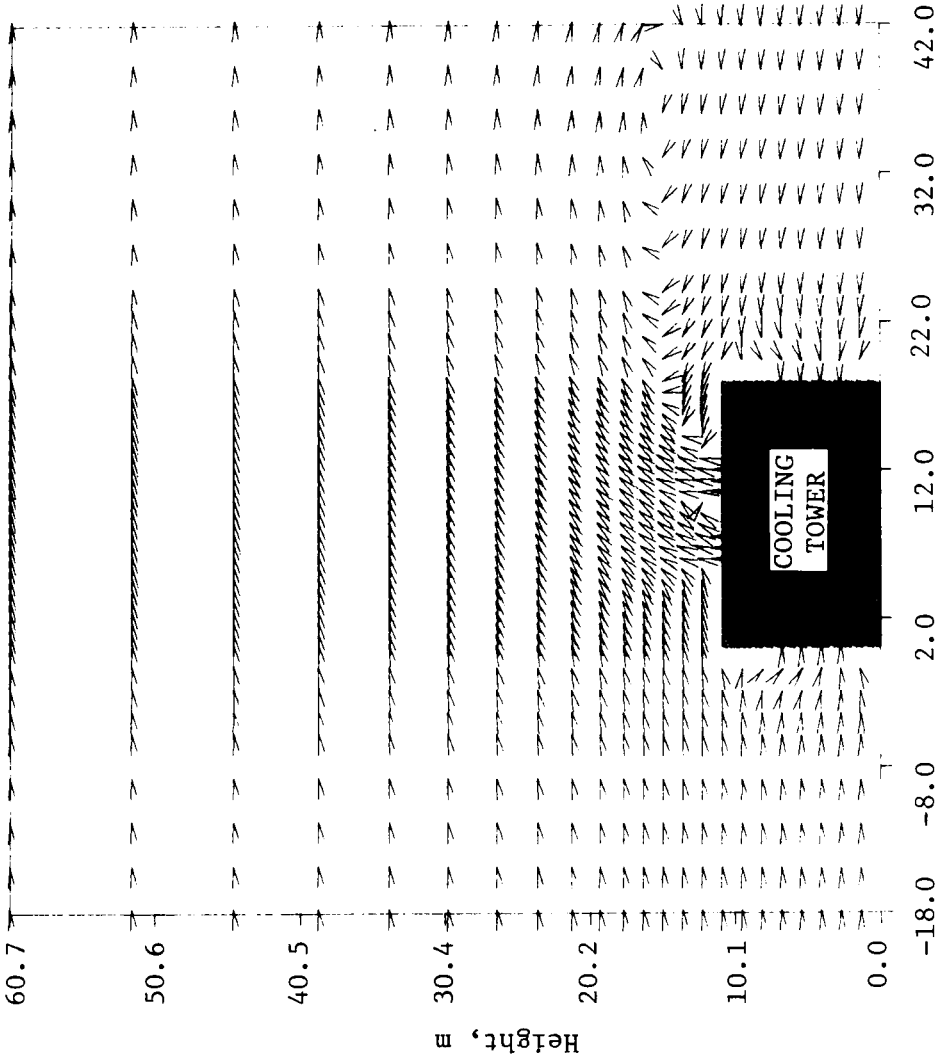


Figure 5.20. Flow direction for wind speed of 4 m/s.

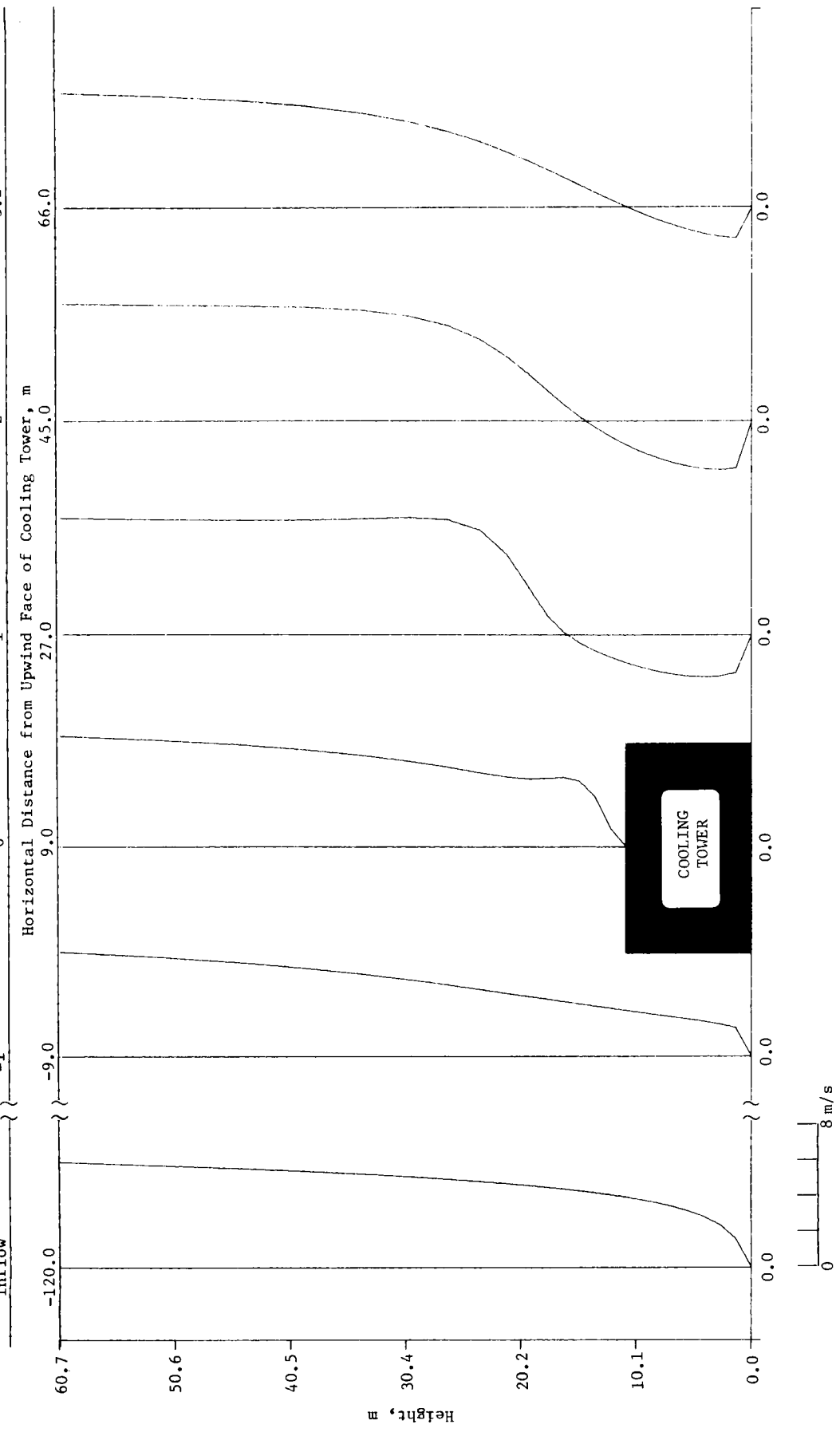


Figure 5.21. Profiles of the horizontal velocity for wind speed of 4 m/s.

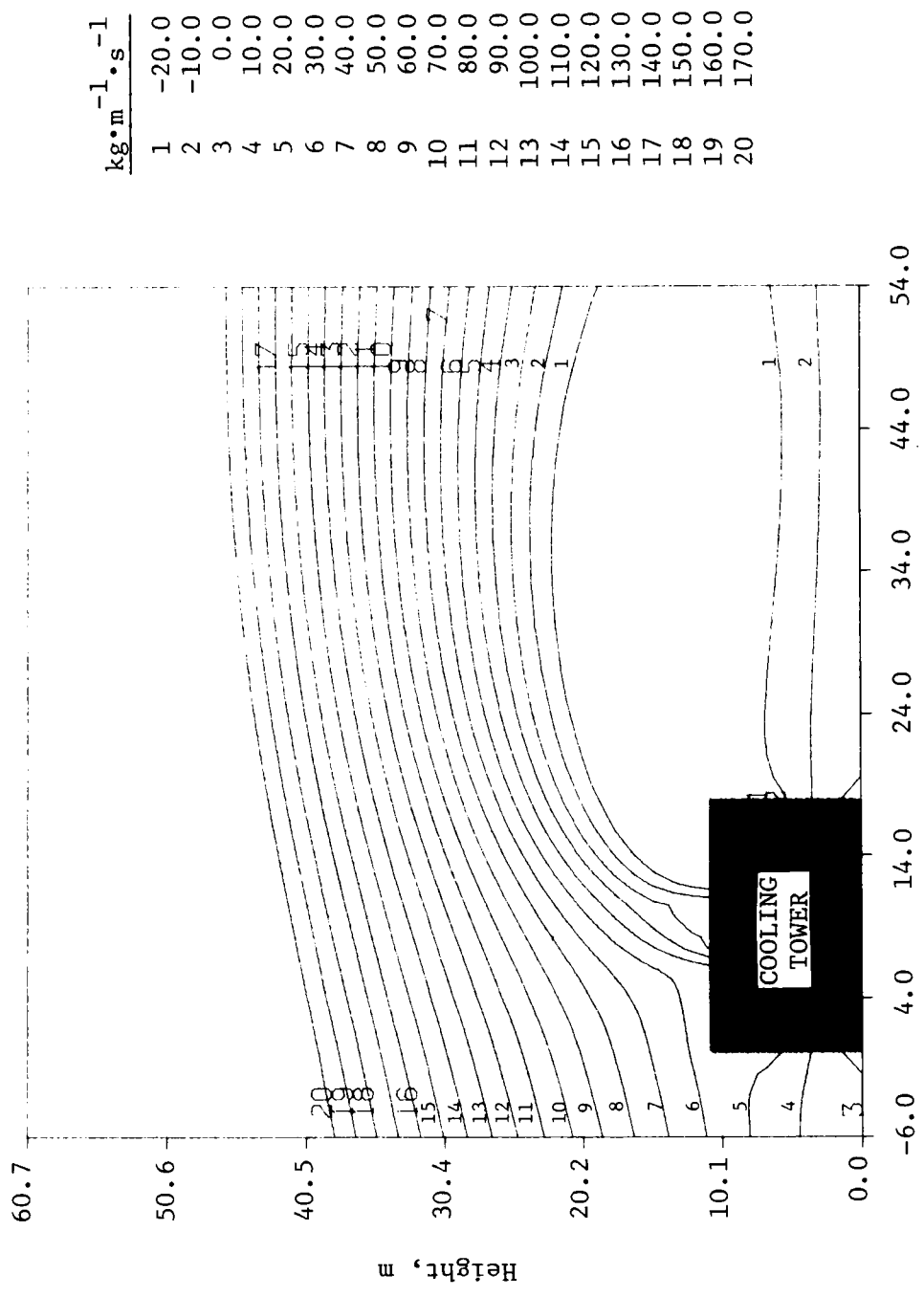


Figure 5.22. Stream function contours for wind speed of 4 m/s.

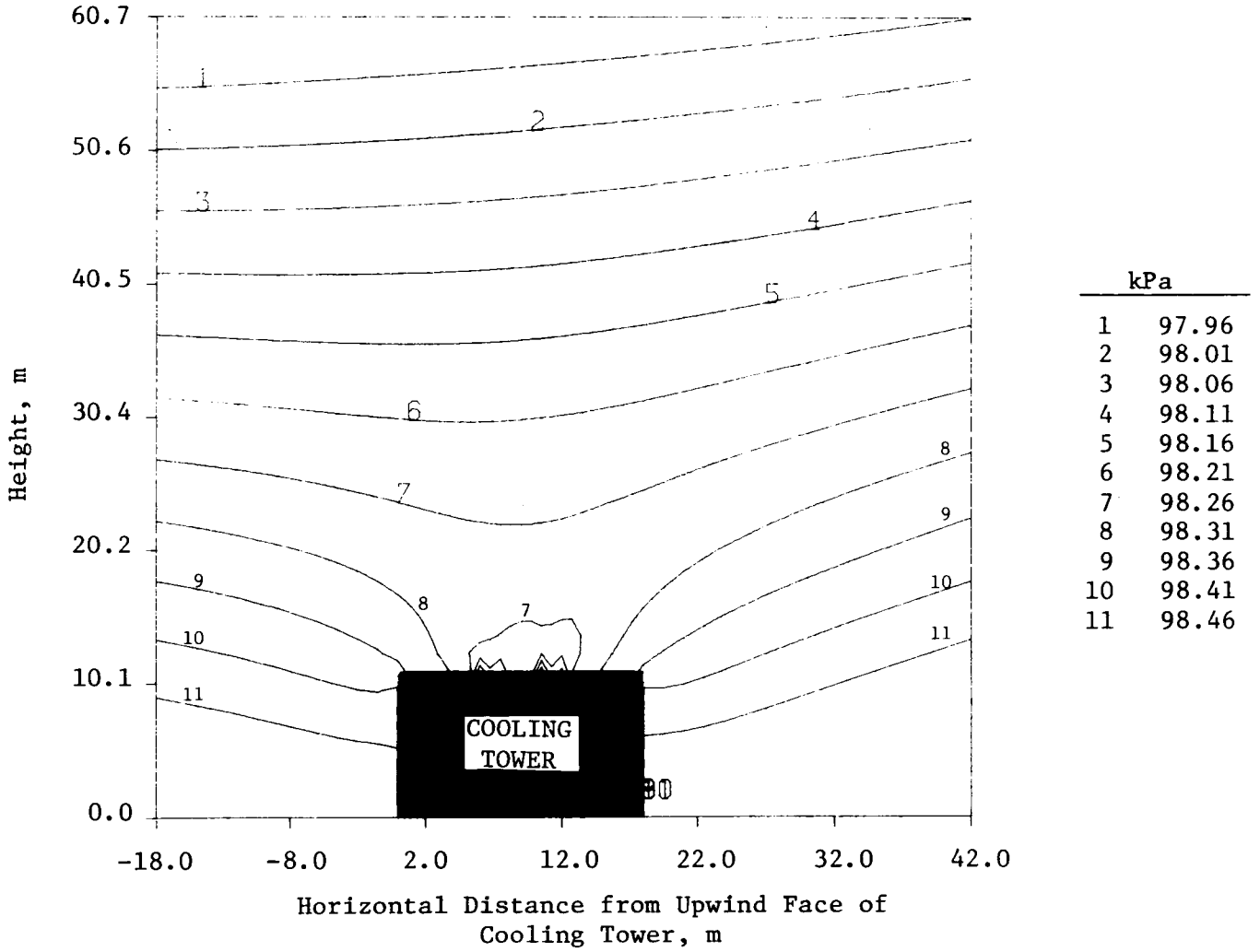


Figure 5.23. Pressure contours for wind speed of 4 m/s.

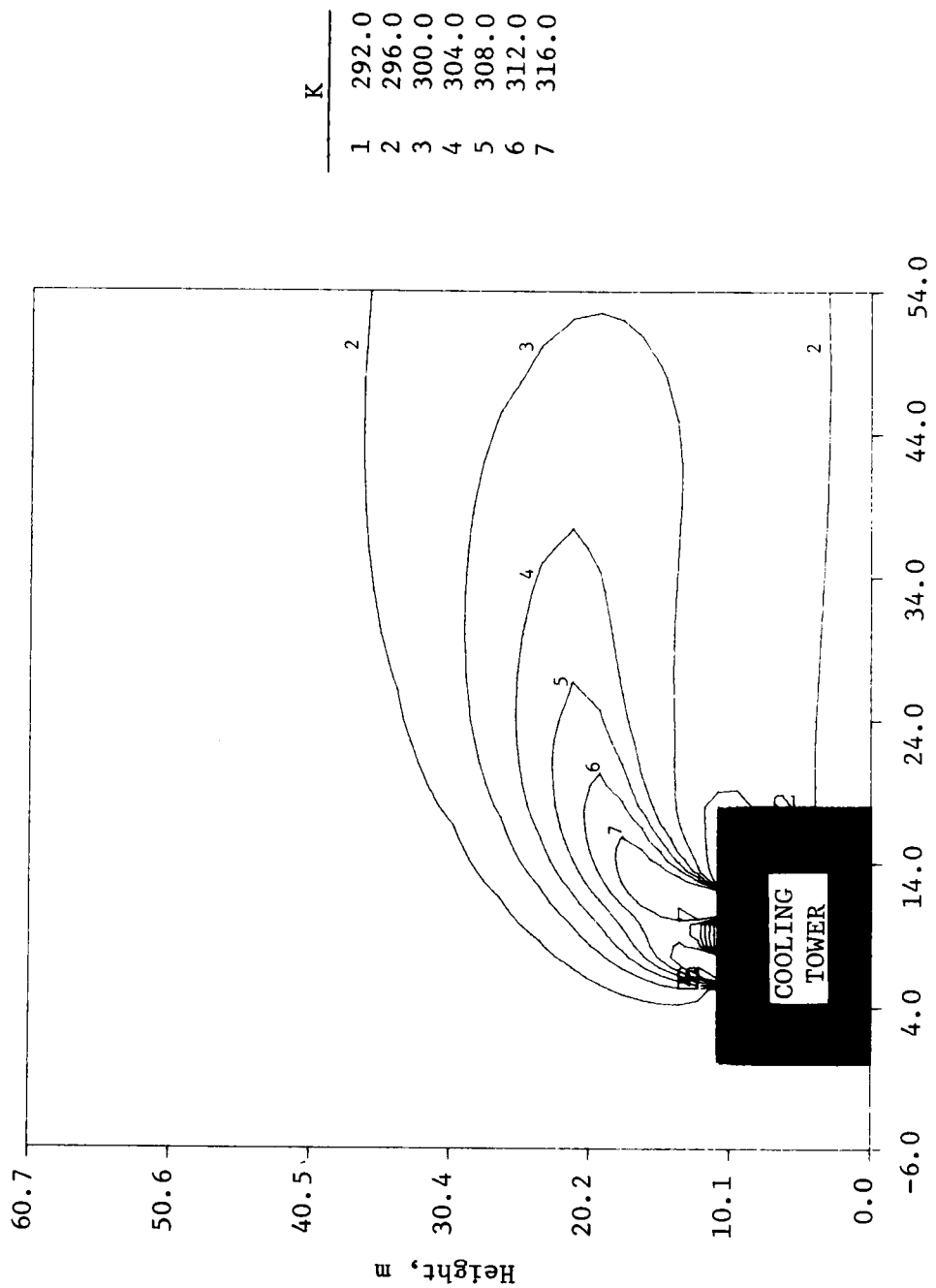


Figure 5.24. Temperature contours for wind speed of 4 m/s.

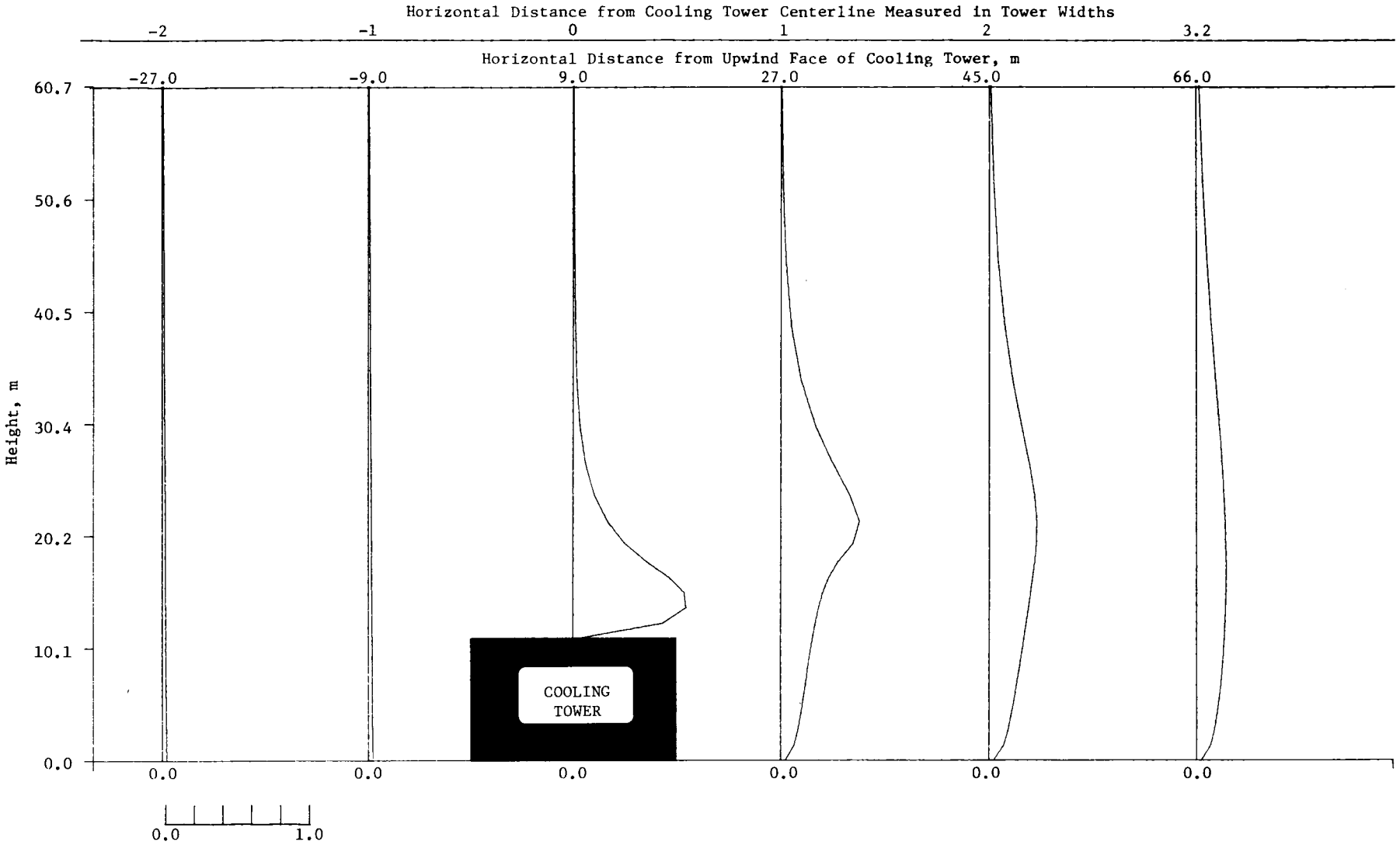


Figure 5.25. Profiles of temperature ratio, $(\overline{T} - \overline{T}_G)/(\overline{T}_{fan} - \overline{T}_G)$, for wind speed of 4 m/s.

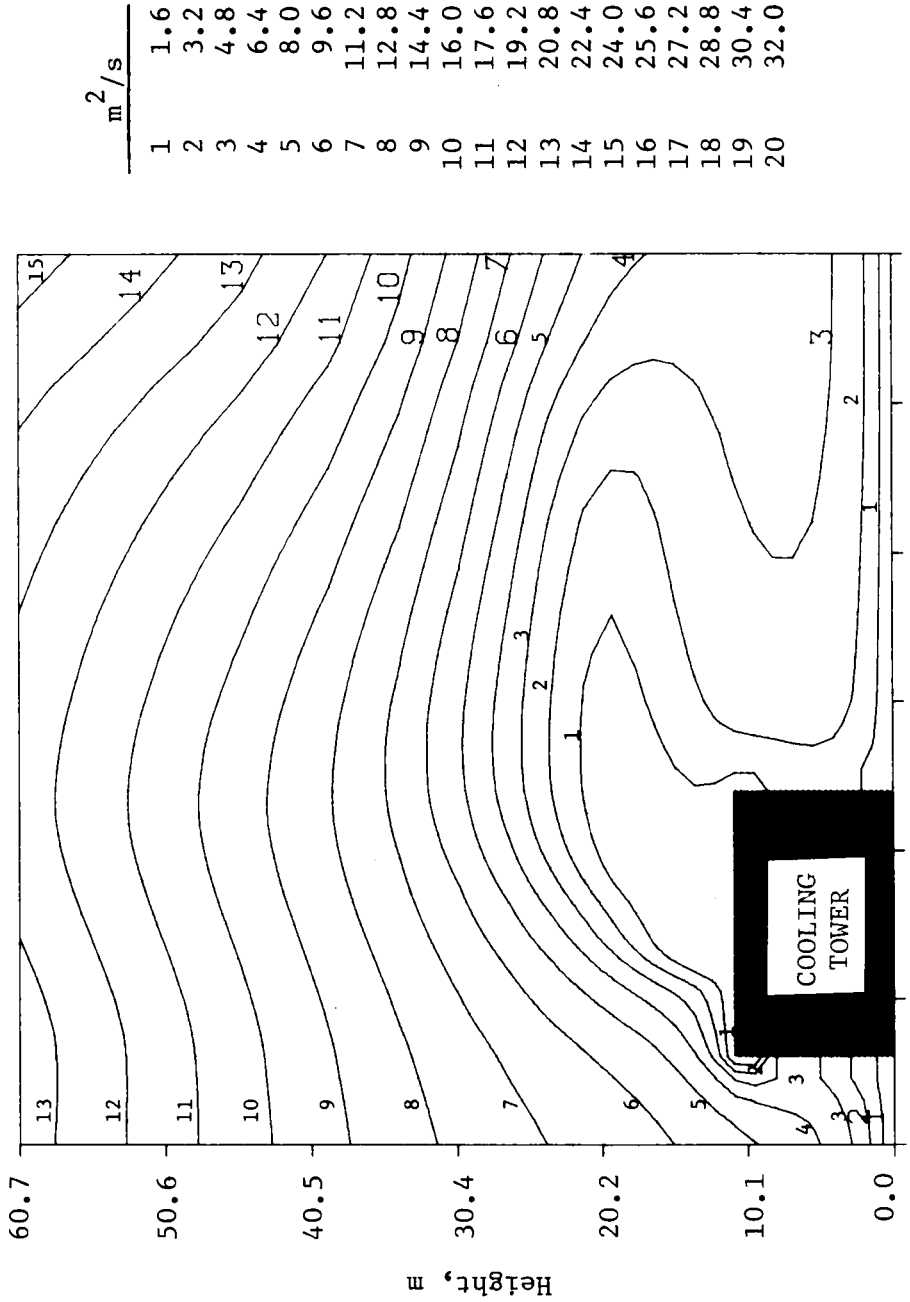


Figure 5.26. Effective thermal diffusivity contours for wind speed of 4 m/s.

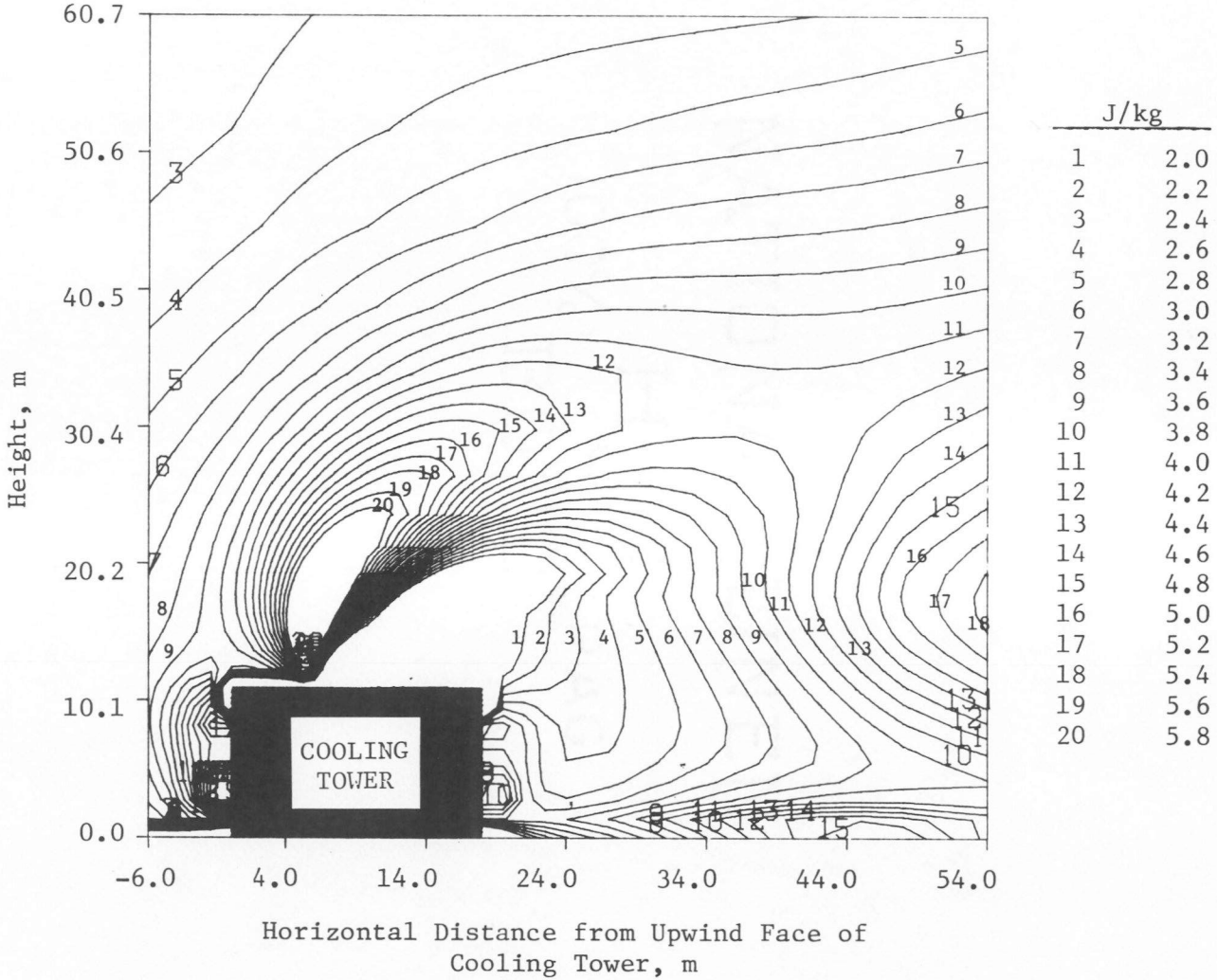


Figure 5.27. Turbulence kinetic energy contours for wind speed of 4 m/s.

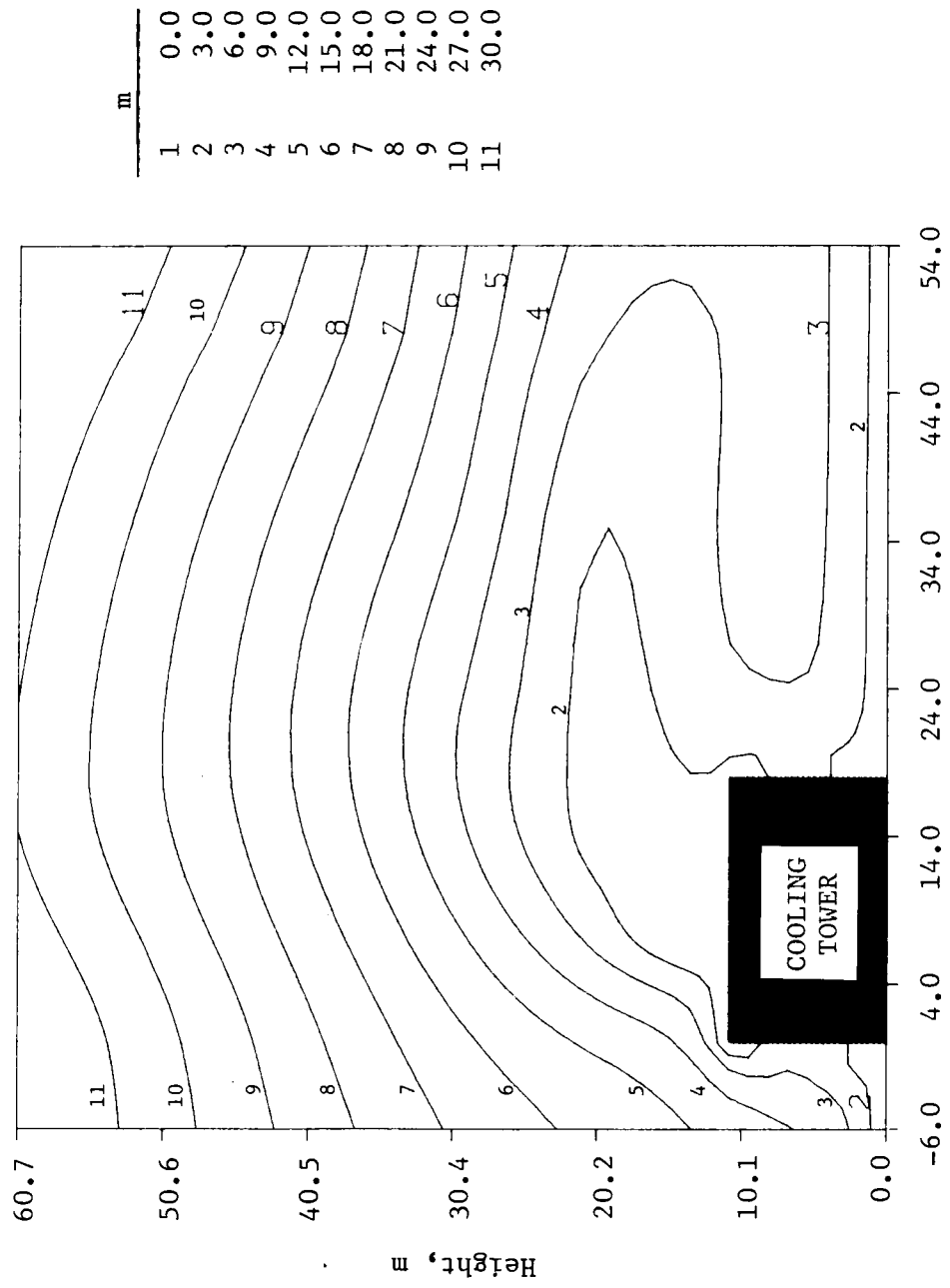


Figure 5.28. Turbulence length scale contours for wind speed of 4 m/s.

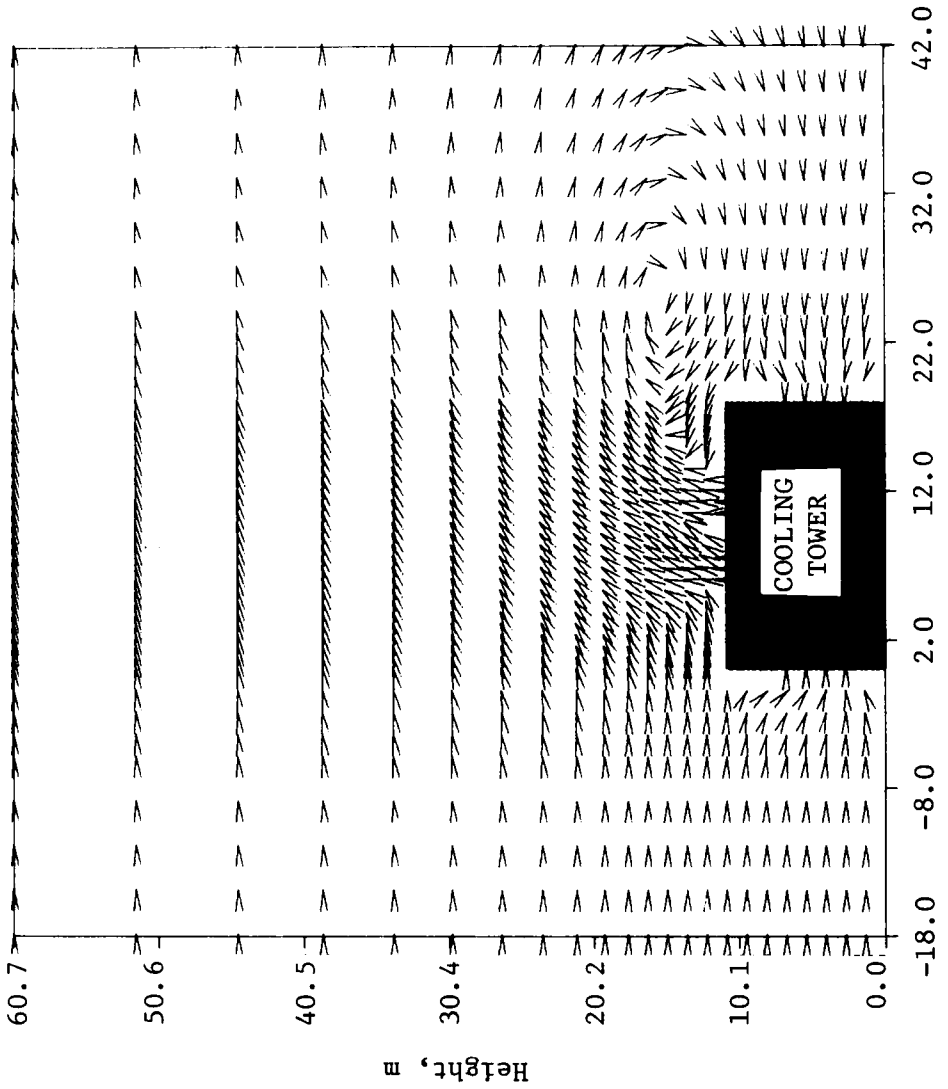


Figure 5.29. Flow direction for wind speed of 2 m/s.

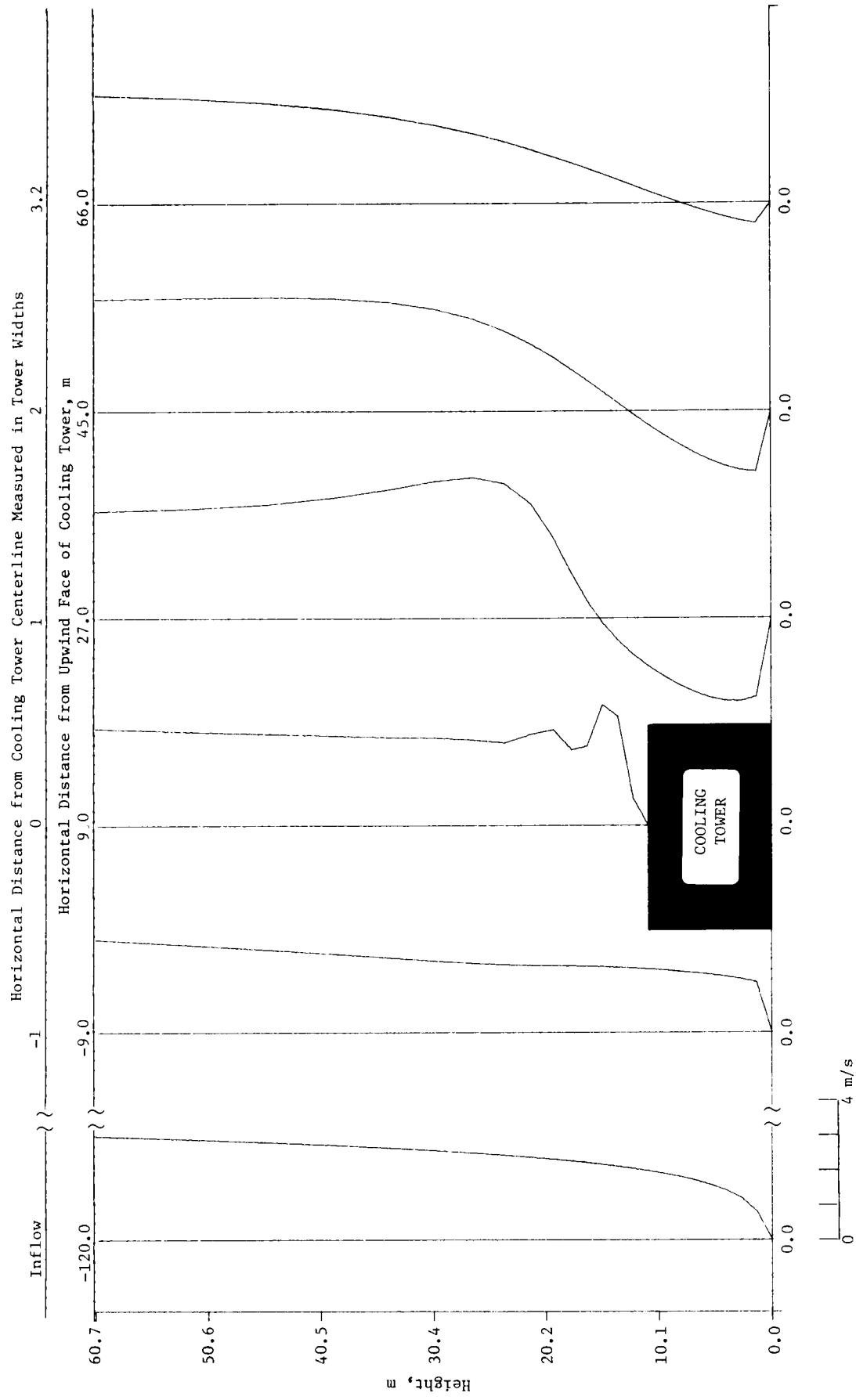


Figure 5.30. Profiles of the horizontal velocity for wind speed of 2 m/s.

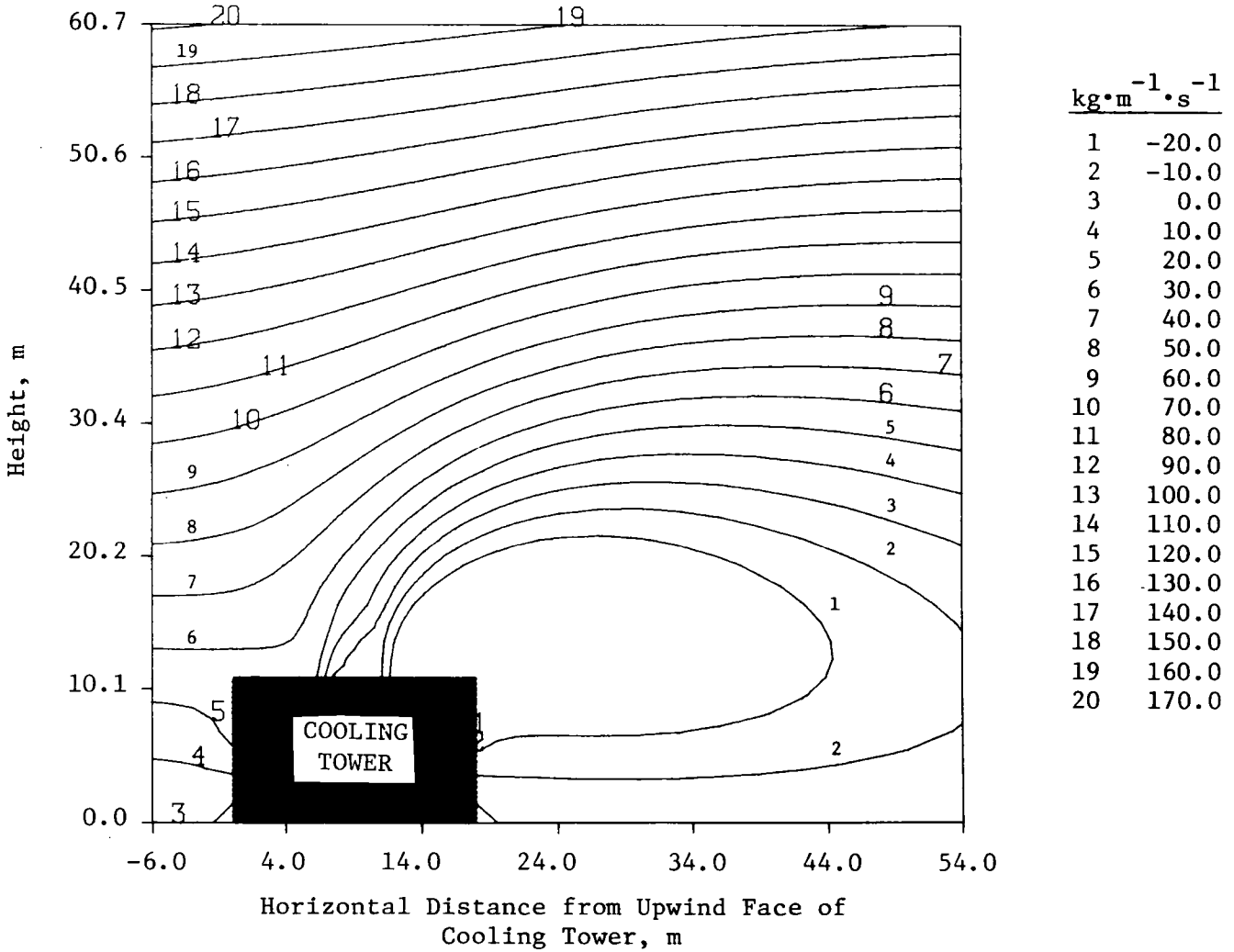


Figure 5.31. Stream function contours for wind speed of 2 m/s.

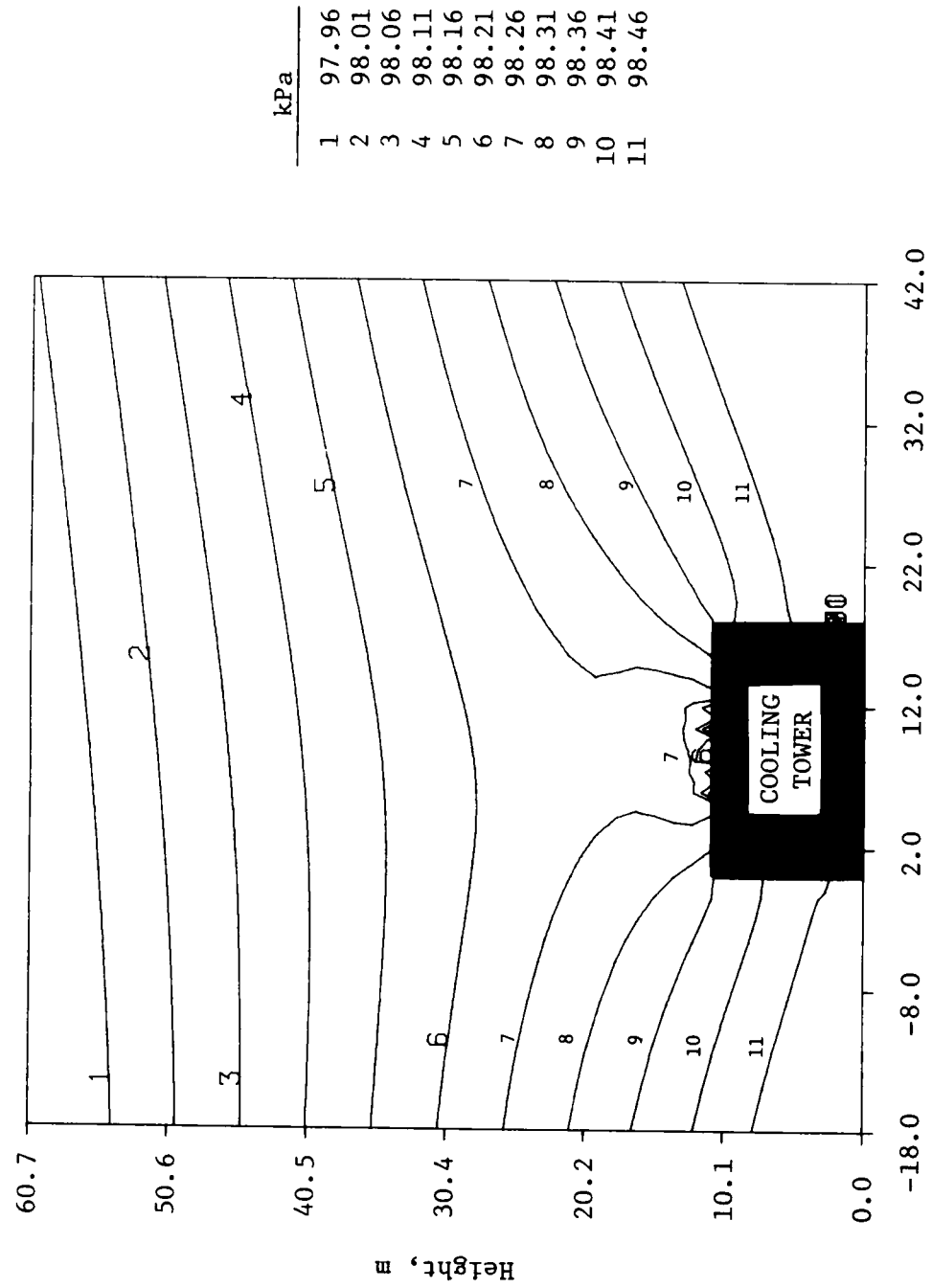


Figure 5.32. Pressure contours for wind speed of 2 m/s.

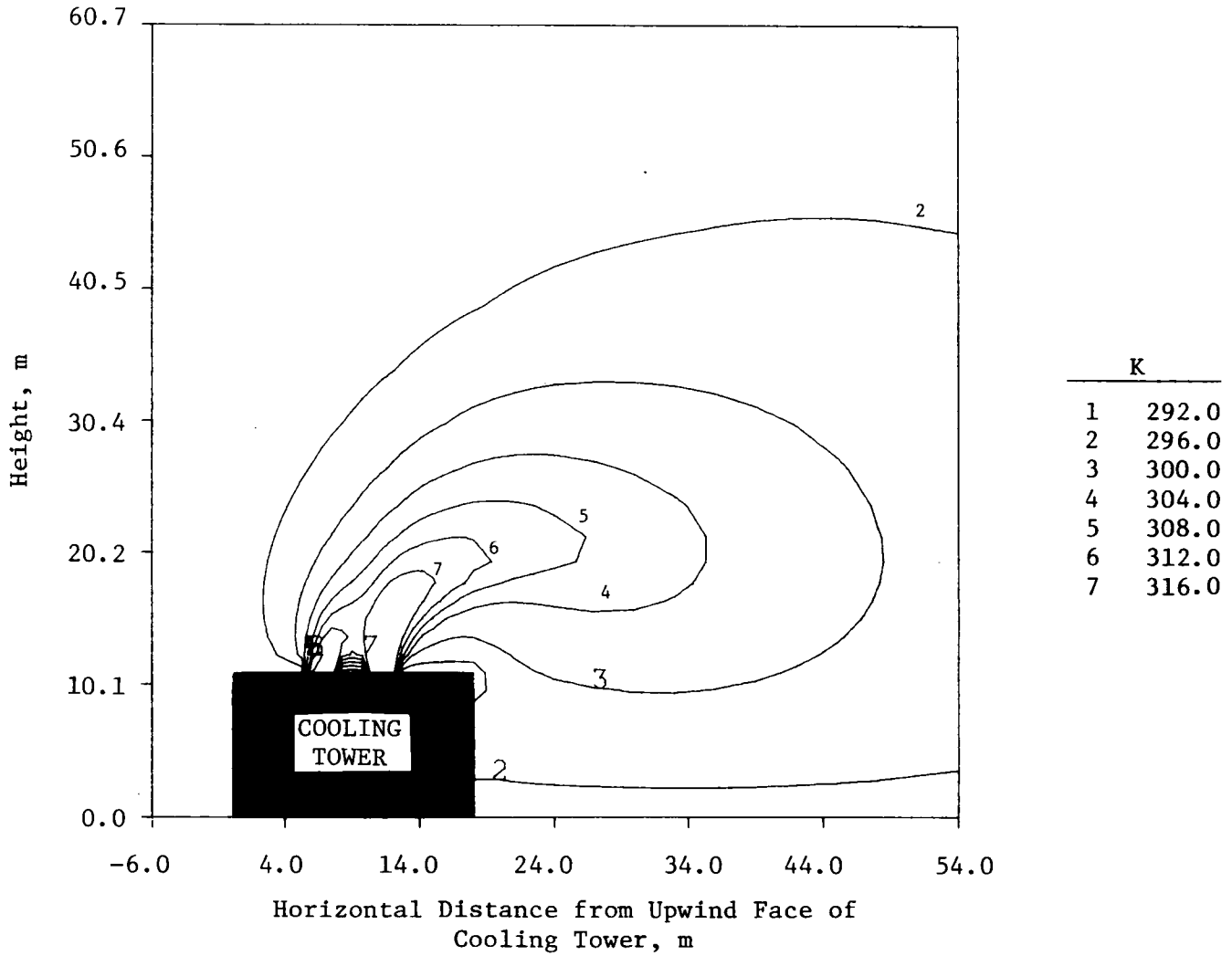


Figure 5.33. Temperature contours for wind speed of 2 m/s.

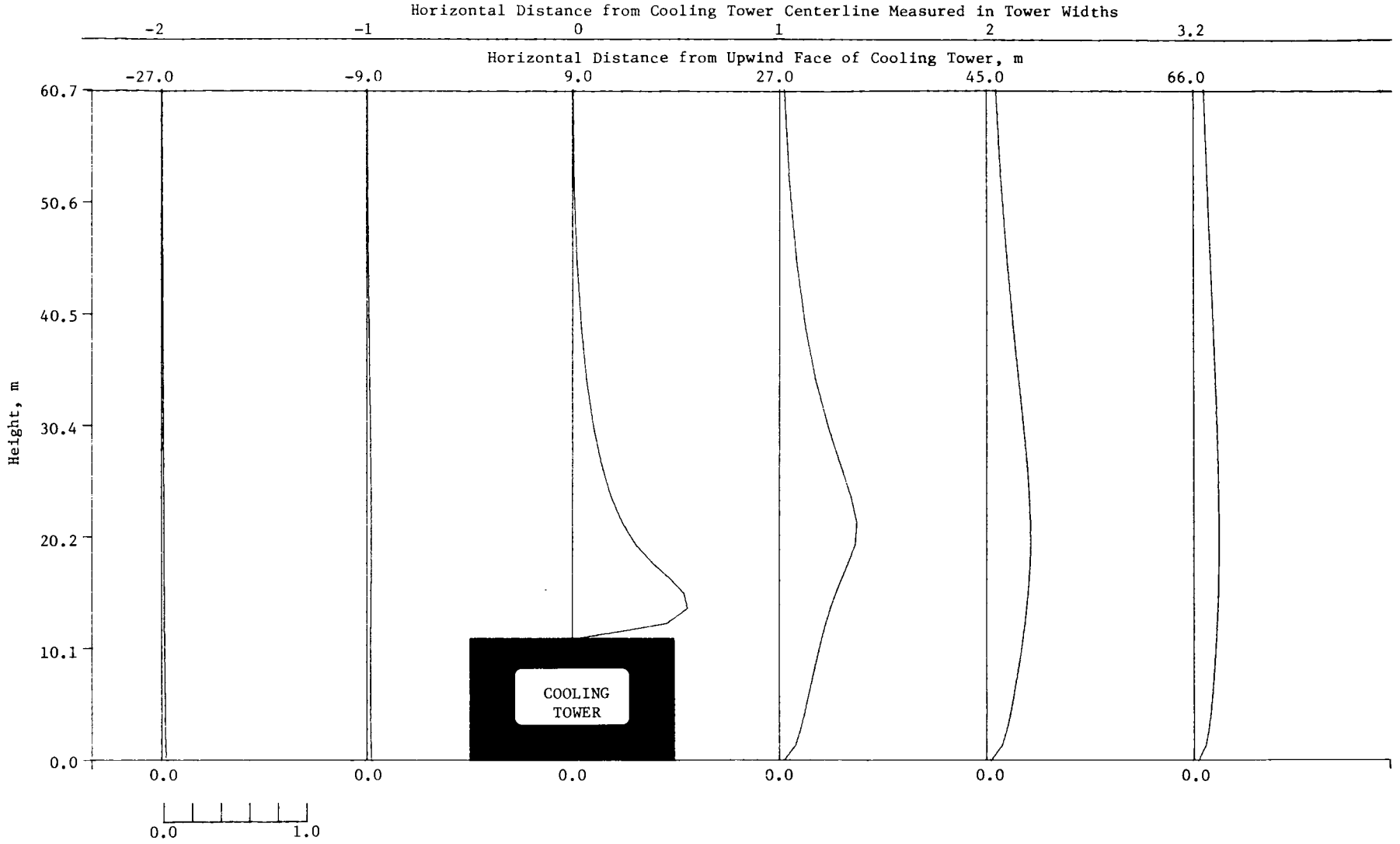
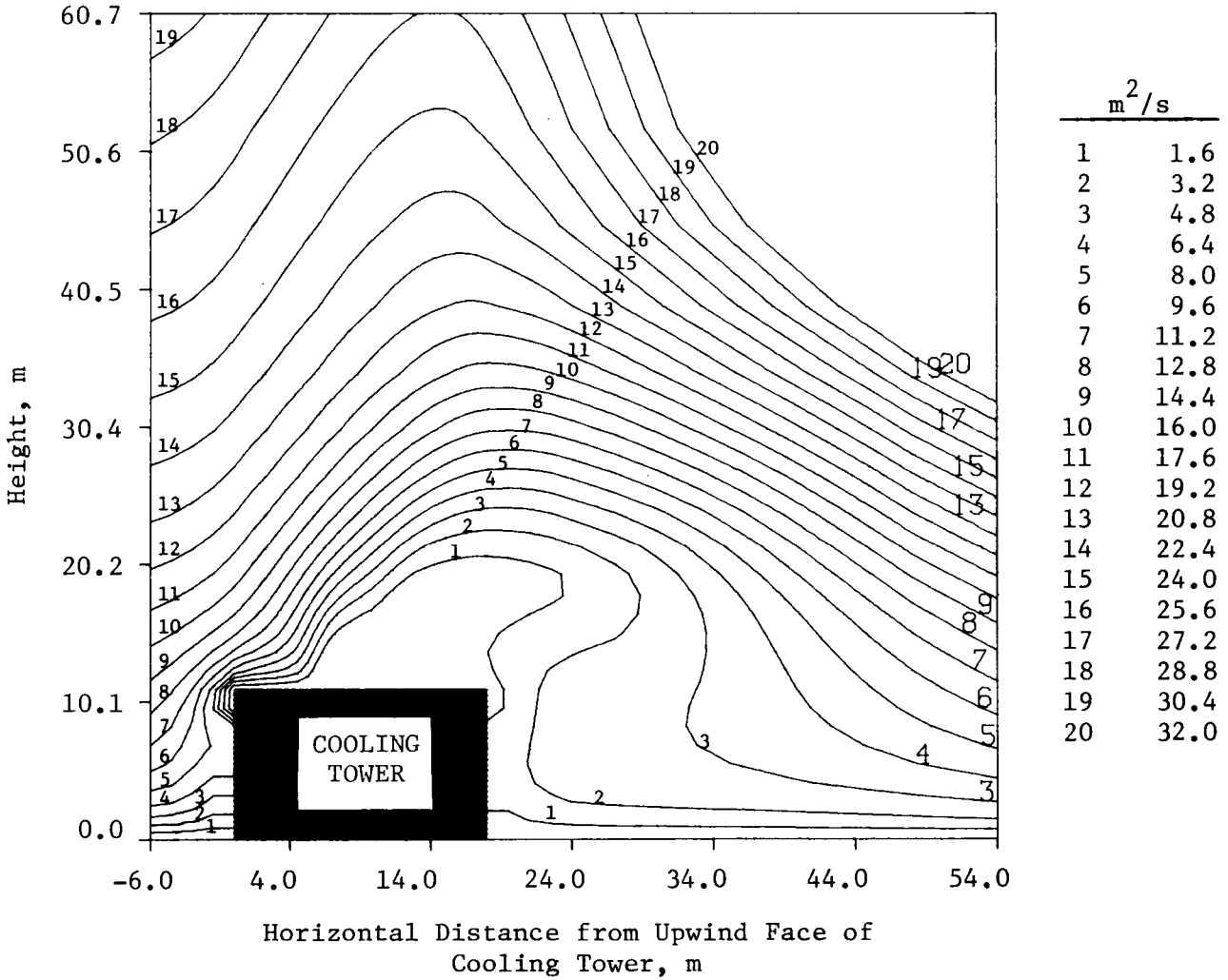
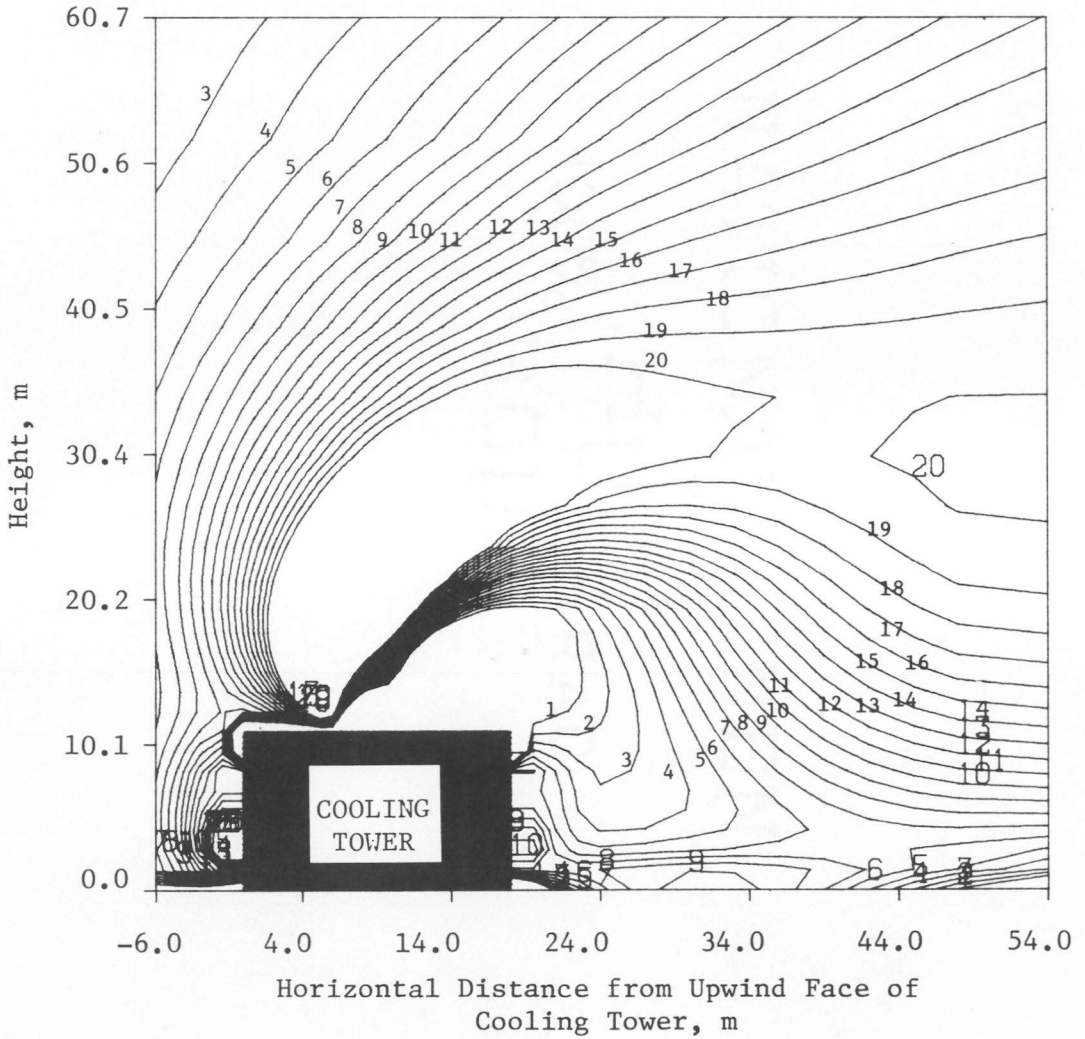


Figure 5.34. Profiles of temperature ratio, $(\overline{T} - \overline{T}_G)/(\overline{T}_{fan} - \overline{T}_G)$, for wind speed of 2 m/s.



	m^2/s
1	1.6
2	3.2
3	4.8
4	6.4
5	8.0
6	9.6
7	11.2
8	12.8
9	14.4
10	16.0
11	17.6
12	19.2
13	20.8
14	22.4
15	24.0
16	25.6
17	27.2
18	28.8
19	30.4
20	32.0

Figure 5.35. Effective thermal diffusivity contours for wind speed of 2 m/s.



	J/kg
1	2.0
2	2.2
3	2.4
4	2.6
5	2.8
6	3.0
7	3.2
8	3.4
9	3.6
10	3.8
11	4.0
12	4.2
13	4.4
14	4.6
15	4.8
16	5.0
17	5.2
18	5.4
19	5.6
20	5.8

Figure 5.36. Turbulence kinetic energy contours for wind speed of 2 m/s.

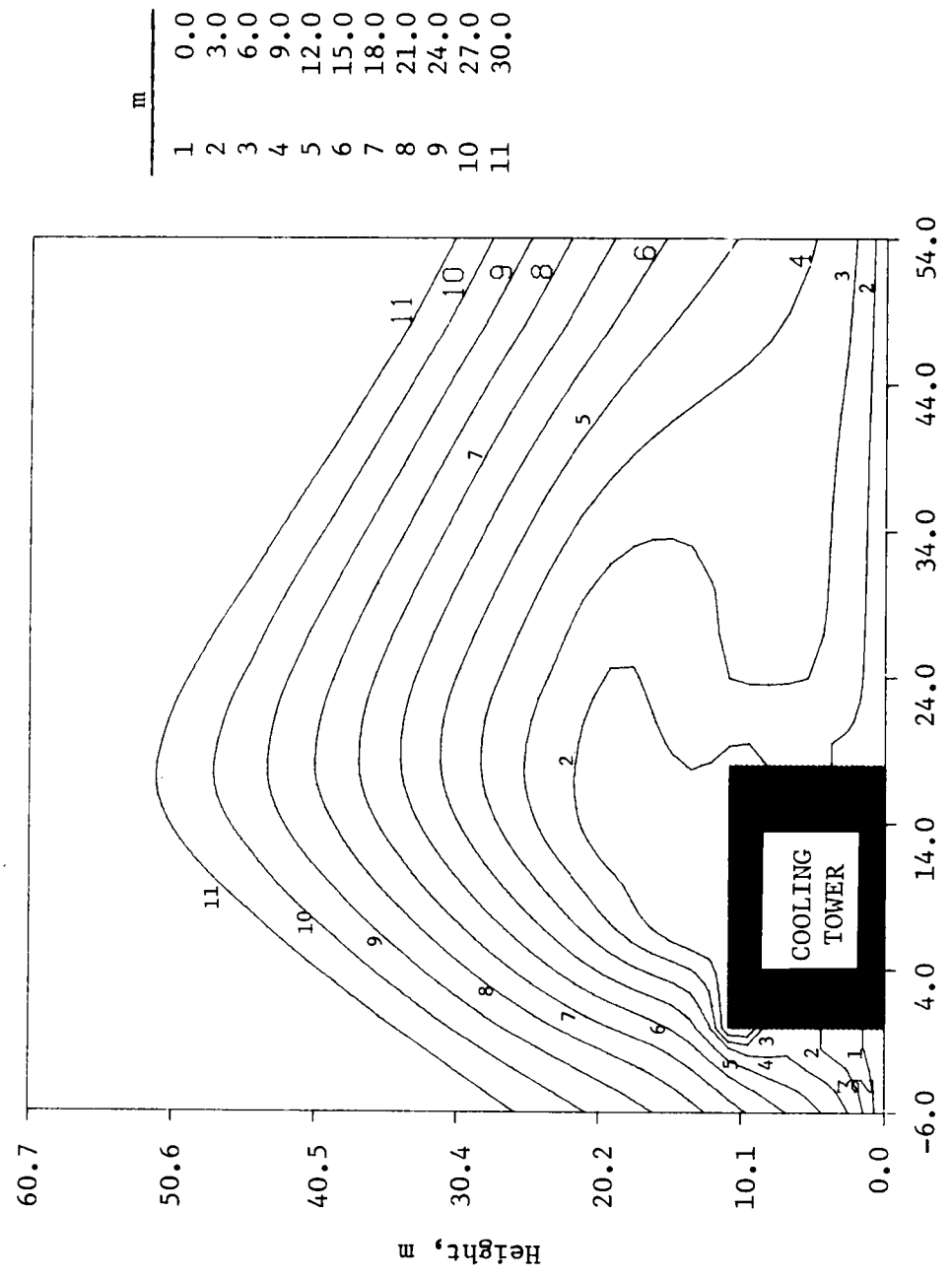


Figure 5.37. Turbulence length scale contours for wind speed of 2 m/s.

12 m/s case, there is some outflow at the top of the louvers on the downwind side of the tower due to the low pressures in the wake region just behind the tower. This type of outflow at the top of the downwind louver face has been observed at the K-31 cooling tower under conditions of gusting winds [56].

Profiles of the horizontal component of the mean velocity are given in Figures 5.2, 5.12, 5.21, and 5.30. The first profile in each of these figures is the logarithmic velocity profile of the approaching, undisturbed ambient wind at the inflow boundary.

The second profile in each of these figures is located a half tower width from the front of the cooling tower. This profile shows that the flow is decelerated as it approaches the cooling tower; this deceleration becomes stronger as the ambient velocity increases.

The third profile of each figure is positioned at the tower centerline, directly over the hub of the fan atop the tower. This profile shows that the flow is accelerated as it passes over the obstruction due to the displacement of the flow by the tower and by the jet exiting vertically from the top of the tower. This centerline profile in Figure 5.2 has a smooth shape which is very near that of a logarithmic profile, hence, the vertical jet has a minimal effect upon the 12 m/s ambient flow. However, the centerline profile of Figure 5.12 has a steeper, less smooth slope just above the top of the tower because the 6 m/s ambient flow is more displaced by jet. In the centerline profile of Figure 5.21, it is evident that the ambient flow is more greatly accelerated directly above the fan due to the much greater displacement of the 4 m/s ambient flow by the 13.7 m/s vertical jet. Finally, the

centerline profile of the 2 m/s case, Figure 5.30, shows a much greater acceleration of the flow directly above the tower than in the higher speed cases. Then, moving vertically upwards along this profile, it can be seen that the velocity at first is decreased and then again increased before returning to a smooth profile. This increase and decrease of velocity is due to the displacement of the flow around the eddy shown in Figure 5.29. As discussed above, this eddy is located much nearer to the tower centerline in the 2 m/s case than in the other cases. Hence, the centerline profile of the horizontal component of the ambient velocity is more directly affected by this eddy in the 2 m/s case.

The remaining three profiles in each of the four figures, Figures 5.2, 5.12, 5.21, and 5.30, pass through the recirculation zone behind the cooling tower. Comparison of these figures shows that the reversed flow in the wake region is more accelerated in the lower ambient wind speeds. The first profile behind the tower shows that the ambient flow above the wake is accelerated due to the displacement of the flow by the wake region. The last two profiles, located at 45 m and 66 m from the front of the cooling tower, show that the ambient flow over the wake decelerates as the recirculation bubble becomes smaller. Comparing the 6 m/s, 4 m/s, and 2 m/s cases shows that this deceleration becomes more pronounced as the ambient wind speed is decreased. As discussed in Section 5 of this chapter, this deceleration in the flow direction has an important effect upon the thermal plume.

3. STREAMLINES, RECIRCULATION BUBBLE AND REATTACHMENT POINT

The streamline plots, Figures 5.3, 5.13, 5.22, and 5.31, show some chatacteristics of the recirculation bubble. As the wind speed increases from 2 m/s to 6 m/s, the recirculation bubble becomes longer and thinner as the wake region moves downstream with increasing velocity. However, the 12 m/s case shows a reversal of this trend with a much smaller wake region than occurred in the 2 m/s case.

Table 5.2 gives the location of the reattachment point of the free streamline which divides the wake region from the ambient flow. As can be seen in this table, the reattachment point moves further downwind as the wind speed increases from 2 m/s to 6 m/s, but then moves upstream as the wind speed increases to 12 m/s. This phenomenon may possibly be explained as an interaction of the momentum of the ambient flow with the momentum of the vertical jet. The velocity or momentum per unit mass of the vertical jet as it leaves the cooling tower is 13.7 m/s. Thus, the 2 m/s, 4 m/s, and 6 m/s ambient flows transport much less momentum per unit mass than the jet does and, hence, these ambient flows see this jet as a porous curtain or obstruction. The wake behind this porous obstruction moves downstream with increasing wind speed just as the wake region behind a porous fence moves downstream with increasing wind speed. Kennedy and Fordyce [21] report that in their water flume tests a plane jet in a cross flow acted as a porous curtain which blocked the cross flow and created a relatively large separation region. However, in the current study, as the momentum per unit mass of the ambient flow approaches the momentum per unit mass of the jet, as is the case for the

TABLE 5.2

Reattachment Point Location Measured Downwind
from Back of Cooling Tower

Wind Speed (m/s)	Reattachment Point Location (m)
2.0	63
4.0	77
6.0	88
12.0	49

12 m/s wind, the ambient flow is less disturbed by the jet and reattachment occurs much closer to the cooling tower as would be the case in the absence of the jet.

The same values are used for the contour levels in each of the stream function plots, Figures 5.3, 5.13, 5.22, and 5.31. These contour levels completely fill Figure 5.31 but move lower and closer together as the wind speed is increased. Since an equal amount of mass flows between any two of these contours, comparison of the stream function plots shows that the mass flow through the computational region greatly increased as the wind speed increased; more mass flows through the lower third of Figure 5.3 than through the entire region depicted in Figure 5.37.

4. WIND FIELD PRESSURE DISTRIBUTION

Figures 5.4, 5.14, 5.23, and 5.32 give the wind field pressure distribution for the four different cases. Comparison of Figures 5.4, 5.14, and 5.23 shows a greater pressure differential between upwind and downwind faces of the tower at higher wind speeds. The pressure distribution for the 4 m/s case, Figure 5.23, appears nearly symmetrical. These results agree with Reisman's wind tunnel results. The pressure distribution for the 2 m/s case, Figure 5.32, shows a slightly higher pressure downwind of the tower than upwind of the tower. This is most probably a result of the inaccuracy of the solution for the 2 m/s case.

5. WIND FIELD TEMPERATURE DISTRIBUTION AND TURBULENT DIFFUSION

Comparison of Figures 5.5, 5.15, 5.24, and 5.33 shows that the plume, as traced by the temperature contours, is more bent over and much thinner in the 12 m/s case than in the lower wind speed cases. The high ambient wind convects the hot effluent plume downwind faster than the turbulent diffusion can cause it to spread. Comparing the temperature profiles of the 12 m/s, 6 m/s, 4 m/s, and 2 m/s cases, Figures 5.6, 5.16, 5.25, and 5.34, shows that the thermal energy of the 12 m/s case is not as widely spread in the vertical direction. Also, the peak temperatures of the 12 m/s profiles are less than those of the lower wind speeds. This is due to the much stronger dilution effect in the 12 m/s case; the plume is more diluted by the incoming ambient which also causes lower temperatures in the wake region behind the tower as shown in Figure 5.5. These results coincide with those of the wind tunnel tests made by Reisman [20] and the water flume tests of Kennedy and Fordyce [21].

In the lower wind speed cases, the effects of turbulent diffusion can be seen in the temperature contours, Figures 5.15, 5.24, and 5.33, and in the temperature profiles, Figures 5.16, 5.25, and 5.34. As the wind speed is reduced from 6 m/s to 2 m/s, the temperature contours show that the plume becomes more widely spread due to the turbulent diffusion. Also, the temperature profiles show that the turbulent diffusion reduces the peak temperatures and produces more widely spread, flatter profiles as the wind speed decreases.

The effective thermal diffusivity, shown in Figures 5.7, 5.17, 5.26, and 5.35, pages 87, 97, 106, and 115, is a measure of the turbulent diffusion. Comparison of these figures shows that the turbulent diffusion is the highest in the 12 m/s case. However, as discussed above, this diffusion is overpowered by the strong convection of the high speed ambient wind which sweeps the plume downstream before the diffusion can cause it to spread. In the 6 m/s, 4 m/s, and 2 m/s cases, the turbulent diffusion increases as the ambient wind speed decreases. This increase in turbulent diffusion explains the increased spreading of the thermal plume as the wind speed decreases.

As shown in Eq. (A.32), the turbulent diffusion varies with the turbulent viscosity which, in turn, is a function of the turbulence length scale and the square root of the turbulence kinetic energy as shown in Eq. (A.37). As can be seen in Figures 5.18, 5.19, 5.27, 5.28, 5.36, and 5.37, pages 98, 99, 107, 108, 116, and 117, both the turbulence kinetic energy and the turbulence length scale increase in the region above and downwind of the tower as the ambient flow decreases from 6 m/s to 2 m/s.

The turbulence length scale used in this study is an integral length scale which is considered a measure of the largest eddy size. Shieh et al. [49] report that acceleration in the flow direction always shrinks this length scale while deceleration tends to increase the length scale. As previously discussed in Section 2 of this chapter, the velocity profiles located 45 m and 66 m downstream from the front of the tower show that the ambient flow is more sharply decelerated behind the tower in the lower wind speed cases. According to Shieh et al. [49], this deceleration would then increase the turbulence length scale; this increase would be

greater at the lower wind speeds. Also, as discussed in Section 2 of this chapter, the vortex behind the tower moves first vertically upwards as the wind is reduced from 6 m/s to 4 m/s and then upstream toward the centerline of the tower as the wind speed decreases from 4 m/s to 2 m/s. As reported by Shieh et al. [49], the presence of this vortex would also tend to increase the turbulence length scale behind the tower.

Shieh et al. [49] also report that deceleration of the velocity in the flow direction tends to increase the turbulence kinetic energy while acceleration in the flow direction tends to decrease the turbulence kinetic energy. Thus, the same analysis as applied to the turbulence length scale also explains the increased turbulence kinetic energy at the lower wind speeds.

In summary, the increased spread of the plume as the ambient flow is reduced from 6 m/s to 2 m/s results from the increase in turbulent diffusion which occurs as the ambient flow is decreased from 6 m/s to 2 m/s. This increased turbulent diffusion as measured by the effective thermal diffusivity results from the increased turbulence kinetic energy and length scale which, in turn, are results of the greater deceleration of the ambient flow behind the tower.

6. PLUME RISE AND BUOYANCY EFFECTS

The temperature contours given in Figures 5.5, 5.15, 5.24, and 5.33, pages 85, 95, 104, and 113, can also be used to determine the height of the plume centerline. This height is taken to be the height of the maximum temperature along a vertical line at each downwind location. Table 5.3 compares this height as calculated by the current model to the corresponding height calculated from the plume rise formula given by Briggs [29].

TABLE 5.3

Comparison of Current Model to the Plume Rise Equation Given by Briggs [29]

Wind Speed (m/s)	Height of Plume Centerline as Calculated by Current Numerical Model (m)	Height of Plume Centerline as Calculated from Briggs' Plume Rise Equation [29] (m)	Downwind Location of Maximum Plume Height Measured from Back Face of Cooling Tower (m)
2.0	21.6	35.7	8.3
4.0	21.6	23.5	8.7
6.0	19.7	20.8	13.0
12.0	14.6	14.8	6.0

Briggs gives the height of the plume centerline as follows,

$$\text{Height of Plume Centerline} = H_s + \Delta H \quad , \tag{5.1}$$

where H_s is the height of the cooling tower stack and ΔH, the plume rise, is given as

$$\Delta H = 1.6(F^{1/3})(\bar{U}_s^{-1})(x_s^{2/3}) \quad . \tag{5.2}$$

In Eq. (5.2), $\bar{U}_s$ is the ambient wind velocity at the height of the stack opening, x_s is the distance downwind from the stack centerline, and F is the buoyancy flux parameter defined as

$$F = \frac{\bar{T}_s - \bar{T}_a}{\bar{T}_s} \cdot g \cdot \bar{W}_s \cdot r_s^2 \quad . \tag{5.3}$$

In Eq. (5.3), $\bar{T}_s$ is the effluent temperature at the stack opening, $\bar{T}_a$ is the ambient temperature, g is the gravitational constant, $\bar{W}_s$ is the vertical velocity of the jet leaving the stack, and r_s is the radius of the stack opening.

Table 5.3 shows that these two methods of calculation plume height are in excellent agreement for the cases of 12 m/s, 6 m/s, and 4 m/s ambient winds. However, the agreement is not very good for the 2 m/s case which could be due to the less accurate convergence tolerance used for this case as discussed above. Also, the current model does not include the thermodynamics of latent heat release which contributes a significant buoyancy effect [35].

As discussed in Section 2 of Appendix A, the current model uses the Boussinesq approximation to account for buoyancy effects. This

approximation includes only those buoyancy effects due to density variations which result from mean flow field temperature variations. Thus, the current model includes only those buoyancy effects which are caused by the difference between the temperature of the effluent and the ambient temperature.

For a plume with initial temperature of 315 K (42°C) exiting into an environment with ambient temperature of 295 K (22°C) and ambient relative humidity of 60%, Hanna [35] reports that the buoyancy due to latent heat release would be 5.7 times the buoyancy due to the difference between the temperature of the effluent and the ambient temperature. In the current study, the temperature of the plume at the cooling tower fan is 323 K (50°C) and the ambient temperature at the ground is 293 K (20°C). Thus, buoyancy forces in the current study would be at least as large as those reported by Hanna.

Hanna explains this buoyancy mechanism as follows. As the plume leaves the cooling tower, it is at the saturation humidity corresponding to the elevated temperature at the cooling tower mouth. As the plume rises from the tower, it cools by entraining ambient air and by transferring heat to the environment. As the plume cools, the excess water vapor condenses and falls out of the plume, releasing the corresponding latent heat which increases the buoyancy of the plume. The magnitude of this buoyancy force is independent of the ambient wind speed and, hence, for a given initial temperature difference and ambient humidity, this buoyancy effect would become more important as the momentum effects are reduced, that is, as the ambient velocity is reduced. In the higher wind speed cases, the buoyancy effects due to the latent heat of vaporization are of the same magnitude as in

the 2 m/s case; however, these effects are overwhelmed by the momentum at the higher wind speeds.

7. GENERAL DISCUSSION OF COOLING TOWER RECIRCULATION

The literature survey discussed in Chapter 1 revealed three reports of investigations of cooling tower recirculation: Reisman [20] studied recirculation using a wind tunnel; Kennedy and Fordyce [21] utilized a water flume to model recirculation; and Moore et al. [22] performed field studies to measure recirculation in large mechanical draft cooling towers. The reports of the first two investigations discuss a similar hypothesis concerning the mechanism of recirculation, the data of the last report support this hypothesis.

The phenomenon of recirculation as discussed by Reisman [20] and by Kennedy and Fordyce [21] is controlled by the interaction of two opposing mechanisms. When the ambient wind speed is nearly zero, the plume rises almost vertically from the top of the cooling tower to a very high altitude. In this case, the recirculation is nearly zero. As the ambient wind, especially the component normal to the major axis of the mechanical draft cooling tower, is increased, the vertical jet is bent more and more towards the leeward side of the tower. The jet is thus entrained into the wake behind the tower and reingested into the tower inlet louvers. This mechanism of the ambient wind works to increase the recirculation as the wind speed increases. However, an opposing mechanism of the ambient wind also becomes important at higher wind speeds: as the ambient velocity increases, the jet is more and more diluted by the incoming ambient air in the region just above and downstream of the tower.

This dilution of the jet decreases the concentration of the effluent in the plume just before it is entrained into the tower wake and reingested into the intake louvers. Thus, this dilution mechanism of the ambient wind works to decrease recirculation as the wind speed increases.

The interaction of these two opposing mechanisms controls the value of the recirculation as a function of wind speed. Both Reisman and Kennedy and Fordyce report the same type of trend: recirculation increased as the wind speed increased until a maximum value of recirculation was achieved, then further increases of the wind speed resulted in a decrease in the recirculation. As is discussed later, this type of behavior was also present in the field measurements of Moore et al. [22]. The results of the current model are compared with those of these earlier investigations forthwith. This discussion will show that the results of the current study tend to substantiate the aforementioned hypothesis concerning the mechanisms controlling the phenomenon of cooling tower recirculation.

8. COMPARISON OF COMPUTED RESULTS AND WIND TUNNEL EXPERIMENTAL DATA

Reisman [20] conducted a wind tunnel investigation of plume recirculation in mechanical draft cooling towers. He used a cooling tower model constructed of 3/16 inch mahogany to a scale of one inch equals 10 feet. The model was constructed so that tower configurations of 4, 8, 12, or 16 cells could be tested. Each model cell represented a cooling tower cell 36 feet long. Thus, he tested a range of tower lengths from 144 feet to 576 feet. Figure 5.38 is a schematic of

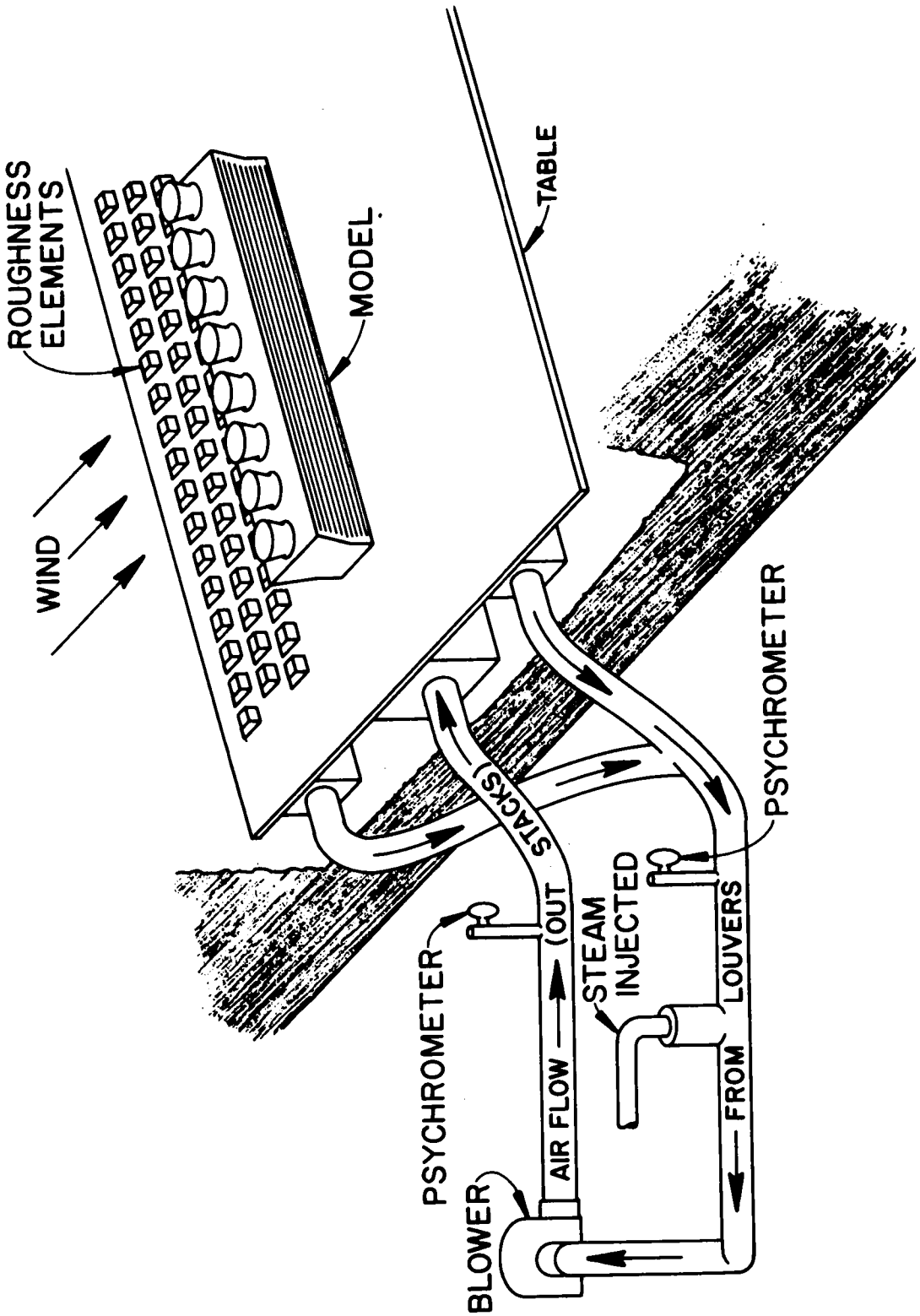


Figure 5.38. Schematic of cooling tower model and associated equipment used in wind tunnel investigations by Reisman [20].

Reisman's model and associated equipment. He maintained geometric similitude by keeping linear dimensions proportional to those of the actual cooling tower. Kinematic similitude was maintained by operating the cooling tower model at actual inlet and exhaust velocities. The Reynolds number and modified Froude number must usually be considered in satisfying dynamic similitude in model tests of this kind. However, Reisman [20] reports that the minimum Reynolds number used in these tests was 13,200, and that the minimum modified Froude number used was 25. Since both of these values are above the critical values of these parameters, Reisman reports that Reynolds number scaling and modified Froude number scaling were not essential in his experiments. The atmospheric velocity profile simulated by Reisman is shown in Figure 5.39. Reisman experimentally determined recirculation for various ambient velocities, measured at a model height of 10 m, and various orientations of the wind direction with respect to the cooling tower axis. All of his results are for three-dimensional flows; however, the case of the ambient flow normal to the tower axis is very similar to the two-dimensional model used in the current study. Thus, his results for the case of the ambient flow normal to the tower axis are compared to the numerical results of the current model.

Reisman [20] calculates plume recirculation in terms of enthalpy in the report of his wind tunnel tests by using the following equation,

$$\text{Recirculation} = \frac{h_2 - h_a}{h_1 - h_a} \times 100\% \quad , \tag{5.4}$$

where h_a is the ambient enthalpy, h_1 is the effluent enthalpy, and h_2 is the mass average enthalpy at the intake louvers. The results of the current model can also be analyzed in terms of enthalpy by assuming a

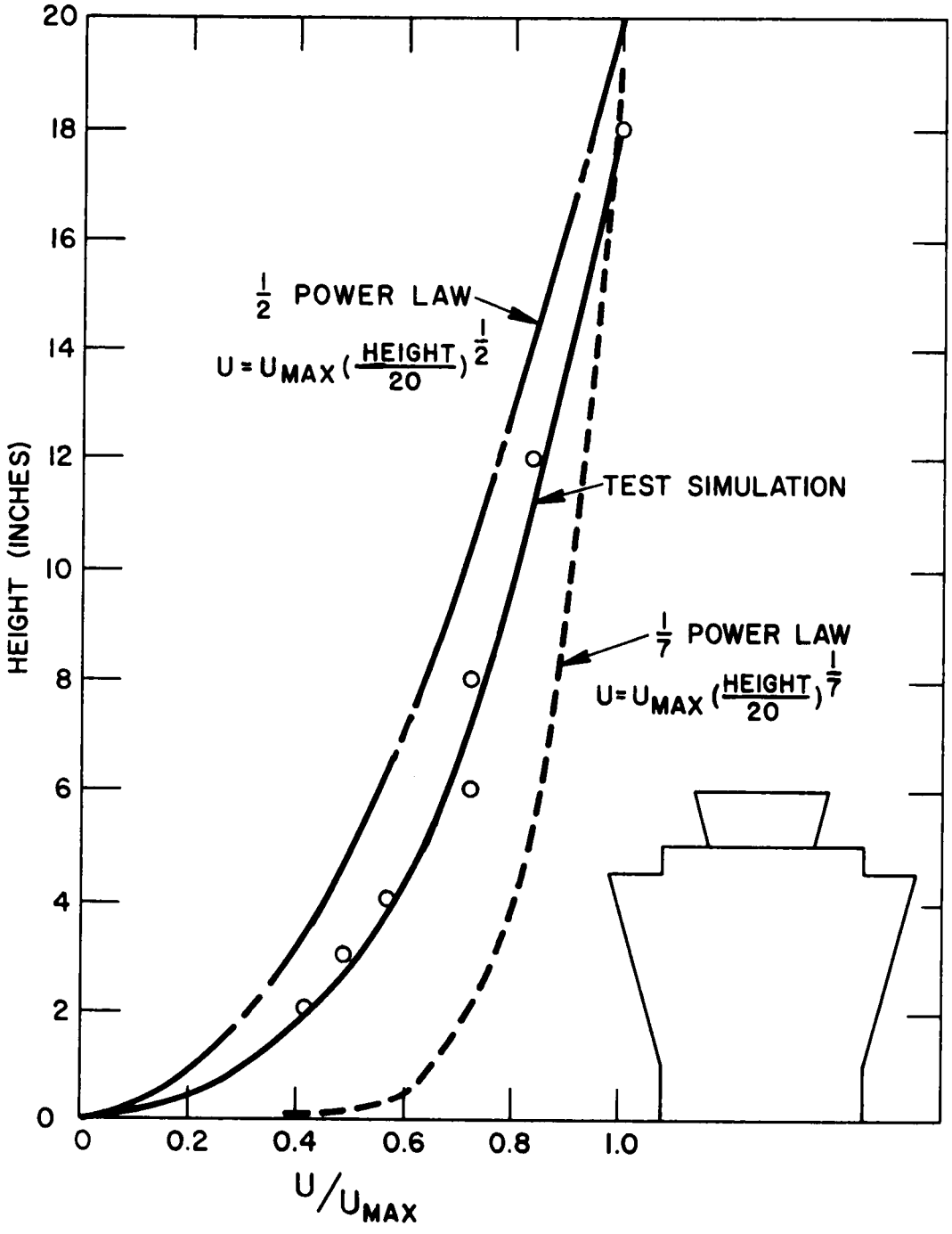


Figure 5.39. Atmospheric velocity profile used in wind tunnel investigations by Reisman [20].

saturated atmosphere. The temperature distribution calculated by the current model is then related to the enthalpy at saturation using a psychometric chart. These values of enthalpy are then used in Eq. (5.4) to calculate values of recirculation which can be compared to Reisman's results. This comparison is given in Table 5.4.

The results of the current model agree very well to those of Reisman for the 4 m/s and 6 m/s cases. The disagreement in the 2 m/s case again can be blamed on the inaccuracy of the 2 m/s results and on the absence of plume thermodynamics which may have a large effect on plume rise and hence recirculation at lower wind speeds. Although Reisman does not give data for winds as high as 12 m/s, he does report that recirculation increased with increasing wind speed to a maximum which occurred at 3.6 m/s. For winds higher than 3.6 m/s, Reisman reports that recirculation tended to diminish due to the increased dilution effect of the strong wind blowing normal to the tower. The exhaust plume was dispersed and diluted with ambient air, thus reducing the recirculation. The results of the current model for the 4 m/s, 6 m/s, and 12 m/s cases follow this trend reported by Reisman with the recirculation of the 12 m/s case greatly reduced from that of the 6 m/s case.

9. COMPARISON OF COMPUTED RESULTS AND WATER FLUME EXPERIMENTAL DATA

Kennedy and Fordyce [21] conducted a water flume investigation of plume recirculation in mechanical draft cooling towers. They used 1/150-scale models of mechanical draft towers in a 2.5 foot wide, 3.0 foot deep, 22.5 foot long, free surface water flume. Figures 5.40 and 5.41 are two schematic views of their test setup. They maintained geometric similitude

TABLE 5.4

Comparison of Current Model to Wind Tunnel Test Data Reported by Reisman [20]

Wind Speed (m/s)	Recirculation as Calculated by the Current Model Using the Method of Reisman %	Recirculation as Reported by Reisman %
2.0	3.6	2.2
4.0	2.8	2.9
6.0	2.1	2.5
12.0	0.6	--*

*The highest wind speed Reisman reports is 5.7 m/s (12.7 miles/hour).

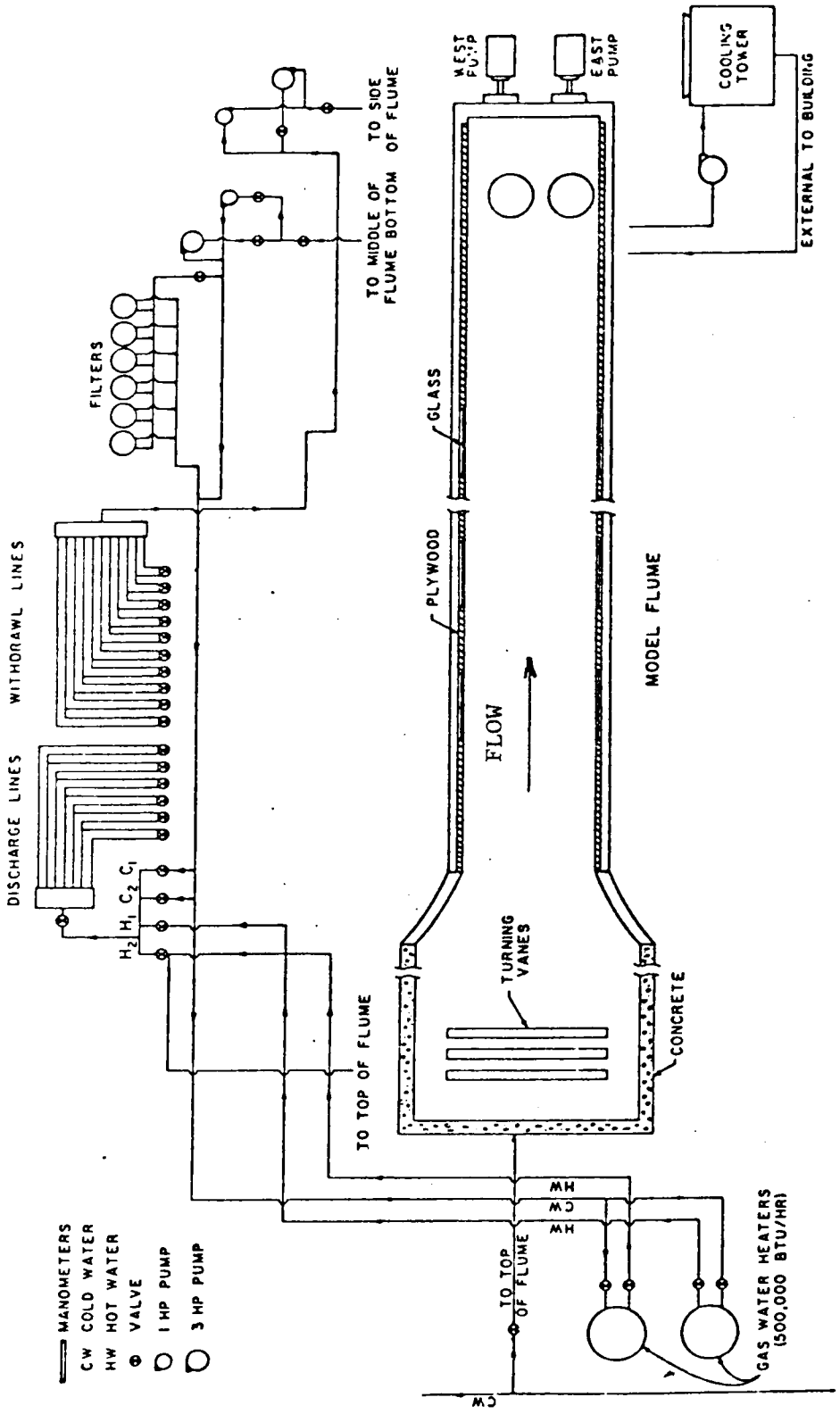


Figure 5.40. Top view of water flume used in cooling tower recirculation investigation by Kennedy and Fordyce [21].

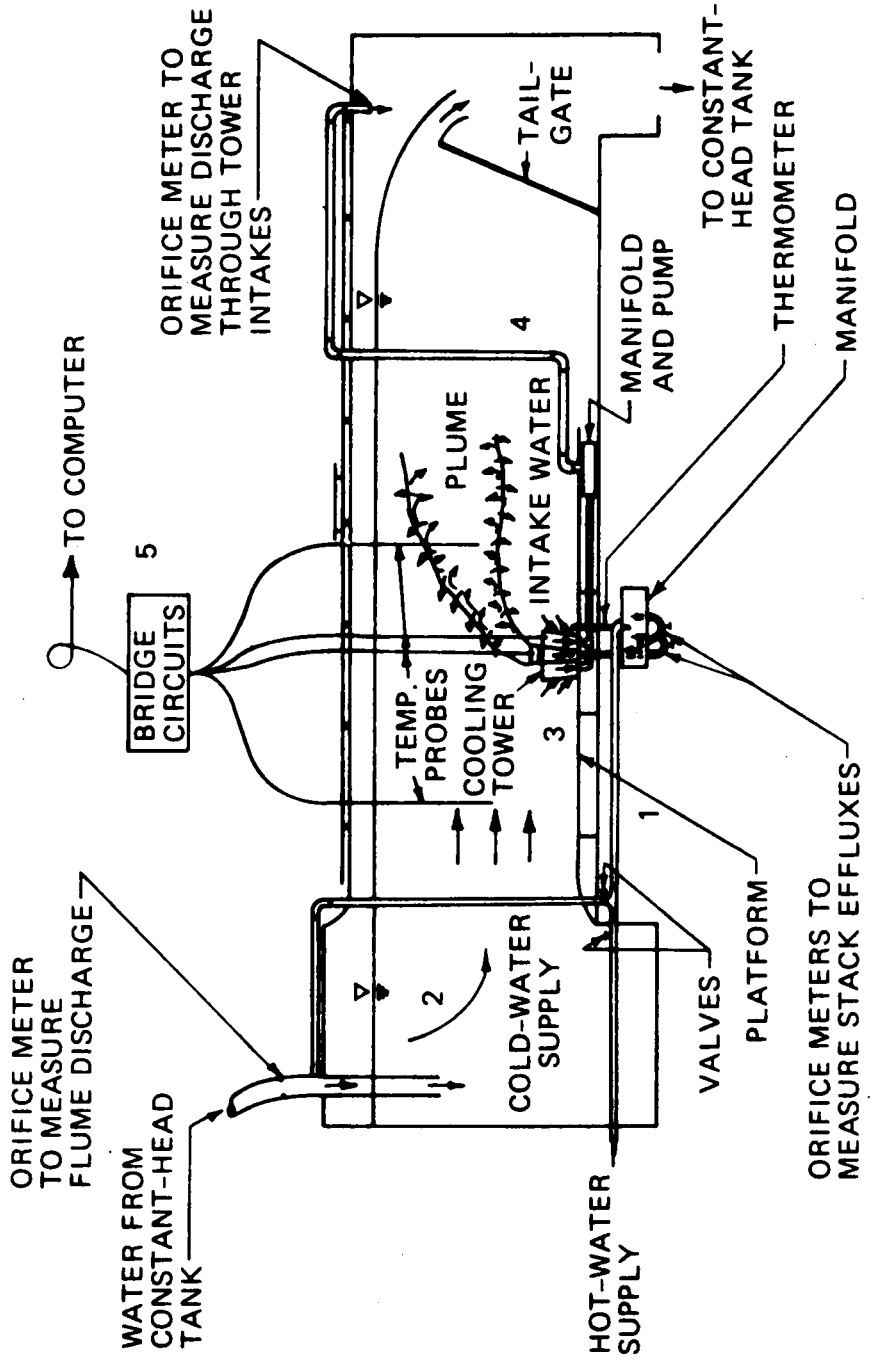


Figure 5.41. Elevation view of cooling tower model and water flume used by Kennedy and Fordyce [21].

by keeping linear dimensions proportional to those of the actual cooling tower. Kinematic similitude was maintained in terms of the ratio of the efflux velocity to the ambient velocity. They maintained dynamic similitude in terms of the modified Froude number exclusively, since they assumed that the turbulent mixing was Reynolds-number independent. Although they do not give a velocity profile, Kennedy and Fordyce report that the flow distribution across the test section was uniform and had a relatively low background turbulence as it approached the tower. They experimentally determined recirculation for various ambient velocities and various orientations of the wind direction with respect to the cooling tower axis. All of their results were for three-dimensional flows; however, the case of the ambient wind normal to the tower axis is similar to the two-dimensional model of the current study. Thus, their results for an ambient wind normal to the cooling tower axis are compared to the numerical results of the current model.

Kennedy and Fordyce [21] calculate recirculation in terms of temperature in the report of their water flume tests by using the following equation,

$$\text{Recirculation} = \frac{\overline{T}_2 - \overline{T}_a}{\overline{T}_1 - \overline{T}_a} \times 100\% \quad , \tag{5.5}$$

where $\overline{T}_a$ is the ambient temperature, $\overline{T}_1$ is the effluent temperature, and $\overline{T}_2$ is the mass average temperature at the intake louvers. The results of the current model can also be used to determine recirculation in terms of temperature by using Eq. (5.5).

Kennedy and Fordyce base their recirculation calculations on the flow through the downwind louver face only, rather than on the total flow

through the tower. Taking this into account, their results are compared to those of the current model in Table 5.5. The current model agrees well with water flume data for the 6 m/s case. However, agreement is poor at the other wind speeds. Since Table 5.4 shows good agreement between the results of the current model and those reported by Reisman, it can be inferred that the results of Reisman's wind tunnel tests would also not agree well with those of the water flume tests of Kennedy and Fordyce. While Reisman reports that the maximum recirculation occurred at 3.6 m/s, Kennedy and Fordyce report that this maximum occurred at an ambient wind speed corresponding to 34.3 m/s.

This discrepancy between the results of Kennedy and Fordyce and those of Reisman may be due in part because Kennedy and Fordyce are working in a water flume while Reisman is working in a wind tunnel. Also, the size and shape of the cooling tower being modeled by each may have an effect. More importantly, however, Kennedy and Fordyce report that the cooling tower model was mounted on a platform that formed a smooth transition for the incoming ambient flow. They report that the boundary layer of the approaching flow was about 0.5 in. thick near the model and the flow distribution across the test section was uniform and had a relatively low background turbulence as it approached the tower. Reisman, however, used a curved velocity profile between a 1/2 power law profile and a 1/7 power law profile for the incoming ambient flow, as shown in Figure 5.39. He reports that upwind of the tower, screens were placed across the wind tunnel and roughness elements were placed on the floor of the tunnel to insure a turbulent flow. Thus, Reisman is modeling recirculation in a much more turbulent flow than Kennedy and Fordyce. This would result in

TABLE 5.5

Comparison of Current Model to Water Flume Data
Reported by Kennedy and Fordyce [21]

Wind Speed (m/s)	Recirculation as Calculated by the Current Model Using the Method of Kennedy and Fordyce %	Recirculation as Reported by Kennedy and Fordyce %
2.0	6.6	--*
4.0	5.32	2.8
6.0	3.92	3.4
12.0	1.33	5.3

*The lowest wind speed Kennedy and Fordyce report is 3.4 m/s (velocity ratio of 4.0).

more turbulent mixing and diffusion of the effluent at lower wind speeds. Thus, the second mechanism controlling recirculation discussed above, that is, the dilution of the plume by the cooler ambient, is strengthened in Reisman's work. This increased turbulent dilution of the plume would cause the maximum recirculation to occur at a much lower wind speed than in the less turbulent flow modeled by Kennedy and Fordyce.

The current model uses a logarithmic wind velocity profile for the approaching ambient flow which is similar in shape to the profile used by Reisman and certainly much different from the uniform, parallel flow used by Kennedy and Fordyce. The results reported in Table 5.4 and Table 5.5 show that the current model supports the results of Reisman. However, in terms of the general type of trend reported, both Reisman and Kennedy and Fordyce, as well as the current model, all agree: the recirculation increased as the wind speed increased until a maximum value of recirculation was achieved, then further increases of the wind speed resulted in a decrease in the recirculation. The discrepancy involved only the wind speed at which this maximum recirculation occurs: Kennedy and Fordyce report that the maximum occurs at a much higher wind speed than reported by Reisman or determined by the current model.

10. COMPARISON OF COMPUTED RESULTS AND FIELD MEASUREMENT DATA

To assess the degree of recirculation experienced by mechanical draft cooling towers, Moore et al. [22] measured the distribution of wet bulb temperature over the louver faces of large mechanical draft towers in the field. Inlet wet bulb temperature measurements were made using a

network of nine sensors on each side of the tower within approximately two meters of the air inlet. These nine sensors were positioned in a three-by-three grid on each louver face. Each sensor was located at the center point of one of nine equal area segments. Three wet bulb sensors were also located upwind of the tower to measure the ambient wet bulb temperature consistent with the approach specified in ASME PTC-23, 1958, the ASME test code for Atmospheric Water Cooling Equipment. The ambient wind speed and direction relative to the tower axis were also measured at an altitude of 10 m.

With this test setup, Moore et al. determined the wet bulb temperature distribution over the louver faces. From this distribution, they determined the average wet bulb temperature at the inlet to the cooling tower louvers. The increase of this average inlet wet bulb over the ambient wet bulb is a measure of the recirculation. Assuming a saturated atmosphere, a similar calculation can be made using the results of the current model. A subset of their findings is compared to the results of the current model in Table 5.6. This table shows both the wind speed and the component of the wind normal to the cooling tower axis. The agreement is reasonable considering the differences in wind speed and orientation of the wind with respect to the tower axis.

The increase in inlet wet bulb as measured by Moore et al. and the increase as determined by the current model are plotted versus the normal component of the wind in Figure 5.42. This figure shows that the field test data reported by Moore et al. substantiates the general trend of recirculation as discussed above: the recirculation increased as the normal wind speed increased until a maximum value of recirculation

TABLE 5.6

Comparison of Current Model to Field Test Data Reported by Moore et al. [22]

Test Number	Wind Speed (m/s)	Normal Component of Wind (m/s)	Increase in Wet Bulb (K)
Field Test 1	3.13	1.80	1.28
Current Model	2.0	2.0	1.99
Field Test 2	2.24	2.16	1.56
Field Test 3	2.68	2.67	2.17
Field Test 4	3.58	3.24	2.50
Current Model	4.0	4.0	1.60
Field Test 5	8.05	5.69	2.06
Current Model	6.0	6.0	1.18
Field Test 6	8.94	7.74	1.50
Current Model	12.0	12.0	0.40

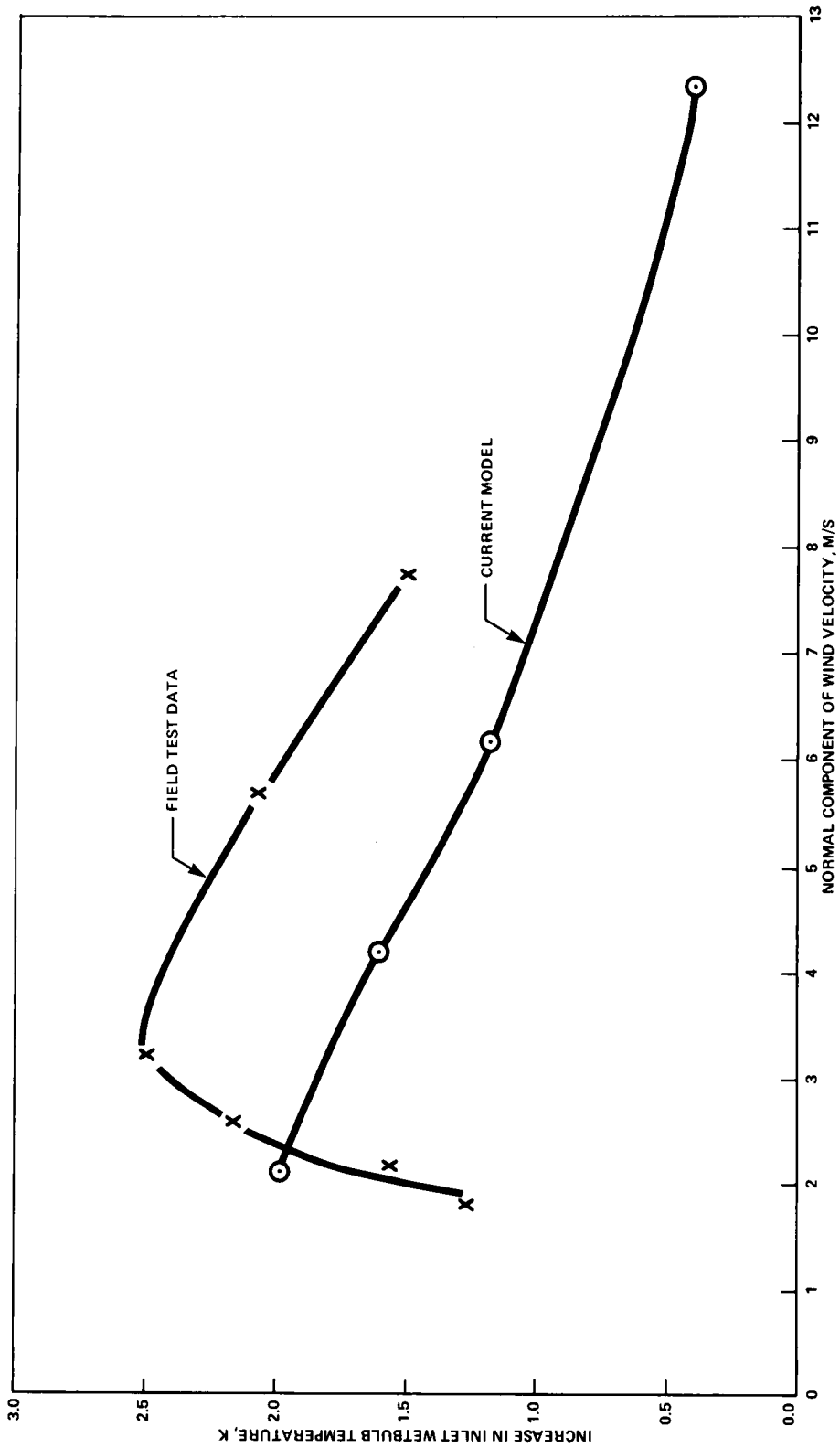


Figure 5.42. Increase in the inlet wet bulb temperature as a function of the normal wind velocity.

was achieved, then further increases in the normal wind speed resulted in a decrease in the recirculation. Figure 5.42 shows that the maximum recirculation determined by the field test data occurred at 3.24 m/s, which compares well with Reisman's result of a maximum recirculation at 3.6 m/s. Also, as can be seen in Figure 5.42, the results of the current model follow the same trend as the field test data. The fact that the results of the current model lie below those of the field data in Figure 5.42 may be due to experimental error or, more probably, due to three-dimensional effects which exist in the field but not in the current model.

11. COOLING TOWER PERFORMANCE DEGRADATION DUE TO RECIRCULATION

Recirculation calculated using Reisman's technique is directly related to the degradation of cooling tower performance. It is a measure of the ratio of the amount of exhaust air which reenters the tower divided by the total amount of air going through the tower. Thus, for example, in the 6 m/s case, a recirculation of 2.1% implies that 2.1% of the entering air is reingested exhaust air. Assuming this exhaust air can absorb no energy from the hot circulating water, the effective size of the tower is reduced. In the 6 m/s case, the cooling capacity of the tower is 97.9% of its capacity with no recirculation. Alternatively, to maintain a given cooling capacity during a 6 m/s cross wind, the cooling tower should be oversized to 102.1% of the design size needed for a still day. Table 5.7 gives the effective size and required oversize of the cooling tower as a result of the recirculation calculated by the current model.

TABLE 5.7

Cooling Tower Effective Size and Required Design Oversize Due to Recirculation

Wind Speed (m/s)	Effective Size %	Required Design Oversize %
2.0	96.4	103.7
4.0	97.2	102.9
6.0	97.9	102.1
12.0	99.4	100.6

CHAPTER 6

CONCLUSIONS

The present model of cooling tower recirculation as influenced by the local atmospheric flow field has been shown to yield results which are in good agreement with physical intuition and compare well with the basic theory. These results also compare well with reported laboratory and field results, both quantitatively and in terms of general trends.

The discussion in Section 2 of Chapter 5 presents some interesting features of the current model such as the movement of the vortex center behind the tower as a function of the ambient wind speed. The prediction by the model of the outflow at the top of the downwind louver face in the 12 m/s case is a unique feature which coincides well with observation of the tower in conditions of gusting wind [56]. The flow patterns over the tower and vertical jet relate well to physical intuition while the centerline velocity profile for the 2 m/s case gives much detail of the flow around the vortex behind the jet. The velocity profiles behind the tower are important as they help to explain the mechanism of the increased turbulent diffusion and spreading of the plume in the lower wind speed cases.

The movement of the reattachment point as discussed in Section 3 of Chapter 5 is a very interesting phenomenon predicted by the model which coincides well with the basic theory of flow through porous fences and with the experimental results of Kennedy and Fordyce [21]. The pressure distribution predicted by the model is in good agreement with physical intuition.

As discussed in Section 5 of Chapter 5, in the 12 m/s case, the model predicts the strong dilution of the plume and the lower temperatures in the wake region behind the tower. These results coincide well with observations reported by both Reisman [20] and Kennedy and Fordyce [21]. Also in the lower wind speed cases, the model predicts increased turbulent diffusion and spreading of the plume due to the deceleration of the ambient flow over the wake in the region where the recirculation bubble is diminishing. In addition, the turbulence kinetic energy and turbulence length scale both increase in this region of decelerated flow which is the same type of trend as reported by Shieh et al. [49].

Comparison of the plume rise calculated by the current model and that calculated using the plume rise formula reported by Briggs [29] shows excellent agreement for the 4 m/s, 6 m/s, and 12 m/s cases with an average difference of 4.9% for these wind speeds. However, the agreement is poor in the 2 m/s case with a 39.5% difference. As discussed in Section 6 of Chapter 5, this error may be due to the absence of plume thermodynamics in the present model. The error introduced by this absence is of greater consequence at the lower wind speeds where the buoyancy is more important due to the decreased momentum.

The results from the current model coincide well with those reported by Reisman [20] for the 4 m/s and 6 m/s cases with an average disagreement of 9.5% for these cases. The current model also predicts the same trend as reported by Reisman: recirculation decreased as the ambient wind speed increased from 4 m/s to 12 m/s. In the 2 m/s case, however, there was a 63% disagreement between Reisman's results and those of the current model.

The current model did not agree well with the water flume tests reported by Kennedy and Fordyce [21]; there was an average of 60% difference for the 4 m/s, 6 m/s, and 12 m/s cases. As discussed in Section 9 of Chapter 5, this difference probably resulted from the uniform ambient velocity profile used by Kennedy and Fordyce.

The results of the current model predicted the same type of trend as reported by Moore et al. [22]; however, the magnitude of recirculation calculated by the current model was consistently less than that reported by Moore et al. This difference is probably due to the three-dimensional effects which exist in the field but not in the model.

As reported in the literature and as shown in Table 5.7, recirculation can have a significant effect upon tower performance and should be considered in the design of the tower. In the discussion of their field tests, Moore et al. [22] report that the component of the wind perpendicular to the tower's major axis was significantly correlated with the recirculation. Thus, by using the normal component of the wind, the current model can give an estimate of the recirculation as experienced in the three-dimensional case.

As funding becomes available, this numerical work could be expanded. Parametric studies could be made in which the wind speed and ambient temperature are systematically varied. The results of such a study would give the cooling tower designer an estimate of the effects of recirculation upon cooling capacity and thus he could size the tower so as to provide adequate cooling under adverse conditions.

Various modifications could be made to the model to make it more accurate. A moisture transport equation could be added to the

model. The temperature transport equation could also be expanded into a more complete energy equation by including sink and source terms to account for the latent heat of vaporization. With these improvements, the thermodynamics of the plume could be modeled which would improve the overall performance of the model in the low wind speed cases. By allowing the plume to condense and release the corresponding latent heat which would increase the plume buoyancy, the physical process of plume rise would be more accurately modeled, especially in the low wind speed cases.

Moore et al. report that recirculation is very much site-dependent. The current model could be adapted to accommodate major features of a particular terrain or industrial site by modifying the lower boundary shape to account for such topographic effects. However, even at the present stage of development, this model gives a good estimate of cooling tower plume recirculation as influenced by the local atmospheric flow field.

LIST OF REFERENCES

LIST OF REFERENCES

1. Hanna, S. R. "Fog and Drift Deposition from Evaporative Cooling Towers," Nuclear Safety, Vol. 15, No. 2, March-April 1974.

2. ASME Research Committee on Atmospheric Emissions and Plume Behavior from Cooling Towers, "Cooling Tower Plume Modeling and Drift Measurement - A Review of the State of the Art," Library of Congress Catalog Card Number 75-21277, 1975.

3. Higgins, John T., "The Thermal Pollution Problem: A Preliminary Study of Atmospheric Effects of Cooling Towers," Paper No. 69-51, Proc. 62nd Annual Meeting, Air Pollution Control Assoc., New York, 1969.

4. Stewart, R., "Thermal Discharges from Nuclear Plants and Related Weather Modifications," Proc. 12th Conf. Great Lakes Research, Intern. Assoc. Great Lakes Res., 1969, pp. 488-491.

5. Lowry, W. P., "Environmental Effects of Nuclear Cooling Facilities," Bull. Amer. Meteor. Soc., 51, 1970, pp. 23-24.

6. Hewson, E. W., "Moisture Pollution of the Atmosphere by Cooling Towers and Cooling Ponds," Bull. Amer. Meteor. Soc., 51, 1970, pp. 21-22.

7. Aynsley, E., "Environmental Aspects of Cooling Tower Plumes," TP 78A, Cooling Tower Inst. Publ., Houston, Texas, 1970, pp. 1-10.

8. Decker, F. W., "Report on Cooling Towers and Weather," Report to Federal Water Pollution Control Admin., Oregon State University, Corvallis, Oregon, 1969.

9. Ackermann, William C., "Research Needs on Waste Heat Transfer from Large Sources into the Environment," Report on Conference at Zion, Illinois, NSF Grant GI-30971, Illinois State Water Survey, University of Illinois, Urbana, Illinois, 1971.

10. Hanna, Steven R. and Searle D. Swisher, "Meteorological Effects of the Heat and Moisture Produced by Man," Nuclear Safety, 12, 1971, pp. 114-122.

11. Carson, J. E., "The Atmospheric Consequences of Thermal Discharges from Power Generating Stations," ANL-7869, Part 3, Annual Report for 1971, Radiological Physics Div., Argonne National Laboratories, Argonne, Illinois, 1971, pp. 250-269.

12. Carson, J. E., "Meteorology, Cooling Towers, and Environmental Impact Statements," Symposium on Atmospheric Diffusion and Air Pollution, Amer. Meteor. Soc., Santa Barbara, California, Sept. 9-13, 1974, pp. 396-399.

13. Boyack, B. E. and D. W. Kearney, "Plume Behavior and Potential Environmental Effects of Large Dry Cooling Towers," Final Report, Contract AT(04-3)-167, Gulf General Atomic Company, Division of Reactor Technology, USAEC, 1973. (Also in "Dry and Wet/Dry Cooling Towers," ASME, New York.)

14. Moore, D. J., "Recent G.E.G.B. Research on Environmental Effects of Wet Cooling Towers," Cooling Tower Environment - 1974, ERDA Symposium Series, available as CONF-740302 from the National Technical Information Service, U. S. Department of Commerce, Springfield, Virginia 22161, 1975.

15. Aynsley, E. and J. E. Carson, "Environmental Effects of Water Cooling for Power Plants: A Status Report," ANL/ES-20 (Draft), Argonne National Laboratory (unpublished), 1973.

16. Roffman, A. et al., "The State of the Art of Saltwater Cooling Towers for Steam Electric Generating Plants," WASH-1244, Prepared for the U. S. Atomic Energy Commission by Westinghouse Electric Corporation, Environmental Systems Department, Pittsburgh, Pennsylvania, 1973.

17. Glade, D. O., Cooling Towers, A Bibliography, March 1976 - May 1977, available as TID-3360-S1 from the National Technical Information Service, U. S. Department of Commerce, Springfield, Virginia 22161, July 1977.

18. Glade, D. O., Cooling Towers, A Bibliography, June 1977 - December 1977, available as TID-3360-S2 from the National Technical Information Service, U. S. Department of Commerce, Springfield, Virginia 22161, February 1978.

19. Glade, D. O., Cooling Towers, A Bibliography, January - December 1978, available as TID-3360-S3 from the National Technical Information Service, U. S. Department of Commerce, Springfield, Virginia 22161, February 1979.

20. Reisman, J. I., "A Study of Cooling Tower Recirculation," presented at the ASME 93rd Winter Annual Meeting, November 26-30, 1972, New York, New York, available from Ecodyne Cooling Products Division, P. O. Box 1267, Santa Rosa, California 95403.

21. Kennedy, J. F. and H. Fordyce, "Plume Recirculation and Interference in Mechanical-Draft Cooling Towers," Cooling Tower Environment - 1974, ERDA Symposium Series, available as CONF-740302 from the National Technical Information Service, U. S. Department of Commerce, Springfield, Virginia 22161, 1975.

22. Moore, R. D., D. E. Wheeler, K. R. Wilber and A. E. Johnson, "An Evaluation of Schemes for the Prediction of Recirculation on Crossflow Rectangular Mechanical Draft Cooling Towers," presented at Cooling Tower Institute Annual Meeting, January 22-24, 1979.

23. Davis, L. R. and M. A. Shirazi, "A Review of Thermal Plume Modeling," presented at the International Heat Transfer Conference, August 1978.

24. Dunn, W. E., G. K. Cooper and P. M. Gavin, "Evaluation of Methods for Predicting Plume Rise from Mechanical-Draft Cooling Towers," University of Illinois at Urbana-Champaign, Urbana, Illinois, 1978.

25. Carhart, R. A., A. J. Policastro, S. Ziemer and K. Kaake, "Critical Review of Thirteen Models for Plume Dispersion from Natural Draft Cooling Towers," Division of Environmental Impact Studies, Argonne National Laboratory, Argonne, Illinois, 1978.

26. Gifford, F. A., "Use of Routine Meteorological Observations for Estimating Atmospheric Dispersion," Nuclear Safety, 2, 4, 1961, pp. 47-51.

27. Pasquill, F., "The Estimation of the Dispersion of Windborne Material," Meteorol. Mag., 90, 1963, pp. 33-49.

28. Morton, B. R., A. I. Taylor and J. S. Turner, "Turbulent Gravitational Convection from Maintained and Instantaneous Sources," Proc. Roy. Soc., A234, 1956, pp. 1-23.

29. Briggs, G. A., Plume Rise, AEC Critical Review Series, available as TID-25075 from the National Technical Information Service, U. S. Department of Commerce, Springfield, Virginia 22161, 1969.

30. Wessels, H. R. A. and J. A. Wisse, "A Method for Calculating Sizes of Cooling Tower Plumes," Atmos. Environ., 5, 1971, pp. 743-750.

31. McVehil, G. E., "Evaluation of Cooling Tower Effects at Zion Nuclear Generating Station," Final Report, Sierra Research Corporation, Boulder, Colorado, to Commonwealth Edison Company, 1970.

32. Altomare, Philip M., "The Application of Meteorology in Determining the Environmental Effects of Evaporative Heat Dissipation Systems," Paper No. 71-56, 64th Annual Meeting, Air Pollution Control Assoc., Atlantic City, New Jersey, 1971.

33. Csanady, G. T., "Bent-Over Vapor Plumes," J. Appl. Meteor., 10, 1971, pp. 36-42.

34. Wigley, T. M. L. and P. R. Slawson, "On the Condensation of Buoyant Moist, Bent-Over Plumes," J. Appl. Meteor., 10, 1971, pp. 253-259.

35. Hanna, S. R., "Rise and Condensation of Cooling Tower Plumes," J. Appl. Meteor., 11, 1972, pp. 793-799.

36. Hanna, S. R., "Meteorological Effects of the Mechanical-Draft Cooling Towers of the Oak Ridge Gaseous Diffusion Plant," Cooling Tower Environment - 1974, ERDA Symposium Series, available as CONF-740302 from the National Technical Information Service, U. S. Department of Commerce, Springfield, Virginia 22161, 1975.

37. Hanna, Steven R., "Cooling Tower Plume Rise and Condensation," Paper No. 53, Air Pollution Turbulence and Diffusion Symposium, Los Cruces, New Mexico, 1971.

38. Slawson, P. R., J. H. Coleman and J. W. Frey, "Some Observations on Cooling Tower Plume Behavior at the Paradise Steam Plant," Cooling Tower Environment - 1974, ERDA Symposium Series, available as CONF-740302 from the National Technical Information Service, U. S. Department of Commerce, Springfield, Virginia 22161, 1975.

39. Meyer, J. H., T. W. Eagles, L. C. Kohlenstein, J. A. Kagan and W. D. Stanbro, "Mechanical Draft Cooling Tower Visible Plume Behavior: Measurements, Models, Predictions," Cooling Tower Environment - 1974, ERDA Symposium Series, available as CONF-740302 from the National Technical Information Service, U. S. Department of Commerce, Springfield, Virginia 22161, 1975.

40. EG & G, Inc., "Potential Environmental Modifications Produced by Large Evaporative Cooling Towers," Series #16130 DNH, Water Pollution Control Rec., Water Quality Office, Environmental Protection Agency, 1971.

41. Stephen, Donald W. and William J. Moroz, "Plume Rise from Wet Cooling Towers in Strong Winds," Eng. Res. Bull. B-107, College of Eng., The Pennsylvania State University, University Park, 1972.

42. Bogh, P., "Experience with Combined 'Wind Tunnel/Plume Model' Analysis of Cooling Tower Environmental Impact," Cooling Tower Environment - 1974, ERDA Symposium Series, available as CONF-740302 from the National Technical Information Service, U. S. Department of Commerce, Springfield, Virginia 22161, 1975.

43. Winiarski, L. D. and W. F. Frick, "Cooling Tower Plume Model," USEPA Corvallis Environmental Research Lab, EPA-600/3-76-100, September 1976.

44. England, W. G., L. H. Teuscher and J. R. Taft, "Cooling Tower Plumes - Defined and Traced by Means of Computer Simulation Models," presented at Cooling Tower Institute Annual Meeting, January 29-31, 1973.

45. Taft, James, "Numerical Model for the Investigation of Moist Buoyant Cooling Tower Plumes," Cooling Tower Environment - 1974, ERDA Symposium Series, available as CONF-740302 from the National Technical Information Service, U. S. Department of Commerce, Springfield, Virginia 22161, 1975.

46. Junod, A., R. J. Hopkirk, D. Schneiter and D. Haschke, "Meteorological Influences of Atmospheric Cooling Systems as Projected in Switzerland," Cooling Tower Environment - 1974, ERDA Symposium Series, available as CONF-740302 from the National Technical Information Service, U. S. Department of Commerce, Springfield, Virginia 22161, 1975.

47. Gosman, A. D., W. M. Pun, A. K. Runchal, D. B. Spalding and M. Wolfshtein, Heat and Mass Transfer in Recirculating Flows, Academic Press, Inc., New York, 1973.

48. Bitte, J. and W. Frost, "Atmospheric Flow over Two-Dimensional Bluff Surface Obstructions," NASA CR-2750, report prepared under NASA Contract No. NAS8-29584 by the University of Tennessee Space Institute, Tullahoma, Tennessee, 1975.

49. Shieh, C. F., W. Frost and J. Bitte, "Neutrally Stable Atmospheric Flow over a Two-Dimensional Rectangular Block," Report prepared under NASA Contract No. NAS8-29584 by the Atmospheric Science Division, The University of Tennessee Space Institute, Tullahoma, Tennessee, November 1976.

50. Pechinthorn, S., "Atmospheric Boundary Layer Flow over a Flat Surface with a Sudden Change in Surface Temperature," M. S. Dissertation, University of Tennessee, Knoxville, Tennessee, June 1977.

51. Park, J. E., "Utility Routines for Tridiagonal Matrices," Union Carbide Corporation, Nuclear Division, Oak Ridge, Tennessee, available as UCCND/CSD/INF-74 from the National Technical Information Service, U. S. Department of Commerce, Springfield, Virginia 22161, November 1975.

52. Slade, D. H. (Editor), Meteorology and Atomic Energy - 1968, available as TID-24190 from the National Technical Information Service, U. S. Department of Commerce, Springfield, Virginia 22161, July 1968.

53. Tennekes, H., "The Logarithmic Wind Profile," Journal of the Atmospheric Sciences, Vol. 30, March 1973, pp. 234-238.

54. Tennekes, H. and J. L. Lumley, A First Course in Turbulence, The MIT Press, Cambridge, Massachusetts, 1972.

55. Roache, P. J., Computational Fluid Dynamics, Hermosa Publishers, Albuquerque, New Mexico, 1972.

56. Private communication with S. H. Park, Gaseous Diffusion Development Division, Oak Ridge Gaseous Diffusion Plant, Union Carbide Corporation, Nuclear Division, Oak Ridge, Tennessee, November 1977.

57. Uglow, R. R., "Background Information on the Heat Exchange System for CIP/CUP: Structural Details and Maintenance History of the K-31 and K-33 Cooling Towers," Union Carbide Corporation, Nuclear Division, Oak Ridge, Tennessee, available as K/GD-505, Part 5, from the National Technical Information Service, U. S. Department of Commerce, Springfield, Virginia 22161, May 1974.

58. Launder, B. E. and D. B. Spalding, Mathematical Models of Turbulence, Academic Press, London and New York, 1972.

59. Private communication with I. Kuharic, The Marley Company, Mission Kansas, May 23, 1975.

60. Bear, Jacob, Dynamics of Fluids in Porous Media, American Elsevier Publishing Co., Inc., New York, 1972.

61. Kelly, N. W., Kelly's Handbook of Cross-Flow Cooling Tower Performance, available from Neil W. Kelly and Associates, 525 Brush Creek Blvd., Kansas City, Missouri 64110, 1976.

62. Wilson, E. L. and R. E. Nickell, "Application of the Finite Element Method to Heat Conduction Analysis," Nuclear Engineering and Design, 4, 1966, pp. 276-286.

63. Zienkiewicz, O. C. and Y. K. Cheung, "Finite Elements in the Solution of Field Problems," The Engineer, September 24, 1965, pp. 507-510.

64. Plate, E. J., "Aerodynamic Characteristics of Atmospheric Boundary Layers," available as TID-25075 from the National Technical Information Service, U. S. Department of Commerce, Springfield, Virginia 22161, 1971.

65. Hinze, J. O., Turbulence, McGraw-Hill Book Company, Inc., New York, Toronto and London, 1975.

66. Rotta, J. C., "Temperaturverteilungen in der Turbulenten Grenzchict an der Ebenen Platte," Inst. J. Heat Mass Transfer, 7, 1964, pp. 215-228.

67. Private communication with C. F. Shieh, Atmospheric Science Division, The University of Tennessee Space Institute, Tullahoma, Tennessee, June 1978.

68. Zienkiewicz, O. C., The Finite Element Method in Engineering Science, McGraw-Hill Publishing Company Limited, London, 1971.

69. Hildebrand, F. B., Advanced Calculus for Applications, Prentice-Hall, Inc., Englewood Cliffs, New Jersey, 1962.

APPENDICES

APPENDIX A

DEVELOPMENT OF THE WIND FIELD EQUATIONS

1. TIME AVERAGED MOMENTUM AND CONTINUITY EQUATIONS

The atmospheric flow is modeled as a steady flow of an incompressible fluid with constant molecular viscosity. With these assumptions, the instantaneous momentum equations are given as

$$\rho\tilde{U}_j \frac{\partial\tilde{U}_i}{\partial x_j} = -\frac{\partial\tilde{P}}{\partial x_i} + \mu \frac{\partial^2\tilde{U}_i}{\partial x_j \partial x_j} + \rho B_i \quad , \tag{A.1}$$

wherein ~ denotes the instantaneous value of the variable. The instantaneous continuity equation is given by:

$$\frac{\partial\tilde{U}_i}{\partial x_i} = 0 \quad . \tag{A.2}$$

The instantaneous value of a variable, $\tilde{A}$, can be expressed as the sum of the mean value of the variable, $\overline{A}$, and the fluctuating component of the variable about its mean, a. It is assumed that the variable can be represented as an ergodic random process so that $\overline{A}$ is the time average value of the variable which is equal to the ensemble average value. Thus:

$$\tilde{A} = \overline{A} + a \quad . \tag{A.3}$$

The sum of the mean value plus the fluctuating component can be substituted for the instantaneous value of each of the variables in Eqs. (A.1) and (A.2). Then, the resulting equations can be Reynolds

averaged to produce the following:

Momentum

$$\rho\bar{U}_j \frac{\partial\bar{U}_i}{\partial x_j} = -\frac{\partial\bar{P}}{\partial x_i} + \mu \frac{\partial^2\bar{U}_i}{\partial x_j \partial x_j} - \frac{\partial}{\partial x_j}(\overline{\rho u_i u_j}) + \rho B_i \quad . \tag{A.4}$$

Continuity

$$\frac{\partial\bar{U}_i}{\partial x_i} = 0 \quad . \tag{A.5}$$

The Reynolds shear stress can be expressed in terms of an eddy or turbulent viscosity, μ_t, times the mean strain rate as follows:

$$-\overline{\rho u_i u_j} = \mu_t\left(\frac{\partial\bar{U}_i}{\partial x_j} + \frac{\partial\bar{U}_j}{\partial x_i}\right) \quad . \tag{A.6}$$

The eddy or turbulent viscosity which is a function of the turbulence in the flow field is discussed in the section on Turbulence Modeling.

The momentum equations can be transformed with the use of Eq. (A.5) and Eq. (A.6). The result of this transformation is given as follows:

$$\rho\bar{U}_j \frac{\partial\bar{U}_i}{\partial x_j} = -\frac{\partial\bar{P}}{\partial x_i} + \frac{\partial}{\partial x_j}\left[\mu\left(\frac{\partial\bar{U}_i}{\partial x_j} + \frac{\partial\bar{U}_j}{\partial x_i}\right)\right]$$

$$+ \frac{\partial}{\partial x_j}\left[\mu_t\left(\frac{\partial\bar{U}_i}{\partial x_j} + \frac{\partial\bar{U}_j}{\partial x_i}\right)\right] + \rho B_i \quad . \tag{A.7}$$

An effective viscosity, μ_{eff}, can be defined as the sum of the molecular viscosity, μ, and the turbulent viscosity, μ_t:

$$\mu_{eff} = \mu + \mu_t \quad . \tag{A.8}$$

The effective viscosity is a function of the flow field conditions and hence a function of the space variables. The effective viscosity is discussed in the section on Turbulence Modeling. With the inclusion of the effective viscosity, the momentum equations become:

$$\rho\bar{U}_j \frac{\partial\bar{U}_i}{\partial x_j} = - \frac{\partial\bar{P}}{\partial x_i} + \frac{\partial}{\partial x_j} [\mu_{eff}(\frac{\partial\bar{U}_i}{\partial x_j} + \frac{\partial\bar{U}_j}{\partial x_i})] + \rho B_i \quad . \tag{A.9}$$

2. BOUSSINESQ APPROXIMATION

The Boussinesq Approximation is used to account for the buoyancy effects due to spatial perturbations of the mean flow field temperature about the adiabatic temperature profile. These effects are considered only in the body force term, B_i, of the momentum equation. That is, the fluid density is treated as a constant except in the body force term which is determined as:

$$\rho\vec{B} = - \rho g\hat{k} = - (\rho_0 + \Delta\rho)\ g\hat{k} \quad . \tag{A.10}$$

In Eq. (A.10), the ρ_0 is the fluid density at the reference temperature, $\bar{T}_0$, which is determined from the temperature profile of an adiabatic atmosphere as defined in Eq. (2.17).

Treating the fluid as an ideal gas, we have the following equation of state:

$$\rho = \frac{P}{RT} \quad . \tag{A.11}$$

In particular, at the reference state:

$$\rho_0 = \frac{\bar{P}_0}{R\bar{T}_0} \quad . \tag{A.12}$$

The density perturbation corresponding to a small perturbation from the reference state can be approximated as

$$\Delta\rho = \left.\frac{\partial\rho}{\partial T}\right|_0 \Delta T + \left.\frac{\partial\rho}{\partial P}\right|_0 \Delta P \quad . \tag{A.13}$$

Since the flow field velocities encountered in this study are much less than sonic, pressure effects on density can be neglected. The derivative of density with respect to temperature which appears in Eq. (A.13) can be evaluated at the reference state by using Eqs. (A.11) and (A.12). The density perturbation of Eq. (A.13) is then given by

$$\Delta\rho = \left.\frac{\partial\rho}{\partial T}\right|_0 \Delta T = -\frac{\rho_0}{\overline{T}_0}(\overline{T} - \overline{T}_0) \quad , \tag{A.14}$$

in which $\overline{T}$ is the mean temperature at the region of the flow field being considered.

Substituting Eqs. (A.14) and (A.10) into Eq. (A.9) gives the following form for the momentum equation:

$$\rho_0 \overline{U}_j \frac{\partial \overline{U}_i}{\partial x_j} = -\frac{\partial \overline{P}}{\partial x_i} + \frac{\partial}{\partial x_j}\left[\mu_{eff}\left(\frac{\partial \overline{U}_i}{\partial x_j} + \frac{\partial \overline{U}_j}{\partial x_i}\right)\right]$$

$$- g_i\left[\rho_0 - \rho_0\left(\frac{\overline{T} - \overline{T}_0}{\overline{T}_0}\right)\right] \quad . \tag{A.15}$$

In Eq. (A.15), $\overline{T}_0$ is the reference temperature determined from the adiabatic lapse rate as defined in Eq. (2.17), page 22, and $\overline{P}$ is the mean value of the absolute pressure which is the sum of the static pressure and the hydrodynamic or flow pressure. Throughout this study, the density, ρ, is treated as constant and equal to the reference density, ρ_0. Hereafter, the subscript 0 will be dropped from the reference density.

3. INTRODUCTION OF THE STREAM FUNCTION AND VORTICITY

For the modeling of the two-dimensional flow over a cooling tower, the momentum and continuity equations simplify to the following.

Momentum in the x-direction

$$\rho\bar{U}\frac{\partial\bar{U}}{\partial x} + \rho\bar{W}\frac{\partial\bar{U}}{\partial z} = -\frac{\partial\bar{P}}{\partial x} + \frac{\partial}{\partial x}\left[\mu_{eff}\left(2\frac{\partial\bar{U}}{\partial x}\right)\right]$$

$$+ \frac{\partial}{\partial z}\left[\mu_{eff}\left(\frac{\partial\bar{U}}{\partial z} + \frac{\partial\bar{W}}{\partial x}\right)\right] \qquad (A.16)$$

Momentum in the z-direction

$$\rho\bar{U}\frac{\partial\bar{W}}{\partial x} + \rho\bar{W}\frac{\partial\bar{W}}{\partial z} = -\frac{\partial\bar{P}}{\partial z} + \frac{\partial}{\partial x}\left[\mu_{eff}\left(\frac{\partial\bar{W}}{\partial x} + \frac{\partial\bar{U}}{\partial z}\right)\right]$$

$$+ \frac{\partial}{\partial z}\left[\mu_{eff}\left(2\frac{\partial\bar{W}}{\partial z}\right)\right] + \frac{\rho g\bar{T}}{\bar{T}_0} - 2\rho g \qquad (A.17)$$

Continuity

$$\frac{\partial\bar{U}}{\partial x} + \frac{\partial\bar{W}}{\partial z} = 0 \qquad (A.18)$$

Rather than solve the above fundamental equations for the primitive variables, $\bar{U}$, $\bar{W}$, and $\bar{P}$, the stream function, ψ, and vorticity, ω, are introduced. The stream function is defined in terms of the velocity components as:

$$\frac{\partial\psi}{\partial z} = \rho\bar{U} \quad , \qquad (A.19)$$

$$\frac{\partial\psi}{\partial x} = -\rho\bar{W} \quad . \qquad (A.20)$$

The vorticity is defined by:

$$\omega = \frac{\partial \overline{W}}{\partial x} - \frac{\partial \overline{U}}{\partial z} \quad . \tag{A.21}$$

A transport equation for the stream function can be derived by substituting Eqs. (A.19) and (A.20) into Eq. (A.21). The resulting stream function equation is:

$$\frac{\partial^2 \psi}{\partial x^2} + \frac{\partial^2 \psi}{\partial z^2} = - \rho\omega \quad . \tag{A.22}$$

A transport equation for the vorticity, including buoyancy effects, can be derived from the momentum equations. The x-momentum equation is differentiated with respect to z; the z-momentum equation is differentiated with respect to x. Then, one of the differentiated equations is subtracted from the other and, after various algebraic manipulations, the vorticity transport equation with buoyancy effects results:

$$\frac{\partial}{\partial x}\left[\omega \frac{\partial \psi}{\partial z}\right] - \frac{\partial}{\partial z}\left[\omega \frac{\partial \psi}{\partial x}\right] - \frac{\partial^2}{\partial x^2}\left[\mu_{eff}\omega\right]$$

$$- \frac{\partial^2}{\partial z^2}\left[\mu_{eff}\omega\right] - S_\omega = 0 \tag{A.23}$$

where:

$$S_\omega = 2\{- \frac{\partial^2}{\partial x \partial z}\left[\mu_{eff}\left[\frac{\partial \overline{U}}{\partial x} - \frac{\partial \overline{W}}{\partial z}\right]\right] + \frac{\partial^2}{\partial x^2}\left[\mu_{eff}\frac{\partial \overline{U}}{\partial z}\right]$$

$$- \frac{\partial^2}{\partial z^2}\left[\mu_{eff}\frac{\partial \overline{W}}{\partial x}\right]\} + \frac{\rho g}{\overline{T}_0}\frac{\partial \overline{T}}{\partial x} \quad . \tag{A.24}$$

The source term, S_ω, can be rearranged as follows:

$$S_\omega = 2.0\{- \frac{\partial \overline{U}}{\partial x} \frac{\partial^2 \mu_{eff}}{\partial x \partial z} + \frac{\partial \overline{U}}{\partial z} \frac{\partial^2 \mu_{eff}}{\partial^2 x} - \frac{\partial \overline{W}}{\partial x} \frac{\partial^2 \mu_{eff}}{\partial^2 z}$$

$$+ \frac{\partial \overline{W}}{\partial z} \frac{\partial^2 \mu_{eff}}{\partial z \partial x}\} + \frac{\rho g}{\overline{T}_0} \frac{\partial \overline{T}}{\partial x} \quad . \tag{A.25}$$

A more complete derivation for the vorticity transport equation is given in the work by Gosman, et al. [47].

4. TEMPERATURE TRANSPORT EQUATION

The energy equation, which is simplified by neglecting radiation heat flux and dissipation of kinetic energy, becomes identical to the transport equation of a scalar quantity as given by Hinze [65]:

$$\tilde{U}_j \frac{\partial \tilde{T}}{\partial x_j} = \frac{\partial}{\partial x_j} [\alpha \frac{\partial \tilde{T}}{\partial x_j}] \quad , \tag{A.26}$$

where $\tilde{T}$ is the instantaneous temperature and α is the molecular thermal diffusivity. The molecular thermal diffusivity is a fluid property which is assumed to be constant and is defined as:

$$\alpha = \frac{k}{\rho C_p} \quad , \tag{A.27}$$

where k is the thermal conductivity of the fluid and C_p is the constant pressure specific heat of the fluid. The instantaneous temperature, $\tilde{T}$, can be written as the sum of the mean temperature, $\overline{T}$, and the fluctuation about the mean, t:

$$\tilde{T} + T + t \quad . \tag{A.28}$$

Equation (A.28) can be substituted into Eq. (A.26) and the resulting equation Reynolds averaged to give:

$$\overline{U}_j \frac{\partial \overline{T}}{\partial x_j} + \frac{\partial}{\partial x_j} (\overline{tu_j}) = \frac{\partial}{\partial x_j} [\alpha \frac{\partial \overline{T}}{\partial x_j}] \quad . \tag{A.29}$$

Multiplying Eq. (A.29) by the constant fluid density and rearranging gives the following:

$$\rho \overline{U}_j \frac{\partial \overline{T}}{\partial x_j} = \frac{\partial}{\partial x_j} [\rho\alpha \frac{\partial \overline{T}}{\partial x_j}] - \frac{\partial}{\partial x_j} \rho\overline{tu_j} \quad . \tag{A.30}$$

The product of density times molecular thermal diffusivity can be expressed in terms of the Prandtl number, Pr, which is defined as follows:

$$Pr = \frac{\mu/\rho}{\alpha} \quad . \tag{A.31}$$

Thus,

$$\rho\alpha = \frac{\mu}{Pr} \quad . \tag{A.32}$$

In Eq. (A.30), the term $\overline{tu_j}$ is the correlation of the temperature fluctuation and the velocity fluctuation, similar to the Reynolds stress term of the momentum equation. This correlation can be modeled in a manner analogous to the modeling of the Reynolds stress term in Eq. (A.6) by using the turbulent viscosity of Eq. (A.6) and introducing a turbulent Prandtl number, Pr_t, as follows:

$$-\rho\overline{tu_j} = \frac{\mu_t}{Pr_t} \frac{\partial \overline{T}}{\partial x_j} \quad . \tag{A.33}$$

Eq. (A.32) and Eq. (A.33) can be substituted into Eq. (A.30) to give:

$$\rho\bar{U}_j \frac{\partial\bar{T}}{\partial x_j} = \frac{\partial}{\partial x_j}\left[\frac{\mu}{Pr} \frac{\partial\bar{T}}{\partial x_j}\right] + \frac{\partial}{\partial x_j}\left[\frac{\mu_t}{Pr_t} \frac{\partial\bar{T}}{\partial x_j}\right] \quad . \tag{A.34}$$

An effective Prandtl number, Pr_{eff}, can be defined such that:

$$\frac{\mu_{eff}}{Pr_{eff}} = \frac{\mu}{Pr} + \frac{\mu_t}{Pr_t} \quad . \tag{A.35}$$

Equation (A.34) with the inclusion of Eq. (A.35) yields the temperature transport equation as follows:

$$\rho\bar{U}_j \frac{\partial\bar{T}}{\partial x_j} = \frac{\partial}{\partial x_j}\left[\frac{\mu_{eff}}{Pr_{eff}} \frac{\partial\bar{T}}{\partial x_j}\right] \quad . \tag{A.36}$$

The effective Prandtl number is discussed in the section on Coefficient Functions.

5. TURBULENCE MODELING

As discussed earlier, the effects of turbulence in the flow field can be accounted for by a turbulent or eddy viscosity as in Eq. (A.6). As discussed by Bitte and Frost [48], the Prandtl-Kolmogorov formulation of the turbulent viscosity is used, whereby the turbulent viscosity is assumed to be dependent upon the turbulence kinetic energy, K, and the turbulence length scale, ℓ, as follows:

$$\mu_t = C_{\mu_\infty} \rho K^{1/2} \ell \quad . \tag{A.37}$$

C_{μ_∞} is an empirical constant which is discussed in the section on Coefficient Functions.

The turbulence kinetic energy, which characterizes the local level of turbulence, is defined to be the mean kinetic energy of the velocity fluctuations:

$$K = \frac{1}{2} (\overline{u^2} + \overline{v^2} + \overline{w^2}) \quad . \tag{A.38}$$

A transport equation for the turbulence kinetic energy is derived in the section on the Turbulence Kinetic Energy Equation.

The turbulence length scale represents the largest local velocity correlation distance or typical local eddy size. A transport equation for the length scale is discussed in the section on the Turbulence Length Scale Equation.

The turbulent viscosity, μ_t, and the molecular viscosity, μ, are both incorporated into an effective viscosity:

$$\mu_{eff} = \mu_t + \mu \quad . \tag{A.39}$$

Then, in regions of intense turbulence, the effective viscosity is due primarily to the turbulent contribution. However, in regions of low turbulence, the molecular viscosity becomes important. Thus, the effective viscosity adjusts to the flow field conditions.

6. TURBULENCE KINETIC ENERGY EQUATION

A detailed derivation of the turbulence kinetic energy equation is given in the work by Hinze [65]. This equation is derived from the momentum and continuity equations for turbulent flow. When applied to

the steady flow of an incompressible fluid, this equation becomes:

$$\rho\overline{U}_j \frac{\partial K}{\partial x_j} = -\frac{\partial}{\partial x_j}\left[\overline{u_j(p + \rho K)}\right] - \rho\overline{u_i u_j}\frac{\partial \overline{U}_i}{\partial x_j}$$

$$+ \mu \frac{\partial^2 K}{\partial x_j \partial x_j} - \mu \overline{\frac{\partial u_i}{\partial x_j}\frac{\partial u_i}{\partial x_j}} + g_j \frac{\rho\overline{u_j t}}{\overline{T}_0} \quad . \tag{A.40}$$

To solve this equation, various modeling assumptions must be made concerning the correlations of the fluctuating components [48, 49, 50].

The turbulent diffusion term is modeled by analogy to molecular diffusion as follows:

$$-\frac{\partial}{\partial x_j}\left[\overline{u_j(p + \rho K)}\right] = \frac{\partial}{\partial x_j}\left[\frac{\mu_t}{Sc_{K,t}}\frac{\partial K}{\partial x_j}\right] \quad , \tag{A.41}$$

wherein $Sc_{K,t}$ is a turbulent Schmidt number for turbulence kinetic energy. This model of the turbulent diffusion term can be combined with the molecular diffusion term as follows:

$$-\frac{\partial}{\partial x_j}\left[\overline{u_j(p + \rho K)}\right] + \mu \frac{\partial^2 K}{\partial x_j \partial x_j} = \frac{\partial}{\partial x_j}\left[\left(\frac{\mu_t}{Sc_{K,t}} + \mu\right)\frac{\partial K}{\partial x_j}\right]$$

$$= \frac{\partial}{\partial x_j}\left[\frac{\mu_{eff}}{Sc_{K,eff}}\frac{\partial K}{\partial x_j}\right] \quad , \tag{A.42}$$

wherein an effective Schmidt number for turbulence kinetic energy, $Sc_{K,eff}$, has been used. This effective Schmidt number is discussed in the section on Coefficient Functions.

The turbulence production term is modeled by making use of the Reynolds stress model already developed in Eq. (A.6):

$$-\rho\overline{u_i u_j}\frac{\partial \overline{U}_i}{\partial x_j} = \mu_t\left[\frac{\partial \overline{U}_i}{\partial x_j} + \frac{\partial \overline{U}_j}{\partial x_i}\right]\frac{\partial \overline{U}_i}{\partial x_j} \quad . \tag{A.43}$$

With justification from a dimensional argument, the dissipation term can be modeled as follows:

$$\mu \overline{\frac{\partial u_i \partial u_i}{\partial x_j \partial x_j}} = C_D \frac{\rho K^{3/2}}{\ell} \quad , \tag{A.44}$$

wherein C_D is an empirical coefficient function which will be discussed in the section on Coefficient Functions and ℓ is the turbulence length scale.

The buoyancy production term is modeled by making use of the model developed for the temperature-velocity correlation given by Eq. (A.33). The buoyancy production term then becomes:

$$g_j \frac{\overline{\rho u_j t}}{\overline{T}_0} = - \frac{g_j}{\overline{T}_0} \frac{\mu_t}{Pr_t} \frac{\partial \overline{T}}{\partial x_j} \quad . \tag{A.45}$$

Then, by substituting Eqs. (A.42), (A.43), (A.44), and (A.45) into Eq. (A.40), the modeled turbulence kinetic energy equation becomes:

$$\rho \overline{U}_j \frac{\partial K}{\partial x_j} = \frac{\partial}{\partial x_j} [\frac{\mu_{eff}}{Sc_{K,eff}} \frac{\partial K}{\partial x_j}] + \mu_t [\frac{\partial \overline{U}_i}{\partial x_j} + \frac{\partial \overline{U}_j}{\partial x_i}] \frac{\partial \overline{U}_i}{\partial x_j}$$

$$- C_D \frac{\rho K^{3/2}}{\ell} - \frac{g_j}{\overline{T}_0} \frac{\mu_t}{Pr_t} \frac{\partial \overline{T}}{\partial x_j} \quad . \tag{A.46}$$

The second term on the right-hand side of the turbulence kinetic energy equation can be rearranged to give the following:

$$\rho \overline{U}_j \frac{\partial K}{\partial x_j} = \frac{\partial}{\partial x_j} [\frac{\mu_{eff}}{Sc_{K,eff}} \frac{\partial K}{\partial x_j}] + \mu_t \{2[(\frac{\partial \overline{U}}{\partial x})^2 + (\frac{\partial \overline{W}}{\partial z})^2]$$

$$+ (\frac{\partial \overline{U}}{\partial z} + \frac{\partial \overline{W}}{\partial x})^2\} - C_D \frac{\rho K^{3/2}}{\ell} - \frac{g_j}{\overline{T}_0} \frac{\mu_t}{Pr_t} \frac{\partial \overline{T}}{\partial x_j} \quad . \tag{A.47}$$

7. TURBULENCE LENGTH SCALE EQUATION

Rotta (1951) first derived a differential equation for the turbulence length scale from the momentum equations. Following Rotta's example, Gosman et al. [47] derived an empirical form of the length scale transport equation. This equation was cast as an elliptic partial difference equation. This equation, with the inclusion of buoyancy effects, is given by:

$$\rho\bar{U}_j \frac{\partial \ell}{\partial x_j} = \frac{\partial}{\partial x_j}\left[\frac{\mu_{eff}}{Sc_{\ell,eff}} \frac{\partial \ell}{\partial x_j}\right] - C_B \mu_t \left[\frac{\partial \bar{U}_j}{\partial x_i} + \frac{\partial \bar{U}_i}{\partial x_j}\right] \frac{\partial \bar{U}_i}{\partial x_j} \frac{\ell}{K}$$

$$+ C_S \rho K^{1/2} - \frac{g_i}{\bar{T}_0} \frac{\ell}{K} \frac{\mu_t}{Pr_t} \frac{\partial \bar{T}}{\partial x_i} \quad . \tag{A.48}$$

The second term on the right side of the turbulence length scale equation can be rearranged to give the following:

$$\rho\bar{U}_j \frac{\partial \ell}{\partial x_j} = \frac{\partial}{\partial x_j}\left[\frac{\mu_{eff}}{Sc_{\ell,eff}} \frac{\partial \ell}{\partial x_j}\right] - C_B \frac{\ell}{K} \mu_t \{2[(\frac{\partial \bar{U}}{\partial x})^2 + (\frac{\partial \bar{W}}{\partial z})^2]$$

$$+ (\frac{\partial \bar{U}}{\partial z} + \frac{\partial \bar{W}}{\partial x})^2\} + C_S \rho K^{1/2} - \frac{\ell}{K} \frac{g_i}{\bar{T}_0} \frac{\mu_t}{Pr_t} \frac{\partial \bar{T}}{\partial x_i} \quad . \tag{A.49}$$

In Eq. (A.49), $Sc_{\ell,eff}$ is an effective turbulent Schmidt number for the turbulence length scale which is discussed in the section on Coefficient Functions. C_B and C_S are empirical functions which are also discussed in that section.

As discussed by Bitte and Frost [48], Eq. (A.49) consists of a convection term set equal to the sum of a diffusion term and three source terms. The first source term accounts for the tendency of the shear stress

to reduce the length scale by rupturing the larger eddies. The second term accounts for the rate of growth of the length scale, ℓ, as a result of the dissipation of energy, especially from the smaller eddies. As discussed by Pechinthorn [50], the last term represents the contributions to the length scale due to the buoyancy effects. This term originates from a proposal by Launder and Spalding [58].

8. COEFFICIENT FUNCTIONS

As discussed in the previous sections of this chapter, various empirical coefficients and coefficient functions appear in the transport equations and turbulence modeling. These will be discussed in the order in which they appeared in the foregoing text.

The quotient of effective viscosity divided by effective Prandtl number occurs in the temperature transport equation, Eq. (A.36). The effective Prandtl number is determined as a function of height, z, as proposed by Rotta [66]:

$$Pr_{eff}(z) = 0.9 \cdot (1.0 - 0.44(\frac{z}{\delta})^2) \quad . \tag{A.50}$$

In Eq. (A.50), δ is the thickness of the atmospheric boundary layer, which is assumed in this study to coincide with the top of the computational region.

An empirical constant, C_{μ_∞}, is used in the expression for the turbulent viscosity, Eq. (A.37). Following a proposal of Shieh [67], C_{μ_∞} is assigned the following value:

$$C_{\mu_\infty} = 0.416 \quad . \tag{A.51}$$

In Eq. (A.39), an effective viscosity is introduced as the sum of the turbulent viscosity plus the molecular viscosity. The effective viscosity can also be written, for purposes of theoretical analysis, as a function of the turbulence kinetic energy, the turbulence length scale, and a coefficient function, C_μ, as follows:

$$\mu_{eff} = C_\mu \rho K^{1/2} \ell \quad . \tag{A.52}$$

This coefficient function, C_μ, can then be written in terms of a turbulence Reynolds number, R_t, as follows:

$$C_\mu = C_{\mu_\infty} + \frac{1}{R_t} \tag{A.53}$$

where

$$R_t = \frac{\rho K^{1/2} \ell}{\mu} = \frac{\mu_t}{C_{\mu_\infty} \mu} \quad . \tag{A.54}$$

Then, at low levels of turbulence, R_t is very small and the function C_μ tends to the value $1/R_t$ which in turn causes the effective viscosity to tend towards the value of the molecular viscosity. Likewise, at high levels of turbulence, the function C_μ tends toward the value of C_{μ_∞}, which implies that the effective viscosity tends toward the value of the turbulent viscosity.

The above analysis shows that the function C_μ approaches the value C_{μ_∞} as the turbulence level increases. For this reason, the empirical constant, C_{μ_∞}, can be viewed as an asymptotic value of the coefficient function, C_μ, for turbulent recirculating atmospheric flows.

In Eq. (A.41), an effective Schmidt number, $Sc_{K,eff}$, is introduced for the diffusion of turbulence kinetic energy. Following the example of Shieh [49], $Sc_{K,eff}$ is assigned the value of unity which is consistent with most turbulent flow analyses and implies that the exchange rates of momentum and of turbulence kinetic energy are comparable.

An empirical coefficient function, C_D, is introduced in the dissipation term of the turbulence kinetic energy equation, Eq. (A.44). This function is a measure of the dissipation rate per unit volume of turbulence kinetic energy. It is assumed to have a form similar to that given for the function C_μ in Eq. (A.53):

$$C_D = C_{D_\infty} + \frac{1}{R_t} \quad . \tag{A.55}$$

Following a proposal of Shieh [67], C_{D_∞} is assigned the following value:

$$C_{D_\infty} = 0.416 \quad . \tag{A.56}$$

In Eq. (A.48), an effective Schmidt number, $Sc_{\ell,eff}$, is introduced for the diffusion of the turbulence length scale. As in the case of the turbulence kinetic energy, the effective Schmidt number for the length scale is assigned the value unity.

Also in Eq. (A.48), there occurs two coefficient functions, C_B and C_S. The function C_B represents the reduction of the turbulence length scale as a result of the rupturing of larger eddies. The function C_S represents the growth of the turbulence length scale as a result of the dissipation of smaller eddies. These functions are assumed to be of the

following form:

$$C_B = C_{B_\infty} + \frac{1}{R_t} \quad , \tag{A.57}$$

$$C_S = C_{S_\infty} + \frac{1}{R_t} \quad . \tag{A.58}$$

Following a proposal of Shieh [67], C_{B_∞} and C_{S_∞} are assigned the following values:

$$C_{B_\infty} = 1.55 \tag{A.59}$$

$$C_{S_\infty} = 0.645 \quad . \tag{A.60}$$

9. WIND FIELD PRESSURE EQUATION

The equation governing the wind field pressure distribution is derived from the momentum equations, Eq. (A.16) and Eq. (A.17), with the use of the continuity equation, Eq. (A.18). The x-momentum equation, Eq. (A.16), can be rearranged to give

$$\frac{\partial \overline{P}}{\partial x} = - \rho \overline{U} \frac{\partial \overline{U}}{\partial x} - \rho \overline{W} \frac{\partial \overline{U}}{\partial z} + 2 \frac{\partial \mu_{eff}}{\partial x} \frac{\partial \overline{U}}{\partial x} + 2\mu_{eff} \frac{\partial^2 \overline{U}}{\partial x^2}$$

$$+ \frac{\partial \mu_{eff}}{\partial z} \left(\frac{\partial \overline{U}}{\partial z} + \frac{\partial \overline{W}}{\partial x}\right) + \mu_{eff} \left(\frac{\partial^2 \overline{U}}{\partial z^2} + \frac{\partial^2 \overline{W}}{\partial z \partial x}\right) \tag{A.61}$$

The z-momentum equation, Eq. (A.18), can be rearranged to give

$$\frac{\partial \overline{P}}{\partial z} = - \rho \overline{U} \frac{\partial \overline{W}}{\partial x} - \rho \overline{W} \frac{\partial \overline{W}}{\partial z} + 2 \frac{\partial \mu_{eff}}{\partial z} \frac{\partial \overline{W}}{\partial z} + 2\mu_{eff} \frac{\partial^2 \overline{W}}{\partial z^2} + \frac{\partial \mu_{eff}}{\partial x} \left(\frac{\partial \overline{U}}{\partial z} + \frac{\partial \overline{W}}{\partial x}\right)$$

$$+ \mu_{eff} \left(\frac{\partial^2 \overline{U}}{\partial x \partial z} + \frac{\partial^2 \overline{W}}{\partial x^2}\right) + \frac{\rho g \overline{T}}{\overline{T}_0} - 2\rho g \quad . \tag{A.62}$$

The result of taking the horizontal derivative of Eq. (A.61) is shown in Table A.1. The result of taking the vertical derivative of Eq. (A.62) is shown in Table A.2.

The Poisson equation for the wind field pressure distribution is derived by adding the second derivatives of pressure as shown in Table A.1 and Table A.2. The sum of the corresponding 25 terms shown in these two tables can be simplified and combined using the fundamental law of continuity, Eq. (A.18), and the definition of vorticity, Eq. (A.21). The details of this simplification process are given forthwith.

Term number 2 and term number 14 combine using continuity, Eq. (A.18), to give zero. Term number 4 and term number 16 also combine to give zero using continuity. Terms 8, 12, 20, and 24 also drop out by combining and applying continuity.

Squaring the law of continuity, Eq. (A.18), leads to the following identity,

$$- \left[\left(\frac{\partial \overline{U}}{\partial x}\right)^2 + \left(\frac{\partial \overline{W}}{\partial z}\right)^2\right] = 2\left(\frac{\partial \overline{U}}{\partial x}\ \frac{\partial \overline{W}}{\partial z}\right) \quad . \tag{A.63}$$

This identity is used when combining terms 1, 3, 13, and 15 to give the following result,

$$+ 2\rho\left[\frac{\partial \overline{U}}{\partial x}\ \frac{\partial \overline{W}}{\partial z} - \frac{\partial \overline{U}}{\partial z}\ \frac{\partial \overline{W}}{\partial x}\right] \quad . \tag{A.64}$$

Terms 6, 7, 11, and 22 can be combined using the definitions of vorticity, Eq. (A.21), and stream function, Eq. (A.19) and Eq. (A.20), to give the following term,

$$- 2\ \frac{\partial \mu_{eff}}{\partial x}\ \frac{\partial \omega}{\partial z} \quad . \tag{A.65}$$

TABLE A.1

Derivative of Equation (A.61)

$$\left(\frac{\partial^2 \overline{P}}{\partial x^2} = \quad\right)$$

Term Number	Term
1	$-\rho\left(\frac{\partial \overline{U}}{\partial x}\right)^2$
2	$-\rho\overline{U}\,\frac{\partial^2 \overline{U}}{\partial x^2}$
3	$-\rho\,\frac{\partial \overline{W}}{\partial x}\,\frac{\partial \overline{U}}{\partial z}$
4	$-\rho\overline{W}\,\frac{\partial^2 \overline{U}}{\partial x \partial z}$
5	$+2\,\frac{\partial^2 \mu_{eff}}{\partial x^2}\,\frac{\partial \overline{U}}{\partial x}$
6	$+2\,\frac{\partial \mu_{eff}}{\partial x}\,\frac{\partial^2 \overline{U}}{\partial x^2}$
7	$+2\,\frac{\partial \mu_{eff}}{\partial x}\,\frac{\partial^2 \overline{U}}{\partial x^2}$
8	$+2\mu_{eff}\,\frac{\partial^3 \overline{U}}{\partial x^3}$
9	$+\frac{\partial^2 \mu_{eff}}{\partial x \partial z}\left(\frac{\partial \overline{U}}{\partial z} + \frac{\partial \overline{W}}{\partial x}\right)$
10	$+\frac{\partial \mu_{eff}}{\partial z}\left(\frac{\partial^2 \overline{U}}{\partial x \partial z} + \frac{\partial^2 \overline{W}}{\partial x^2}\right)$

TABLE A.1 (Continued)

Term Number	Term
11	$+\frac{\partial \mu_{eff}}{\partial x}\left(\frac{\partial^2 \overline{U}}{\partial z^2}+\frac{\partial^2 \overline{W}}{\partial z \partial x}\right)$
12	$+\mu_{eff}\left(\frac{\partial^3 \overline{U}}{\partial x \partial z^2}+\frac{\partial^3 \overline{W}}{\partial z \partial x^2}\right.$

TABLE A.2

Derivative of Equation (A.62)

$$\left(\frac{\partial^2 \overline{P}}{\partial z^2} = \quad\right)$$

Term Number	Term
13	$-\rho \frac{\partial \overline{U}}{\partial z} \frac{\partial \overline{W}}{\partial x}$
14	$-\rho \overline{U} \frac{\partial^2 \overline{W}}{\partial z \partial x}$
15	$-\rho \left(\frac{\partial \overline{W}}{\partial z}\right)^2$
16	$-\rho \overline{W} \frac{\partial^2 \overline{W}}{\partial z^2}$
17	$+2 \frac{\partial^2 \mu_{eff}}{\partial z^2} \frac{\partial \overline{W}}{\partial z}$
18	$+2 \frac{\partial \mu_{eff}}{\partial z} \frac{\partial^2 \overline{W}}{\partial z^2}$
19	$+2 \frac{\partial \mu_{eff}}{\partial z} \frac{\partial^2 \overline{W}}{\partial z^2}$
20	$+2\mu_{eff} \frac{\partial^3 \overline{W}}{\partial z^3}$
21	$+\frac{\partial^2 \mu_{eff}}{\partial z \partial x} \left(\frac{\partial \overline{U}}{\partial z} + \frac{\partial \overline{W}}{\partial x}\right)$
22	$+\frac{\partial \mu_{eff}}{\partial x} \left(\frac{\partial^2 \overline{U}}{\partial z^2} + \frac{\partial^2 \overline{W}}{\partial z \partial x}\right)$

TABLE A.2 (Continued)

Term Number	Term
23	$+\frac{\partial \mu_{eff}}{\partial z}\left(\frac{\partial^2 \overline{U}}{\partial x \partial z}+\frac{\partial^2 \overline{W}}{\partial x^2}\right)$
24	$+\mu_{eff}\left(\frac{\partial^3 \overline{U}}{\partial x \partial z^2}+\frac{\partial^3 \overline{W}}{\partial z \partial x^2}\right)$
25	$+\frac{\rho g}{\overline{T}_0}\frac{\partial \overline{T}}{\partial z}$

Performing a similar manipulation using the definitions of vorticity and stream function, terms 10, 18, 19, and 23 can be combined to give the following term,

$$+ 2 \frac{\partial \mu_{eff}}{\partial z} \frac{\partial \omega}{\partial x} \quad . \tag{A.66}$$

Term 9 and term 21 are simply added to give

$$+ 2 \frac{\partial^2 \mu_{eff}}{\partial x \partial z} \left(\frac{\partial \overline{U}}{\partial z} + \frac{\partial \overline{W}}{\partial x}\right) \quad . \tag{A.67}$$

The final result of this derivation is given as the sum of Eq. (A.64), Eq. (A.65), Eq. (A.66), Eq. (A.67) and terms 5, 17, and 25,

$$\frac{\partial^2 \overline{P}}{\partial x^2} + \frac{\partial^2 \overline{P}}{\partial z^2} = 2\rho\left[\frac{\partial \overline{U}}{\partial x} \cdot \frac{\partial \overline{W}}{\partial z} - \frac{\partial \overline{U}}{\partial z} \cdot \frac{\partial \overline{W}}{\partial x}\right] - 2 \frac{\partial \mu_{eff}}{\partial x} \frac{\partial \omega}{\partial z} + 2 \frac{\partial \mu_{eff}}{\partial z} \frac{\partial \omega}{\partial x}$$

$$+ 2 \frac{\partial^2 \mu_{eff}}{\partial z \partial x} \left[\frac{\partial \overline{U}}{\partial z} + \frac{\partial \overline{W}}{\partial x}\right] + 2 \frac{\partial^2 \mu_{eff}}{\partial x^2} \frac{\partial \overline{U}}{\partial x}$$

$$+ 2 \frac{\partial^2 \mu_{eff}}{\partial z^2} \frac{\partial \overline{W}}{\partial z} + \frac{\rho g}{\overline{T}_0} \frac{\partial \overline{T}}{\partial z} \quad . \tag{A.68}$$

This result, Eq. (A.68), is the Poisson equation which governs the wind field pressure distribution.

APPENDIX B

BOUNDARY CONDITIONS APPLIED TO THE WIND FIELD PRESSURE CALCULATION

The wind field pressure calculation, discussed in Section 8, Chapter 2, uses an alternating direction implicit technique. In this technique, the wind field computational region is swept first by rows, using Eq. (2.67), and then by columns, using Eq. (2.68). For row iteration, boundary conditions are required at the inflow, outflow, cooling tower front face, and cooling tower back face. For column iteration, boundary conditions are required at the upper boundary, ground level boundary, and along the top of the cooling tower, These boundary conditions are derived from the x-direction momentum equation, Eq. (2.70), and from the z-direction momentum equation, Eq. (2.69). These momentum equations are repeated here for convenience.

Momentum in the x-direction

$$\frac{\partial \overline{P}}{\partial x} = - \rho \overline{U} \frac{\partial \overline{U}}{\partial x} - \rho \overline{W} \frac{\partial \overline{U}}{\partial z} + 2 \frac{\partial \mu_{eff}}{\partial x} \frac{\partial \overline{U}}{\partial x}$$

$$+ \frac{\partial \mu_{eff}}{\partial z} \left(\frac{\partial \overline{U}}{\partial z} + \frac{\partial \overline{W}}{\partial x}\right) - \mu_{eff} \frac{\partial \omega}{\partial z} \qquad \text{(B.1)}$$

Momentum in the z-direction

$$\frac{\partial \overline{P}}{\partial z} = - \rho \overline{U} \frac{\partial \overline{W}}{\partial x} - \rho \overline{W} \frac{\partial \overline{W}}{\partial z} + 2 \frac{\partial \mu_{eff}}{\partial z} \frac{\partial \overline{W}}{\partial z} + \frac{\partial \mu_{eff}}{\partial x} \left(\frac{\partial \overline{U}}{\partial z} + \frac{\partial \overline{W}}{\partial x}\right)$$

$$+ \mu_{eff} \frac{\partial \omega}{\partial x} + \frac{\rho g \overline{T}}{\overline{T}_0} - 2\rho g \qquad \text{(B.2)}$$

Let F_x denote the forcing function or right-hand side of the x-direction momentum equation, Eq. (B.1), and let F_z denote the corresponding part of the z-direction momentum equation, Eq. (B.2). Then Eq. (B.1) and Eq. (B.2), when evaluated at node (i,j), become

$$\frac{\partial \overline{P}}{\partial x}(i,j) = F_x(i,j) \tag{B.3}$$

and,

$$\frac{\partial \overline{P}}{\partial z}(i,j) = F_z(i,j) \quad . \tag{B.4}$$

At node (i,j), the horizontal derivative of pressure in Eq. (B.3) can be approximated as a forward difference,

$$\frac{\partial \overline{P}}{\partial x}(i,j) \approx \frac{\overline{P}(i+1,j) - \overline{P}(i,j)}{\Delta x} \quad . \tag{B.5}$$

Substituting Eq. (B.5) into Eq. (B.3) yields a forward difference formulation for the x-direction momentum equation which can be solved for the pressure at node (i,j) to give

$$\overline{P}(i,j) = \overline{P}(i+1,j) - (\Delta x) \cdot F_x(i,j) \quad . \tag{B.6}$$

This is the boundary condition applied at a node (i,j) on the back face of the cooling tower.

Likewise, at node (i,j), the derivative of pressure in Eq. (B.3) can be approximated as a backward difference,

$$\frac{\partial \overline{P}}{\partial x}(i,j) \approx \frac{\overline{P}(i,j) - \overline{P}(i-1,j)}{\Delta x} \tag{B.7}$$

Substitution of Eq. (B.7) into Eq. (B.3) gives a back difference formulation which can also be solved for the pressure at node (i,j),

$$\overline{P}(i,j) = \overline{P}(i-1,j) + (\Delta x) \cdot F_x(i,j) \quad . \tag{B.8}$$

This is the condition which is applied to nodes (i,j) which lie either on the front face of the cooling tower or on the outflow boundary.

The vertical derivative of pressure in Eq. (B.4) can be approximated at node (i,j) as a forward difference,

$$\frac{\partial \overline{P}}{\partial z}(i,j) \approx \frac{\overline{P}(i,j+1) - \overline{P}(i,j)}{\Delta z} \tag{B.9}$$

which can be substituted into Eq. (B.4) to give a forward difference formulation of the z-direction momentum equation. This equation can be solved for the pressure at node (i,j) to give

$$\overline{P}(i,j) = \overline{P}(i,j+1) - (\Delta z) \cdot F_z(i,j) \quad . \tag{B.10}$$

This is the condition applied to nodes (i,j) which lie either on the ground level boundary or along the top of the cooling tower.

A backward difference formulation of the z-direction momentum equation can be derived by approximating the vertical derivative of pressure in Eq. (B.4) as a backward difference,

$$\frac{\partial \overline{P}}{\partial z}(i,j) \approx \frac{\overline{P}(i,j) - \overline{P}(i,j-1)}{\Delta z} \tag{B.11}$$

Substituting Eq. (B.11) into Eq. (B.4) and solving for the pressure at node (i,j) yields

$$\overline{P}(i,j) = \overline{P}(i,j-1) + (\Delta z) \cdot F_z(i,j) \quad . \tag{B.12}$$

This is the condition on the pressure at a node (i,j) on the upper boundary.

In summary, the row iteration requires boundary conditions at the inflow, outflow, cooling tower front face, and cooling tower back face. As discussed in Section 8, Chapter 2, the boundary condition at the inflow is given by integrating Eq. (B.2) with the ground level pressure

at the inflow set equal to the local ambient barometric pressure. At the outflow and at the cooling tower front face, the pressure boundary condition is given by Eq. (B.8). At the cooling tower back face, the condition is given by Eq. (B.6).

The column iteration requires boundary conditions at the upper boundary, ground level boundary and along the top of the cooling tower. The condition at the upper boundary is given by Eq. (B.12). At the ground level and along the top of the cooling tower, the boundary condition is specified in Eq. (B.10). The wind field pressure distribution is then calculated from Eq. (2.66) with the above boundary conditions using the alternating direction implicit technique discussed in Section 8, Chapter 2.

APPENDIX C

APPLICATION OF THE METHOD OF WEIGHTED RESIDUALS WITH THE GALERKIN PROCESS TO THE COOLING TOWER INTERNAL PRESSURE MODEL

The cooling tower internal pressure model makes use of a finite element algorithm given by Wilson and Nickell [62] which is based upon the work of Zienkiewicz and Cheung [63]. This algorithm for the analysis of heat transfer in plane and axisymmetric structures uses a linear triangular subelement to approximate the field variable. Thus, as discussed in Section 4, Chapter 3, and shown in Figure 3.7, page 61, each quadrilateral element of the cooling tower finite element discretization, Figure 3.5, page 55, is divided into four triangular subelements. This situation is depicted in Figure C.1, where the quadrilateral element, Q, with nodes 1 through 4, is divided into four triangular subelements, e_1, e_2, e_3, and e_4. This subdividing results in the creation of an additional center node, node 5 on Figure C.1.

As discussed in Section 4, Chapter 3, within each of these subelements the field variable, ϕ, is expressed as the sum of linear functions of the coordinates, called shape functions [63]. For example, in subelement e_1, ϕ is given as

$$\phi(x,z) = \phi_1 N_1(x,z) + \phi_2 N_2(x,z) + \phi_5 N_5(x,z) \quad , \tag{C.1}$$

wherein ϕ_i is the value of the field variable at node i and N_i is the linear shape function associated with node i.

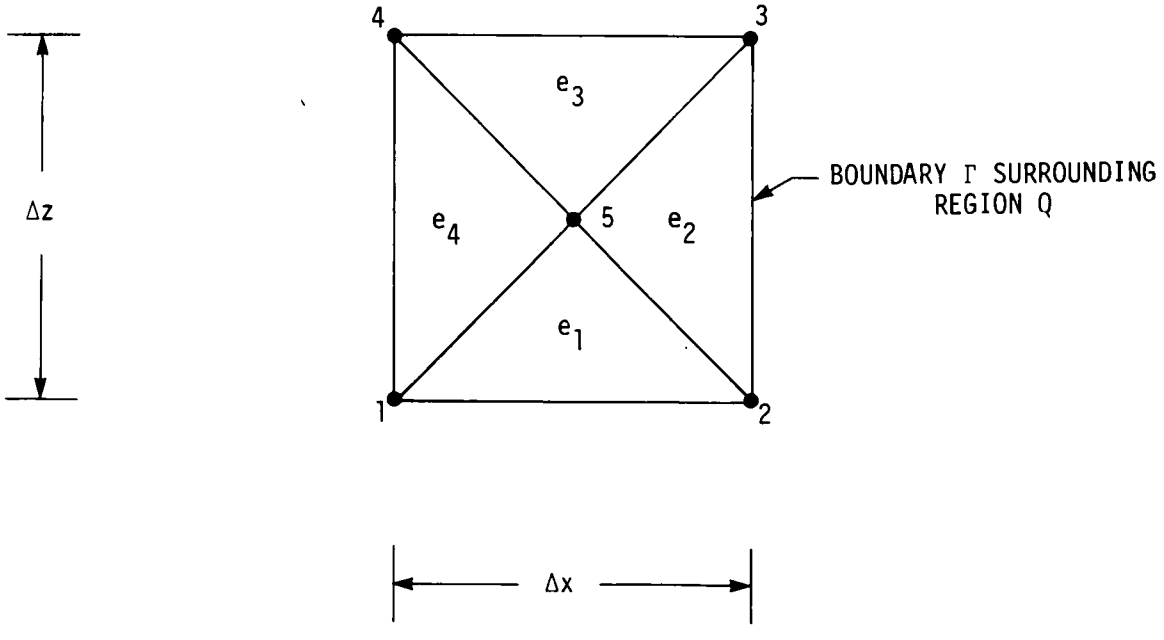


Figure C.1. Schematic of the subdivision of quadrilateral region Q.

The values of the shape functions N_1 through N_5 at the nodes 1 through 5 of Figure C.1 are given in Table C.1. Along the boundaries of each subelement, the shape function is a linear interpolation between the values of the shape function at the nodes forming the end points of the boundary. For example, shape function N_1 has the value one at node 1 and the value zero at node 5; between nodes 1 and 5, N_1 varies linearly between the values one and zero.

In the development of the finite element formulation using the method of weighted residuals with the Galerkin process, Zienkiewicz [68] shows that a function ϕ which satisfies the differential equation,

$$\nabla^2\phi = 0 \tag{C.2}$$

on a region Q must also satisfy the integral equation,

$$\iint_Q N_i \nabla^2\phi \, dA = 0 \quad , \tag{C.3}$$

wherein N_i is any shape function. Hildebrand [69] gives the first form of Green's theorem as

$$\iint_Q [N_i \nabla^2\phi + (\nabla N_i) \cdot (\nabla\phi)] \, dA = \oint_\Gamma N_i \frac{\partial\phi}{\partial n} \, ds \quad , \tag{C.4}$$

wherein Γ is the boundary of the region Q and $\frac{\partial\phi}{\partial n}$ is the normal derivative of ϕ at the boundary, Γ, of region Q. Rearranging Eq. (C.4) gives

$$- \iint_Q N_i \nabla^2\phi \, dA = \iint_Q (\nabla N_i) \cdot (\nabla\phi) \, dA - \oint_\Gamma N_i \frac{\partial\phi}{\partial n} \, ds \quad . \tag{C.5}$$

Combining Eq. (C.3) with Eq. (C.5) gives

$$\iint_Q (\nabla N_i) \cdot (\nabla\phi) \, dA - \oint_\Gamma N_i \frac{\partial\phi}{\partial n} \, ds = 0 \quad . \tag{C.6}$$

TABLE C.1

Values of the Shape Functions at the Nodes
of Region Q Shown in Figure C.1

Shape Function Number	Value of Shape Function at Node Number				
	1	2	3	4	5
N_1	1	0	0	0	0
N_2	0	1	0	0	0
N_3	0	0	1	0	0
N_4	0	0	0	1	0
N_5	0	0	0	0	1

Let the region, Q, of Eq. (C.6) be the quadrilateral element, Q, of Figure C.1 and let the arbitrary shape function, N_i, of Eq. (C.6) be the shape function, N_5, as evaluated in Table C.1, then Eq. (C.6) becomes

$$\iint_Q (\nabla N_5) \cdot (\nabla \phi)\, dA - \oint_\Gamma N_5 \frac{\partial \phi}{\partial n}\, ds = 0 \quad . \tag{C.7}$$

Since the shape function, N_5, as evaluated in Table C.1 is zero everywhere on the boundary, Γ, of the quadrilateral region, Q, the second integral in Eq. (C.7) vanishes,

$$\oint_\Gamma N_5 \frac{\partial \phi}{\partial n}\, ds = 0 \quad . \tag{C.8}$$

By using Eq. (C.1), ϕ can be expressed as

$$\phi = \sum_{i=1}^{5} N_i \phi_i \quad . \tag{C.9}$$

Substituting Eq. (C.8) and Eq. (C.9) into Eq. (C.7) gives

$$\iint_Q \nabla\left(\sum_{i=1}^{5} N_i \phi_i\right) \cdot (\nabla N_5)\, dA = 0 \quad . \tag{C.10}$$

Since the ϕ_i are constant values, Eq. (C.10) can be rearranged as

$$\sum_{i=1}^{5} \phi_i \iint_Q (\nabla N_i) \cdot (\nabla N_5)\, dA = 0 \quad . \tag{C.11}$$

As shown in Figure C.1, the region Q is the sum of the subelements, e_1, e_2, e_3, and e_4, thus Eq. (C.11) can be rewritten as

$$\sum_{i=1}^{5} \phi_i \sum_{j=1}^{4} \iint_{e_j} (\nabla N_i) \cdot (\nabla N_5)\, dA = 0 \quad . \tag{C.12}$$

Since the N_i are linear on each subelement, e_j, then the gradient of any of these shape functions, ∇N_i, is constant on each subelement, e_j, and can be moved outside the integral in Eq. (C.12),

$$\sum_{i=1}^{5} \phi_i \sum_{j=1}^{4} [(\nabla N_i) \cdot (\nabla N_5)]_{e_j} \iint_{e_j} dA = 0 \quad . \tag{C.13}$$

Now, for each j,

$$\iint_{e_j} dA = \frac{1}{4}(\Delta x)(\Delta z) \quad . \tag{C.14}$$

Thus, dividing Eq. (C.13) by the result of Eq. (C.14) gives

$$\sum_{i=1}^{5} \phi_i \sum_{j=1}^{4} [(\nabla N_j) \cdot (\nabla N_5)]_{e_j} = 0 \quad . \tag{C.15}$$

By using the values of the shape functions given in Table C.1, the values of the products of the gradients of the shape functions shown in Eq. (C.15) can be evaluated. These values are given in Table C.2.

Substituting the values given in Table C.2 into Eq. (C.15) and solving for the value of the field variable at node 5 gives the desired result,

$$\phi_5 = \frac{1}{4}(\phi_1 + \phi_2 + \phi_3 + \phi_4) \quad . \tag{C.16}$$

As discussed in Section 4, Chapter 3, this result is then used in Eq. (3.15) to evaluate the mass flux at the cooling tower inlet louvers.

TABLE C.2

Evaluation of the Products of the Gradients of the Shape Functions on the Subelements of Figure C.1

Product of the Gradients of the Shape Functions	Values of the Products of the Gradients of the Shape Functions Evaluated on Subelement Number			
	e_1	e_2	e_3	e_4
$(\nabla N_1) \cdot (\nabla N_5)$	$-\frac{2}{(\Delta z)^2}$	0	0	$-\frac{2}{(\Delta x)^2}$
$(\nabla N_2) \cdot (\nabla N_5)$	$-\frac{2}{(\Delta z)^2}$	$-\frac{2}{(\Delta x)^2}$	0	0
$(\nabla N_3) \cdot (\nabla N_5)$	0	$-\frac{2}{(\Delta x)^2}$	$-\frac{2}{(\Delta z)^2}$	0
$(\nabla N_4) \cdot (\nabla N_5)$	0	0	$-\frac{2}{(\Delta z)^2}$	$-\frac{2}{(\Delta x)^2}$
$(\nabla N_5) \cdot (\nabla N_5)$	$\frac{4}{(\Delta z)^2}$	$\frac{4}{(\Delta z)^2}$	$\frac{4}{(\Delta z)^2}$	$\frac{4}{(\Delta x)^2}$

APPENDIX D

METHOD OF DATA INPUT

The current model requires three different types of data: wind field parameters, wind field alphabetic data, and data controlling the cooling tower internal pressure model. The wind field parameters are input via a BLOCK DATA program segment. The alphabetic data which includes the title of the test case and the names of the variables is read from logical unit 5. The data to control the cooling tower internal pressure model is read from logical unit 25.

The wind field parameters are organized into nine common blocks which are initialized in the BLOCK DATA program segment shown in Figure D.1. As shown in this figure, the BLOCK DATA is self-explanatory with comment statements to define each variable. The names of the common blocks were chosen so as to organize the variables logically according to function.

The alphabetic data is used for headings and titles in the output of the current model. A sample of this data is given in Figure D.2. The first variable read is the title of the test case which can be up to 108 characters long. This title is read as the first three lines of Figure D.2, each of which is 36 characters long. The next 12 lines of Figure D.2 contain the names of the 12 variables being computed. The names appear in the same order as the variables appear in common block VFLAG, shown in Figure D.1. Each variable name can be up to 36 characters long. The last line of Figure D.2 contains five abbreviated titles which denote the residuals of the first five variables listed in common block VFLAG. Each of these abbreviated titles is six characters long. These titles are

```
      BLOCK DATA
C*************************************************************************
C*************************************************************************
C
C**** THIS BLOCK DATA IS USED TO INITIALIZE PROGRAM CONTROL VARIABLES
C****** AND WIND FIELD PARAMETERS INCLUDING FLOW FIELD GEOMETRY.
C
C*************************************************************************
C*************************************************************************
C
C** VARIABLES TO CONTROL PROGRAM RESTART
C
C=======================================================================
C**** NREAD IS A FLAG TO DETERMINE WHETHER INITIAL CONDITIONS
C****** SHOULD BE READ FROM ONLINE DATA SET.
C****** NREAD=0    MEANS NO ONLINE RESTART DATA SET.
C****** NREAD=1    MEANS READ INITIAL CONDITIONS FROM ONLINE DATA SET.
C
C**** NSTORE IS THE INTERVAL OF ITERATIONS BETWEEN WHICH THE VALUES OF
C****** THE VARIABLES ARE TO BE OUTPUT TO THE DATA SET FOR FUTURE
C****** RESTART PURPOSES.
C
C**** NSKIP IS THE NUMBER OF SETS OF RESTART DATA WHICH ARE TO BE
C****** SKIPPED BEFORE READING THE DESIRED RESTART DATA SET.
C=======================================================================
      COMMON/RESTRT/ NREAD,NSTORE,NSKIP
      DATA NREAD/1/,NSTORE/100/,NSKIP/3/
C
C
C*************************************************************************
C*************************************************************************
C
C** VARIABLES TO CONTROL PROGRAM PRINT-OUT AND CONVERGENCE
C
C=======================================================================
C**** NPRINT IS THE NUMBER OF ITERATIONS BETWEEN PRINT-OUT CYCLES
C
C**** IP IS THE NUMBER OF SUCCESSIVE ITERATIONS FOR WHICH PRINT-OUT IS
C****** TO BE PRODUCED IN EACH PRINT-OUT CYCLE.
C
C**** NMAX IS THE MAXIMUM NUMBER OF ITERATIONS TO BE PERFORMED.
C
C**** CC IS THE CONVERGENCE CRITERION.
C
C**** RP(K) IS THE RELAXATION PARAMETER FOR VARIABLE NUMBER K.
C
C**** FCC IS THE FINAL CONVERGENCE CRITERION.
C=======================================================================
      COMMON/CONTRL/ CC,RP(9),NPRINT,IP,NMAX,FCC
      DATA NPRINT/10000/,IP/1/,NMAX/10000/,CC/0.05/,FCC/0.30/
      DATA RP/.6D0,1.8D0,7*.1D0/
C
C
C*************************************************************************
```

Figure D.1. Example of the BLOCK DATA program segment used to initialize the values of the wind field parameters.

```
C*************************************************************************
C
C** FLAGS TO IDENTIFY THE VARIABLES
C
C=========================================================================
C**** NW=VORTICITY
C
C**** NF=STREAM FUNCTION
C
C**** NK=TURBULENCE KINETIC ENERGY
C
C**** NL=TURBULENCE LENGTH SCALE
C
C**** NT=TEMPERATURE
C
C**** NV1=DIRECTION 1 VELOCITY
C
C**** NV2=DIRECTION 2 VELOCITY
C
C**** NMU=EFFECTIVE VISCOSITY
C
C**** NRO=DENSITY
C
C**** NDIF=EFFECTIVE THERMAL DIFFUSIVITY
C
C**** NP=PRESSURE
C
C**** NTAU=TURBULENT SHEAR STRESS
C
C**** NEQN=NUMBER OF EQUATIONS TO BE SOLVED BY THE
C****** SUCCESSIVE SUBSTITUTION METHOD.
C=========================================================================
   COMMON/VFLAG/ NW,NF,NK,NL,NT,NV1,NV2,NMU,NRO,NDIF,NP,NTAU,NEQN
   DATA NW,NF,NK,NL,NT,NV1,NV2,NMU,NRO,NDIF,NP,NTAU,NEQN/
VFLAG2        1,2,3,4,5,6,7,8,9,10,11,12,5/
C
C
C*************************************************************************
```

Figure D.1. (Continued)

```
C*********************************************************************
C
C** VARIABLES TO CONTROL GRID GENERATION
C
C=====================================================================
C**** NCORD IS A FLAG TO SPECIFY WHICH COORDINATE SYSTEM
C****** IS BEING USED.
C****** NCORD=1 MEANS 2-D CARTESIAN COORDINATES.
C****** NCORD=2 MEANS 2-D CYLINDRICAL-POLAR COORDINATES.
C
C**** NNDDX IS THE NUMBER OF X1 GRID GROWTH FACTORS TO BE APPLIED--
C****** AT MOST 20.
C
C**** NDDX(I) IS THE NUMBER OF TIMES GROWTH FACTOR DDX(I) IS TO BE
C****** APPLIED.
C
C**** DDX(I) IS THE I-TH X1 GRID GROWTH FACTOR.
C
C**** NBACK IS THE NUMBER OF ADDITIONAL X1 GRID LINES TO BE GENERATED
C****** BEHIND THE COOLING TOWER.
C=====================================================================
C**** THE SUM OF THE 'NDDX(I)' ,WHERE I GOES  FROM I=1, TO I='NNDDX',
C****** MUST EQUAL TO 'ICTFRT'-1, WHERE 'ICTFRT' IS INITIALIZED
C****** IN COMMON/CTGEOM/ BELOW.
C=====================================================================
C**** NNDDY IS THE NUMBER OF X2 GRID GROWTH FACTORS TO BE APPLIED--
C****** AT MOST 20.
C
C**** NDDY(J) IS THE NUMBER OF TIMES GROWTH FACTOR DDY(J) IS TO BE
C****** APPLIED.
C
C**** DDY(J) IS THE J-TH X2 GRID GROWTH FACTOR.
C
C=====================================================================
C**** THE SUM OF THE 'NDDY(J)' ,WHERE J GOES  FROM J=1, TO J='NNDDY',
C****** MUST EQUAL TO 'JN' - 1.  'JN' IS INITIALIZED IN THE MAIN
C****** ROUTINE.
C=====================================================================
   COMMON/GRIDS/ DDX(20),DDY(20),NDDX(20),NDDY(20),
GRIDS2                 NNDDX,NNDDY,NBACK,NCORD
   DATA NCORD/1/,NNDDX/8/,NBACK/10/,NNDDY/2/
   DATA DDX/2.0D0,1.0D0,2.0D0,1.0D0,2.0D0,1.0D0,2.0D0,1.0D0,
     2           12*0.0D0/
   DATA NDDX/   1,    3,    1,    7,    1,    2,    1,    5,
     2           12*0/
   DATA DDY/1.0D0,1.2D0,18*0.0D0/
   DATA NDDY/  13,   19,    18*0/
C
C
C*********************************************************************
```

Figure D.1. (Continued)

```
C*********************************************************************
C
C** VARIABLES TO CONTROL COOLING TOWER SIZE
C
C=====================================================================
C**** CTHIGH IS THE COOLING TOWER HEIGHT (CM)
C
C**** CTWIDE IS THE COOLING TOWER WIDTH (CM)
C
C**** JCTTOP IS THE NUMBER OF THE X2 GRID LINE FORMING THE TOP OF THE
C****** COOLING TOWER.
C
C**** ICTFRT IS THE NUMBER OF THE X1 GRID LINE FORMING THE FRONT OF
C****** THE COOLING TOWER.
C
C**** ICTBAK IS THE NUMBER OF X1 GRID LINE FORMING THE BACK OF THE
C****** COOLING TOWER.
C
C**** JTOPLV IS THE NUMBER OF THE X2 GRID LINE FORMING THE TOP OF THE
C****** COOLING TOWER LOUVER.
C
C**** JBOTLV IS THE NUMBER OF THE X2 GRID LINE FORMING THE BOTTOM OF
C****** THE COOLING TOWER LOUVER.
C
C**** IFAN(1) IS THE NUMBER OF THE X1 GRID LINE FORMING THE LEFT EDGE
C****** OF THE FRONT FAN SLOT.
C
C**** IFAN(2) IS THE NUMBER OF THE X1 GRID LINE FORMING THE RIGHT EDGE
C****** OF THE FRONT FAN SLOT.
C
C**** IFAN(3) IS THE NUMBER OF THE X1 GRID LINE FORMING THE LEFT EDGE
C****** OF THE BACK FAN SLOT.
C
C**** IFAN(4) IS THE NUMBER OF THE X1 GRID LINE FORMING THE RIGHT EDGE
C****** OF THE BACK FAN SLOT.
C=====================================================================
C**** 'NBACK' + 'ICTFRT' + 'ICTBAK' - 1 MUST EQUAL TO 'IN'.
C****** 'IN' IS INITIALIZED IN THE MAIN ROUTINE.
C=====================================================================
   COMMON/CTGEOM/ CTHIGH,CTWIDE,JCTTOP,ICTFRT,ICTBAK,
TGEOM2                  JTOPLV,JBOTLV,IFAN(4)
   DATA CTHIGH/1100.0/,CTWIDE/1800.0/,JCTTOP/9/,ICTFRT/22/,
     2       ICTBAK/46/,JTOPLV/7/,JBOTLV/2/,IFAN/30,32,36,38/
C
C
C*********************************************************************
```

Figure D.1. (Continued)

```
C*************************************************************************
C
C** VARIABLES TO CONTROL THE LOGARITHMIC WIND VELOCITY PROFILE
C
C=========================================================================
C**** ZO IS SURFACE ROUGHNESS (CM) AT GROUND LEVEL.
C
C**** ZOCT IS SURFACE ROUGHNESS (CM) ON THE COOLING TOWER.
C
C**** USTR IS FRICTION VELOCITY (CM/SEC)
C=========================================================================
      COMMON/LOGPRO/ ZO,ZOCT,USTR
      DATA ZO/40.0/,ZOCT/1.0D0/,USTR/73.66/
C
C
C*************************************************************************
C*************************************************************************
C
C** COEFFICIENTS FOR TURBULENCE MODELING
C
C=========================================================================
C**** CCC IS THE CONSTANT, C-SUB-MU-SUB-INFINITY, OF THE COEFFICIENT
C******* FUNCTION, C-SUB-MU, FOR THE EFFECTIVE VISCOSITY.
C
C**** CDD IS THE CONSTANT, C-SUB-D-SUB-INFINITY, OF THE COEFFICIENT
C******* FUNCTION, C-SUB-D.  C-SUB-D IS THE COEFFICIENT FUNCTION FOR THE
C******* DISSIPATION TERM IN THE TURBULENCE KINETIC ENERGY EQUATION.
C
C**** CBB IS THE CONSTANT, C-SUB-B-SUB-INFINITY, OF THE COEFFICIENT
C******* FUNCTION, C-SUB-B.  C-SUB-B IS THE COEFFICIENT FUNCTION FOR THE
C******* REDUCTION TERM IN THE SOURCE TERMS FOR THE TURBULENCE LENGTH
C******* SCALE.
C
C**** CSS IS THE CONSTANT, C-SUB-S-SUB-INFINITY, OF THE COEFFICIENT
C******* FUNCTION, C-SUB-S.  C-SUB-S IS THE COEFFICIENT FUNCTION FOR THE
C******* GROWTH TERM IN THE SOURCE TERMS FOR THE TURBULENCE LENGTH SCALE.
C=========================================================================
      COMMON/TURBCO/ CCC,CDD,CBB,CSS
      DATA CCC/0.416D0/,CDD/0.416D0/,CBB/1.550D0/,CSS/0.645D0/
C
C
C*************************************************************************
```

Figure D.1. (Continued)

```
C*********************************************************************
C
C** FLUID PROPERTIES
C
C=====================================================================
C**** ROREF IS THE REFERENCE DENSITY (GM/CM**3)
C
C**** ZMUREF IF THE REFERENCE (MOLECULAR) VISCOSITY (DYNE-SEC/CM**2)
C
C**** PR(K) IS THE PRANDTL NUMBER OR SCHMIDT NUMBER OF VARIABLE K.
C=====================================================================
      COMMON/FLUIDP/ ROREF,ZMUREF,PR(9)
      DATA ROREF/0.00125D0/,ZMUREF/0.000181D0/
      DATA PR/4*1.0D0,.9D0,4*1.0D0/
C
C
C*********************************************************************
C*********************************************************************
C
C** VARIABLES TO CONTROL TEMPERATURE DISTRIBUTION
C
C=====================================================================
C**** TGRND IS THE TEMPERATURE AT THE GROUND LEVEL BOUNDARY (DEGREES K)
C
C**** TCTTOP IS THE TEMPERATURE AT THE TOP OF THE COOLING TOWER
C******  (DEGREES K)
C=====================================================================
      COMMON/TMPTUR/ TGRND,TCTTOP
      DATA TGRND/293.0D0/,TCTTOP/323.0D0/
C
C
C*********************************************************************
C*********************************************************************
C
C** GEOMETRY NOTATION USED BY BITTE AND GOSMAN
C
C=====================================================================
      COMMON/GEOMTY/ IBM,IB,IBB,IBP,INM,JB,JNM
C
C
C*********************************************************************
C*********************************************************************
C** DIMENSIONS OF ARRAY A AS USED BY GOSMAN.
C=====================================================================
      COMMON/N1N2N3/ N1,N2,N3
C
C
C*********************************************************************
C*********************************************************************
C
C
      DATA RSDU(1),RSDU(2),RSDU(3),RSDU(4),RSDU(5),RSDU(6),RSDU(7),
     1RSDU(8),RSDU(9)/0.,0.,0.,0.,0.,0.,0.,0.,0./
C
      END
```

Figure D.1. (Continued)

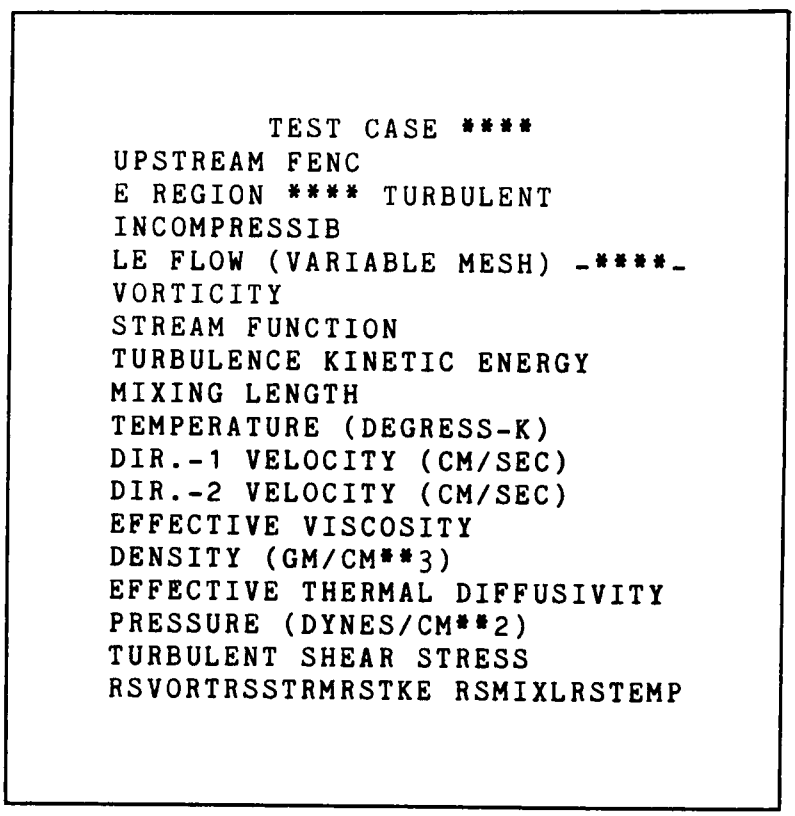


Figure D.2. Example of the wind field alphabetic data which is read from logical unit 5.

used in the printout of the residuals or maximum relative error which is the convergence criterion discussed in Section 1 of Chapter 4, Computational Technique.

The last type of data is that which controls the cooling tower internal pressure model. As discussed in Chapter 3, the cooling tower internal pressure model is a finite element model which, in its present form, contains 227 nodes, 202 elements, and 4 materials. The input data gives the hydraulic mass conductivities of each of the four materials followed by geometric data concerning the nodes and elements. A sample of this data is given in Figure D.3.

This data requires four different types of cards which are formatted as follows:

1. Control Card - (3I5)

Columns	1 - 5	Number of node points (227)
	6 - 10	Number of elements (202)
	11 - 15	Number of materials (4)

2. Material Property Cards - (I10, F10.0)

One card for each material.

Columns	1 - 10	Material number
	11 - 20	Hydraulic mass conductivity

3. Node Point Cards - (2I5, 2F10.0)

One card for each node point except those generated by the code. See below.

Columns	1 - 5	Node point number
	10	= 0 or blank if a specified mass flow boundary condition is used
		= 1 if a specified pressure boundary condition is used

```
227   202     4
          1  1.06253D0
          2  1.6340D-1
          3  1.50000D0
          4  1.0000D-7
  1       0        0.0          0.0
 25       0     1800.0          0.0
 26       0        0.0        137.5
 34       0      600.0        137.5
 35       0      650.0        137.5
 36       0      700.0        137.5
 37       0      775.0        137.5
 38       0      900.0        137.5
 39       0     1025.0        137.5
 40       0     1100.0        137.5
 41       0     1150.0        137.5
 42       0     1200.0        137.5
 50       0     1800.0        137.5
 51       1        0.0        275.0
 59       0      600.0        275.0
 60       0      650.0        275.0
 61       0      725.0        275.0
 62       0      825.0        275.0
 64       0      975.0        275.0
 65       0     1075.0        275.0
 66       0     1150.0        275.0
 67       0     1200.0        275.0
 75       1     1800.0        275.0
 76       1        0.0        412.5
100       1     1800.0        412.5
101       1        0.0        550.0
107       0      450.0        550.0
108       0      500.0        550.0
109       0      550.0        550.0
110       0      625.0        550.0
111       0      675.0        550.0
117       0     1125.0        550.0
118       0     1175.0        550.0
```

Figure D.3. Example of the data which controls the cooling tower internal pressure model and is read from logical unit 25.

119	0	1250.0			550.0
120	0	1300.0			550.0
121	0	1350.0			550.0
127	1	1800.0			550.0
128	1	0.0			687.5
134	0	450.0			687.5
135	0	500.0			687.5
136	0	575.0			687.5
137	0	675.0			687.5
143	0	1125.0			687.5
144	0	1225.0			687.5
145	0	1300.0			687.5
146	0	1350.0			687.5
152	1	1800.0			687.5
153	0	0.0			825.0
177	0	1800.0			825.0
178	0	0.0			962.5
186	0	600.0			962.5
194	0	1200.0			962.5
202	0	1800.0			962.5
203	0	0.0			1100.0
210	0	525.0			1100.0
211	0	600.0			1100.0
212	0	675.0			1100.0
213	0	750.0			1100.0
217	0	1050.0			1100.0
218	0	1125.0			1100.0
219	0	1200.0			1100.0
220	0	1275.0			1100.0
227	0	1800.0			1100.0
1	1	2	27	26	2
2	2	3	28	27	3
3	3	4	29	28	1
4	4	5	30	29	1
10	10	11	36	35	3
11	11	12	37	36	2
12	12	13	38	37	3
14	14	15	40	39	2

Figure D.3. (Continued)

15	15	16	41	40	3
16	16	17	42	41	1
22	22	23	48	47	1
23	23	24	49	48	3
24	24	25	50	49	2
25	26	27	52	51	2
26	27	28	53	52	3
27	28	29	54	53	1
28	29	30	55	54	1
34	35	36	60	60	3
35	36	37	61	60	2
36	37	62	61	61	3
37	37	38	63	62	3
39	39	65	64	64	3
40	39	40	66	65	2
41	40	41	66	66	3
42	41	42	67	66	1
48	47	48	73	72	1
49	48	49	74	73	3
50	49	50	75	74	2
51	51	52	77	76	2
52	52	53	78	77	1
53	53	54	79	78	1
58	58	59	84	83	3
59	59	60	84	84	3
60	60	61	85	84	2
61	61	86	85	85	3
62	61	62	87	86	3
66	65	91	90	90	3
67	65	66	92	91	2
68	66	67	92	92	3
69	67	68	93	92	3
70	68	69	94	93	1
75	73	74	99	98	1
76	74	75	100	99	2
77	76	77	102	101	2
78	77	78	103	102	1
84	83	84	109	108	3

Figure D.3. (Continued)

85	84	85	110	109	2
86	85	111	110	110	3
87	85	86	112	111	3
93	91	118	117	117	3
94	91	92	119	118	2
95	92	93	120	119	3
96	93	94	121	120	1
102	99	100	127	126	2
103	101	102	129	128	2
104	102	103	130	129	1
110	108	109	135	135	3
111	109	110	136	135	2
112	110	111	137	136	3
120	118	119	145	144	2
121	119	120	145	145	3
122	120	121	146	145	1
128	126	127	152	151	2
129	128	129	154	153	2
130	129	130	155	154	1
135	134	135	159	159	3
136	135	136	160	159	2
137	136	161	160	160	3
138	136	137	162	161	3
146	144	170	169	169	3
147	144	145	171	170	2
148	145	146	171	171	3
149	146	147	172	171	1
154	151	152	177	176	2
155	153	154	179	178	4
162	160	161	186	185	3
172	170	171	196	195	4
179	178	179	204	203	4
186	185	186	211	210	3
196	195	196	221	220	4
202	201	202	227	226	4

Figure D.3. (Continued)

3. Node Point Cards (Contd.)

Columns 11 - 20 x coordinate

21 - 30 z coordinate

For insulated nodes, a mass flow boundary condition of zero mass flow is specified.

Node point cards must be in numerical sequence. If cards are omitted, the omitted nodal points are generated at equal intervals along a straight line between the specified nodal points. For the generated points, the information equivalent to column 10 and columns 31 - 40 is set equal to zero.

4. Element Cards - (6I5)

One card for each element except those generated by the code. See below.

Columns	1 - 5	Element number
	6 - 10	Node point I
	11 - 15	Node point J
	16 - 20	Node point K
	21 - 25	Node point L
	26 - 30	Material identification

Nodal point numbers (I, J, K, and L) must be in counterclockwise order around each element. Maximum difference between nodal point numbers must be less than 30.

Element cards must be in element number sequence. If element cards are omitted, the program automatically generates the omitted information by incrementing the preceding I, J, K, and L. The information in columns 26 - 30 for the generated cards is set equal to the

values given on the preceding card. The last element card must always be supplied.

Triangular elements are also possible and are identified by repeating the last nodal point number (i.e., I, J, K, K).

VITA

Bryan Russell Becker was born in St. Louis, Missouri, on August 6, 1948. He attended primary and secondary schools in that city and was graduated from Lindbergh High School in June, 1966. The following September he entered the University of Missouri at Rolla and in July, 1971, received a Bachelor of Science degree in Mechanical Engineering.

Concurrently, he worked as a co-op student at McDonnell-Douglas Corporation in St. Louis, Missouri, from September, 1967, to May, 1968, and at Xerox Corporation in Rochester, New York, from September, 1969, to June, 1971. He worked as an engineer at Xerox Corporation from March, 1972, to September, 1972. He accepted a position in the Special Education Department of the Rochester School District from August, 1972, to September, 1973.

In the fall of 1973 he accepted a teaching assistantship at the University of Missouri at Columbia and began study toward a Master of Science degree in Applied Mathematics. This degree was awarded in May, 1975.

In June, 1975, he accepted a position with his present employer, Union Carbide Corporation, Nuclear Division, in Oak Ridge, Tennessee. Concurrently, he studied at the University of Tennessee Space Institute and received the Doctor of Philosophy degree in Engineering Science from that institution in December, 1979.

He is married to the former Nancy Ann Laemlein of Honeoye Falls, New York.